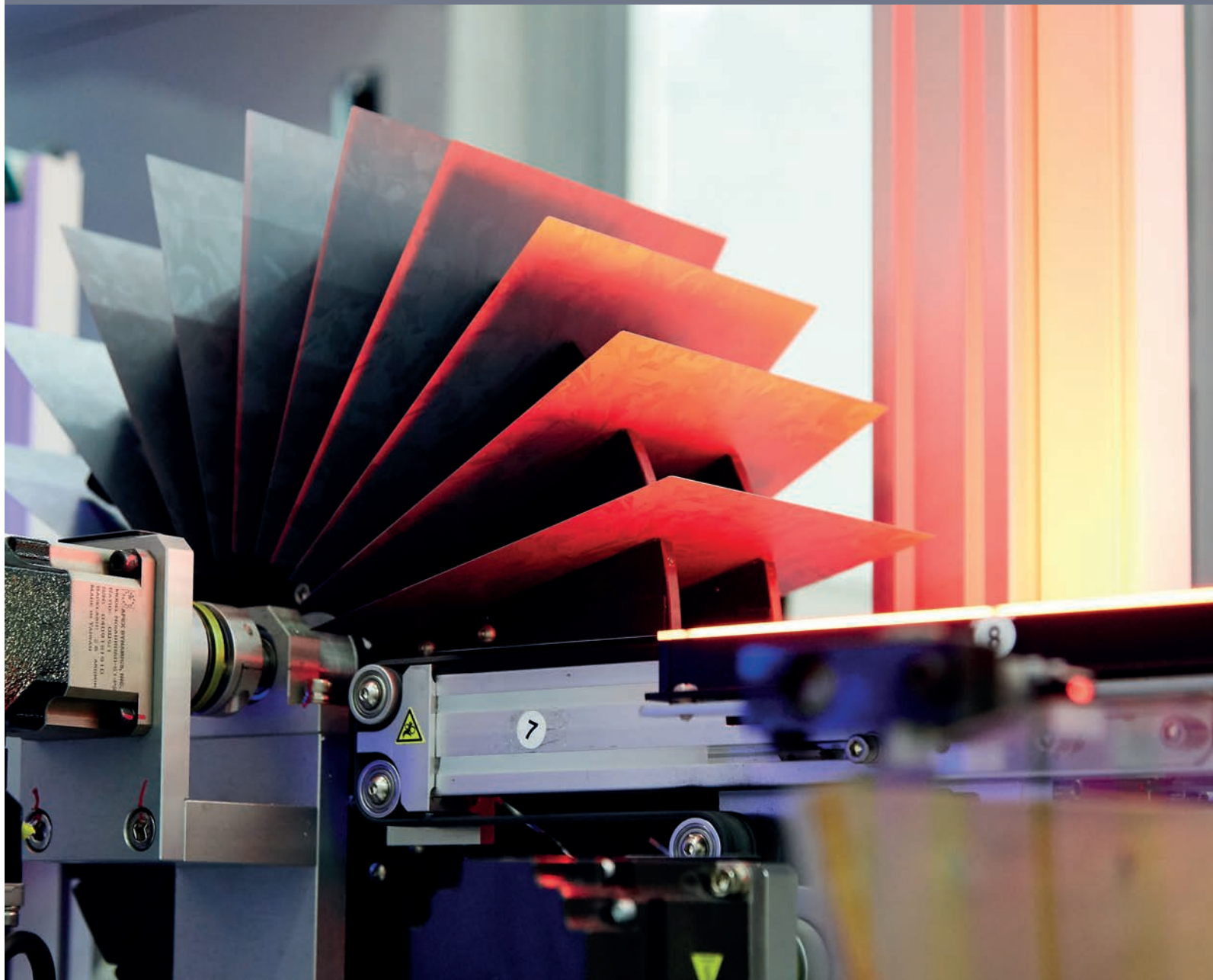


Photovoltaics International

THE TECHNOLOGY RESOURCE FOR PV PROFESSIONALS



Edition 42

Meet MoSoN cell technology

ISC Konstanz shows pathway to low-cost nPERT solar cells at 23% conversion efficiency

Half-cell technology

Fraunhofer CSP explains why solar modules with half-size solar cells could become the standard

ECA interconnection

Led by PCCL research, ECA offers low temperature processing and the potential for higher resolution printing with easier handling

Heterojunction technology

EPFL points to HJ solar cell solutions for driving-down manufacturing cost for mainstream volume production

Industry 4.0

Fraunhofer ISE makes the case for the 'digitalization' of PV cell and module manufacturing to further reduce costs

www.pv-tech.org
PVTECH
ORG

PERC PATENT HOLDER

Harvest the Sunshine

Here Comes Another Reason to Choose JA Solar:

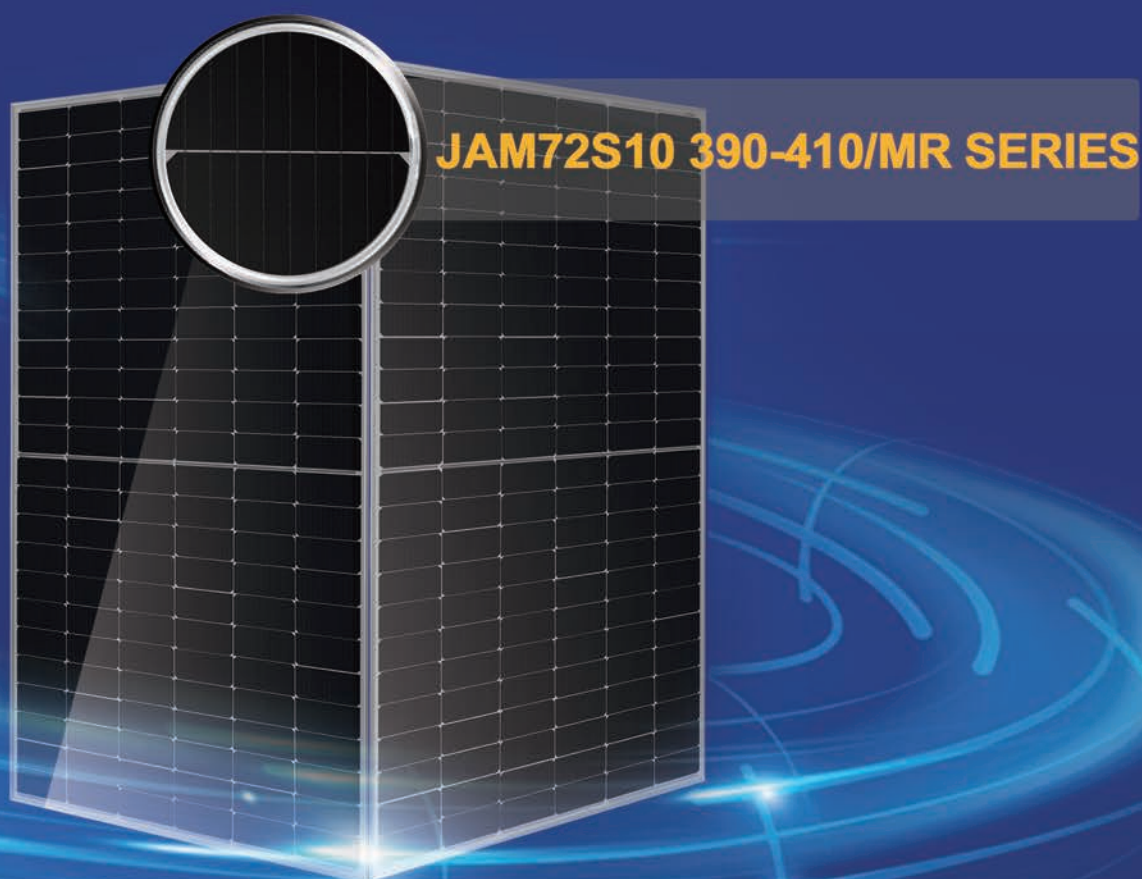
72-Cell Multi-Busbar Half-Cell Module

410W Higher Power Output

20.4% Higher Conversion Efficiency

3.70% Less Shading Loss

-0.35%/°C Better Temperature Coefficient



JA SOLAR

Tel: +86(10) 6361 1888
Email: sales@jasolar.com marketing@jasolar.com
www.jasolar.com

Published by:
Solar Media Ltd.,
123 Buckingham Palace Rd
Victoria, London SW1W 9SH
United Kingdom
T: +44 (0) 207 871 0122
T: +44 (0) 7827 885311
E info@pv-tech.org
www.pv-tech.org

Publisher: **David Owen**

Head of Content: **John Parnell**
Technical Publishing Director: **Mark Osborne**
Commissioning Editor: **Adam Morrison**
Sub-Editor: **Steve D. Brierley**
Design: **Tina Davidian**
Production: **Daniel H Brown, Sarah-Jane Lee**
Sales Director: **David Evans**
Account Managers: **Adam Morrison,**
Graham Davie, Lili Zhu

While every effort has been made to ensure the accuracy of the contents of this journal, the publisher will accept no responsibility for any errors, or opinion expressed, or omissions, or for any loss or damage, consequential or otherwise, suffered as a result of any material here published.

Cover image: Solar cell production line

Image courtesy of Hanwha Q CELLS

Printed by Buxton Press

Photovoltaics International
Forty Second Edition
February 2019
Photovoltaics International is a six monthly journal published in February and September each year.

Distributed in the USA by Mail Right
International, 1637 Stelton Road B4, Piscataway,
NJ 08854.

ISSN: 1757-1197

The entire contents of this publication are protected by copyright, full details of which are available from the publisher. All rights reserved. No part of this publication may be reproduced, stored in a retrieval system or transmitted in any form or by any means – electronic, mechanical, photocopying, recording or otherwise – without the prior permission of the copyright owner.

USPS Information
USPS Periodical Code: 025 313

Periodicals Postage Paid at
New Brunswick, NJ
Postmaster: Send changes to:
Photovoltaics International,
Solar Media Ltd., C/o 1637 Stelton Road,
B-4, Piscataway, NJ 08854, USA

Foreword

Welcome to Photovoltaics International 42. With a recent spate of new solar cell records announced for PERC-based architectures pushing conversion efficiencies past 24%, it is a good time to reflect on the pioneering work at SolarWorld – the first to commercialise and ramp PERC to volume production. A special in-depth paper from former members of SolarWorld's R&D and manufacturing team should be a compelling read and a leading reference paper in the future. Adding to the PERC-based theme is the paper from ISC Konstanz, providing further real world insight into achieving manufacturability of nPERT cells with conversion efficiencies approaching 23%.

As PERC is increasingly becoming the de facto cell technology in the PV industry, the trend for larger wafers has led to greater commercialisation of half-cell modules. It could become a new standard practice, according to the paper by Fraunhofer CSP in this edition. However, challenges still remain in areas such as LID and work being undertaken enable truly PIF-free solutions as characterised by the collaborative paper by ISFH, Leibniz Universität and LONGi Group.

Continuing to be seen as the best post-PERC cell technology, a paper by EPFL, CSEM and CEA-INES researchers explains how close silicon heterojunction technology is to being adopted as the next mainstream cell. Ongoing manufacturing cost reductions strengthen the case.

However, the same could be said of large-area perovskite-based tandem solar cells in a paper presented by imec on the strong potential for this low-cost, high-efficiency technology.

Indeed, the need for further cost reductions is running in parallel with fully-automated un-manned production cell and module lines, characterised by Industry 4.0 developments covered in a paper from Fraunhofer ISE. The paper looks at the impact of digitalization for smart fabs of the near future. An increasing number of PV manufacturers are establishing Industry 4.0 pilot schemes, which is also a special feature of my paper covering new capacity expansion announcements through 2018, data that is now five-years in the making.

With the continued migration to high-efficiency solar cells, new testing approaches such as LED-based solar simulators are required. The second paper from Fraunhofer CSP looks at special solutions for xenon-based systems and LED-based systems to effectively meet industry needs.

This theme is carried over in a paper from researchers at ECN|TNO that have studied the higher temperature factors encountered with bifacial cells and modules when compared to monofacial modules from tests in The Netherlands.

Regular readers of Photovoltaics International will likely spot some subtle changes introduced in this edition, primarily providing greater space for an increased number of technical papers to be showcased but also enabling in-depth papers of special interest. We would like to thank all of our contributors in making this edition possible and look forward to our readers' response.

Mark Osborne

Senior News Editor and Technical Publishing Director
Solar Media Ltd

Editorial Advisory Board

Photovoltaics International's primary focus is on assessing existing and new technologies for "real-world" supply chain solutions. The aim is to help engineers, managers and investors to understand the potential of equipment, materials, processes and services that can help the PV industry achieve grid parity. The Photovoltaics International advisory board has been selected to help guide the editorial direction of the technical journal so that it remains relevant to manufacturers and utility-grade installers of photovoltaic technology. The advisory board is made up of leading personnel currently working first-hand in the PV industry.

Our editorial advisory board is made up of senior engineers from PV manufacturers worldwide. Meet some of our board members below:



Prof Armin Aberle, CEO, Solar Energy Research Institute of Singapore (SERIS), National University of Singapore (NUS)

Prof Aberle's research focus is on photovoltaic materials, devices and modules. In the 1990s he established the Silicon Photovoltaics Department at the Institute for Solar Energy Research (ISFH) in Hamelin, Germany. He then worked for 10 years in Sydney, Australia as a professor of photovoltaics at the University of New South Wales (UNSW). In 2008 he joined NUS to establish SERIS (as Deputy CEO), with particular responsibility for the creation of a Silicon PV Department.



Dr. Markus Fischer, Director R&D Processes, Hanwha Q Cells

Dr. Fischer has more than 15 years' experience in the semiconductor and crystalline silicon photovoltaic industry. He joined Q Cells in 2007 after working in different engineering and management positions with Siemens, Infineon, Philips, and NXP. As Director R&D Processes he is responsible for the process and production equipment development of current and future c-Si solar cell concepts. Dr. Fischer received his Ph.D. in Electrical Engineering in 1997 from the University of Stuttgart. Since 2010 he has been a co-chairman of the SEMI International Technology Roadmap for Photovoltaic.



Dr. Thorsten Dullweber, R&D Group Leader at the Institute for Solar Energy Research Hamelin (ISFH)

Dr. Dullweber's research focuses on high efficiency industrial-type PERC silicon solar cells and ultra-fine-line screen-printed Ag front contacts. His group has contributed many journal and conference publications as well as industry-wide recognized research results. Before joining ISFH in 2009, Dr. Dullweber worked for nine years in the microelectronics industry at Siemens AG and later Infineon Technologies AG. He received his Ph. D. in 2002 for research on Cu(In,Ga)Se₂ thin-film solar cells.



Dr. Wei Shan, Chief Scientist, JA Solar

Dr. Wei Shan has been with JA Solar since 2008 and is currently the Chief Scientist and head of R&D. With more than 30 years' experience in R&D in a wider variety of semiconductor material systems and devices, he has published over 150 peer-reviewed journal articles and prestigious conference papers, as well as six book chapters.



Chen Rulong, Chief Technology Officer, Solar Cell R&D Department, Wuxi Suntech

Chen Rulong graduated from Changchun Institute of Optics and Fine Mechanics, majoring in applied optics. He began working in the field of R&D on solar cells from 2001. He is a visiting fellow at the University of New South Wales in Australia and an expert on the IEC Technical Committee 82, which prepares international standards on PV energy systems.



Florian Clement, Head of Group, MWT solar cells/printing technology, Fraunhofer ISE

Dr. Clement received his Ph.D in 2009 from the University of Freiburg. He studied physics at the Ludwigs-Maximilian-University of Munich and the University of Freiburg and obtained his diploma degree in 2005. His research is focused on the development, analysis and characterization of highly efficient, industrially feasible MWT solar cells with rear side passivation, so called HIP-MWT devices, and on new printing technologies for silicon solar cell processing.



Sam Hong, Chief Executive, Neo Solar Power

Dr. Hong has more than 30 years' experience in solar photovoltaic energy. He has served as the Research Division Director of Photovoltaic Solar Energy Division at the Industry Technology Research Institute (ITRI), and Vice President and Plant Director of Sinonar Amorphous Silicon Solar Cell Co., the first amorphous silicon manufacturer in Taiwan. Dr. Hong has published three books and 38 journal and international conference papers, and is a holder of seven patents. In 2011 he took office as Chairman of Taiwan Photovoltaic Industry Association.



Matt Campbell, Senior Director, Power Plant Products, SunPower

Matt Campbell has held a variety of business development and product management roles since joining the SunPower, including the development of the 1.5MW AC Oasis power plant platform, organized SunPower's power plant LCOE reduction programmes, and the acquisition of three power plant technology companies. Campbell helped form a joint venture in Inner Mongolia, China for power plant project development and manufacturing. He holds an MBA from the University of California at Berkeley and a BBA in Marketing, Finance, and Real Estate from the University of Wisconsin at Madison.



Ru Zhong Hou, Director of Product Center, ReneSola

Ru Zhong Hou joined ReneSola as R&D Senior Manager in 2010 before being appointed Director of R&D in 2012. Before joining ReneSola he was a researcher for Microvast Power Systems, a battery manufacturer. His work has been published in numerous scientific journals. He has a Ph.D. from the Institute of Materials Physics & Microstructures, Zhejiang University, China.

Aiko CELLS

made from the heart

High efficiency bifacial PERC cell

The front efficiency > **22%**

Maximum package power of module exceed **400W+**

Temperature 85°C, humidity 85%, 192H and -1500V, PL ≤ 3%

Get the first bifacial PID certificate



9

Contents



29

9 Product reviews

Section 1: Market Watch

- 11** Top-10 solar cell producers of 2018
By Finlay Colville, Head of Research, PV-Tech and Solar Media Ltd.

- 15** Top 10 module suppliers of 2018
By Finlay Colville, Head of Research, PV-Tech and Solar Media Ltd.

Section 2: Fab & Facilities

- 18** Digitalization meets PV production technology – Outline of a smart production of silicon solar cells and modules
Martin Zimmer, Matthias Demant, Norbert Bergmann, Stefan Rein, Jochen Rentsch & Ralf Preu, Fraunhofer ISE, Freiburg, Germany.

- 29** PV manufacturing capacity expansion announcements in 2018
By Mark Osborne, Senior News Editor, Photovoltaics International

Section 3: Materials

- 38** Reliability of electrically conductive adhesives
*G. Oreski, S. Pötzt, A. Omazic, G.C. Eder, L. Neumaier, C. Hirschl, R. Ebner, J. Scheurer & W. Pranger
PCCL Polymer Competence Center Leoben, Austria; OFI, Austrian Research Institute for Chemistry and Technology, Vienna, Austria; CTR Carinthian Tech Research AG, Villach, Austria; AIT Austrian Institute of Technology GmbH, Vienna Austria; Polytec PT GmbH, Karlsbad, Germany; Ulbrich of Austria GmbH, Müllendorf, Austria*

- 46** Effects of texture additive in large-area diamond wire cut multicrystalline silicon solar cells
S. Saravanan, Ch.S.R. Suresh, V.V. Subraveti, K.C. Kumar & U.K. Jayaram, RenewSys India Pvt Ltd, Hyderabad, India

Section 4: Cell Processing

- 51** Pioneering the industrialization of PERC technology: A review of the development of mono- and bifacial PERC solar cells at SolarWorld
Phedon Palinginis, Christian Kusterer, Stefan Steckemetz, René Köhler, René Härtwig, Torsten Weber, Matthias Müller, Gerd Fischer & Holger Neuhaus, formerly of SolarWorld Innovations GmbH / SolarWorld Industries GmbH

- 74** Low-cost standard nPERT solar cells towards 23% efficiency and 700mV voltage using Al paste technology
*Radovan Kopecek, Zih-Wei Peng, Thomas Buck, Corrado Comparotto, Valentin D. Mihailetchi, Lejo J. Koduvelikulathu, Joris Libal, Jan Lossen, Masahiro Nakahara, Kosuke Tsuji, Marwan Dhamrin & Wolfgang Jooss
International Solar Energy Research Center (ISC) Konstanz, Germany; Hino Solar Laboratory, Core Technology Center, Toyo Aluminium K.K., Hino-cho, Japan; RCT Solutions GmbH, Konstanz, Germany*

- 85** Solving all bottlenecks for silicon heterojunction technology
*Christophe Ballif, Mathieu Boccard, Antoine Descoedres, Christophe Allebé, Antonin Faes, Olivier Dupré, Jan Haschke, Pierre-Jean Ribeyron & Matthieu Despeisse
Ecole Polytechnique Fédérale de Lausanne (EPFL),*



MEYER BURGER



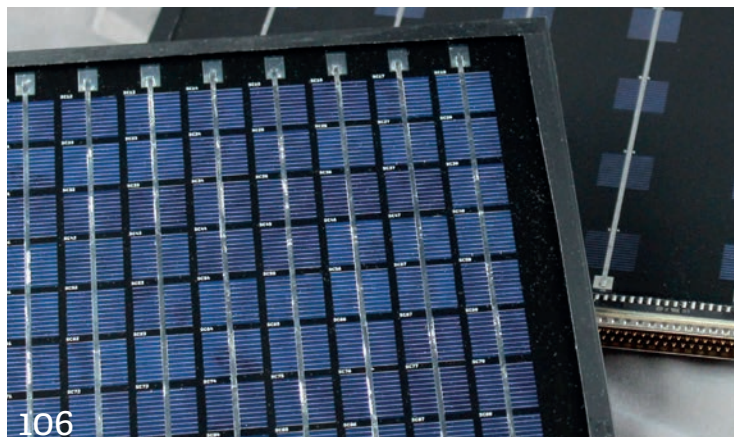
RECORD-BREAKING SOLAR MODULE: Engineered by the technology leader

We maximize energy output. Superior Heterojunction solar cells with efficiencies over 24% combined with outstanding SmartWire Connection Technology delivers record-breaking 480W* bifacial solar modules. Manufactured on Meyer Burger's HELiA® cell coating and SWCT™ connection platforms. Meyer Burger takes you to new energy levels.

meyerburger.com/HJT
meyerburger.com/SWCT

*verified 410W by CEA/INES + 17% albedo = 480W





106

Contents



129

Neuchâtel, Switzerland; CSEM, PV-Center, Neuchâtel, Switzerland; CEA-INES, LITEN, Le Bourget-du-Lac, France

- 98** Beyond boron–oxygen deactivation: Industrially feasible LID-free p-type Czochralski silicon
Bianca Lim, Agnes Merkle, Robby Peibst, Thorsten Dullweber, Yichun Wang & Rui Zhou
Institute for Solar Energy Research Hamelin (ISFH), Emmerthal, Germany; Institute of Electronic Materials and Devices, Leibniz Universität Hannover, Hanover, Germany; LONGi Clean Energy Technology Co., Ltd., Xi'an City, China

- 106** LED solar simulators and new test approaches for high-efficiency solar cells
Marko Turek, Kai Sporleder & Christian Hagendorf, Fraunhofer Center for Silicon Photovoltaics CSP, Halle (Saale), Germany

Section 5: Thin Film

- 112** Efficiency and cost effectiveness of large-area perovskite-based tandem solar cells

Manoj Jaysankar & Tom Aernouts, imec, Genk, Belgium

Section 6: PV Modules

- 119** Taking the temperature of bifacial modules: Are they warmer or cooler than monofacial modules?
Bas Van Aken & Gaby Janssen, ECN.TNO – Solar Energy, Petten, The Netherlands

- 129** Half-cell solar modules: The new standard in PV production?
Jens Schneider, Hamed Hanifi, David Dassler, Matthias Pander, Felix Kaule & Marko Turek, Fraunhofer Center for Silicon Photovoltaics CSP, Halle (Saale), Germany

- 137** Subscription / Advertisers Index

- 138** Mono PERC cell production to lead solar industry in 2019
The PV-Tech blog



85

Product reviews

Cell Processing: **Fraunhofer ISE**

Fraunhofer ISE develops adhesives for industrial production of shingle cell modules



Product Outline: The Fraunhofer Institute for Solar Energy Systems (ISE) has developed a bonding method for the interconnection of silicon solar cells for the industrial production of shingle modules.

Problem: The high efficiency of modules with shingle cells and their aesthetic appearance are currently driving demand on the market. However, shingle cells cannot be soldered by conventional methods, due to mechanical stresses. Only through the use of adhesives can reliable and robust shingle strings be produced.

Solution: Electrically conductive bonding of shingled cells on the industrial stringers can be used with specially developed adhesives. The adhesive can compensate for the thermal expansion of the module glass at changing ambient temperatures and is also lead-free. The stringer from teamtechnik Maschinen und Anlagen GmbH applies the electrically conductive adhesive using the screen printing process and interconnects the cell strips with high precision.

Applications: With the narrow cell strips different module formats can be realized, which creates a lot of scope for specific applications. Currently, the experts at Fraunhofer ISE are working on optimizing the amount of adhesive and cell design as well as on the development of new fields of application.

Platform: Cell gaps are avoided by shingling, allowing the module surface to be used maximally for the generation of energy and a homogeneous, aesthetic overall picture is created. Compared to conventional solar modules, module efficiency is higher as a result of the larger active module area and the lack of shading losses due to overlying cell connectors. The resistance losses are reduced by lower currents in the cell strips. These cell-to-module losses and gains can be achieved with the software tool SmartCalc.CTM of the Fraunhofer ISE.

Availability: Currently available.

Cell Processing: **RENA**

RENA's 'BatchTex SHJ' wet chemical tool offers heterojunction cell surface sensitivity

Product Outline: RENA is offering the 'RENA BatchTex SHJ' wet chemical manufacturing equipment for high throughput mass production of silicon heterojunction solar cells.

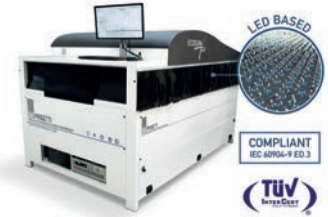
Problem: The texturing and cleaning of silicon wafers for silicon heterojunction (SHJ) application requires adapted etching and advanced surface processing. The high level of sensitivity of the surface prior to amorphous silicon deposition calls for high quality wet chemical texturing, cleaning and drying. Compared to processing of PERC solar cells, adjusted processing with regards to etching and cleaning is needed to account for the high demands of surface passivation using heterojunction layers.

Solution: Alkaline texturing of the wafers is done by using the IPA-free RENA 'monoTEX' process technology, delivering a high quality random pyramid surface with an excellent homogeneity at an outstanding process yield. Subsequent cleaning and surface conditioning is based on ozone technology allowing low operating

PV Modules: **Ecoprogetti**

Ecoprogetti launches 'Extended Spectrum, LED Sun Simulator Ed.3 for high-efficiency modules

Product Outline: Ecoprogetti has launched its new 'Extended Spectrum, LED Sun Simulator Ed.3' for PV panels, driving down production costs and providing key advantages to assembly lines and laboratories.



Problem: The newest generation of high efficiency PV cells (PERC, n-type, HIT, Bifacial, etc...) are no longer compatible with the Xenon technology, decreasing the test reliability and precision of the power measurement due to capacitive effects. Xenon lamps have a short lifetime and high cost, resulting in increased production and testing costs.

Solution: Ecoprogetti's new solution for PV module testing and I-V curve measurements with A+A++ class certified by TÜV InterCert, is suitable for testing all new generation of solar modules and high efficiency solar cells. Extended spectrum= 300nm to 1200nm, fully compliant to the IEC 60904-9 ED. 3. High-efficiency solar cells require a longer flash duration to guarantee an accurate measurement of the maximum power. The LED light source has a long pulse, which simulates more accurately the final installation conditions of the solar panel. The capacitive effects will no longer influence module measurements, making the Ecosun Plus tests reliable and accurate.

Applications: Final testing of PV modules in high capacity module assembly lines and in laboratories.

Platform: The Ecosun Plus tester has a long lifetime LED source, which reduces the costs of consumables, while overall maintenance is lower. Ecoprogetti's LED technology can perform more than 50 million tests (equivalent to 10GW of tested PV panels) with minimum maintenance (< 50 €/year) and without any LED board replacement.

Availability: Currently available.

costs and which is well proven in mass production in the solar industry across Asia. The drying sequence is adapted to account for the special requirements of the silicon surfaces prior to a-Si deposition. Processing of thin wafers is possible using suitable cassettes.



Applications: Mass production of high efficiency silicon solar cells with heterojunction structure and advanced cleaning requirements before passivation layer deposition.

Platform: The solution is based on RENA's Batch N platform which allows the integration of all batch-type wet chemical processes into a state-of-the-art high throughput production platform for crystalline silicon solar cell manufacturing. It is available in different versions: the N400 featuring four cassettes per batch (>400 wafers), N200 with two cassettes per batch (>200 wafers) and for lab and small volume manufacturing the N50 with small cassettes with 50 wafers.

Availability: The RENA BatchTex SHJ is currently available.

inter solar

connecting solar business

The World's Leading Exhibition Series
for the Solar Industry

INTERSOLAR EVENTS 2019

www.intersolar-events.com



MARCH 5–7, 2019, DUBAI, UAE

www.intersolar.ae

APRIL 4–5, 2019, MUMBAI, INDIA

www.intersolar.in

APRIL 10–11, 2019, FORTALEZA, BRAZIL

www.intersolar-summit.com/brasil-nordeste

APRIL 24–25, 2019, BUENOS AIRES, ARGENTINA

www.intersolar-summit.com/argentina

MAY 15–17, 2019, MUNICH, GERMANY

www.intersolar.de

JULY 9–11, 2019, SAN FRANCISCO, USA

www.intersolar.us

AUGUST 27–29, 2019, SÃO PAULO, BRAZIL

www.intersolar.net.br

NOVEMBER 27–29, 2019, BANGALORE, INDIA

www.intersolar.in

FOLLOW US



Top-10 solar cell producers of 2018

Finlay Colville, Head of Research, PV-Tech and Solar Media Ltd.

Solar cell production in 2018 represented change on many fronts, but may be remembered as a year during which Chinese-owned companies made further strategic moves as part of the current Beijing mandate to position the country as a high-tech manufacturing global powerhouse. This article explains how this is having a dramatic impact on solar cell manufacturing outside the control of leading Chinese-funded companies, and what this really means in terms of solar cell technologies and industry-wide technology roadmaps during 2019.

Understanding why cell production has changed

When the first wave of capacity expansions occurred in China about ten years ago, it was followed by various forms of vertical integration during which many companies established GW-scale cell and module manufacturing facilities. While this occurred, there was still a place for pure-play cell production in other countries such as Taiwan.

As a result of this, cell production globally saw top-10 lists comprised of different Chinese and Taiwanese companies, alongside more established producers such as SunPower, REC Solar and Q-CELLS (subsequently South Korean controlled Hanwha Q-CELLS). For a while also, representation was provided by Japan through companies such as Kyocera and Sharp Solar.

At about the same time as Taiwan cell production grew, there was a dramatic decline in cell production in Japan where costs were simply too high to compete with Chinese and Taiwanese manufacturing benchmarks.

During 2018, the top-10 cell producers included 8 Chinese companies, South Korean controlled Hanwha Q-CELLS, and First Solar.

Over time, Chinese companies took more of a lead, based purely on capex to scale from 1GW to the 3-5GW level. Outside China, the only company to match these capacity expansions was Hanwha Q-CELLS, with ambitious new factory builds in South Korea.

However, in the past couple of years, a further shift has occurred during which Taiwan cell production has been scaled back, overlapping with the growth of new pure-play specialists in China, most notably Tongwei and Aiko. These new entrants are woven into the fabric of China manufacturing aspirations, being central to the supply-channels that extends back to wafer supply from the likes of LONGi and Zhonghuan, and forward to anyone making a module in China.

Notably, Tongwei and Aiko did not seek to reinvent the wheel: rather, it was more of the same p-type mono and multi, but with the 1GW benchmark of before becoming a staggering 10GW, and expansion plans in multiples of 5GW that appear to rather ignore any red flags in terms of market supply, trade-wars and upstream over-capacity fears.

In fact, without tariffs in place, it is simply impossible for non-Chinese companies to compete with the likes of Tongwei and Aiko, if p-type cell business was the end game. Thankfully, this is not the case. What is has done however is force cell production outside China to concentrate on value-added differentiation, which is basically another way of introducing n-type into the discussion here. More on this below as in relates to the 2019 cell production landscape expected.

Top 10 Solar Cell Producers of 2018

Ranking	Cell Producer
1	JA Solar
2	Tongwei
3	Trina Solar
4	Hanwha Q-CELLS
5	JinkoSolar
6	LONGi
7	Shunfeng (incl. Wuxi Suntech)
8	Canadian Solar
9	Aiko Solar
10	First Solar

© PV-Tech &
Solar Media Ltd, Jan. 2019



Revealing the top-10 cell producers by volume

The first thing to point out is that the list below is preliminary and will be subject to some minor tweaks once we learn more about cell line utilization rates during the past few months of 2018 of all the major cell producers today.

We have a grouping of four companies (JA Solar, Trina Solar, JinkoSolar and Canadian Solar) that can be viewed as global module brand-recognized integrated cell/module producers that all produce multi-GW of cells in-house (in both China and Southeast Asia facilities), while using domestic Chinese third-party cell supply from the likes of Tongwei and Aiko, for example. JA Solar and JinkoSolar have largely repositioned as p-mono PERC cell producers, Trina Solar is in the process of making the change, and Canadian Solar still retaining a multi-loyalty of sorts.

"Well defined scope and speakers covering the whole topic of PV modules"

Ronald Sastrawan, Munich Re

"A must-attend for procurement professionals looking to make smart technology choices"

Brian O'Rorke, BNRG Renewables

**20% OFF FOR
OUR READERS.
USE CODE **PVTP****



PVMODULETECH CONFERENCE

22-23 OCTOBER 2019
Penang, Malaysia

Understand the technical and logistical supply chains that determine the production and performance of solar modules.



moduletech.solarenergyevents.com

ORGANISED BY:



SOLAR MEDIA
EVENTS | PUBLISHING | RESEARCH

Hanwha Q-CELLS is largely one of a kind when looking at the companies, and the closest thing in solar today that allows us to draw parallels with Korean conglomerate activities in the flat panel display sector. From a global module brand perspective, the company is similar to the four major Silicon Module Super League (SMSL) players above. Cell production differs as having a major contribution from South Korea that has been prioritised in recent years for capex, versus the legacy Solarfun sites in China and Q-CELLS in Malaysia.

LONGi Solar also is unique in our top-10 listing in many ways, most notably in the extent of its full value-chain (ingot to module), but in particular the scale and positioning of its ingot pulling business in China. More coverage on LONGi Solar will feature in our subsequent reviews of poly/ingot/wafer production and module-supply blogs on PV-Tech over the next few weeks.

Shunfeng (or from a cell production standpoint Wuxi Suntech) is another one-off in the category above, and the leading example of a legacy Chinese cell/module powerhouse (Suntech) that has managed to sustain production levels at meaningful levels, propped up by the domestic market and in the absence of overseas cell/module options or strong global module business levels. Capex limitations have prevented any major shift from p-type multi production.

As mentioned earlier, Tongwei and Aiko should be grouped together. These companies have been one factor behind the demise of the Taiwan cell industry, and their contributions to cell production will only increase during 2019. It remains to be seen if 20GW cell capacities per company with single-digit margins will simply cause a domino effect of removing even more cell competitors, or if they will get diverted from their current raison d'être through illusions of grandeur (such as trying to become global module suppliers).

Finally, we have the only meaningful thin-film solar cell producer globally today, First Solar, more on which below.

China n-type innovation: a global threat or another turn-key thin-film capex flurry?

Normally one would expect announcements of GW n-type expansions to come from companies that had either spent years learning R&D and pilot-line skills, or companies that had a proven track record in multi-GW of p-type mono cell manufacturing. Or indeed from companies that had existing n-type knowledge and were seeking to grow business levels.

Therefore, it is not crazy to have doubts about n-type capacity expansions in China that have occurred in 2018 and will continue during this year. I will return to this more in other blogs, as trying to explain fully does merit discussion in its own right.

For now however, it should be pointed out that virtually nothing from the top-10 companies shown above is coming from n-type in 2018, and the

strategies of almost all the n-type entrants in China in the past 12-18 months are focussed entirely on meeting domestic carve-out needs from Top Runner variants.

But for equipment makers, it is for now a period of capex excitement. And why not? The stakes are very high, and if a few of the new n-type GW plants shows success, this could change the entire solar industry overnight and force n-type onto the immediate roadmap of every solar cell maker globally. In 2018 also, many of the p-type cell leaders made first moves into n-type territory and new capacity will come online here in 2019 for sure.

The last major expansion for bespoke deposition equipment in the solar industry (PVD/PECVD) was about ten years ago, in the form of turn-key a-Si based production lines. Several billion dollars was spent with the likes of Applied Materials, Oerlikon and ULVAC, endless resources were afforded to marketing campaigns; today, a-Si is no more than a token gesture and for all purposes dead.

The current n-type landscape is very different however, as it is still the natural roadmap evolution of everything p-type which is over 90% of solar industry annual consumption. And today mono is dominating multi, and we have low-cost ingot pulling in China ready to flip to supply n-type capacity additions. This changes everything, suggesting it is a matter of time for n-type, but just maybe not via the first wave of companies undertaking major investments during 2017/2018.

First Solar gains the technology award for 2018

If awards existed for most-impressive achievement for cell technology in mass production, one may decide First Solar was the winner here in 2018. It is hard to convey how impressive the move from Series 4 to Series 6 has been, or indeed the mere fact that it occurred in the first instance.

In contrast to almost all the capex in China by c-Si cell market-leaders - which was low-risk, low barrier-to-entry large-scale roll-out of known p-type multi or mono (Al-BSF or PERC) that was originally pioneered in mass production by Western companies - First Solar's Series 4 to Series 6 came on the back of 20 years of in-house R&D investments and a relationship with equipment suppliers that is unique within the solar industry today.

Add to this running Series 4 lines typically at 95-99% utilization rates and moving CdTe module efficiencies to uncharted waters, and you begin to see how First Solar from a cell production standpoint is not simply differentiated in technology (thin-film, not c-Si) but from a manufacturing business perspective.

2018 marks a return to thin-film being a feature of the top-10 cell production rankings, and while Series 6 is still in a ramp-up phase and costs still need to be fully established, it is likely First Solar's ranking will improve when the summary of cell production in 2019 is undertaken.

Empowering Solar

with Quentys™ encapsulant film and Polypropylene based compounds for producing backsheets

Encapsulant film

- Reduced environmental footprint
- Reduced lamination cycle time
- Thermoplastic in nature
- Free of organic peroxide

PP compound backsheet

- Reduced environmental footprint
- Hydrolytic stability
- Lower WVTR
- Co-extrusion possibilities with PP

Borealis Empowering Solar

Building on over 50 years' experience in the global energy industry, Borealis is empowering solar by making it more efficient and affordable. The innovative solar brand Quentys™ offers a step-change in production cost efficiency for photovoltaic modules. In addition to lowering production costs, it improves module reliability, increases power output, and ensures longer lifetimes. Because it is fully recyclable, Quentys helps achieve a lower environmental footprint. Fields of application for the globally available products in the pioneering Quentys portfolio include solar backsheet compounds and encapsulant films.

www.borealisempoweringsolar.com



Top 10 module suppliers of 2018

Finlay Colville, Head of Research, PV-Tech and Solar Media Ltd.

This article reveals the top-10 module suppliers of 2018, based purely on own-brand shipped module MWp-dc volumes.

For the past few years, we have sought to compile the top-10 module supplier list before the end of January (or at the latest before the Chinese new year). In practice, with the first two weeks of the year being a reset from any prior-year shipment rush or inventory clear-out, we end up having a couple of weeks to get the top-10 module supplier rankings done.

By carefully tracking the main contenders during 2018, this gives us a good idea of what the top-10 will look like, but when we get initial (unreported) confirmation during January, there are always a few surprises.

The counting in the past couple of weeks did not disappoint, and while the industry leader for 2018 was largely known from the start of the year, a few contenders did perform strongly during 2H'18 which is confirmed by the rankings list shown in the article here.

Some others – more reliant on China for shipments – suffered more during 2H'18 owing to the reset that occurred after China-531, and especially those module suppliers lacking access to overseas markets, being cash-constrained and with no Southeast Asia manufacturing to utilize then.

Before we get to the Top-10 listing shown, it is essential to understand what 'module supply' means, because this still remains broadly misunderstood in the PV industry today. Even when we check companies for numbers, we find we are having to constantly explain to them what module-shipment really means!

Methodology explained

Ranking the module suppliers purely on branded end-user (whether in-house EPC or third-party installer/EPC) shipments has become increasingly harder in the past few years, with an uptick in both module tolling (where production numbers do not translate to shipment figures) and the use of rebranded OEM module outsourcing (which count as module supply).

For example, some multi-GW module producers in China may have 'produced' very high levels of modules, but shipment numbers are markedly lower owing to these companies being used heavily on a tolling basis by peers in China that have access to module sales pipelines to downstream outlets. Using underutilized production lines as a tolling service for other companies does not count as a module shipment!

This is also relevant for some module producers today in Southeast Asia, in particular Vietnam, as it has always been for contract modules

manufacturers like Flex (formerly Flextronics), Celestica and Jabil, to name just three.

Similarly, other companies in China that have global brand recognition, or have downstream operations that drive the need for in-house branded modules – and who lack readily available owned cell/module operations outside China – typically have module shipment numbers much higher than in-house module production levels (or indeed any nameplate of effective module capacity levels).

In fact, looking across the top-20 module suppliers for 2018, almost every c-Si player (19 of the top-20) is subject to the above two caveats when ranking module supply figures for the year. By default somewhat, First Solar remains the only (top-10) company that can lay claim to having 100% own-produced module supply.

Another challenge in rankings relates to the numbers being reported (or not) by PV companies these days, particularly in light of the current trend of delisting from non-Chinese stock exchanges where the expectation from western observers for production clarity tends to be far greater than any other reporting channels.

Ultimately, the methodology behind all companies' shipment levels has become rather bespoke, even for the ones that are still releasing MW or revenue numbers on a quarterly basis on NASDAQ or the NYSE for example. Some companies also like to quote a-sum-of-all shipments (wafers, cells, modules, and tolling services), which misleads certain third-party observers each year.

Thankfully however, the delta between the top-10 and then to the nearest number-11 is modest, meaning that the current (preliminary) ranking shown below is probably the final and correct version that will unfold over the next 3-4 months as reported data of sorts trickles out into mainstream press and social media outlets. We will correct any changes in a few months of course.

The top-8 are pretty much known with high certainty at this point; the final two entries are likely correct, with any other lists probably not differentiating between the various categories outlined above (in particular module-only numbers and tolling services).

For reference, during 2018, the top-10 module suppliers shipped nearly 60% of all modules to the industry.

And finally, here is our estimate of the top-10 module supplier ranking table for 2018:

Commenting on the top-10 companies

While JinkoSolar's position as leading global module supplier during 2018 was barely in doubt

during the year, the most interesting changes were seen across the remaining companies in the rankings table above.

JA Solar established itself as JinkoSolar's closest rival globally, with the two companies having made strong investments into mono PERC and being firmly committed to Southeast Asia manufacturing hubs to compliment Chinese factories.

Trina Solar saw its ranking fall in 2018, as the company went through a year of adjustment coupled with cost savings exercises. However a strong second-half maintained top-3 status for the company.

LONGi was another winner in 2018, with a strong company focus on seeking non-Chinese module supply growth in most major end-markets. This strategy is expected to continue during 2019.

Hanwha Q-CELLS saw its ranking fall in 2018, with the company adjusting to previous Section 201 implications for US shipments, technology upgrades to lines in China, and a less ambitious growth trajectory that overlapped with its going-private actions during the year.

Canadian Solar set less ambitious module shipment targets during 2018, with its business model still fundamentally driven by downstream project acquisition, build-out and phased sales to global secondary market long-term owners.

Risen Energy made strong gains in 2018, driven largely by highly effective downstream project activity across Asia that puts the company on a par with Canadian Solar in the grouping above.

GCL-SI maintained top-10 status, but the company's non-China operations is still a work-in-progress, with all capacity still located in China.

Having been just outside the top-10 in 2017, Talesun is a new entrant to the global top-10 listing for 2018. The company had been one of the first multi-GW capacity Chinese-based companies to focus on non-domestic business (similar to Risen Energy) and its inclusion in the top-10 in 2018 should not come as a surprise.

Finally in the top-10 rankings above, First Solar remains the only non-Asian and only non-c-Si based company to feature. The company went through most of 2018 with sales demand outstripping module supply, allowing the company to control the phasing of Series 4 and Series 6 line utilizations and ramp-ups.

Just outside the top-10 there were other multi-GW module producers, some of which produced more modules than companies in the top-10 list, but were often used as tolling sources for other companies, pulling down their final estimated module shipment figures.

What to expect in 2019

When we come to review the top-10 module suppliers in 2019, do not expect too many adjustments; rather some internal reshuffling. In fact, it is likely nine or the top-10 will almost certainly be in the top-10 for 2019, with the top-6 the same.

Like 2018, the top-5 are likely to be all Chinese companies, depending on whether Hanwha Q-CELLS has a successful rebound in 2019 or not, with Jinko's #1 status again simply not in doubt.

First Solar is expected to move further up the rankings, but this depends on the success of Series 6 during the year.

Of course, aside from being a dream for marketing teams looking to claim leading-supply status or show Y/Y progress, shipment-by-MW-volume is just one part of what really matters in 2019. Module ASPs, cost-structures and profit margins reign supreme of course.

But for those multi-GW players that are satisfied with 10-15% gross margins, then the more product that ships, the better.

Perhaps again, leading multi-GW status in 2019 will owe a considerable part to being one-step ahead of the industry when enacting flexibility in the use of in-house and third-party suppliers, having the correct balance of cell/module capacity inside and outside China, and always offering the optimum performing product to each key global market at ASPs that work also for key customers.

JinkoSolar retained its status as leading module supplier during 2018, with strong market-share gains seen by JA Solar, LONGi Solar and Risen Energy.

Top 10 Solar Module Suppliers of 2018

#	Module Supplier	Y/Y
1	JinkoSolar	≡
2	JA Solar	↑
3	Trina Solar	↓
4	LONGi Solar	↑
5	Canadian Solar	↓
6	Hanwha Q-CELLS	↓
7	Risen Energy	↑
8	GCL-SI	↓
9	Talesun	↑
10	First Solar	↑

© PV-Tech &
Solar Media Ltd, Jan. 2019





24-25 APRIL 2019

DELHI, INDIA



Understand India's multi-GW production roadmap:

- What stages in c-Si manufacturing are of value for Make-in-India?
- Which manufacturing technologies need to be selected?
- How can GW-scale factories be built quickly yet remain adaptable to technology-adoption cycles?
- What is needed to manufacture with profitability?
- What is the role of overseas companies?
- How can Indian developers/EPCs/investors benefit from Indian-made PV modules?
- What is needed from government policy?

indiatech.solarenergyevents.com

Organised by:



SOLAR MEDIA
EVENTS | PUBLISHING | RESEARCH

Digitalization meets PV production technology – Outline of a smart production of silicon solar cells and modules

Martin Zimmer, Matthias Demant, Norbert Bergmann, Stefan Rein, Jochen Rentsch & Ralf Preu,
Fraunhofer ISE, Freiburg, Germany.

Abstract

Ever since the manufacturing of PV modules began suffering from a huge price decline, the reduction of the production cost has been a task of high priority. Digitalization is a subsequent further development of the automation of today's PV cell and module manufacturing processes and can help to decrease production costs. A central concept of digitalization is the *digital twin*, which represents the properties and behaviours of physical assets, materials, processes or eventually the entire production line (the so-called *smart fab*). Different cases of its use are presented in this paper, along with a discussion of the corresponding applications of such digital twins. Finally, a smart fab for PV production is described.

Introduction

Digitalization has been an ongoing process for over two hundred years, reducing production costs in many industries. The development of digital manufacturing goes back to the beginning of the 19th century, when the first digital production tools were invented, allowing a fast and cost-effective production combined with a high-quality

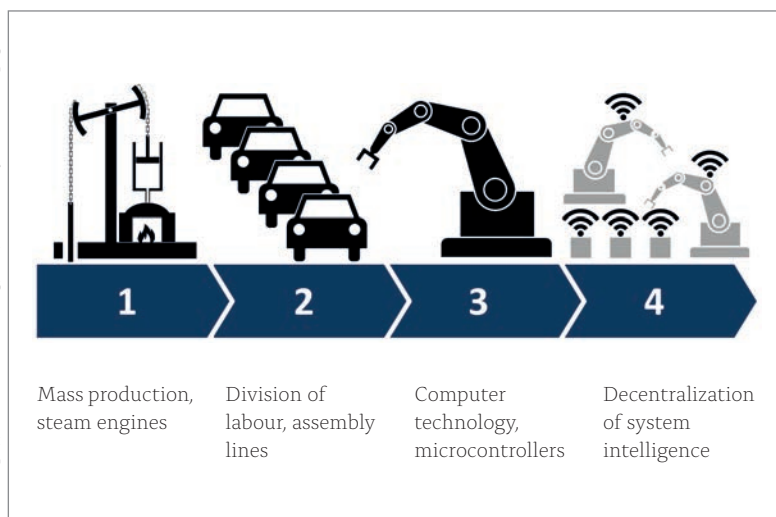
standard. One of the first digital production tools was the *Jacquard loom*, where the pattern of a loomed tissue was stored on punched cards. Today, four industrial ages can be distinguished, which were ushered in by industrial revolutions (Fig. 1).

The first industrial revolution was the introduction of mass production, together with the use of steam engines as an energy source; this first industrial revolution can be dated to the late 18th century. The second industrial revolution is characterized by the division of labour and assembly-line production; this started at the beginning of the 20th century, with the most famous example being the switch to a moving assembly line system in 1913 for the production of Henry Ford's Model T. The introduction of computer technology in industrial production in the 1970s is considered to be the third industrial revolution. Central tasks were shifted to microcontrollers – the classical machine controls with hardwired relays and contactors were successively replaced by programmable logic controllers. The whole manufacturing process was increasingly managed by different enterprise resource planning (ERP) applications. The fourth, and current, industrial revolution has been proclaimed to be an ongoing process, where a decentralization of the system intelligence is enforced by the price decline in computing and storage capacity, as well as by the availability of very fast communication networks.

The production of PV devices has shown significant cost reduction over the last decade; on the one hand, this leads to the worldwide success of PV power generation, but on the other, it has put many manufacturers under enormous price and innovation pressure. One important factor for the strong decline is represented by the 'economy of scale' of single manufacturing units up to the multi-GW scale, necessitating also a high degree of automation. Digitalization is now regarded as the next promising strategy for achieving further reductions in production costs [1]. But how can the concrete implementation of digital technologies help to reduce production costs and simultaneously increase product quality?

"Digitalization is now regarded as the next promising strategy for achieving further reductions in production costs."

Figure 1. Schematic of the four industrial revolutions.



Degree of digitalization of today's PV production

At the beginning of mass production of PV modules, almost the entire logistics were done manually. Process tools with a throughput of approximately 1,000 wafers per hour were fed and unloaded by operators. Increasing labour cost prompted an urgent development of fast and reliable automation solutions.

Today, a high degree of automation is accomplished in most PV manufacturing sites. The cell manufacturing process begins with the inspection and automated loading of wafers into the required process carriers. All the subsequent process equipment is able to unload wafers from carriers, process the wafers and reload the carriers. The logistic units employed are equipped with radio-frequency identification (RFID) tags, which allow the tracking of the process batches along the whole production chain. The information about the processed batches, together with the process data, is collected by a manufacturing execution system (MES), which centrally collects all the relevant data from the tools.

In summary, the actual state of the art in PV production is what is called *industry 3.0*, characterized by mass production in assembly lines, which is highly supported by central software services.

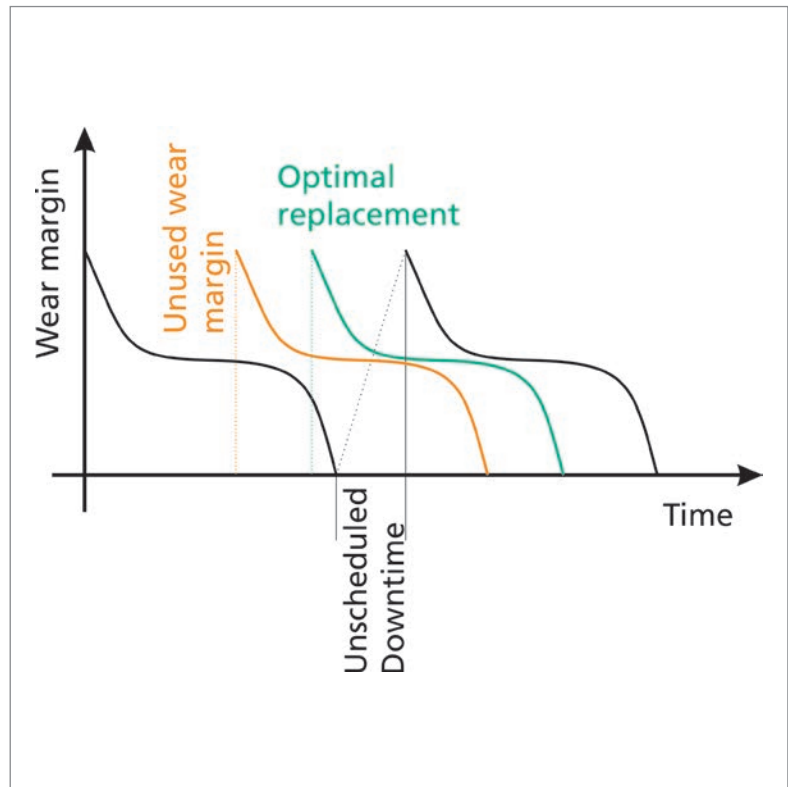


Figure 2. Wear margin usage in different maintenance strategies (black: reactive maintenance; orange: preventive maintenance; green: predictive maintenance).



INSPECTION AND PROCESS OPTIMIZATION ALL IN ONE



VINSPEC SOLAR – For High Cell Quality and Stable Processes

In the photovoltaic industry, efficiency in every production step is essential to success. VINSPEC SOLAR systems from VITRONIC guarantee highly efficient automated optical inspection – delivering superior defect detection and classification. Simultaneously Industry 4.0 features, such as data correlation within and between production equipment, enable an ongoing optimization of the production process.

More info at www.vitronic.com

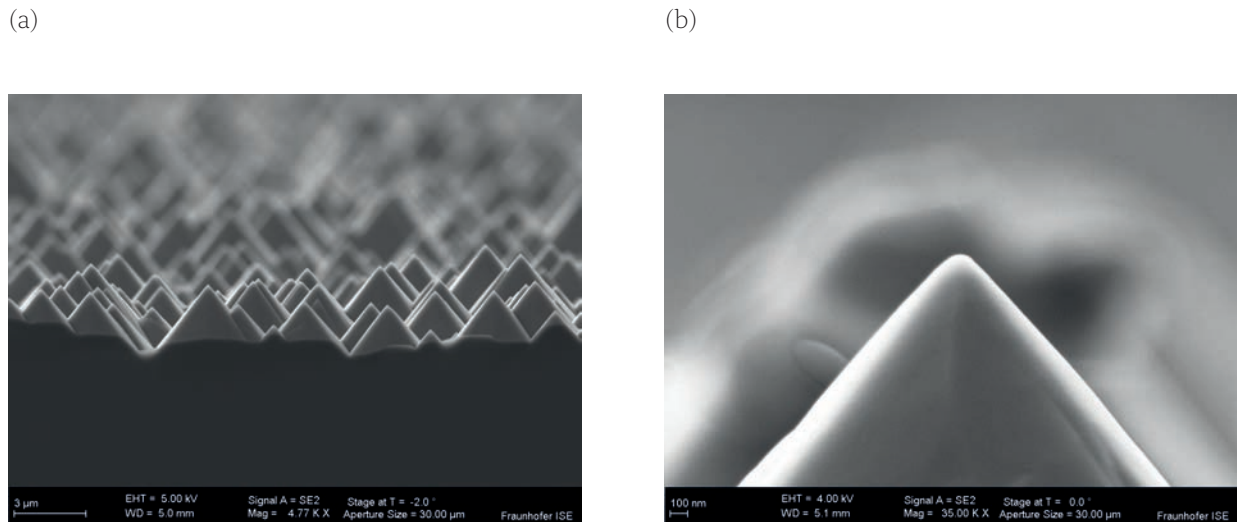


Figure 3. (a) Random pyramids are created in an alkaline etching process on monocrystalline silicon. (b) After an etching in $\text{HF}/\text{HCl}/\text{O}_3$, the pyramid tip is rounded.

A digital future for production

Although the actual production system for PV modules incorporates a central intelligence, which collects, evaluates and reports the entire process and equipment data, a paradigm shift is predicted during the fourth industrial revolution. While equipment data, process data, quality data and metrology data are stored more or less in a single database in common MESs, this business intelligence will be completely distributed over the whole production system.

Digital twin concept

In the new paradigm, the intelligence is distributed over several instances, each with a defined task. The concept of a digital twin – also called a *digital shadow* – plays an important role in this. A *digital twin* is a digital representation of a real object which represents the properties and behaviour of this object. A very simple example of a digital twin is a stored ID number, which represents one single instance of a real object; the properties of this object can then be assigned to this ID, so that a digital twin represents the *properties* of this object. A more complex digital twin also represents the *behaviour* of the object. This allows the user to obtain the properties of an object, even if the object is temporarily not connected to the network; moreover, it allows a prediction of the properties of this object in the future. Digital twins of the materials used provide data on the origin

“Future process tools will be expected to increasingly work autonomously.”

and the material properties, while the digital twins of process tools provide all the necessary data for the entire life cycle of the tool. The construction plans from the engineering phase enable the simulation and optimization of the core parts of a tool. Furthermore, this data can be used by virtual reality applications, which facilitate an assisted maintenance: for example, a virtual reality which creates a virtual three-dimensional image of the tool can help in carrying out maintenance tasks.

Digital twin of a process tool

The digital twin of a process tool can provide the geometrical and mechanical data relating to the tool; this enables simulations of the functional properties of the tool to be performed. The digital twin can also contain (or even reference) the digital twins of parts: for example, the digital twin of a wet chemical process tool can contain the digital twins of the circulation pumps used. This can help in the implementation of various useful systems, such as a *predictive maintenance* system.

Predictive maintenance is a maintenance strategy which tries to combine the advantages of preventive maintenance and reactive maintenance [2]. *Reactive maintenance* uses a system until it breaks down, when the wear margin has been

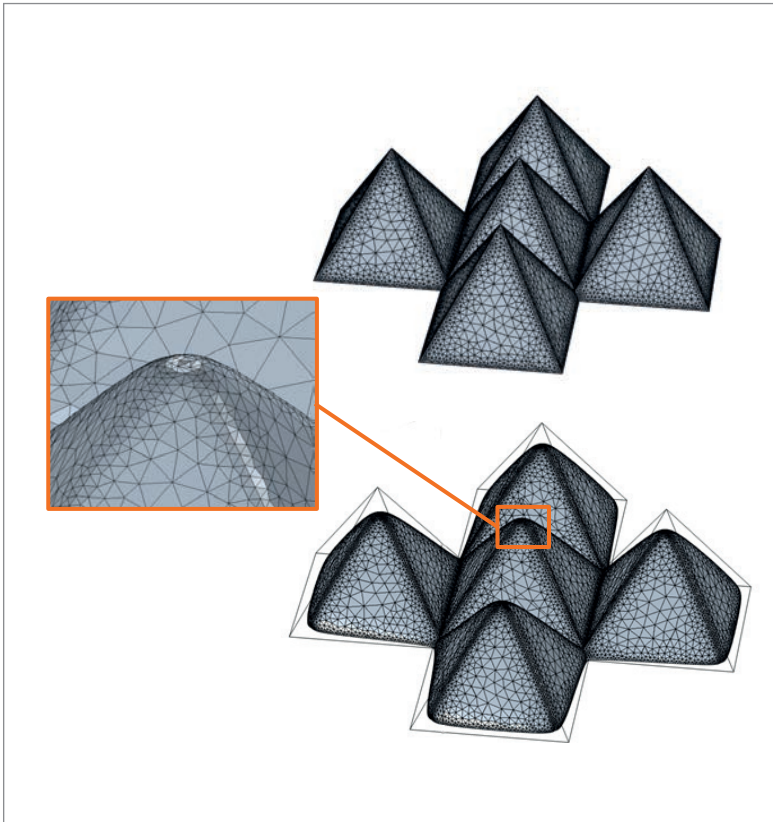


Figure 4. Simulation model for the pyramid rounding in HF/HCl/O₃ (top). Result of the simulated etching on the pyramid tip (bottom).

completely consumed. This strategy makes optimal usage of the wear margin on the one hand, but has to accept unscheduled downtimes of the tool on the other.

In the *preventive maintenance* strategy, consumables are replaced according to a schedule that has been created from empirical values, with no consideration of the individual wear conditions. The resulting avoidance of unscheduled downtimes is achieved by replacing parts with a residual wear margin.

A combination of both the above strategies attempts to find the optimal point for the replacement of each individual component (Fig. 2). This can be done either by direct condition monitoring using sensors, or by evaluating a model which predicts the condition of the components as a function of usage and environmental conditions.

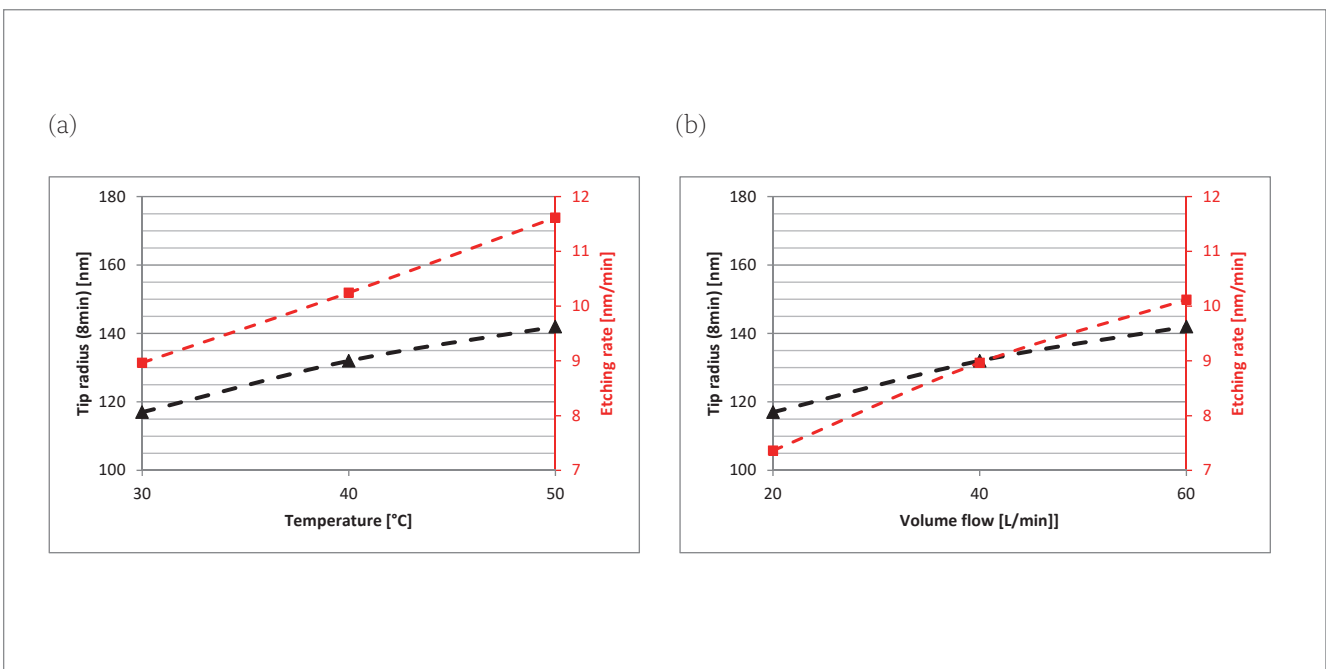
The individual monitoring of components requires additional sensors that enable the prediction of future system breakdowns. An example of such a sensor is ABB's smart sensor [3], which consists of a box that can be mounted on pump motors and contains vibration and temperature sensors. The box monitors the rotational speed of the pump, operating hours, blade problems, looseness, misalignment and pump imbalance, and enables the identification of maintenance requirements.

The implementation of additional sensors can help to monitor the health of critical systems; however, it also runs counter to the need for further reducing cost. Therefore, the implementation of models which predict the wear state by means of usage data (which is accessible via the digital twin) will be an important task in the future, to reduce maintenance costs and unscheduled downtimes.

Modelling of production processes

Digital twins are useful for understanding and optimally using the process equipment. The primary interest, however, is the interaction between the materials used and the equipment. This means that a prediction of process quality has to combine the information from a digital twin of a material with that of a process tool. Meta-models are very important for such an implementation,

Figure 5. Development of the pyramid tip radius and etching rate with respect to (a) temperature, and (b) volume flow.



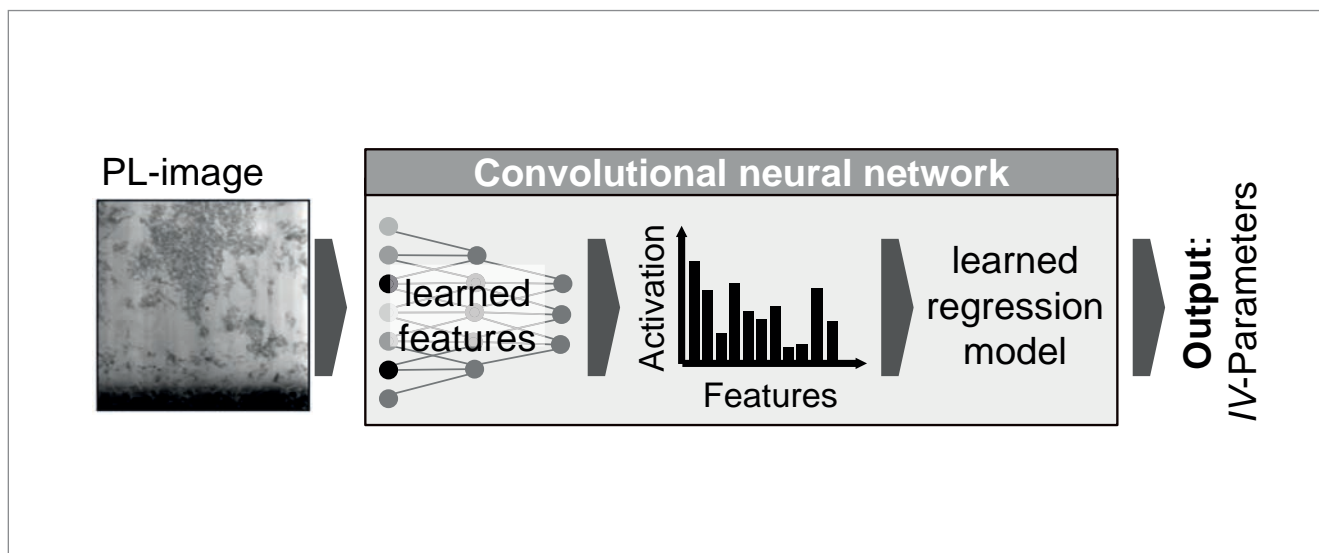


Figure 6. A convolutional neural network directly evaluates PL images of as-cut wafers to predict the solar cell efficiency.

since they allow a correlation between process conditions and process results. The most important parameters in PV production are, of course, the performance data of the final module, as well as the production costs. The implementation of these meta-models is one of the main tasks to take advantage of the digital twins.

Meta-models can use different approaches. In consequence, a digital twin should contain the exact physical parameters of every part of the object. This being the case, fundamental physical equations would predict the state of the object for a defined point in time in the future and a sufficiently well-behaving system. Since this approach is computationally very time intensive, it can only be used in the early stages of the construction of the process tools. For a real-time prediction of production parameters, more advanced semi-empiric and empiric approaches are needed; in this field especially, enormous progress has been made in recent years.

Example of an ab initio process model

Future process tools will be expected to increasingly work autonomously: optimization of the process recipes will be done by the tool itself. To achieve this target, simulations predicting the process results are necessary. An interesting process to simulate is the etching and rounding of pyramid tips in the ozone clean, where a diluted mixture of hydrofluoric acid (HF) and hydrochloric acid (HCl) is used for silicon wafer cleaning. The presence of ozone has an oxidizing effect on the surface cleaning, while the HF removes SiO_2 immediately from the surface; this leads to a slow etching in this process, which rounds the tip of the pyramid slightly (Fig. 3).

It is known from the literature [4], that these tip-rounding processes are useful in the production of heterojunction solar cells, since the round tip results in better passivation of the surface defects.

A further understanding and optimization of the process in the given flow environment can help in optimizing the lateral homogeneity of the process. A process simulation for this etching process was therefore conducted. The model for the process simulation was built up from five pyramids which are located on the silicon surface. The flow of the process media was directed parallel to the diagonal of the pyramid base (Fig. 4, top). The simulation consists of a flow simulation in the volume considered and the transport of the diluted species in the circulated process solution, as well as the surface reaction, where O_3 and HF are consumed, while hexafluorosilicic acid (H_2SiF_6) is generated.

The etching process is isotropic with respect to the crystal orientations; therefore, the tip of the pyramid is attacked from several sides, while the pyramid surfaces are etched only from one direction. In consequence, the tip is rounded during this process (Fig. 4, bottom).

In addition to the qualitative result that the pyramid tips were rounded, quantitative results are also available. The dependence of the etching rate and the tip radius on the temperature and volume flow can be predicted using such a process simulation. The etching rate increases with increasing temperature as well as with an increasing volume flow, as seen in Fig. 5. Both effects also lead to a more pronounced rounding of the pyramid tips.

Empirical process modelling using artificial intelligence

The application of data-intensive deep-learning technology is promising for the quality control of high-throughput production in future PV fabrication. Fraunhofer ISE is working on a transfer of deep-learning algorithms to the levels of the PV value chain. A high-throughput characterization and production in the photovoltaic technology evaluation centre (PV-TEC) [5], and in cooperation

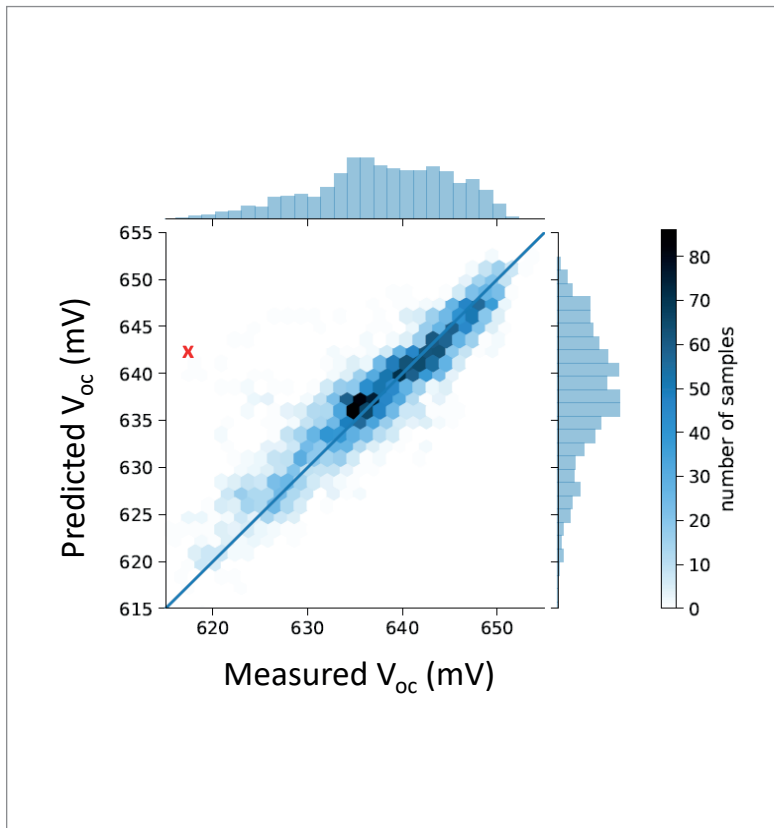


Figure 7. Predicted open-circuit voltage based on Fraunhofer ISE's deep-learning model; the red cross indicates an outlier, which is investigated in more detail.

with industrial partners, allows the collection of empirical data to establish reliable tools for predictive analytics and maintenance.

In Fraunhofer ISE's recent studies, a successful application of deep-learning algorithms for an inline quality rating of multicrystalline silicon (mc-Si) wafers was presented. Highly accurate prediction results allow the use of the model for fault detection. Nevertheless, machine-learning techniques are seen as a 'black box', which provides fewer physical insights. To broaden the acceptance of neural networks by the PV community, visualization techniques are presented here in order to help overcome any objections. Indeed, the network learns a semantic representation of the data, which can be used for defect analysis and localization.

Details on the leading application of novel machine-learning and visualization techniques for material characterization can be found in Fraunhofer ISE's studies on learning [6] and on visualization [7].

For mc-Si solar cells, the cell efficiency is heavily dependent on material quality. Crystallization-related defects – such as contaminations from the crucible, grain boundaries and dislocations –

reduce the lifetime of the excess charge carriers. Lifetime-reducing defects can be observed in photoluminescence (PL) images [8].

Physical device simulations (e.g. ELBA [9]) can be used to predict the solar cell efficiencies from lifetime maps. Nevertheless, this approach is not well established for as-cut wafers before solar cell production: the lifetime of the excess charge carriers changes during thermal processes, and the measurement is limited as a result of the surface recombination of non-passivated samples. An empirical approach to rating the quality of mc-Si wafers using the novel deep-learning algorithms was therefore investigated.

A new era of machine-learning algorithms started in 2012: for the first time, machine-learning algorithms matched human-level performance [10] for the classification of a thousand different object classes in the ImageNet [11] dataset. Although the so-called *deep-learning techniques* have been known for decades (e.g. LeNet by LeCun et al. [12]), the breakthrough was delayed because of limited computational power and data. The emerging algorithms are fast and reliable. In an end-to-end manner, they directly connect high-dimensional input data, such as measurements during solar cell production, to quality parameters, such as solar cell efficiency.

A successful rating model can be established on the basis of known PL images of as-cut wafers and solar cell efficiencies. A sufficiently large amount of empirical data containing a huge material variation has been collected. PL images were measured during incoming control. The samples were processed within an industrial solar cell process for passivated emitter and rear cells (PERCs) [13]. The current–voltage characteristics (I – V) were measured for each sample, and pairs of corresponding data from incoming control and I – V data were identified through the marking of each sample with a data matrix code. A *convolutional neural network* (CNN) learns a mapping from PL images to I – V data on the basis of this comprehensive data set, as shown in Fig. 6.

For the model validation, the most complicated data distribution was defined: the test set contained only those samples from bricks (or even from manufacturers) that had not been used for the training of the model. The model validation showed a mean absolute error as low as $0.11\%_{abs}$ for the efficiency prediction, and 2.0mV for the open-circuit voltage (V_{oc}) prediction, when materials of 'unknown' bricks were tested. A correlation graph for the open-circuit voltage is shown in Fig. 7. Comparable results were achieved for the prediction with 'unknown' manufacturers. The evaluation demonstrates the generalizability of the prediction model in terms of dealing with materials from different crystallization processes and feedstock variations.

“A generalized data collection opens up possibilities of using advanced data analysis and modern data science technologies and learn-from data.”

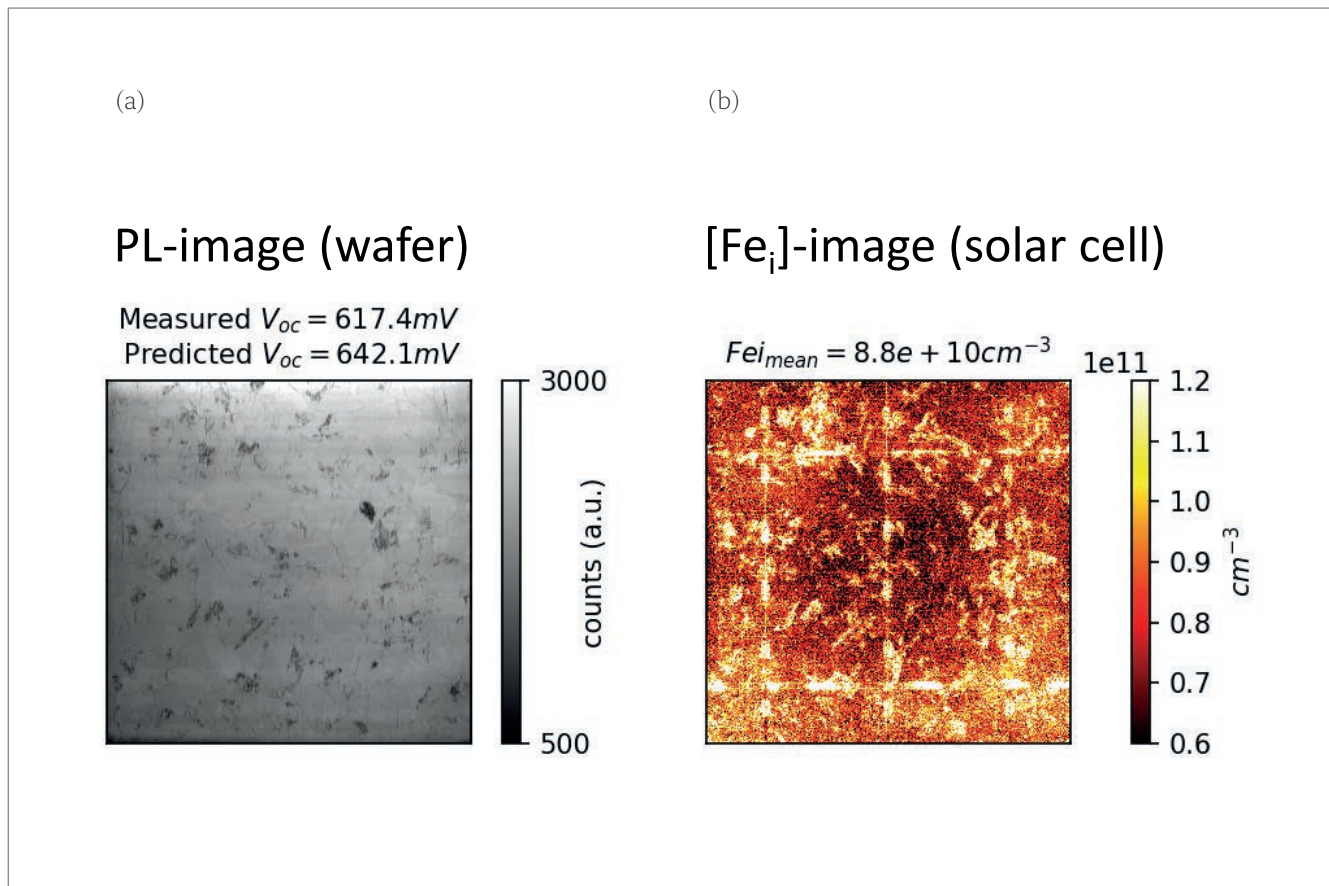


Figure 8. (a) PL image with a few visible structural defects, causing prediction errors. (b) The root-cause analysis reveals an increased iron concentration for samples with high prediction error.

Because of the high prediction accuracy, the network model can be used for fault detection and analysis. Deviations between predicted and measured quality parameters are indicators for process errors or variations in material quality, which cannot be observed in PL images. In the example here, a systematic overestimation of materials from one manufacturer was observed. For a detailed root-cause analysis of failure cases, advanced characterization techniques, such as the modulated luminescence (MODULUM) imaging method [14,15], can be utilized.

The data sample highlighted by a red cross in Fig. 7 was analysed in more detail. As illustrated in Fig. 8, the MODULUM technique reveals that prediction errors are correlated with an increased concentration of interstitial iron observed in the top regions of the ingot.

In the application under study, the CNN learns a direct connection between the 2D PL image of wafers and the I - V parameters of the solar cell. The end-to-end approach means that no expert knowledge needed to be provided to the model.

How do we know that we are right for the right reasons? To answer this, it is necessary to take a closer look at the network. By feeding a PL image into the CNN for open-circuit voltage prediction, the spatial resolution of the data is reduced at different stages of the network. The data are compressed to retain the relevant features, as previously shown in Fig. 6. The activations

in the final layers can be combined to create an activation map and scaled to open-circuit voltage. It is now possible to localize regions of reduced material quality in the activation map which has been learnt by the network.

The network learns a semantically meaningful representation of the data which corresponds to the expectations of PV experts. Despite the low resolution at the final stages of the network, regions of reduced open-circuit voltage coincide with the crystallization-related defects (such as contaminated regions from the crucible and dislocations), as shown in Fig. 9. A comparison of the image of the dark-saturation current density (j_0) [16] of the solar cell with the activation map of the network for an input PL image of the as-cut wafer shows a striking similarity of the data.

Data flow in future production lines

Ideally, production lines correspond to the conventional automation pyramid, regarded as the so-called *industry 3.0* implementation. As a result, various communication systems, tailored to fulfil individual requirements, are in use in order to establish a highly structured vertical and horizontal data flow – taking into account all organization levels from the shop floor upwards through the whole company. The key business requirements that are to be met in this way exist on the vertical plane for all production planning and

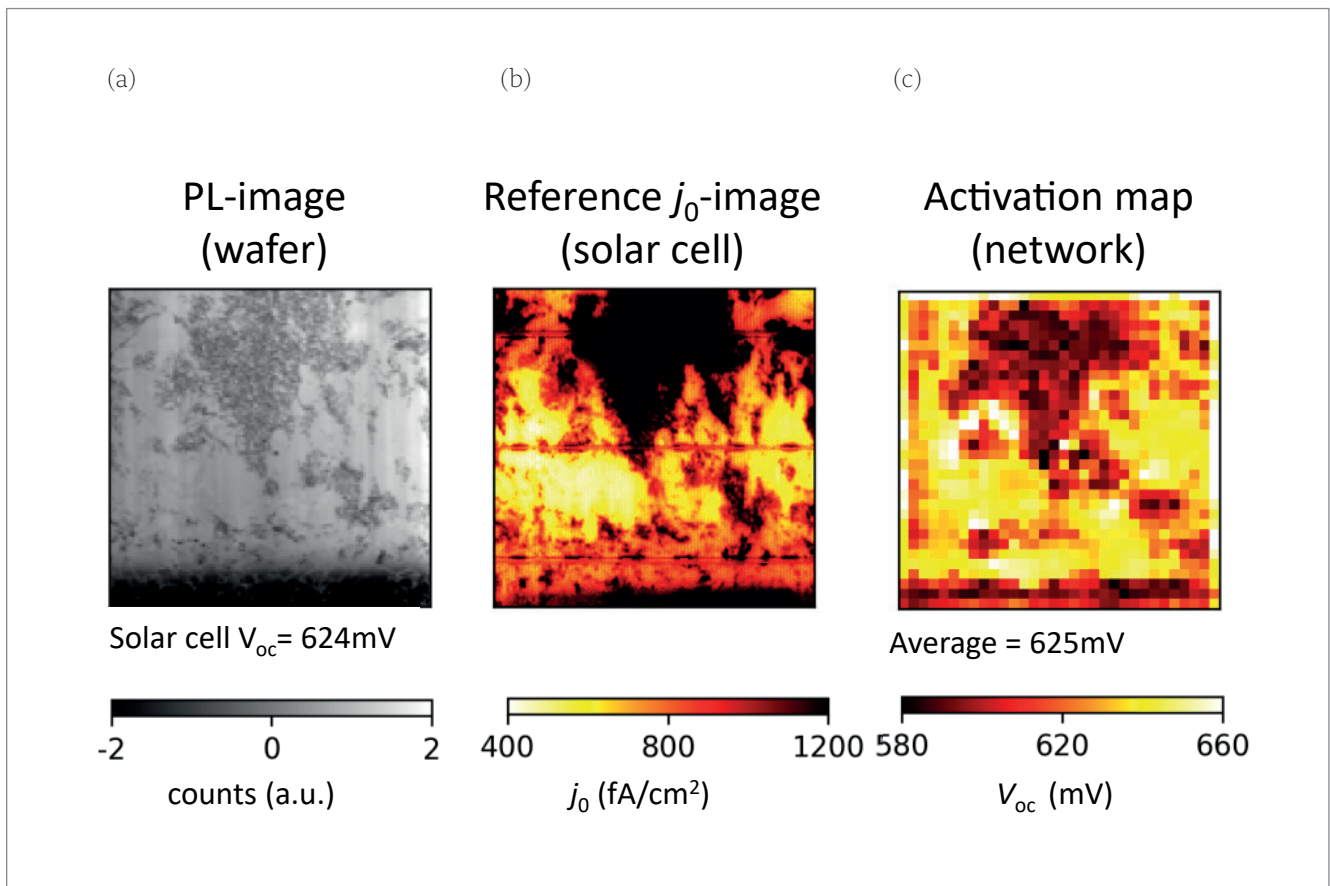


Figure 9. (a) PL image of the wafer, (b) image of the dark-saturation current density j_0 , and (c) the calculated activation map according to the network model for the PL image in (a). The activation map reveals the expected V_{oc} distribution due to the material defects observed in the PL image and shows a high correlation with the j_0 image. The average activation value of 625mV represents the predicted result, which is similar to the measured value of 624mV of the solar cell.

data collection purposes, with a view to achieving general business objectives. On the vertical plane, only organizational and practical needs which contribute to fulfilling these vertical requirements are considered. The degree of digitalization and complexity of data flows in production lines are focused on these higher requirements and consequently only form reduced data structures with limited information value, such as stringent process specifications and conventional key performance indicators (KPIs). That typical approach leads production lines to keep almost 90% of industrially generated data decentralized, and to disclose only 10% of data which was previously declared to be important data.

In terms of industry 4.0 approaches, the data acquisition has to collect as much data as possible in order to generate a comprehensive pool of 'all data', without knowing or preselecting what is important and what is not, because that decision cannot yet be made at this point in this context. Because these data pools are meant to support a tremendous amount and variety of data structures, conventional data centralization and storage technologies need to be replaced by modern schema-less technologies. These technologies also enable concepts of distributed data pools and support dynamic data retrieval.

A generalized data collection opens up possibilities of using advanced data analysis and modern data science technologies and learn-from data. This is what is commonly regarded as *Big Data*; it makes all data accessible and allows learning from it. Whether it be simple data patterns or machine-learning results, it is the raw material for future product and process development and also paves the way to deeper process optimization in a more and more sensitive production environment. The main core idea is that not just data whose meaning and relationships are already known and deemed relevant are collected, but *all data* should be collected.

Of course, intensive data investigation and post-processing are necessary in order to extract new and relevant knowledge from Big Data pools. As soon as novel relationships become apparent in the data, appropriate data analyses can be standardized, simplified and introduced into production. However, the conventional requirements in terms of general business intelligence mentioned earlier must not be neglected and must be included in the new concepts from the start.

Data inherently require formalized structures that allow automated handling and ultimately

allow processing and evaluation. Data of this type also form the basis of every digital communication – human to human, machine to machine, or human to machine. For centralization and organization, data are arranged in databases and permanently archived. In doing so, the database maps the formalized representation of the data in question through its database schema. The basic features of such a typically relational database are the standardization of the data structures that are fundamental to an application, the precision and consistency of the data in the database, and the routine of all operations within the database, as well as data exchange with applications external to the database. Usually, ERP and MES solutions are based on these approaches and are focused on these features as the main requirements to support business processes. All of these aspects are the strengths of a traditional, relational database system. However, these strengths are equally associated with limitations and restrictions when industry 4.0 concepts come into play. First of all, modern ‘not only standard query language’ (NoSQL) database technologies have to be integrated into existing business intelligence solutions.

The variety of different proprietary interface protocols for any type of digital communication also needs to be consolidated and unified. In addition, all components involved must be able to communicate bidirectionally with one another for intelligent communication. Open platform communication unified architecture (OPC-UA [17]) shows much promise for that purpose and is actually becoming a de facto standard for machine-to-machine communication. In contrast to the widely used SEMI PVo2 interface, OPC-UA allows simultaneous communication with multiple clients; this enables a flexible implementation of several applications that can all access the data, which is provided in the entire production line.

Discussion and outlook

The fourth industrial revolution will change production technology in a sustainable way. Primarily, the rapid development of microcontroller technology, as well as the rapid drop in price of processors and memory devices, leads to an increasing variety of applications – from intelligent sensors and production tools to simulation models for the prediction of process results.

Empirical methods based on data-intensive deep-learning technologies are promising for the quality control of high-throughput production in future PV fabrication. Fraunhofer ISE’s leading investigation was capable of modelling, on the basis of empirical data alone, the influence of material quality on the solar cell process.

One perspective on the acceleration of material development based on machine learning was put forward by Correa-Baena et al. [18]. Those authors

“Digitalization as well as equipment intelligence, in combination with highly automated future GW-scale production chains, will represent the future of PV manufacturing.”

propose that a balance between actionable results and inferring physical insights should be found in order to advance engineering and scientific objectives.

It is assumed that this is especially true when it is a question of inline quality monitoring: a ‘white box’ model is not required for many characterization tasks in PV production, such as crack detection or even rating fracture strength, as long as sufficient data are available. Nevertheless, high predictability and physical insights are not mutually exclusive and can be tackled by developing methods for theory-guided data analysis.

Digitalization as well as equipment intelligence, in combination with highly automated future GW-scale production chains, will represent the future of PV manufacturing, offering interesting perspectives and technology differentiators for equipment manufacturers in the years ahead.

References

- [1] Roth, T. (ed.) 2016, *Einführung und Umsetzung von Industrie 4.0*. Heidelberg: Springer Verlag.
- [2] Bateman, J.F. 1995, “Preventive maintenance: stand alone manufacturing compared with cellular manufacturing”, *Ind. Manag.*, Vol. 37, No. 1, pp. 19–21.
- [3] ABB 2018, “ABB Ability Smart Sensor for pumps” [<https://search-ext.abb.com/library/Download.aspx?DocumentId=3AUA0000230035&LanguageCode=en&DocumentPartId=&Action=Launch>].
- [4] Moldovan, A. et al. 2016, “Ozone-based surface conditioning focused on an improved passivation for silicon heterojunction solar cells”, *Energy Procedia*, Vol. 92, pp. 374–380.
- [5] Biro, D. et al. 2009, “PV-TEC: Retrospection to the three years of operation of a production oriented research platform”, *Proc. 24th EU PVSEC*, Hamburg, Germany, pp. 1901–1905.
- [6] Demant, M. et al. 2018, “Learning quality rating of multicrystalline Si-wafers via convolutional regression networks”, *IEEE, J. Photovolt.* [submitted].
- [7] Demant, M. et al. 2018, “Visualizing material quality and similarity of mc-Si wafers learned by convolutional regression networks”, *IEEE J. Photovolt.* [submitted].
- [8] Trupke, T. et al. 2006, “Photoluminescence imaging of silicon wafers”, *Appl. Phys. Lett.*, Vol. 89, No. 4, p. 44107.

- [9] Schubert, M.C. et al. 2013, "Impact of impurities from crucible and coating on mc-silicon quality – The example of iron and cobalt", *IEEE J. Photovolt.*, Vol. 3, No. 4, pp. 1250–1258.
- [10] Krizhevsky, A., Sutskever, I. & Hinton, G.E. 2012, "ImageNet classification with deep convolutional neural networks", *Proc. 26th Ann. Conf. Neural Info. Proc. Syst.*, Lake Tahoe, Nevada, USA, pp. 1106–1114.
- [11] Russakovsky, O. et al. 2015, "ImageNet large scale visual recognition challenge", *Int. J. Comput. Vis.*, Vol. 115, No. 3, pp. 211–252.
- [12] LeCun, Y. et al. 1998, "Gradient-based learning applied to document recognition", *Proc. IEEE*, Vol. 86, No. 11, pp. 2278–2324.
- [13] Werner, S. et al. 2017, "Key aspects for fabrication of p-type Cz-Si PERC solar cells exceeding 22% conversion efficiency", *Proc. 33rd EU PVSEC*, Amsterdam, The Netherlands.
- [14] Fraunhofer ISE 2018, "MODULUM" [available online: https://www.ise.fraunhofer.de/content/dam/ise/de/documents/infomaterial/brochures/photovoltaik/16_en_ISE_Flyer_modulum.pdf].
- [15] Schubert, M.C., Habenicht, H. & Warta, W. 2011, "Imaging of metastable defects in silicon", *IEEE J. Photovolt.*, Vol. 1, No. 2, pp. 168–173.
- [16] Glatthaar, M. et al. 2010, "Evaluating luminescence based voltage images of silicon solar cells", *J. Appl. Phys.*, Vol. 108, No. 1, 2010.
- [17] OPC Foundation [<https://opcfoundation.org/>].
- [18] Correa-Baena, J.P. et al. 2018, "Accelerating materials development via automation, machine learning, and high-performance computing", *Joule*, Vol. 2, pp. 1410–1420.

About the Authors



Martin Zimmer is head of the wet-chemical process technology group at Fraunhofer ISE. After finishing his studies in chemistry in Heidelberg, he received his Ph.D. from the Albert Ludwig University of Freiburg in cooperation with Fraunhofer ISE, where he investigated industrial texturization processes. His current research focuses on new wet-chemical production technologies in the context of industry 4.0.



Matthias Demant works on machine-learning techniques for material characterization and process control in the field of renewable energy at Fraunhofer ISE. He received his Ph.D. in engineering sciences from the University of Freiburg in 2016. As a postdoc he joined the vision group of the International Computer Science Institute (ICSI) at UC Berkeley in 2017. Since 2019 he has led a team involved in image processing and machine learning at Fraunhofer ISE.



Norbert Bergmann studied industrial engineering in Freiberg, and joined Fraunhofer ISE in 2008 to undertake his thesis on the topic of data management and analysis. Since 2010 he has been involved in the digitalization process for the Photovoltaic Technology Evaluation Center (PV-TEC) pilot line, and has been working in the fields of manufacturing execution systems and automatic data collection.



Stefan Rein is head of the quality assurance, characterization and simulation department within the PV division at Fraunhofer ISE. He studied physics at the Albert Ludwig University of Freiburg, where he obtained his diploma degree in 1998. He received his Ph.D. in 2004 from the University of Konstanz for his work on lifetime spectroscopy for defect characterization in silicon, and since then has been working in the PV-TEC at Fraunhofer ISE. His research at Fraunhofer ISE focuses on inline metrology, production control, machine learning, solar cell simulation and new silicon materials.



Jochen Rentsch is head of the production technologies – surfaces and interfaces department at Fraunhofer ISE. He studied physics at the Technical University of Braunschweig, obtaining his diploma degree in 2002. He then received his Ph.D. in physics in 2005 from the Albert Ludwig University of Freiburg. His work at Fraunhofer ISE focuses on R&D in rear-passivated solar cells and new wet- and dry-chemical processing technologies, as well as on coordinating cell technology transfer projects.



Ralf Preu is director of the photovoltaics (production technology) division at Fraunhofer ISE and also teaches photovoltaics at the University of Freiburg. He studied physics at the Universities of Freiburg and Toronto, and economics at the University of Hagen, Germany, and holds a Ph.D. in electrical engineering. He joined Fraunhofer ISE in 1993 and has worked in different fields in PV, including system monitoring, silicon solar cell and module technology, characterization and simulation. His main focus is R&D in advanced silicon solar cell technology and its transfer to industrial production.

Enquiries

Email: martin.zimmer@ise.fraunhofer.de

**SNEC 13th (2019) International Photovoltaic Power Generation
and Smart Energy Exhibition & Conference**

2019 | June 3-6
Shanghai · China

Shanghai New International Expo Center
(2345 Longyang Road, Pudong District, Shanghai, China)

Follow Us at WeChat



Chinese Version



English Version

© Asian Photovoltaic Industry Association / Shanghai New Energy Industry Association

© Show Management: Follow Me Int'l Exhibition (Shanghai), Inc.

Add: RM905-907 No 425 Yishan Rd, Xuhui District, Shanghai 200235, PRC

Tel: +86-21-33685117 / 33683167

© For exhibition: info@snec.org.cn

For conference: office@snec.org.cn

PV manufacturing capacity expansion announcements in 2018

Mark Osborne, Senior News Editor, *Photovoltaics International*

Abstract

PV manufacturing capacity expansion announcements in 2018 were significantly impacted by major policy changes mid-year in China. This paper looks in detail at the contrasting developments in the first half of the year, compared with the second half. Attention will also be given to the regional site selection changes as well as to the advanced manufacturing trends emerging in 2018. Finally, after five years of tracking capacity expansion plans, an overview of cumulative expansions, coupled to global solar demand and to capacity trends specifically in China, will be provided.

First half 2018 announcements review

PV manufacturing capacity expansion announcements in the first half of 2018 almost mirrored the total figures reported in the first half of 2017 (Fig. 1). In the first half of 2018 a total of just over 55.2GW of combined (cell, module, thin-film and integrated) capacity expansions were

announced, up from over 52.7GW in the prior year period, indicating very little change.

Thin-film plans topped 3,340MW in the first half of 2018, compared with 2,720MW announced in the prior year period (Fig. 2). This level of activity has been relatively high compared with any other period since 2014. As in previous years, the majority of thin-film capacity announcements came from First Solar and Hanergy Thin Film Power Group (Hanergy TF).

CdTe (cadmium telluride) leader, First Solar, announced the building of a new 1.2GW manufacturing plant near its existing flagship facility in Perrysburg, Ohio, both part of its Series 6 large-area module transition.

Hanergy TF's plans were announced as part of a new business model in 2017 that provides new industrial parks with a selection from a portfolio of a-Si, CIGS (copper indium gallium selenide), GaAs and c-Si heterojunction (HJ) turnkey production lines to give local governments access to solar technology and attract other hi-tech companies to new industrial parks. In releasing its 2017 annual financial report, Hanergy TF noted that, as a result of its new business, dubbed 'Industrial Parks Projects', Hanergy Mobile Energy Holdings Co., Ltd., a company subsidiary, took a 20% stake in local government planned industrial parks, which were also owned by the local government and various third-party investors. The shareholders of the industrial park project become the ultimate purchaser of Hanergy TF equipment and technology, as the Hanergy subsidiary limits its shareholding to below the 30% equity interest rules, when Hanergy would be deemed an associate of a connected party. Partners have already signed up to participate in the new business model, primarily related to CIGS plants, which totalled 2,140MW.

The significant change, however, was in the shift away from c-Si solar cell expansion plans that dominated proceedings in the first half of 2017, to much greater attention to module assembly. Total solar cell expansion plans topped 17,340MW in the first half of 2018, while in the prior year period this

“PV manufacturing capacity expansion announcements in the first half of 2018 almost mirrored the total figures reported in the first half of 2017.”

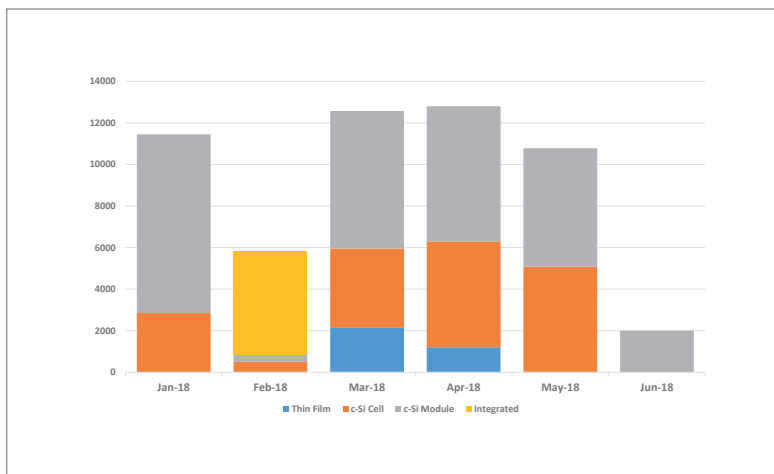


Figure 1. Capacity expansion announcements by product type in 1H 2018 (MW).

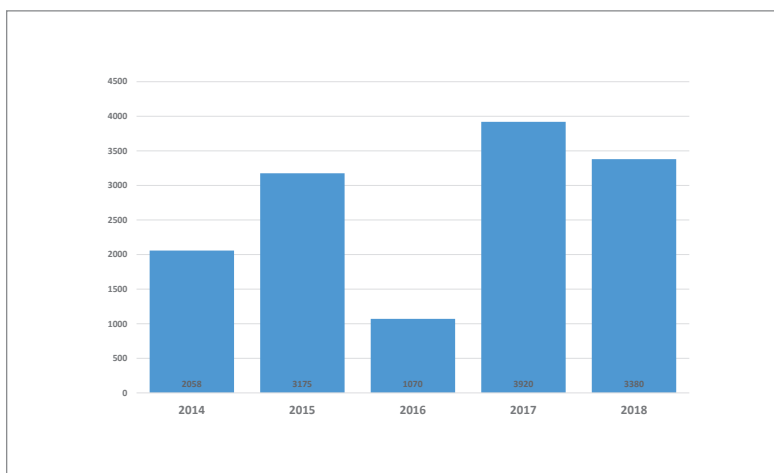


Figure 2. Total thin-film capacity expansion announcements 2014–2018 (MW).

stood at 35,439MW, more than double that in the first half of 2018.

In contrast, new module assembly plans amounted to 29,570MW in the first half of 2018, compared with 14,595MW in the prior year period, less than half the figure announced in the first half of 2018. Adding to the contrast was a single announcement from major China-based PV module manufacturer Risen Energy, which entered PV Tech's top-10 module manufacturer's rankings for the first time in 2017.

Very few integrated facilities were announced in 2017, totalling only 1,150MW. Risen announced a 5,000MW phased capacity expansion for a single-site integrated cell and module assembly complex to be situated in the Yiwu Information Optoelectronics High-tech Industrial Park, Zhejiang, China. The initial production capacity in the Phase 1 expansion was said to be 2GW, which would be operational in the next three years. Volume production would be highly flexible, enabling p-type mono PERC (passivated emitter and rear cell) production, as well as bifacial cell production and half-cut cells for 5BB/6BB high-efficiency single- and double-glass modules. Risen had previously announced that total capital expenditures for the new production facility, as well as R&D activities, would be approximately RMB 8bn (US\$1.23bn). The company started construction of the new manufacturing hub in July 2018.

In hindsight, arguably the biggest change to occur in the first half of 2018 was China's decision to suddenly cap utility-scale and distributed generation (DG) projects at the end of May, now known as the '531 New Deal'. The impact was immediately felt in China, as no China-based company announced new capacity expansion plans in the month of June. Indeed, June stands out for being the only month in the first half of 2018 when a Chinese manufacturer did not announce new expansions.

Capacity announcements in June only related to module assembly plans, which totalled 2,000MW from just three companies. June would prove to be a significant milestone in that respect.

First half 2018 geographical review

On a geographical basis, the first half of 2018 would, on the surface, seem to be business as usual (Fig. 3). Capacity expansion plans in China totalled 20,740MW, the clear preferred country for expansions. In the second quarter, however, only 1.5GW was announced, all from JA Solar. Though China was dominant, four other countries (India, Egypt, USA and Turkey), all with multi-megawatt totals combined, reached 31,790MW. Leading the pack was India at 15,710MW of new capacity plans, which included over 6,000MW in the first quarter of 2018 and 9,500MW in the second quarter.

A notable contrast with the prior year period was the lack of new activity across South East Asia. In the first half of 2017, Malaysia at 4,050MW was second to China as a major destination, followed

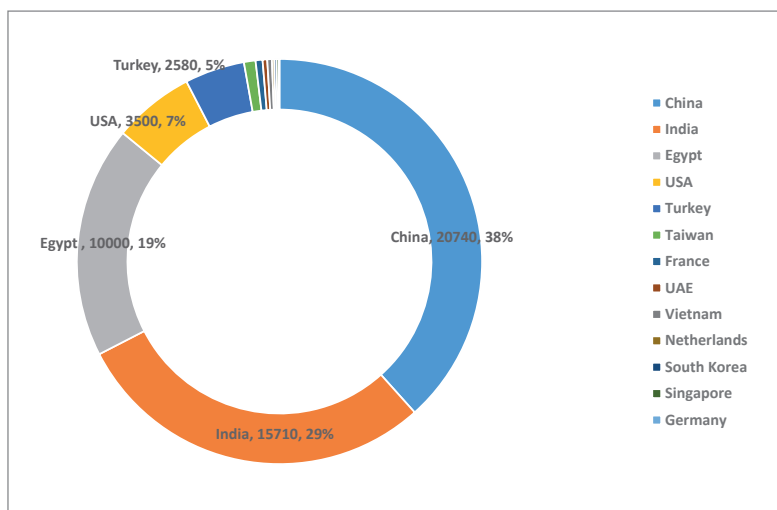


Figure 3. Total capacity expansion announcements by country in 1H 2018 (MW).

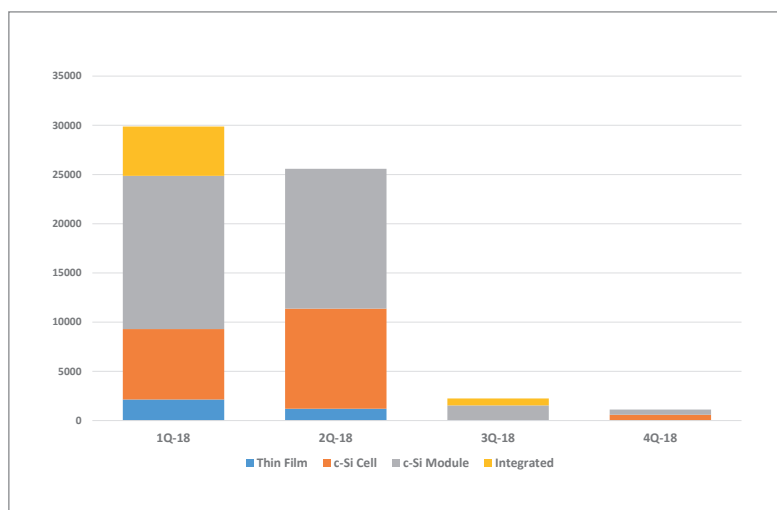


Figure 4. Quarterly capacity expansion announcements by product in 2018 (MW).

by Taiwan at 3,900MW. In the first half of 2018, however, Taiwan could only muster 500MW, while no new capacity expansions were announced for Malaysia.

Second half 2018 announcements review

Following on from June 2018, when only 2,000MW of total module assembly capacity expansion plans were generated by India (1,500MW) and the USA (500MW), July saw a total of only 150MW of capacity plans, all in the module assembly segment and all outside China.

In the third quarter of 2018, new capacity expansion announcements totalled 2,245MW, compared with 4,121MW in the prior year period, although this is typically a slow quarter (Fig. 4). The majority of new expansion plans (1,205MW) came from the module assembly segment, while integrated cell and module accounted for 700MW

“The biggest change to occur in the first half of 2018 was China's decision to suddenly cap utility-scale and distributed generation projects at the end of May.”

and flexible thin-film (CIGS) accounted for a preliminary estimate of 40MW. No new solar cell expansions were announced in the third quarter of 2018, which is significant because of the fact that there has not been a quarter in the last five years when there have not been any expansion announcements related to solar cells.

The situation drastically deteriorated in the fourth quarter of 2018, with total combined capacity expansions reaching only 1,120MW. Not only was this a significant decline, quarter-on-quarter, but it was in stark contrast to the 40,100MW total capacity announced in the fourth quarter of 2017. Although solar cell expansions rebounded to 590MW in the fourth quarter of 2018, the prior year had witnessed announcements totalling 28,100MW. Module assembly plans fell to just 530MW in the fourth quarter, compared with 9,800MW in the fourth quarter of 2017.

Second half 2018 geographical review

In line with the collapse in capacity expansion announcements in the second half of 2018 (primarily due to the lack of activity in China), which plummeted to a staggering 40MW, the number of countries where expansions were announced declined to only nine, down from 13 in the first half of the year (Fig. 5). Following China in the lack of announcements were key manufacturing hubs in South East Asia (Taiwan, Malaysia, Indonesia and Vietnam).

Historically strong countries in Asia gave way completely to three countries (Armenia, Ukraine and South Africa) that have few, if any, PV manufacturing facilities, and to a further three (Canada, France and Russia) that have rarely logged any meaningful expansions in the last five years. Of note, this included European PV manufacturer Recom, which would soon have a 700MW integrated manufacturing plant online in Armenia to serve the US, European and Middle East markets. The company would also be expanding module assembly capacity (150MW) at its existing facility in France.

In December 2018, China-headquartered Seraphim Solar System Co announced a new 500MW solar cell plant in Port Elizabeth and a module assembly expansion at a recently opened plant in Eastern Cape, both in South Africa. These facilities are expected to primarily serve the US market.

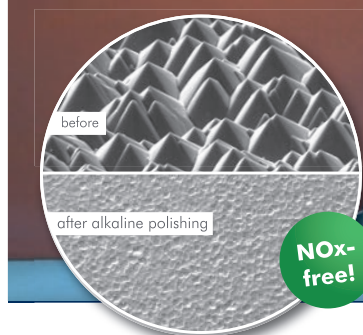
2018 round-up

Total manufacturing capacity expansion announcements totalled 58,815MW in 2018, down from 96,996MW in 2017. On a segment basis, thin-film expansion plans reached 3,380MW, compared with 3,920MW in 2017 (Fig. 6), while solar cell (c-Si) manufacturing expansions reached 17,930MW in 2018, significantly down from 64,630MW in 2017.

Module assembly expansion plans reached 31,805MW in 2018, up from 26,265MW in the previous year. Integrated manufacturing plant announcements were 5,700MW from only two companies in 2018, although significantly higher than the 1,151MW announced in 2017 (also from two, but different, companies).

On a geographical basis, China accounted for a total of 20,780MW of combined capacity expansion announcements in 2018, down from 71,110MW in 2017 (Fig. 7). However, China retained its position for the second year running as the number

Key Processes for High-Efficiency Cell Production



Our new **alkaline edge isolation and rear-side polishing systems** combine several process steps in one modular system.

- Significantly lower consumable and waste disposal costs than acid-based processes
- Free of NOx emissions to meet tomorrow's environmental regulations today
- High efficiency cells at lowest process costs

Our **APCVD systems** continue to be the benchmark in high efficiency cell production.

- Very high throughput (up to 4000 w/h)
- Wide range and flexibility of emitter design
- Individual tailoring of layer stack systems
- Low consumable cost and simple process integration



one destination for expansion announcements in 2018.

India bounced back in 2018 with announcements totalling 15,710MW, compared with only 2,790MW in 2017. India had been the top destination in 2016 with 17,040MW of capacity expansion announcements.

Egypt was ranked third in 2018 with solar cell and module assembly each at 5GW, which was entirely thanks to plans approved by the National Authority for Military Production for the China-based GCL Group to establish a manufacturing hub that would include wafer production in the country. This project remains at an early stage of evaluation, despite being rubber stamped by the Egyptian government.

2018 manufacturing trends

Outside of the significant fall-off in announcements, notably from China-based manufacturers in the second half of 2018, it is interesting to observe several other trends at play during the year.

Industry 4.0

The drive for high-efficiency solar cells (PERC, n-PERT, HJ, IBC) and modules (half-cut, shingled, half-module) is proving to be a catalyst for higher levels of manufacturing automation, beyond the conventional drivers such as high quality at high volumes and reductions in workforce in order to reduce manufacturing costs. The PV industry is also starting to adopt the general concept of 'Industry 4.0', which includes a suite of advanced tool processing control technologies through to data logging and analysis in order to further drive manufacturing efficiencies at the wafer, cell and module levels.

In late 2017, China-based integrated and merchant PV manufacturer Tongwei Group opened its completed high-efficiency p-type mono PERC solar cell plant (S2), which included the world's first technically unmanned monocrystalline solar cell production line. The S2 plant, located in Chengdu, China, has an initial nameplate capacity of 2GW, while housing an Industry 4.0-inspired 200MW solar cell line that is completely unmanned in order to test intelligent fully automated manufacturing tools and software systems (Fig. 8).

Barely nine months later, in August 2018, Tongwei announced that it would begin pilot production of heterojunction (HJ) solar cells by the end of 2018, primarily as a result of the success of its 200MW Industry 4.0 line. Importantly, the favourable evaluation of the Industry 4.0 line could lead to the longer-term migration of all cell production to intelligent manufacturing. Tongwei said that ongoing R&D activities, as part of an advanced collaboration effort on next-generation HJ solar cells, would lead to pilot volume production evaluations by the end of 2018. HJ cell production requires more stringent cleanroom contamination requirements and automated

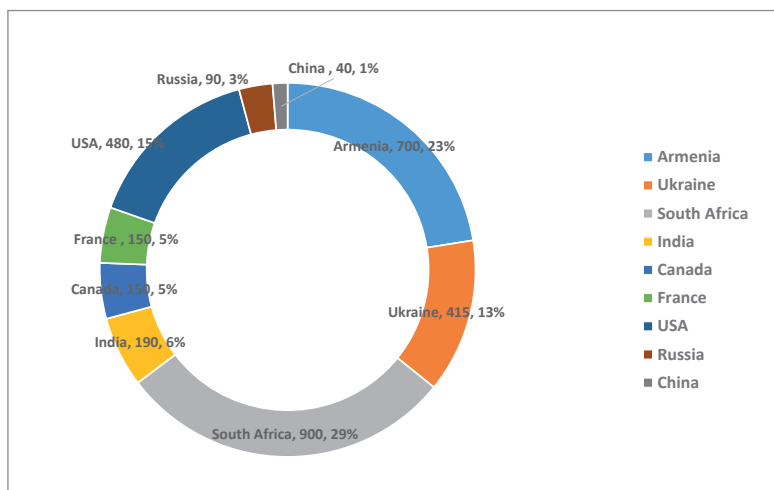


Figure 5. Total capacity expansion announcements by country in 2H 2018 (MW).

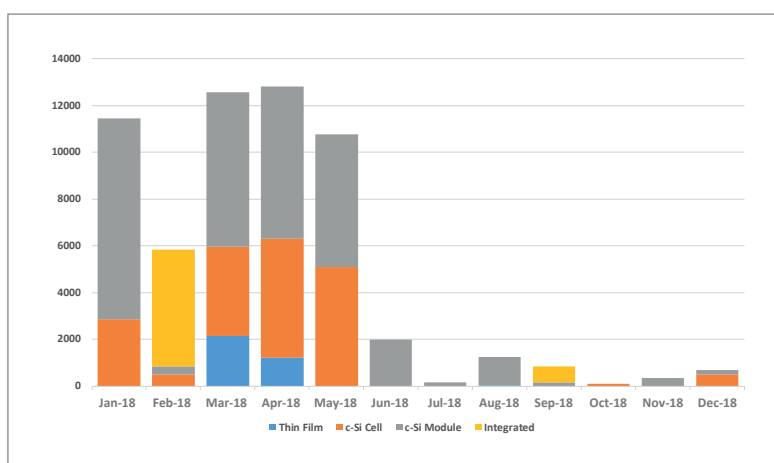


Figure 6. Monthly capacity expansion announcements by product type in 2018 (MW).

handling and processing, in line with Industry 4.0 objectives. Any contamination of an HJ cell before the deposition of the a-Si layers degrades the cell conversion efficiency.

Importantly, Tongwei noted that, on the basis of the current data analysis, the Industry 4.0 cell line had operated in a stable condition, while improving cell product quality and overall productivity, compared with non-fully automated lines. The company indicated that, when conversion efficiency, yield and CTM (cell to module) criteria were used, the overall in-house cell production in the first half of 2018 was as much as 60% higher than the Chinese industry benchmark average. The company claimed that it was at the leading level within the industry in view of the operating stability of the line, coupled with the ability to reduce production costs, which were said to be in the range of 0.2–0.3 yuan/W (US\$0.029/W). These costs were significantly below benchmarked Chinese cell producers' costs of more than 0.45 yuan/W, according to data released in January 2018

“Total manufacturing capacity expansion announcements totalled 58,815MW in 2018, down from 96,996MW in 2017.”

by the China Photovoltaic Association.

The company has also been ramping up R&D spending for several years now, and spent almost US\$55m on solar-related (polysilicon, cell and module) R&D in 2017. Group R&D spending in 2017 was over US\$80m.

Other pilot projects have been ongoing at SMSL (silicon module super league) member GCL System Integrated (GCL-SI), which established a module assembly workshop that is completely unmanned in order to test intelligent, fully automated, manufacturing tools and software systems (Fig. 9). The company indicated that it is cooperating closely with Chinese domestic equipment manufacturers, and has independently researched and developed a series of intelligent tools and systems, which include a high-speed automated tabbing machine, a high-precision layout machine and a robotic palletizing system. In all, GCL-SI said that 26 separate systems developed so far have been industry firsts. Key aims of the tests are to achieve a 50% improvement in efficiency, a 60% decrease in online manpower, and a 30% reduction in processing costs. Product quality improvement targets were being set at an overall improvement of 21%. The intention is to implement the improvements across the company's volume manufacturing operations in the future.

In 2018 leading SMSL member JinkoSolar also initiated intelligent, highly automated, manufacturing tools and software systems into its volume PV module assembly facilities in China, followed by its 600MW assembly plant in Florida, USA, which is expected to be operational in early 2019. The company is expected to implement a range of Industry 4.0 initiatives at its manufacturing plants in 2019.

SunPower, a leading high-efficiency solar cell and module producer, is planning its first 100MW 'NGT' cell line in Malaysia within the Industry 4.0 framework, following on from development work at a pilot line established at its California headquarters in mid-2017.

REC Group's Singapore integrated cell and module facility also has a pilot line for evaluating a range of Industry 4.0 initiatives, ahead of the small-scale production of heterojunction solar cells, a major departure from its volume production of multicrystalline products.

Preliminary analysis indicates that the mainstream (SMSL) and niche high-efficiency PV manufacturers combined have Industry 4.0 migration plans in excess of 10,000MW, although the migrations, which include retrofit as well as new manufacturing plants announced in 2018, could stretch over several years. However, such Industry 4.0 adoption is ongoing and is highly expected to surpass 20,000MW of capacity in the next few years as more and more companies develop migration plans in order to remain competitive with the early adopters.

It should also be noted that thin-film module leader First Solar is also driving advanced manufacturing strategies with its complete migration (including retrofit and new build) to its Series 6 large-area CdTe modules. The manufacturing plants, including those in the USA, Malaysia and Vietnam, are in many respects Industry 4.0.

Of particular note is that specialist manufacturing equipment suppliers have also benefited from the



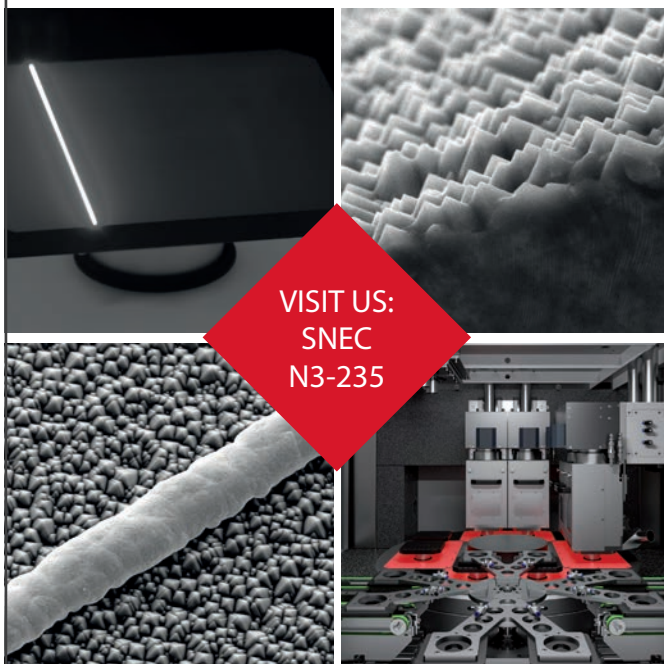
INNOLAS
solutions



COMING SOON

7500 wafer/ hour for all PERC
and LDSE applications

SEE US AT SNEC SHANGHAI!



InnoLas Solutions GmbH
www.innolas-solutions.com

Industry 4.0 activity. China-based PV module assembly equipment specialist Yingkou Jinchen Machinery Co has provided fully automated module assembly lines to SMSL members LONGi Solar, GCL-SI and JA Solar, as well as to Risen Energy, a top-10-ranked PV manufacturer in 2018.

Section 201

The US anti-dumping Section 201 case rulings by President Trump at the beginning of 2018 had already sparked a renaissance in PV module assembly announcements in the country in 2017, and were a key driver of further announcements in 2018.

A total of around 2,000MW of new module manufacturing plans were announced for the USA in 2017, which increased to over 4,000MW in 2018. With a downstream market demand of around 10,000MW per annum, major PV manufacturers were forced to establish production bases in the country, or expect to lose a key volume business to rivals that took the decision to produce modules in the country in order to avoid at least one layer of the initial 30% import tariffs. Notable major announcements included SMSL leader JinkoSolar (600MW), Hanwha Q Cells (1,200MW) and LG Electronics (500MW).

Section 201 also forced US-headquartered SunPower Corporation to buy the bankrupt facilities of SolarWorld Americas and establish 200MW of capacity for its P-Series (performance-series, p-type mono PERC, shingled) modules. Indirectly, Section 201 included a retrofit of an existing facility by First Solar, dubbed 'Ohio S6 Factory 1', with 600MW of capacity, and later a new plant close to the existing facility, dubbed 'Ohio S6 Factory 2', with a nameplate capacity of 1,200MW, which should be fully operational in 2020.

Announcements of new capacity plans at existing US manufacturing plants extended through to November 2018; these announcements included plans by Canadian module assembly firm Silfab (150MW estimated) to invest in ITEK Solar, and by Seraphim USA to add an expected 330MW of module capacity to its plant in Mississippi.

India

Should there be a debate over the validity of tracking capacity announcements, then it would be hard to refute India as an example. In 2014 total capacity expansion announcements were 1,425MW, jumping to 7,850MW in 2015 (Fig. 10). During that two-year period, less than 400MW was converted to 'effective capacity'.

A similar trend extended through 2016, with total capacity announcements reaching 17,040MW while effective capacity touched around 1,500MW.

“Specialist manufacturing equipment suppliers have also benefited from the Industry 4.0 activity.”

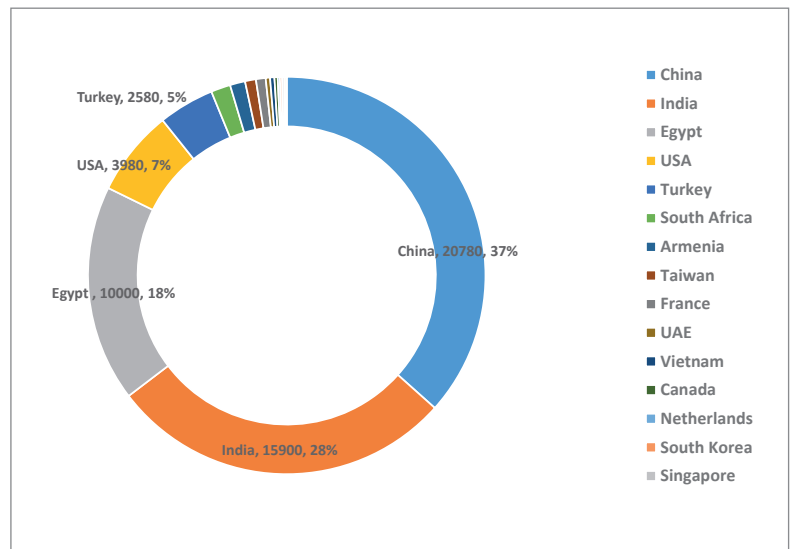


Figure 7. Total capacity expansion announcements by country in 2018 (MW).

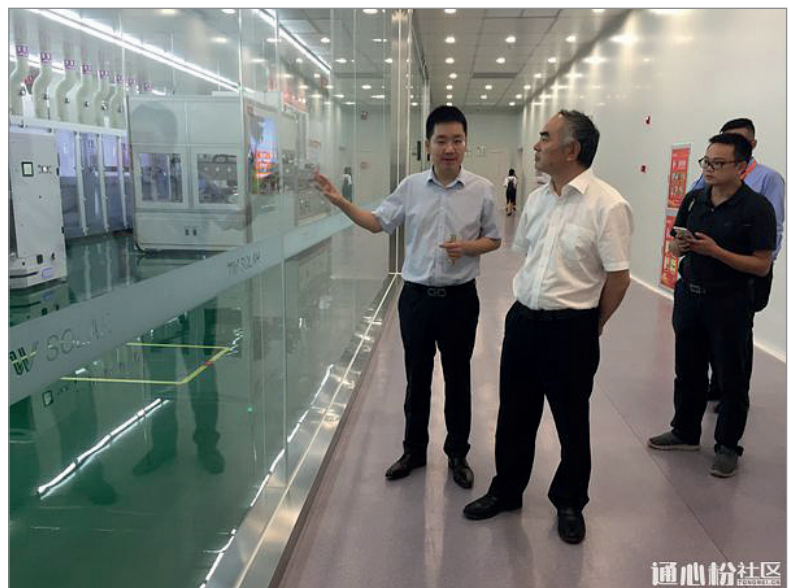


Figure 8. The S2 plant in Chengdu, China, which has an initial nameplate capacity of 2GW, while housing an Industry 4.0-inspired 200MW solar cell line.



Figure 9. GCL-SI's module assembly workshop: a completely unmanned set-up, with the aim of testing intelligent, fully automated, manufacturing tools and software systems.

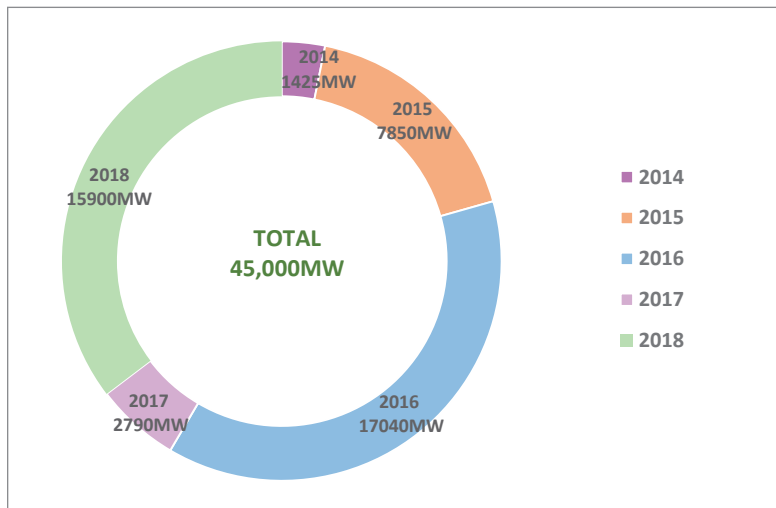


Figure 10. India: total capacity expansion announcements (cell and module) 2014 to 2018 (MW).

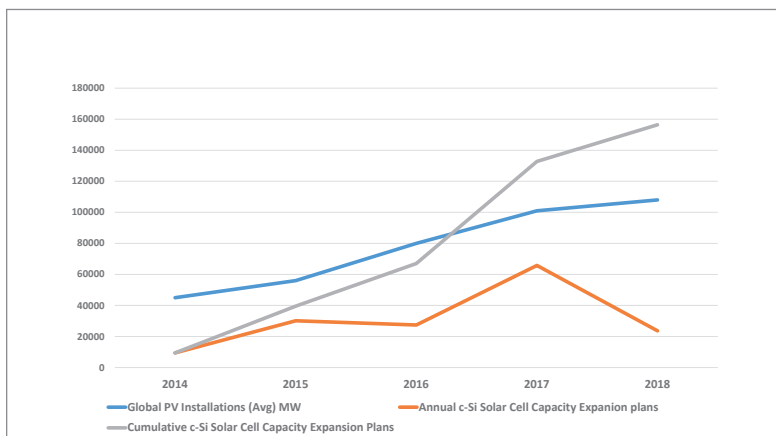


Figure 11. Annual global PV installations in relation to annual and cumulative solar cell capacity expansion plans 2014–2018 (MW).

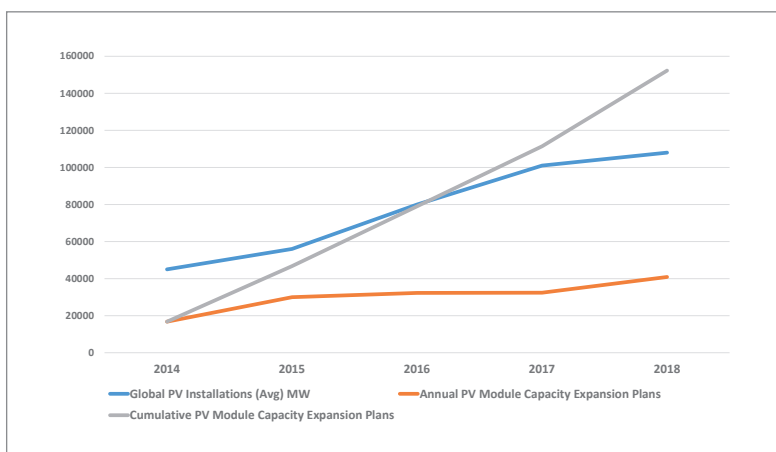


Figure 12. Annual global PV installations in relation to annual and cumulative module capacity expansion plans 2014–2018 (MW).

A lull ensued in 2017, when only 2,790MW of total capacity expansion announcements were made, yet rebounded in 2018 to reach 15,900MW. The cumulative total of announcements since 2014 has reached 45,000MW.

Since 2014 only a handful of India-based companies have converted announcements to effective capacity at volume nameplate figures; these

companies include Adani Solar, Waaree Energies and Vikram Solar. Although there are many reasons why India-based companies have struggled to convert announcements to effective capacity, raising finance at competitive rates has been a prevailing issue.

There have been a number of grand speculative announcements in this timeframe, however, from foreign firms, such as Softbank and SunEdison (who have meaningfully added to the cumulative 45,000MW figure), which failed to be converted to effective capacity.

Multiple gigawatts have also come from China-based PV manufacturers in this period, but many plans have remained on the drawing board. Nevertheless, some examples, although delayed for various reasons, are in a drawn-out process of becoming effective capacity sometime in the next few years. These include manufacturing plants by Trina Solar (500MW cell and module) and LONGi Group (1,000MW cell and module), which go back to 2015 and 2017 respectively.

In 2018 grand speculative announcements included a deal between GCL System Integration Technology Co and Softbank Vision Fund to establish a joint venture company in Andhra Pradesh, India, to operate 4,000MW of integrated wafer, cell and module capacity, which would be implemented in two 2,000MW phases.

At least 28 different India-based PV manufacturers announced plans in the first quarter of 2018 to increase capacity, which totalled around 4,000MW. The vast majority of these plans, however, had not been initiated by the end of 2018.

It should be noted that India was home to around 3,000MW of effective solar cell capacity and close 9,000MW of effective module assembly capacity at the end of 2018; however, with over 100 module producers, utilization rates are low.

Capacity expansion trends since 2014

We now have five years of capacity expansion data to share. The chart in Fig. 11 tracks annual global PV installation figures (an average from market analyst firms, including IHS Markit & BNEF) against both annual and cumulative c-Si solar cell capacity expansion announcements from 2014 through to the end of 2018. The period 2014 through 2016 highlights the strong cumulative growth in solar cell expansion plans, closing the wide gap that had existed between global PV installation figures. However, with a significant increase in cell expansion announcements in 2017, cumulative plans surpassed installation figures by over 30GW.

It should be reiterated that these are cumulative plans, rather than effective capacity. Nevertheless, this chart signifies that, since 2017, cumulative solar cell capacity expansion plans are well ahead of actual global end-market demand. Indeed, if China had not changed its solar policies in 2018, cumulative solar cell capacity expansion plans could have pulled ahead of actual global end-market demand to the tune of over

50GW. With no new capacity expansions announced in China after the 531 New Deal, announcements returned to the levels seen in 2015 and 2016.

In the chart in Fig. 12, which plots the same criteria as above but for c-Si module assembly, a clear crossover point is observed in 2016, when cumulative module assembly capacity expansions matched actual global end-market demand, but then went on to race ahead through 2018. The cumulative module assembly announcements exceeded global end-market demand by 44GW.

With China dominating PV manufacturing, the chart in Fig. 13 highlights the annual global solar installations vs. China's c-Si solar cell capacity expansion announcements and cumulative c-Si solar cell capacity expansion plans. Also included are the Chinese government official figures for effective c-Si solar cell capacity.

Through to 2016, cumulative c-Si solar cell capacity expansion plans were keeping pace with global end-market demand. The significant 53,000MW of announcements in 2017, compared with just under 12,000MW per annum in the previous two years, has meant the difference between end-market demand has narrowed significantly, with a gap of just 20GW, compared with more than 41,000MW in 2014.

Cumulative c-Si solar cell capacity expansion plans were almost identical to effective capacity figures in 2018. Although the lack of announcements in China in the second half of 2018 has masked the gap between effective capacity and expansion plans, much of the 53,000MW of announcements in 2017 were for phased expansions over as much as five years for some companies. However, many plans remain multi-gigawatt in scale and could further close the gap with end-market demand, as many projects are ongoing from 2017.

The final chart, shown in Fig. 14, again highlights the same criteria but in terms of c-Si module assembly. The plots of cumulative and effective module assembly actually follow similar paths, but have not shown any signs of expansion plans exceeding either end-market demand or outpacing effective capacity. Part of the reason for this has been the greater emphasis on adding solar cell capacity than on increasing module assembly in China. However, through this period major Chinese producers, such as Trina Solar, JinkoSolar and Canadian Solar, had been adding primarily module assembly and some cell capacity in South East Asia, such as Malaysia, Thailand and Vietnam.

As already noted, the likes of JinkoSolar have also added module assembly capacity in the USA. This could also account for the widening of the gap between effective module assembly capacity in China and global PV installations.

Conclusions

As shown, the first half of 2018 kept up the pace of capacity expansions seen in 2017, but the China 531 New Deal significantly impacted announcements

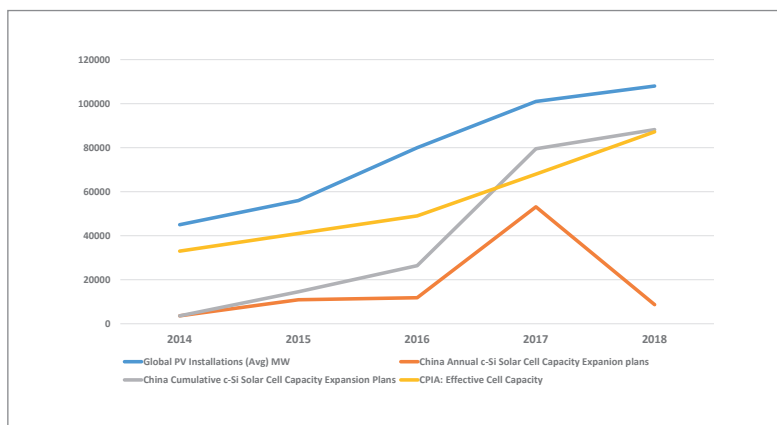


Figure 13. China: solar cell effective capacity in relation to annual and cumulative capacity expansion plans 2014–2018 (MW).

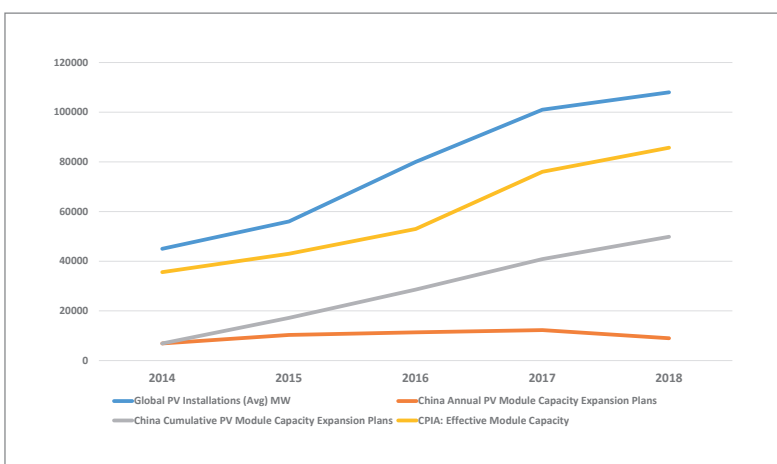



Figure 14. China: solar module effective capacity in relation to annual and cumulative capacity expansion plans 2014–2018 (MW).

from China-based manufacturers, whether for domestic or overseas expansion plans, in the second half of the year. Nevertheless, China was still the main location for planned expansions.

The USA saw a revival in at least module assembly, while South East Asia (Taiwan, Malaysia, Thailand and Vietnam) capacity announcements significantly slowed in 2018, compared with the last few years, potentially indicating the end of an expansion phase. In the case of Taiwan, effective c-Si solar cell capacity in particular is in a sharp decline, because of the competitive position of China, which has driven plant closures and consolidation of manufacturers.

Some emerging markets, notably Turkey, on the other hand, could see several major announcements become effective capacity in 2019, while announcements in other emerging markets such as Egypt and the Middle East remained speculative at the end of 2018.

“The first half of 2018 kept up the pace of capacity expansions seen in 2017, but the China 531 New Deal significantly impacted announcements from China-based manufacturers in the second half.”



ENERGY TAIWAN

📍 Taipei Nangang Exhibition Center, Hall 1

**Seize the Business Opportunities
in Asia's Green Energy Market**



16-18 OCT
2019

-  *PV Taiwan*
-  *Wind Energy Taiwan*
-  *HFC Taiwan*
-  *Smart Storage Taiwan*



TAITRA



semi™

www.energytaiwan.com.tw

Reliability of electrically conductive adhesives

G. Oreski¹, S. Pötz¹, A. Omazic¹, G.C. Eder², L. Neumaier³, C. Hirschl³, R. Ebner⁴, J. Scheurer⁵ & W. Pranger⁶

¹PCCL Polymer Competence Center Leoben, Austria; ²OFI, Austrian Research Institute for Chemistry and Technology, Vienna, Austria; ³CTR Carinthian Tech Research AG, Villach, Austria; ⁴AIT Austrian Institute of Technology GmbH, Vienna Austria; ⁵Polytec PT GmbH, Karlsbad, Germany; ⁶Ulbrich of Austria GmbH, Müllendorf, Austria

Abstract

The application of electrically conductive adhesives (ECAs) is a promising alternative to the soldering process for cell interconnection in today's solar module production. ECAs provide an environmentally friendly solution and offer several other advantages over the conventional solder interconnection technology, such as lower processing temperature, higher mechanical flexibility and replacement of toxic lead. When it is proposed to switch from soldering to adhesive technology in a critical process such as the production of solar cell strings, it is necessary to perform a thorough preliminary analysis of the properties of the materials involved, the material compatibilities and the long-term stability of the interconnections within the PV modules. An investigation has therefore been conducted with regard to the performance, quality and reliability of: 1) isolated bonded joints using ECAs, and 2) the interconnections of ECA-bonded cells within the test modules. Moreover, new formulations with increased flexibility of the polymeric binder within the ECA have been developed in order to increase the resistance to thermomechanical loads and delamination. To better understand the relevant material interactions and the influencing factors, a comprehensive test plan was set up. A characterization of the pure adhesive with respect to the outgassing and migration behaviour of volatile low-molecular compounds was performed using thermogravimetric analysis (TGA) and thermodesorption/gas chromatography–mass spectrometry (TD/GC–MS). Single-cell test modules with different combinations of ribbons and encapsulation and backsheet materials were investigated to achieve the targets. The test modules were exposed to different combined stress factors in accelerated ageing tests, namely damp heat (DH), irradiation with sunlight, and thermal cycling (TC). Even though the screen printing of the ECA on the cell, as well as the module layering, was done manually, the results from the electrical characterization showed excellent reproducibility. All ribbon types (Ag coated, bare Cu, SnAgCu coated) could be processed in the PV module lamination without any problems. Upon accelerated ageing, slight power losses between 1 and 4% were measured for the ECA-connected one- and six-cell sample modules. ECAs are therefore a promising alternative to the soldering process used in cell stringing. Outgassing of molecular compounds was found to be low, and no material incompatibilities of the adhesive with the various types of ribbons and encapsulants were observed.

Introduction and objectives

Resin-based interconnection materials for electronic packaging and interconnection technologies are currently widespread in the fabrication of electronic devices, whereas they are only rarely used in crystalline silicon PV modules for the interconnection of cells.

Creating interconnections via the print application of electrically conductive adhesives (ECAs) offers several advantages over the conventional solder process for electrical

interconnection, such as the possibility of low-temperature processing, the potential for higher-resolution printing and easier handling.

The soldering process requires temperatures of 210°C for conventional tin–lead solders, or even higher for lead-free solders. These high temperatures often cause cell breakage and the introduction of microcracks in the crystalline Si cells. The main limitation in the goal to reduce wafer thickness is therefore imposed by the soldering process. The curing reaction of ECAs, on the other hand, usually takes place below 180°C and can be tailored by modifying the basic polymeric binder. Thus, switching to an adhesive interconnection technology allows further reductions in wafer thickness and opens the door to innovative possibilities in cell design. Another advantage is that the adhesives can be applied by screen printing directly onto the finger grid of the cell, without using additional busbars on the front side of the cell.

Compared with lead-based solder alloys, the use of ECAs is an environmentally cleaner solution for interconnection tasks [1]. By replacing the toxic lead-containing solders, the accompanying challenges concerning waste management and recycling can be avoided. Furthermore, the possibility of using non-solderable materials – such as silver-coated ribbons, which are used as light-capturing ribbons – opens up new possibilities in novel cell and PV module designs. Nevertheless, the replacement of the soldering process by ECAs also has some limitations. A major drawback is the high silver price, which is why the highly filled adhesives are much more expensive than solders; this can be partially offset by cutting down on the number of busbars. Another challenge is the ability to withstand harsh environmental conditions in certain climate zones, where some issues with limited impact resistance, weakened mechanical strength and increased contact resistance (when unsuitable ribbon coatings are chosen) have been observed.

Generally speaking, ECAs are composite materials based on a conductive filler and an insulating polymeric adhesive. Here, thermosetting as well as thermoplastic resins can be used as the matrix material; epoxy resins, silicones or polyurethanes are widely used thermosets, while polyimides are typical examples of thermoplastic resins used in ECAs. Among the conductive fillers, silver (Ag) is

“An important property to consider for the use of ECAs in PV modules is the fracture toughness of the cured resin.”

the most commonly employed; it has the highest electrical conductivity, with an ability to retain its high conductivity, even when the silver particles are oxidized. However, copper coated in gold (Au), nickel (Ni), copper (Cu), tin (Sn), SnBi or SnIn, in various sizes and shapes, is also found in applications as a filler material [2].

Depending on the loading level and type or shape of the electrically conductive filler, ECAs are divided into isotropic conductive adhesives (ICAs) and anisotropic conductive adhesives (ACAs). Because of their high filler content (50–80 wt%), ICAs provide an electrical conductivity in all directions throughout the material (x , y and z directions). Here, the resin is generally cured at higher temperatures to provide the shrinkage force to increase the conductivity, adhesion strength and chemical and corrosion resistance. ICAs are commonly used to replace the traditional SnPb solder alloys in electronic interconnections. In contrast, ACAs provide conductivity only in the vertical direction; this is achieved by using very low amounts (5–20 vol%) of conductive filler with a spherical shape in the adhesive [2–4].

An important property to consider for the use of ECAs in PV modules is the fracture toughness

of the cured resin. With regard to high-efficiency cell concepts and reduced cell thicknesses, the consideration of mechanical straining is essential. Pander et al. found that the application of ECAs in silicon solar cells yields a reduction in strain within the silicon compared with the solder route [5]. There are several possible ways of achieving a more flexible (less cross-linked) network in the cured adhesive, for example the use of reactive diluents, which are basically monoepoxide compounds that can react with the curing agent to become part of the cross-linked epoxy system. Another possibility is to use long-chain hardeners to reduce the effective cross-linking density in order to achieve less tight networks [6–10].

The main objective of the work presented in this paper was to investigate the performance, quality and reliability of different types of electrically conductive adhesives, as well as test modules with ECA-connected cells. Of special interest were:

1. Outgassing behaviour of the cured ECA.
2. Material interactions with the encapsulant.
3. Characterization of fatigue behaviour.
4. Performance of ECA-bonded test modules.

Single-cell modules were used for the studies of material interactions after stress impact, such as temperature, humidity and irradiation, as well as for sequential irradiation-humidity tests, whereas six-cell modules were utilized for thermal cycling (TC) tests.

LOCTITE



**Concerned about module reliability
of new technologies?**

Trust the Materials Experts

**GW Scale. Zero Field Failures.
Minimal \$/kWh impact.
Rely on Henkel Know-how, the future is bright.**

**Inventing Electrically Conductive Adhesives since 1956.
Innovating ECA in PV for 15 years.**

For more information visit us online at henkel-adhesives.com/electronics

All marks used are trademarks and/or registered trademarks of Henkel and its affiliates in the U.S., Germany and elsewhere.
© 2019 Henkel Corporation. All rights reserved. (2/19)

Name	Resin type	Hardener	Mixing ratio
ECA 1	Epoxy based on novolak, type A	Hardener 1	100:11
ECA 2	Epoxy based on bisphenol A/F, type B	Hardener 1	100:10
ECA 3	Epoxy based on bisphenol F, type C	Hardener 1	100:10

Table 1. ECAs under investigation.

Name	Type	Cross-linking	Formation of acetic acid
E1	Ethylene vinyl acetate (EVA)	Yes	Yes
E2	Thermoplastic polyolefin (TPO)	No	No
E3	Polyolefin elastomer (POE)	Yes	No

Table 2. Encapsulation materials used for test modules.

Name	Type	Coating	Solderable
R1	Silver	Ag	No
R2	Bare copper	-	No
R3	Lead free	SnAgCu	Yes

Table 3. Ribbon materials used for test modules.

Type	Duration	Temperature	Humidity	UV dosage	Remarks
Damp heat	1,000h; 2,000h; 3,000h	85°C	85% RH	No	
Irradiation	1,000h; 2,000h	50°C	< 50% RH	120W/m² (300–400nm) Metal halide lamps (300–2,500nm)	
Sequential	S1: 330h S2: 8h S3: 8h	85°C 50°C 30°C	85% RH < 50% RH 85% RH	No 120W/m² (300–400nm) No	Test procedure: S1 + 40× (S2 + S3)

Table 4. Accelerated ageing tests.

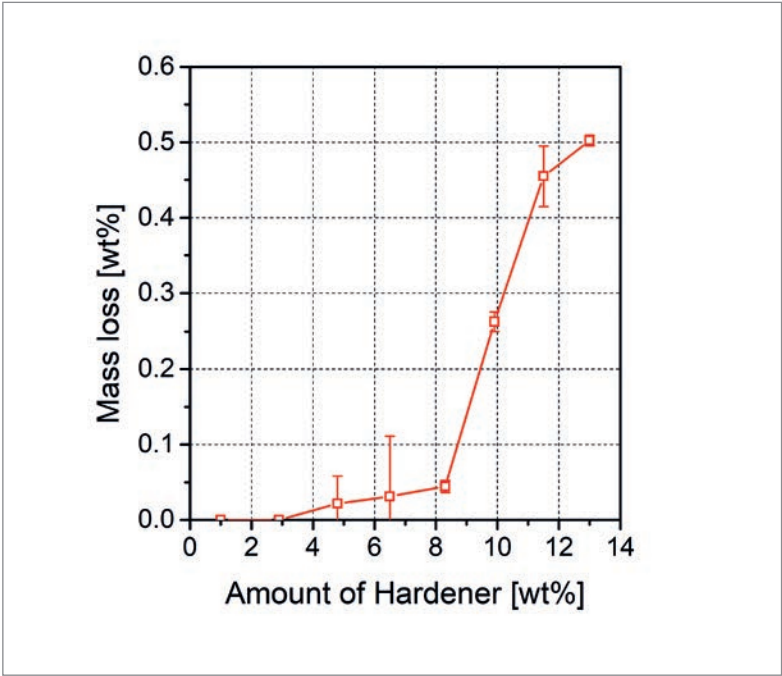


Figure 1. Percentage mass loss of the cured adhesives of type ECA1 with varying hardener content, received from TGA measurements, at a constant temperature of 150°C for 30 min.

Experimental

A main aim of the studies was to investigate the compatibility of ECAs with other module materials, especially different encapsulation and ribbon materials, and to describe possible new ageing-induced failure modes in PV modules using ECA interconnections.

First, the outgassing behaviour of three different ECA formulations (ECA1, ECA2, ECA3) comprising different epoxy components was investigated; the details are given in Table 1. Additionally, the fatigue resistance of ECA1 and ECA3 was investigated by performing cyclic fatigue tests.

In the next step, possible interactions with different encapsulation materials were investigated by printing the three different ECA formulations on glass and encapsulating them with three different encapsulation materials (EVA, TPO, POE) and a cover glass.

Finally, the performance, ageing behaviour and ageing-induced material interactions were investigated in test modules with different combinations of ECAs, ribbons and encapsulation films. As the reference, a soldered test module with

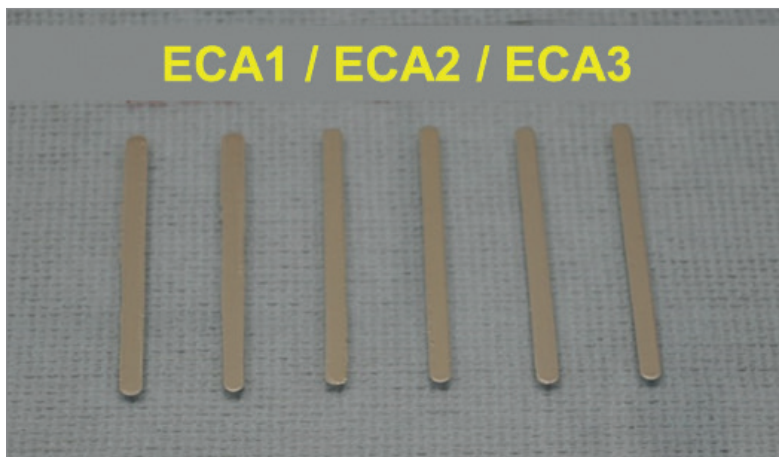


Figure 2. Printed ECA lines on glass substrate and laminated with encapsulants and glass covers.

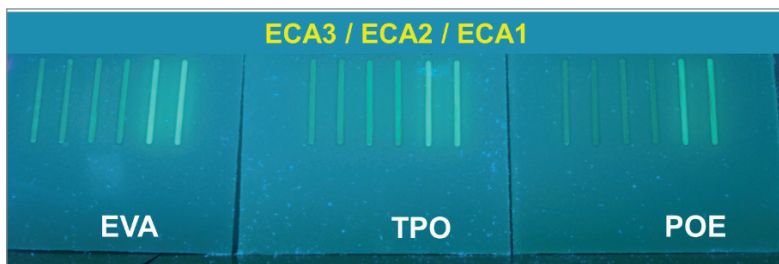


Figure 3. UV fluorescence image of printed ECA specimen (encapsulated) after lamination.

“The lamination process and accelerated ageing do not induce any distinct harmful interactions or degradation modes between the investigated ECA and encapsulant types.”

a standard EVA encapsulation Cu/SnPb ribbon was used. Three different encapsulation materials (see Table 2) were chosen in order to investigate in particular the effect of acetic acid (which is a degradation product of EVA) and the added cross linker. In addition, three different ribbon types were used for the module tests (see Table 3). The accelerated ageing tests are summarized in Table 4.

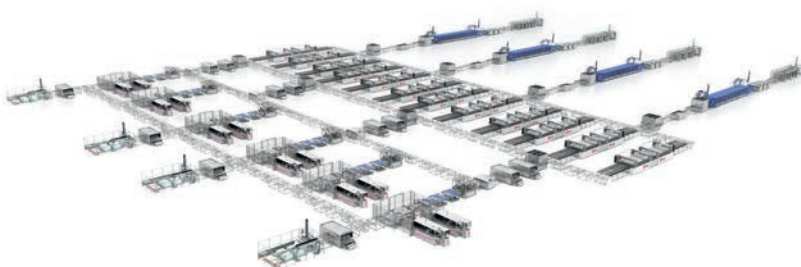
Results and discussion

The main objective was to investigate the performance, quality and reliability of the adhesive bonds, but also of the test modules with ECA-bonded cells.

Since the outgassing behaviour of adhesives applied in PV modules is of great importance, a number of volatile products of the cured adhesives



SOLAR PV MODULES MANUFACTURING LINES



Turnkey solutions from 50MW to 1GW

Solutions and services throughout the entire value chain:

- Tabber & Stringer
- Interconnection
- Laminator
- PV Module Testing
- General automation
- Customized solutions
- Full service package
- Training and know-how transfer

Suitable for different technologies:

- Glass-glass and Bifacial modules
- Half cell modules
- Multiwire technology
- High production capacity

generated at 150°C using thermogravimetric analysis (TGA) were investigated. The temperature of 150°C was chosen because this is the temperature applied during the lamination process for PV modules.

The values of mass loss received from TGA measurements of the different formulations of ECA1 (with varying amounts of hardener) are shown in Fig. 1; it can be seen that the mass loss at 150°C decreases with decreasing amount of hardener. The mass loss decreases steadily, and the formulation with the lowest amount of hardener approaches a mass loss of almost 0 wt%. This finding is in accordance with the results of thermodesorption/gas chromatography–mass spectrometry (TD/GS–MS) measurements, demonstrating that the thermal extractable compounds of the ECAs derive from the hardener. These outgassing products have not been found with formulations with a hardener amount of less than 6.5 wt%.

Possible interactions of the ECAs with the encapsulation materials EVA, TPO, POE were investigated (see Fig. 2). From a visual inspection, no migration of silver particles was observable. With the use of confocal Raman spectroscopy, no corrosion products containing Ag (e.g. silver acetate) were seen in the encapsulant close to the ECA and the ribbon. It can therefore be concluded that the PV module lamination process did not induce a diffusion of Ag particles into the encapsulant.

Fig. 3 shows the UV fluorescence image of the specimens for different encapsulation materials. Because of the various chemical compositions of the ECAs (different polymeric epoxy component – see Table 1), the fluorescence signals of the ECAs were different, with ECA1 showing the highest fluorescence.

A comparable UV fluorescence was also observed in the area next to the ribbon after accelerated ageing tests for the single-cell modules using ECA1 and POE as the encapsulant. This indicates migration of the hardener, which was not converted in the curing reaction, into the surrounding encapsulation material. No correlation with power loss of the test module, however, was observable. In the case of the other ECA encapsulant combinations, no migration effect was observed. It is therefore assumed that the lamination process and accelerated ageing do not induce any distinct harmful interactions or degradation modes between the investigated ECA and encapsulant types.

The fatigue resistance of ECA1 and ECA3 was investigated using a single lap shear (SLS) specimen. Cyclic fatigue tests were performed under a tensile load at a frequency of 10Hz and a stress ratio R of 0.1. (The stress ratio is defined as the ratio of minimum stress to maximum stress in one cycle of loading in a fatigue test.) Tensile stresses are considered positive and compressive stresses negative. Mean stress levels (between 5 and 20MPa) were derived from tensile tests using the SLS specimen.

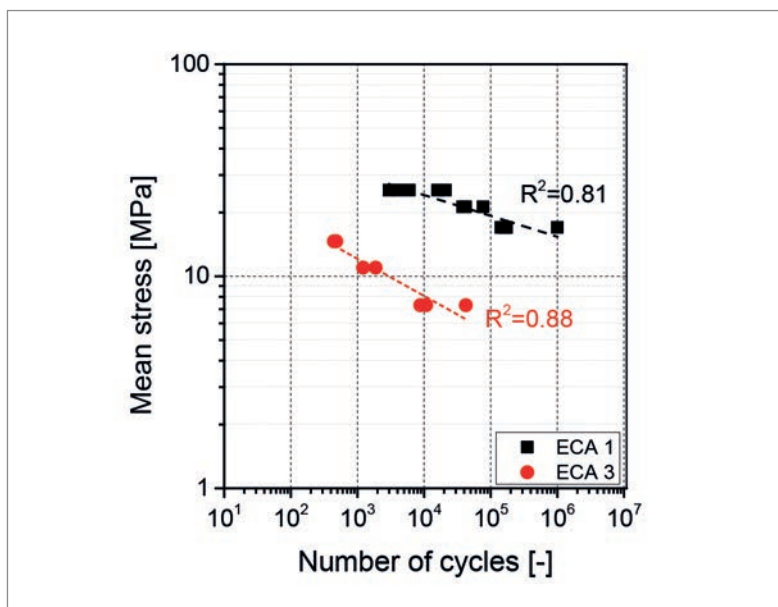


Figure 4. S–N curves for the investigated ECA types.

Fig. 4 shows the S–N curves (also known as *Wöhler curves*) of the investigated adhesives. ECA 1 exhibits significantly better fatigue resistance than ECA 3. One explanation for this can be found in the intrinsic fatigue resistance of the materials; however, the nature of the sample preparation may also be a contributing factor to the lower fatigue resistance. In the investigation of the fractured surfaces of ECA 3, bubbles and a lower degree of curing were detected, which could have strongly influenced the fatigue behaviour.

Only a limited number of papers dealing with the fatigue behaviour of cell interconnection have been published so far [10–12], and these give contradictory values. Pander et al. [11] studied the fatigue of solar cell interconnections, and designed the loading profile during the fatigue test in such a way as to achieve the same strain amplitude in the cell gaps as that found in a full-size module simulation under $\pm 1,000$ Pa, which corresponds to the IEC proposal. Dietrich et al. [10] also investigated fatigue in solar cell interconnections, and chose the test amplitude so that the failure occurs before 10,000 cycles. However, those authors did not give information on the load levels applied in their fatigue tests. Zarmai et al. [12] studied the thermomechanical damage and fatigue life of solar cell solder interconnections, and reported the calculated value of maximum stress concentration in the solder joint to be of the order of 21MPa. This value was obtained within the thermal cycling test in the temperature range -40°C to $+85^{\circ}\text{C}$, in compliance with IEC 61215.

With regard to the cyclic fatigue behaviour of the investigated ECA types in the current paper, both S–N curves are either significantly above the mean stress levels that were reported for interconnections in PV modules [10,11], or in a similar range [12]. The reported values for the number of cycles to failure for soldered bonds are also in a similar range.

In a next step, a series of single-cell test modules was investigated. These modules consisted of

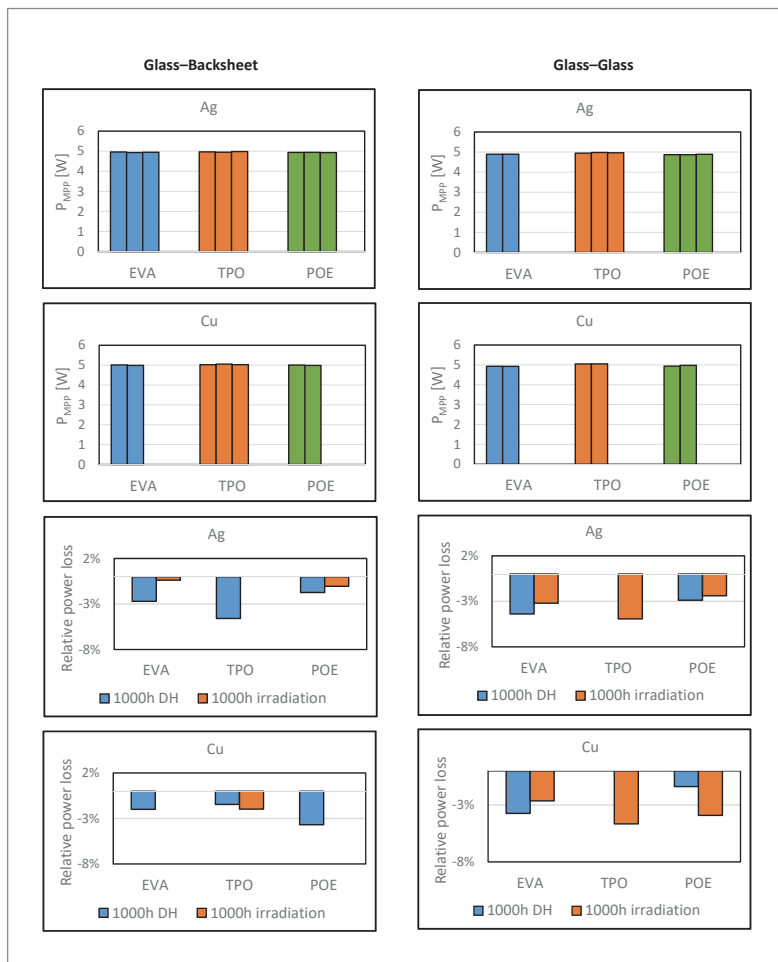


Figure 5. Electrical characterization results for test modules with different ECA-bonded ribbons (Ag, Cu) and different encapsulation materials (EVA, TPO, POE), before and after accelerated ageing (DH and irradiation).

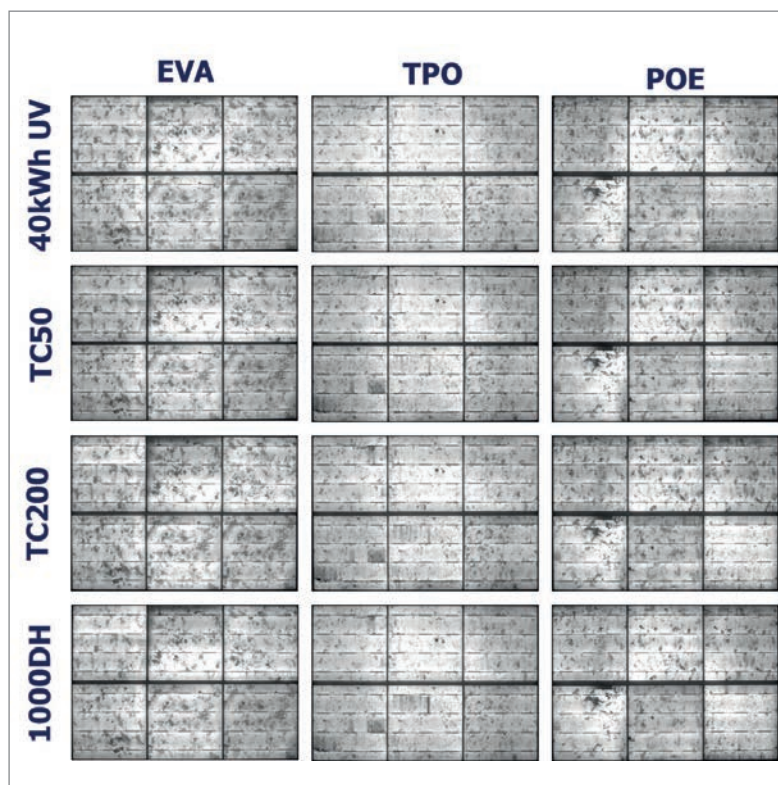


Figure 6. EL images of the six-cell modules with different encapsulation materials, before and after 200 thermal cycles.

identical Si cells, ECA1, front glass, polymeric backsheet (PET laminate) or glass backsheet, and various encapsulants (EVA, TPO and POE) and ribbons (Ag, Cu, SnAgCu) (see Experimental section).

A visual inspection revealed that during module production, ECA1 in contact with all tested ribbons types (Cu, Ag, SnAgCu) did not show any initial problems, such as delamination or discolouration. Fig. 5 presents the electrical characterization results of these test modules before and after accelerated ageing (1,000h damp heat – DH – and 1,000h irradiation). The results showed satisfying reproducibility, even though the strings and modules were fabricated manually. The single-cell modules exhibited maximum power output (P_{MPP}) values between 4.7 and 5W. The glass–glass modules showed slightly lower P_{MPP} values than glass–backsheet modules, which can be explained by the rear reflection of light from the highly reflective white backsheet onto the solar cell.

In regard to ribbon types and encapsulation films (and otherwise identical set-ups), the modules using bare copper ribbons yielded the highest power outputs, followed by the modules with Ag-coated ribbons. This can mainly be explained by the reduced ribbon width and the light-capturing effect. The lowest values were observed for SnAgCu-coated ribbons. The differences, however, were fairly small, at $\pm 0.2\%$. Furthermore, the modules using TPO as the encapsulant demonstrated the highest P_{MPP} values, which can be explained by the slightly higher transparency of the TPO film than that of EVA or POE. It should be noted that, even though the power measurements were reproducible, with standard deviations below 0.5%, some of the observations may not be significant, since the measurement inaccuracy of the electrical measurements was around $\pm 1.5\%$.

Test modules were then exposed either to 1,000h of damp heat or to 1,000h irradiation. The ageing-induced relative power losses were found to lie between 0.5 and 4.5%. Missing values in the figures correspond to test modules that suffered glass breakage during the accelerated ageing test (untempered glass was used for the single-cell test modules). No visible changes – such as discolouration, delamination or cracking – were observable after the accelerated ageing tests. Generally, the glass–glass modules showed higher power loss than the glass–backsheet modules. Other correlations between stress factors (i.e. the ageing test), ribbon type and encapsulation films were not observed, partly because of missing values, and partly because of inconsistent test data. The exact cause of the power loss is therefore still unknown.

In order to investigate the mechanical stability of cell interconnections, six-cell modules were manufactured and subjected to thermal cycling tests. The modules were exposed to the following test sequence:

1. Preconditioning: 40kWh (AM1.5 in compliance with IEC 60904-3).
2. TC: 200 cycles from -40°C to $+85^{\circ}\text{C}$ (in compliance

with IEC 61215), with a first power measurement after 50 cycles.

3. Additional DH: 1,000h of exposure at 85°C/85%RH.

After this test sequence, the modules were characterized by visual inspection, power measurement and electroluminescence (EL) imaging.

Figs. 6 and 7 show the relative power loss and the EL images of the six-cell modules. The visual inspection did not reveal any delamination, while the EL images showed slight brightness differences and only a few crack propagations after the applied test sequences. The identified cracks already existed before the different tests were performed (see Fig. 6), and the reason for the brightness differences in the EL images are explained by the change in contacting properties of the strings. It is assumed that this damage was caused by production failures (e.g. manual handling of the ECA-bonded strings) and/or during transport.

The relative power losses of the six-cell modules (three identical modules for each module design, nine modules in total) after each test sequence are illustrated in Fig. 7. For all test modules, UV preconditioning resulted in a power loss of around 1%. Furthermore, the behaviour after 50 and 200 temperature cycles was similar for all identical test modules; power loss values of around 2 and 4% were measured after 50 and 200 cycles respectively. The I - V curves revealed a decrease in open-circuit voltage (V_{oc}) and in short-circuit current (I_{sc}), and an increase in serial resistance (R_s). The increase in R_s is an indication of an increased contact resistance between ribbon, adhesive and cell. Another explanation for the increased contact resistance could be the cross connector, which was manually soldered. Interestingly, an additional DH exposure led to power regeneration for modules with TPO and POE encapsulant. Generally, modules with TPO yielded the best performance.

Conclusion

The main objective was to investigate the performance, quality and reliability of ECAs, but also of test modules with ECA-bonded cells. Of special interest was 1) the outgassing behaviour of cured ECA; 2) the material interactions with encapsulants; 3) the characterization of thermomechanical and fatigue behaviour; and 4) the performance of ECA-bonded test modules.

No harmful interactions were found between the investigated ECA formulations and the different encapsulant films after lamination and ageing tests. The main outgassing products were identified as fragments of the hardener. In addition, no migration of silver particles was detected. ECAs were found to be compatible with all tested ribbons types (Cu, Ag, SnAgCu), since no delamination or discolouration after lamination or accelerated ageing tests was observed. For ECA-bonded test modules, a slight power loss after thermal cycling, damp heat and irradiance exposure was identified; this power loss can be attributed not only to failure of the ECA

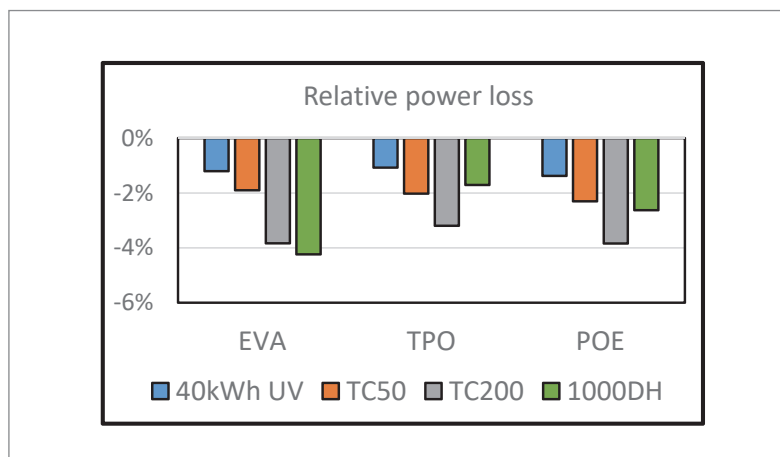


Figure 7. Relative power losses of the six-cell modules after each test sequence.

bond but also to additional factors such as sample preparation and cell damage that was present from the start. To summarize, cell interconnection using ECAs provides an interesting alternative to standard soldering approaches; however, additional work needs to be done, especially with regard to a root cause analysis of the power loss after thermal cycling.

Acknowledgements

This research work was performed within the 'Infinity' project (Energieforschungsprogramm 2015 – Leitprojekte, FFG No. 850414, Klima- und Energiefonds).

References

- [1] Yin, Y.C. & Zhong, J. 2008, "A review of the influencing factors on anisotropic conductive adhesives joining technology in electrical applications", *J. Mater. Sci.*, Vol. 43, pp. 3072–3093.
- [2] Yim, M.J. et al. 2008, "Review of recent advances in electrically conductive adhesive materials and technologies in electronic packaging", *J. Adh. Sci. Technol.*, Vol. 22, pp. 1593–1630.
- [3] Li, Z. et al. 2013, "The conduction development mechanism of silicone-based electrically conductive adhesives", *J. Mater. Chem. C*, Vol. 1, pp. 4368–4374.
- [4] Gomatam, R. & Mittal, K.L. 2008, *Electrically Conductive Adhesives*. Leiden: VSP.
- [5] Pander, M. et al. 2014, "Mechanical modelling of electrically conductive adhesives for photovoltaic applications", *Proc. 29th EU PVSEC*, Amsterdam, The Netherlands.
- [6] May, C.A. & Nixon, A.C. 1961, "Reactive diluents for epoxy adhesives", *Ind. Eng. Chem.* Vol. 53, No. 4, pp. 303–304.
- [7] Bakar, M. et al. 2010, "Effect of reactive diluents and kaolin on the mechanical properties of epoxy resin", *Polymers Polymer Comp.*, Vol. 18, No. 9, pp. 503–510.

"Additional work needs to be done, especially with regard to a root cause analysis of the power loss after thermal cycling."

[8] Urbaczewski-Espuche, E. et al. 1991, "Influence of chain flexibility and crosslink density on mechanical properties of epoxy/amine networks", *Polymer Eng. Sci.*, Vol. 31, No. 22, pp. 1572–1580.

[9] Wang, H. et al. 2009, "Synthesis of rosin based flexible anhydride type curing agents and properties of the cured epoxy", *Polymer Internat.*, Vol. 58, No. 12, pp. 1435–1441.

[10] Zhu, J. et al. 2004, "Curing and mechanical characterization of a soy based epoxy resin system", *J. Appl. Polymer Sci.*, Vol. 91, No. 6, pp. 3513–3518.

[11] Dietrich, S. et al. 2016, "Microstructural optimization approach of solar cell interconnectors fatigue behavior for enhanced module lifetime in extreme climates", *Proc. 6th SiliconPV*, Chambéry, France.

[12] Pander, M. et al. 2013, "Lifetime estimation for solar cell interconnectors", *Proc. 28th EU PVSEC*, Paris, France.

[13] Zarmai, M.T. et al. 2017, "Evaluation of thermo-mechanical damage and fatigue life of solar cell solder interconnections", *Robot. Comput. Integr. Manuf.*, Vol. 47, pp. 37–43.



Lukas Neumaier holds an M.Sc. and has gained extensive knowledge of electrical engineering and biomimetics/bionics through his university studies. He is also an experienced researcher in the field of renewable energy systems, especially PV, focusing on the areas of quality control and characterization of PV modules and components, and PV plant monitoring. He has worked on several research projects concerning smart systems, and has managed national- and international-funded projects as well as many contract research projects.



Dr. Christina Hirschl is the area manager at CTR Carinthian Tech Research AG, an Austrian industry-oriented R&D centre for smart sensors and system integrations. She works on different research topics involving smart system integration and renewable energy.



Dr. Rita Ebner received her Ph.D. in material physics from the University of Vienna. After that, she was a project coordinator at the Austrian Research Promotion Agency (FFG), and since 2003 she has been a lecturer at the College of Renewable Energy (TGM) in Vienna. In 2009 she started work as a scientist at AIT, the Austrian Institute of Technology GmbH, where she currently specializes in crystalline solar cell and PV module characterization, and is responsible for national and international research projects in this field.

Jörg Scheurer studied chemistry at the Johannes-Gutenberg University Mainz, and subsequently began working as a process engineer in the field of microsystem technology/photolithography. He later worked in the R&D department at Polytec PT, with a focus on filled epoxy adhesives, and is currently responsible for application engineering within the company.

Wolfgang Pranger studied materials science at the University of Leoben, after which he was a process engineer focusing on heat treatment and coating of interconnection ribbons. He is currently responsible for R&D at Ulbrich of Austria.

About the Authors



Dr. Oreski is division manager at the Polymer Competence Center Leoben, Austria, and heads the smart material and surface testing division. His main fields of research are polymer science and testing, as well as long-term reliability and degradation behaviour of polymeric materials and components for PV modules. In addition to his work for the PCCL, he is a lecturer in the Department of Polymer Science and Engineering at the University of Leoben.

Dr. Sandra Pötz is a researcher at the PCCL. Her main fields of research are polymer chemistry and polymer analysis.

Antonia Omazic is a Ph.D. student at the PCCL, working in the field of ageing characterization of polymeric materials for PV.



Dr. Gabriele Eder studied technical chemistry at the TU in Vienna, and was then assigned a post as a university lecturer at the University of Twente's Institute of Surface Chemistry and Catalysis in the

Netherlands. Following that, she gained industrial experience through employment in the R&D department at NBG Special Coatings, Lower Austria. Since 2015 she has been a senior researcher at OFI, the Austrian Research Institute for Chemistry and Technology, where she focuses on material characterization, spectroscopy, damage analysis and ageing studies.

Enquiries

Gernot Oreski
PCCL Polymer Competence Center Leoben
Roseggerstraße 12
8700 Leoben, Austria

Tel: +43 3842 42962-51
Email: gernot.oreski@pccl.at

Effects of texture additive in large-area diamond wire cut multicrystalline silicon solar cells

S. Saravanan, Ch.S.R. Suresh, V.V. Subraveti, K.C. Kumar & U.K. Jayaram, RenewSys India Pvt Ltd, Hyderabad, India

Abstract

The silicon PV industry has predominantly used silicon wafers sliced by a steel wire, with silicon carbide particles (slurry wire – SW) as an abrasive and polyethylene glycol as a coolant. Low yield, high total thickness variation (TTV), significant material waste and short wire lifetime (and thus high downtime) of SW cutting technology have prompted the wafer slicing industry to develop an alternative technology. Researchers have developed diamond wire (DW) cutting technology for slicing the silicon and demonstrated that it overcomes the drawbacks of SW cutting technology. Although the DW cutting technology has been demonstrated for slicing wafers, the wafer surface is different after the conventional acidic texturing in a silicon solar cell process. It is therefore important to improve the existing process or to develop a new process, in order to produce a homogeneous texturization on DW-cut wafers. In this work, a systematic approach has been pursued to improve the existing process by using an additional etchant (a texture additive) in the acidic mixture. Different etch depths and the corresponding mean reflectance were studied. Optical and morphological studies on DW-cut wafers processed with and without a texture additive have been carried out and interpreted in terms of electrical performance.

Introduction

Crystalline silicon PV with slurry wire (SW)-cut wafers as the initial raw material has dominated the PV industry since its early beginnings [1,2]. Although SW slicing with a slurry of SiC abrasives is the most widely used in the silicon wafer slicing industry, it produces wafers with high surface mechanical damage and high associated kerf losses [3]. In addition to the wafer production concerns, SW slicing has significant environmental waste because of the inordinate consumption of wire for sawing [4,5].

In order to overcome the aforementioned issues, an alternate sawing method, namely diamond wire (DW) cutting technology, has been introduced in the slicing industry [6,7]. Many research groups have reported [8–13] that DW cutting technology is recognized for its higher productivity and lighter wearing of the wire. However, DW cutting technology has not completely eliminated SW slicing technology, because the DW-cut wafers exhibit a non-uniform surface roughness compared with the SW-cut wafers.

In the conventional silicon solar cell process, saw damage etching, surface texturing and surface cleaning are the crucial steps in fabricating high-efficiency cells in mass production at low cost. Reducing the surface reflectance of the silicon wafers by surface texturing is a significant step in enhancing the efficiency of the solar cells. In the solar cell manufacturing industry, various wafer etching processes for etching SW-cut wafers have become established, such as isotropic and anisotropic etching. Although DW cutting technology has been used initially for slicing monocrystalline silicon wafers [10], it has not been widely adopted because the alkaline texture process is not capable of producing the expected texture surface. Whereas the alkaline texture process on SW-cut monocrystalline silicon wafers leaves deeper damage, in DW-cut wafers the damage is less but concealed by amorphous silicon, which forms because of the high-speed sawing nature of DW technology. In consequence, the DW wafers are left with high saw marks and a badly damaged wafer surface, which results in higher reflection and thus lower performance. Hence an additional, simple precleaning process using tetramethyl ammonium hydroxide (TMAH) has been included [14] along with the regular texture process, so that the high saw marks with amorphous silicon can be removed, resulting in the formation of a random pyramid structure. The texture process has been developed for DW-cut *monocrystalline* silicon wafers; however, it is important to check that this slicing technology is suitable for *multicrystalline* silicon wafers, now that these wafers are gaining a significant share in silicon solar cell production.

As might be expected, the light reflectance is high in the case of the conventional acidic texturing process with DW-cut wafers. In the literature certain processes have been reported to reduce the light reflection and thus enhance the electrical performance, specifically processes such as reactive ion etching [15], metal-assisted texturing [16], the addition of sulphuric acid [11] in the acidic texturing mixture (hydrofluoric acid and nitric acid), vapour blast etching [12] or a texture additive solution [17]. Among these processes, the addition of H_2SO_4 in a HF/HNO_3 mixture [11] and adding a texture additive solution in a HF/HNO_3 mixture are the simplest and least expensive processes. The studies

“DW cutting technology is recognized for its higher productivity and lighter wearing of the wire, but the DW-cut wafers exhibit a non-uniform surface roughness.”

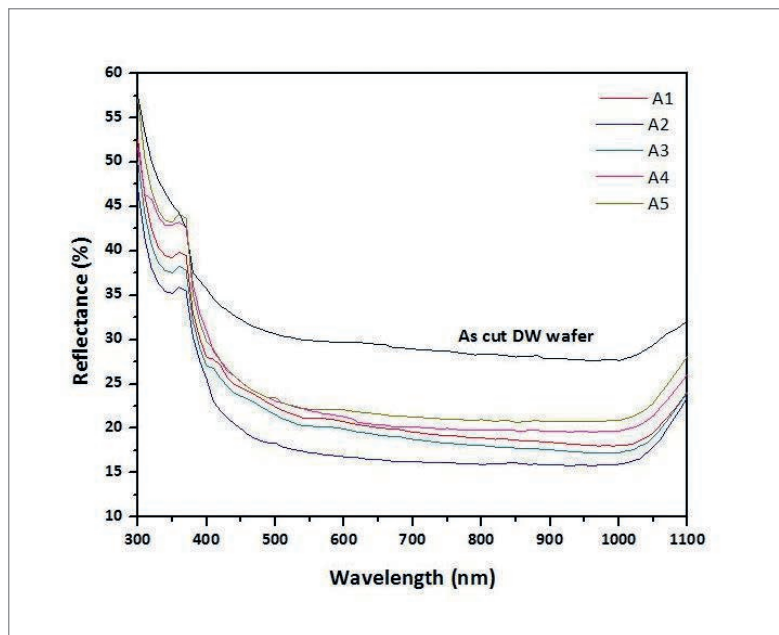


Figure 1. Reflectance of an as-cut DW wafer and of wafers textured without (A1) and with (A2–A5) texture additive A.

on the addition of H_2SO_4 in a HF/HNO_3 mixture have demonstrated a reasonable reduction in light reflection [11], and have also shown that there is still more scope for improvement.

In the present study, an optimization of saw damage removal and texturization for DW-cut wafers by using a texture additive has been carried out. A commercially available texture additive solution, referred to as 'A' (the actual name of the texture additive solution is not disclosed here to maintain confidentiality), was used for optimizing the texturization of DW-cut wafers. In order to achieve the best performance, different etch depths were tried, but keeping the wafer source the same. Mean reflectance and surface morphology investigations were also performed. Different etch depth wafers were processed by using a conventional silicon solar cell process to create the solar cells. *I–V* studies were carried out and the results interpreted with regard to mean reflectance and surface morphology.

Experiment

Boron-doped DW-cut multicrystalline silicon wafers of size $156.75\text{mm} \times 156.75\text{mm}$, with a thickness of $200 \pm 20\mu\text{m}$ and a bulk resistivity of $0.5\text{--}3.0\Omega\text{cm}$, were taken as the starting material. Silicon solar cells were fabricated by employing conventional screen-printing technology and the following process flow (in brief):

- Saw damage removal and texturization
- P diffusion
- Wet edge isolation and phosphosilicate glass (PSG) removal

- Anti-reflection coating (ARC)
- Back-contact and back-surface field (BSF) printing and drying
- Front-contact printing and drying
- Co-firing

Reflectance studies on bare DW-cut wafers, and on wafers processed with and without texture additive A for different etch depths, were carried out in the wavelength range $300\text{--}1100\text{nm}$. The texture uniformity and surface morphology of the DW wafers were examined using scanning electron microscopy (SEM), and the results compared with SW wafers. (The texture additive details, corresponding labelling of samples, reflectance and etch depth of these samples are shown later, in Table 1.) These DW-cut wafers were then processed to create solar cells. The *I–V* studies of the finished solar cells were performed under AM 1.5G simulated solar radiation at 25°C by using an AAA solar simulator.

Results and discussion

Reflectance studies

Fig. 1 shows the reflectance of as-cut DW wafers and of wafers textured without (A1) and with (A2–A5) the texture additive A. For efficient solar cells, the reflectance should be minimal. From Fig. 1 it is seen that the mean reflectance of an as-cut DW Si wafer between 300nm and 1100nm wavelengths is 42.0% , while the etch depth and the mean reflectance of DW-cut wafers processed without texture additive A are $5.5\mu\text{m}$ and 24.18% respectively. The surface of the textured DW-cut wafers is shiny with sawing grooves, whereas SW-cut wafers have a matte finish.

In order to optimize the texturization process recipe with the texture additive A for DW-cut wafers, it was decided to combine the additive as per the supplier's recommendation with existing HF/HNO_3 in the ratio $1.0:1.5$. By varying either the process temperature or the transport speed, experiments for different etch depths were conducted and labelled A2–A5. The texturing process of the texture additive A with HF/HNO_3 leads to reduced mean reflectance. The as-cut DW wafer and the wafer textured without texture additive A have a mean reflectance of 42.0% and 24.18% respectively, whereas after etching to a depth of $1.8\mu\text{m}$ with the additive, the mean reflectance drops to 19.54% (A2). However, in order to determine an optimized etch depth with a suitable mean reflectance, it was decided to perform the experiments with different etch depths. The mean reflectances for the different etch depth experiments are listed in Table 1.

Table 1. Reflectance and etch depth of as-cut and textured wafers, without and with additive A.

Sample	Raw wafer	Textured w/o additive		Textured with additive A		
		A1	A2	A3	A4	A5
Reflectance [%]	42	24.18	19.54	22.09	21.99	24.73
Etch depth [μm]	N/A	5.5	1.8	2.5	3.0	4.5

After incorporating the texture additive, the etch depth and mean reflectance decrease dramatically (for the same temperature and transport speed); for the etch depth of $1.8\mu\text{m}$, the mean reflectance observed is 19.54%. Although the mean reflectance is lower, the surface was not uniformly etched because of the preferential etching over the DW wafer surface. It was therefore decided to study the reflectance at different etch depths. With increasing etch depth, it was found that the reflectance increases: when $2.5\mu\text{m}$ of the Si is removed, the mean reflectance is higher (22.09%) than for $1.8\mu\text{m}$ (19.54%), whereas the mean reflectance for wafers etched $3.0\mu\text{m}$ (21.99%) is almost the same as for $2.5\mu\text{m}$ (22.09%). Further etching was also carried out to study the changes in reflectance. It was observed that for a $4.5\mu\text{m}$ etch depth, the mean reflectance was 24.73%. From Table 1 it is evident that an etch depth of $1.8\mu\text{m}$ yields the lowest reflectance; however, before taking $1.8\mu\text{m}$ to be an optimized etch depth, it is essential to consider the surface morphology and interpret this with respect to etch depth.

Surface morphology

SEM images of the surface morphology of as-cut SW and DW wafers are shown in Fig. 2. The image for the as-cut DW wafer reveals that the wafers contain saw marks, which are due to the scoring by the diamond particles over the silicon surface. From Fig. 2 it can be seen that the regions of surface damage are around $4\mu\text{m}$ in size. Many areas where the silicon has chipped off are also observed, along with the saw marks; this may be caused by the stress of diamond granules on the wire against the multicrystalline silicon surface. The surface of the as-cut SW wafers appears rougher than that of the as-cut DW wafers, and the sawing direction is not noticeable. The initial step in the silicon solar cell process is etching, in which the removal of saw marks and the texturization to reduce the reflection are done simultaneously.

When the surface morphologies are compared, the same kind of etching process for both as-cut DW and SW wafers will clearly never be adequate in removing the saw damage and in texturizing. In general, the surface of the SW wafers lacks amorphous silicon, whereas the surface of the DW wafers is covered with it; this important difference arises because of the nature of the sawing mechanisms. The amorphous silicon safeguards the surface of the DW wafer from conventional acidic etching. It is therefore important to overcome this concern either by changing the etching chemistry or by varying the etching process time. Alternatively, the DW sawing mechanism should be modified in such a way that the formation of amorphous silicon is avoided.

Conventional HF/HNO_3 acidic etching has been carried out on both SW- and DW-cut wafers. Fig. 3 depicts the surface morphologies of both the wafers after undergoing saw damage removal and

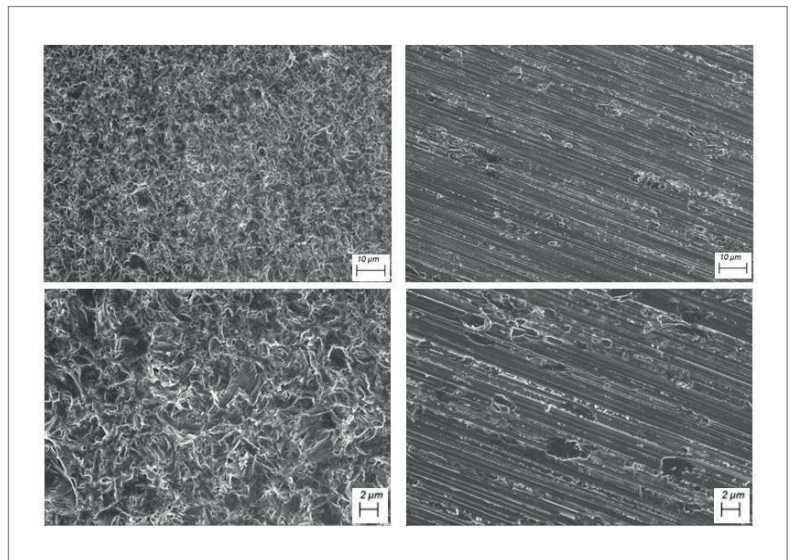


Figure 2. Surface morphology (lower and higher magnification) of as-cut SW (left) and DW (right) wafers.

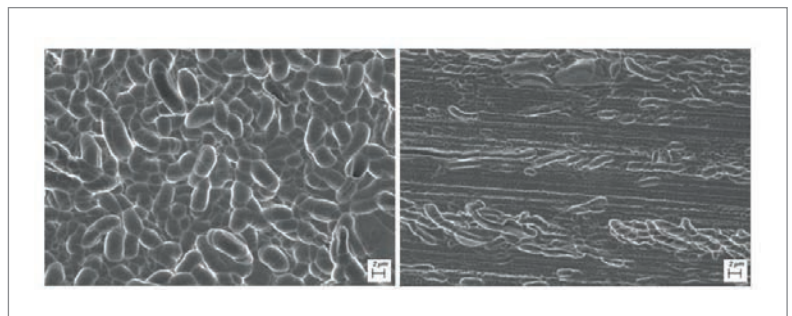


Figure 3. Surface morphology of textured SW and DW wafers.

texturization. As discussed earlier, the sawing mechanisms of SW and DW yield different surface structures on as-cut wafers, which result in significant effects on the wafer surface morphologies because of acidic etching.

The mean reflectances observed for SW and DW wafers after texturing are 23.6% and 24.18% respectively. The etch depth of both DW and SW wafers is the same ($5.5\mu\text{m}$) as a result of acidic etching, but the surface looks different. The SEM image of the surface of the textured SW silicon wafers reveals that the etching has been performed homogeneously, with wormlike pits of width $2\mu\text{m}$ across the wafer. The surface of the textured DW-cut wafers, however, appears to indicate that the texturization is not fully completed. This shows that the same acidic etch mixtures and etch parameters used for etching SW wafers are not suited to etching DW-cut wafers. From Fig. 3 it can be seen that the acidic texturing leads to elliptical pits distributed randomly across the wafer, with grooving also occurring. Although the saw marks are smaller than in the case of the as-cut wafer, the acidic texturing did not remove the saw mark grooves completely. A

“The same kind of etching process for both as-cut DW and SW wafers will clearly never be adequate in removing the saw damage and in texturizing.”

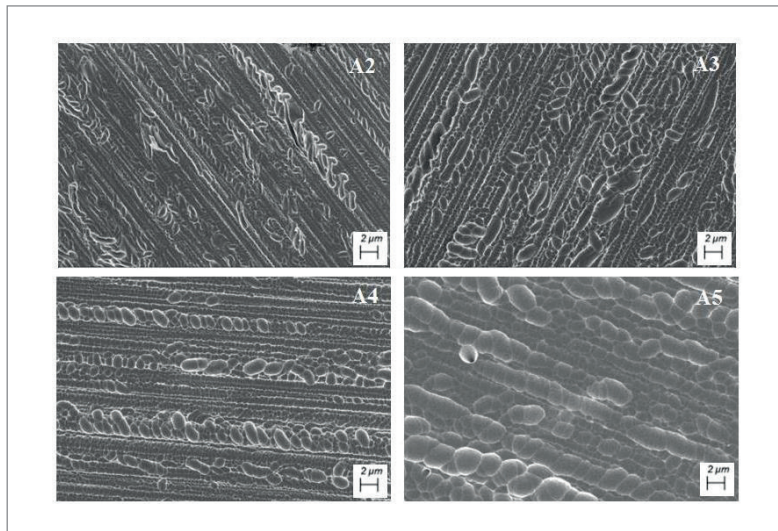


Figure 4. Surface morphologies of textured DW wafers with texture additive A, for different etch depths (A2–A4).

systematic investigation was carried out to eliminate the saw marks by effective surface texturing on DW wafers with the use of a commercially available texture additive.

Fig. 4 shows the surface morphology of DW-cut wafers textured with texture additive A for different etch depths. If the surface of the DW wafers textured with and without additive are compared, it is seen very clearly that the wafers processed without the texture additive in an acidic etching process yield an inhomogeneous silicon surface; this results from the presence of amorphous silicon on the wafer surface, and thus from the non-uniform reactivity of the acidic etchant over the DW wafer surface.

In contrast, the surface of the textured wafers processed with the texture additive are enriched with micro pits, for all the different etch depths. It is observed that the uniformity and size of the pits increases with increasing etch depth. Furthermore, no grooves are found on the wafers processed with etch depths greater than 1.8 μm, from which it can be inferred that the saw marks are completely removed. Since the wafer surfaces possess a uniform texture at an etch depth of 4.0 μm, it was decided to halt the etching experiments, and move on to processing solar cells from wafers with the various etch depths.

Solar cell performance

Table 2 shows the electrical characteristics of solar cells with different etch depths. Solar cells of area 245.71 cm² were measured with a light irradiation of 1,000 W/m². From the electrical characteristics, it is

observed that cells processed with texture additive demonstrate better performance than with just the conventional acidic process.

Wafers with an etch depth of 2.5 μm show better performance than that at other etch depths. Although the mean reflectance is slightly higher than that of the 1.8 μm etch depth, the morphology of wafers etched to 2.5 μm does not exhibit any saw marks. Hence, it is clear that not only do the optical properties of the front surface have an impact on the electrical parameters, but also the surface texturization plays an important role in electrical performance. Similarly, SEM studies revealed that 4.5 μm-etched wafers have a homogeneous textured surface; however, the mean reflectance is higher than that of the 2.5 μm-etched wafers.

A comparison of the electrical parameters for different etch depth wafers reveals that there is not much difference in I_{sc} and FF , but the V_{oc} is higher in 2.5 μm-etched wafers; this may be due to the lower surface and auger recombination. It is important to note that the lower mean reflectance (optical loss) and lower recombination (electrical loss) resulted in the superior performance for 2.5 μm-etched DW-cut wafers.

Conclusions

Current studies on DW-cut wafers, reported in this paper, have revealed that the conventional acidic texturing process is not effective, because of the non-homogeneous texturing and thus the DW saw marks not being completely removed. In this paper, a systematic approach to optimizing the texturing process with the use of a texture additive has been taken, by etching DW wafers at different etch depths. Optical and morphological studies were carried out to interpret the reflectance and surface nature for different etch depths. For investigating all etch depths, multicrystalline silicon solar cells of size 156.75 mm × 156.75 mm were fabricated by using a conventional silicon solar cell process. The wafers processed with a texture additive and an etch depth of 2.5 μm resulted in cells of efficiency 18.40% in an industrial production line. The optical and morphological results confirmed that the enhanced performance is due to the lower mean reflectance (optical loss) and the lower recombination (electrical loss).

Acknowledgements

The authors thank the management and the cell fab team at RenewSys India Pvt. Ltd. for their support.

Table 2. Electrical parameters of solar cells for different etch depths.

Parameter	Textured w/o additive	Textured with additive A			
	A1	A2	A3	A4	A5
Efficiency [%]	18.17	18.13	18.40	18.36	18.29
Power P_{mpp} [Wp]	4.46	4.46	4.52	4.51	4.49
Short-circuit current I_{sc} [A]	8.82	8.86	8.90	8.89	8.86
Open-circuit voltage V_{oc} [mV]	629.0	626.9	631.4	630.9	630.8
Fill factor FF [%]	80.44	80.19	80.37	80.38	80.41

References

- [1] Möller, H.J. et al. 2004, "Basic mechanisms and models of multi-wire sawing", *Adv. Eng. Mater.*, Vol. 6, pp. 501–513.
- [2] Möller, H.J. et al. 2005, "Multicrystalline silicon for solar cells", *Thin Solid Films*, Vol. 487, pp. 179–187.
- [3] Chen, W. et al. 2014, "On the nature and removal of saw marks on diamond wire sawn multicrystalline silicon wafers", *Mater. Sci. Semicon. Proc.*, Vol. 27, pp. 220–227.
- [4] Watanabe, N. et al. 2010, "Characterization of polycrystalline silicon wafers for solar cells sliced with novel fixed-abrasive wire", *Prog. Photovolt: Res. Appl.*, Vol. 18, pp. 485–490.
- [5] Meinel, B., Koschwitz, T. & Acker, J. 2012, "Textural development of SiC and diamond wire sawed sc-silicon wafer", *Energy Procedia*, Vol. 27, pp. 330–336.
- [6] Möller, H.J. et al. 2011, "Growth optimization of multicrystalline silicon", *Energy Procedia*, Vol. 3, pp. 2–12.
- [7] Wu, C. et al. 2001, "Near unity below bandgap absorption by microstructured silicon", *Appl. Phys. Lett.*, Vol. 78, pp. 1850.
- [8] Zhuang, Y.F. et al. 2016, "Versatile strategies for improving the performance of diamond wire sawn mc-Si solar cells", *Sol. Energy Mater. Sol. Cells*, Vol. 153, pp. 18–24.
- [9] Cao, F. et al. 2015, "Next generation multicrystalline silicon solar cells: Diamond wire sawing, nano texture and high efficiency", *Sol. Energy Mater. Sol. Cells*, Vol. 141, pp. 132–138.
- [10] Chen, K. et al. 2015, "Novel texturing process for diamond-wire-sawn single-crystalline silicon solar cell", *Sol. Energy Mater. Sol. Cells*, Vol. 133, pp. 148–155.
- [11] Lippold, M. et al. 2014, "Texturing of SiC slurry and diamond wire sawn silicon wafers by HF-HNO₃-H₂SO₄ mixtures", *Sol. Energy Mater. Sol. Cells*, Vol. 127, pp. 104–110.
- [12] Chen, W. et al. 2014, "On the nature and removal of saw marks on diamond wire sawn multicrystalline silicon wafers", *Mater. Sci. Semicon. Proc.*, Vol. 27, pp. 220–227.
- [13] Bidiville, A. et al. 2009, "Diamond wire sawn silicon wafers – From the lab to the cell production", *Proc. 24th EU PVSEC*, Hamburg, Germany.
- [14] Papet, P. et al. 2006, "Pyramidal texturing of silicon solar cell with TMAH chemical anisotropic etching", *Sol. Energy Mater. Sol. Cells*, Vol. 90, pp. 2319–2328.
- [15] Yoo, J., Yu, G. & Yi, J. 2011, "Large area multicrystalline silicon solar cell fabrication using reactive ion etching (RIE)", *Sol. Energy Mater. Sol. Cells*, Vol. 95, pp. 2–6.
- [16] Kumagai, A. 2015, "Texturization using metal catalyst wet chemical etching for multicrystalline diamond wire sawn wafer", *Sol. Energy Mater. Sol. Cells*, Vol. 133, pp. 216–222.
- [17] Sankarasubramanian, S. et al. 2015, "Impact of surface texturization on overall performance of mono-crystalline silicon solar cells", *ECS Trans.*, Vol. 66, No. 6, pp. 9–17.

"The lower mean reflectance (optical loss) and lower recombination (electrical loss) resulted in the superior performance for 2.5µm-etched DW-cut wafers."

About the Authors



S. Saravanan received his Ph.D. in physics from the Cochin University of Science and Technology, India, in 2005, after which he worked as a postdoctoral fellow at the ADFA at UNSW, Canberra, and at the IISc, Bangalore. Since 2007 he has been working on silicon photovoltaics, initially for TATA BP Solar India Ltd and then for NCPRE, IIT Bombay. In 2016 he joined RenewSys India Pvt. Ltd. as an R&D manager, working on high-efficiency silicon solar cells.



Ch.S.R. Suresh is a deputy manager at RenewSys India Pvt Ltd, Hyderabad, where he is responsible for cell line operations. He specializes in screen-printing technologies for solar cell applications. Prior to joining RenewSys, he gained experience in GaAs MMIC and solar PV.



V.V. Subraveti works as an assistant general manager at RenewSys India Pvt Ltd, Hyderabad, and is responsible for solar PV cell manufacturing operations. Before joining RenewSys, he gained experience in GaAs MMIC technologies and solar PV.



K.C. Kumar is vice president of RenewSys India Pvt Ltd, Hyderabad, where he focuses on cell and module technologies, materials, manufacturing operations and strategic planning. Prior to joining RenewSys, he worked on various semiconductor device technologies, including Si CMOS, GaAs MMIC and Si solar PV.



U.K. Jayaram is executive director of RenewSys India Pvt Ltd, where he oversees activities in solar PV cell and module technologies, materials, components and manufacturing processes.

Enquiries

S. Saravanan
 RenewSys India Pvt Ltd, Hyderabad – 501 359
 Telangana, India
 Tel: +91 9611222788
 Email: saravanan.somasundaram@renewsysindia.com
 Website: www.renewsysworld.com

Pioneering the industrialization of PERC technology: A review of the development of mono- and bifacial PERC solar cells at SolarWorld

Phedon Palinginis, Christian Kusterer, Stefan Steckemetz, René Köhler, René Härtwig, Torsten Weber, Matthias Müller, Gerd Fischer & Holger Neuhaus, formerly of SolarWorld Innovations GmbH / SolarWorld Industries GmbH

Abstract

SolarWorld has played a pioneering role in triggering and implementing the shift from p-type multicrystalline aluminium back-surface field (Al-BSF) to p-type monocrystalline passivated emitter and rear cell (PERC) as the next mainstream solar cell technology, and recognized PERC to be the door opener to an extremely simple and cost-effective implementation of a bifacial solar cell. This paper reviews PERC technology development at SolarWorld, featuring an *industrial* baseline process for monocrystalline five-busbar (5BB) p-type PERC solar cells exceeding 22.0% median (22.5% maximum) cell efficiency by May 2018, before operations at SolarWorld came to a final halt. One major distinguishing and very noteworthy aspect of the PERC technology employed at SolarWorld, which contrasts with mainstream PERC technology implementation, is the use of silicon oxynitride (SiO_xN_y) as rear-side passivation. Open-circuit voltages of 690mV are achieved, thus demonstrating the excellent passivation properties of the rear-side $\text{SiO}_x\text{N}_y/\text{SiN}_x$ passivation stack. At this level, bulk carrier recombination needs to be addressed in an attempt to propel industrial p-type PERC towards > 24% cell efficiency *in mass production*. Therefore, extended attention is given to the results obtained from SolarWorld's dedicated effort to industrialize gallium-doped Czochralski (Cz-Ga) crystals in order to leverage potentially superior properties of Cz-Ga wafers, i.e. low bulk recombination and robustness against light-induced degradation at elevated temperatures. In a section dedicated to PERC bifacial, the paper addresses current weaknesses of PERC bifacial technology, and closes with an analysis of the limitations of 5BB p-type PERC bifacial solar cells as implemented at SolarWorld, namely 1) inevitable front-side efficiency losses compared with PERC monofacial, and 2) rear-side efficiency and thus bifaciality limitations imposed by the optical properties of the cell rear side.

Pioneering the industrialization of PERC technology under adverse market and business conditions

Still competing against different crystalline silicon solar cell architectures such as metal-wrap-through (MWT), emitter-wrap-through (EWT), interdigitated back-contact (IBC) and heterojunction (HJT) technology at the beginning of the 2010 decade, the passivated emitter and rear cell (PERC) concept has meanwhile

established itself as the winning technology, which is currently in the midst of replacing Al-BSF solar cells as the mainstream product technology.

Facing increasing price pressures, SolarWorld pioneered the industrialization of PERC technology based on p-type monocrystalline substrates as early as 2012, with the twofold aim of differentiating technologically and occupying a niche market, ultimately trying to leverage a price premium for high-efficiency solar cells and modules. In doing so, SolarWorld helped substantially in carving out the industrial solar cell technology roadmap, pushing technology shares of the photovoltaic (PV) industry from p-type multicrystalline Al-BSF towards p-type monocrystalline PERC as the next mainstream solar cell technology, with significantly increased efficiency potential. In retrospect, the year 2012 proved to be pivotal on several levels (macro-economic, micro-economic, technological), as it marked:

- A distinct break within the growth phase of the global PV market, with annually installed global PV system capacity contracting for the first time in 2012 after over a decade of strong annual growth (Fig. 1(a)) [1–3].
- The tipping point for business operations at SolarWorld, with earnings before interest, tax, depreciation and amortization (EBITDA) slipping into the negative in 2012 as a result of the aforementioned global market contraction, oversupply and increasing price pressure (Fig. 1(b)).
- The technological tipping point marking 1) the industrialization of PERC technology, and 2) a correlated shift towards monocrystalline substrates, with SolarWorld ramping up its first p-type monocrystalline PERC line in 2012 as a dedicated first mover well ahead of the industry (Fig. 1(c) and (d)) [4–5].

“PERC is currently in the midst of replacing Al-BSF solar cells as the mainstream product technology.”

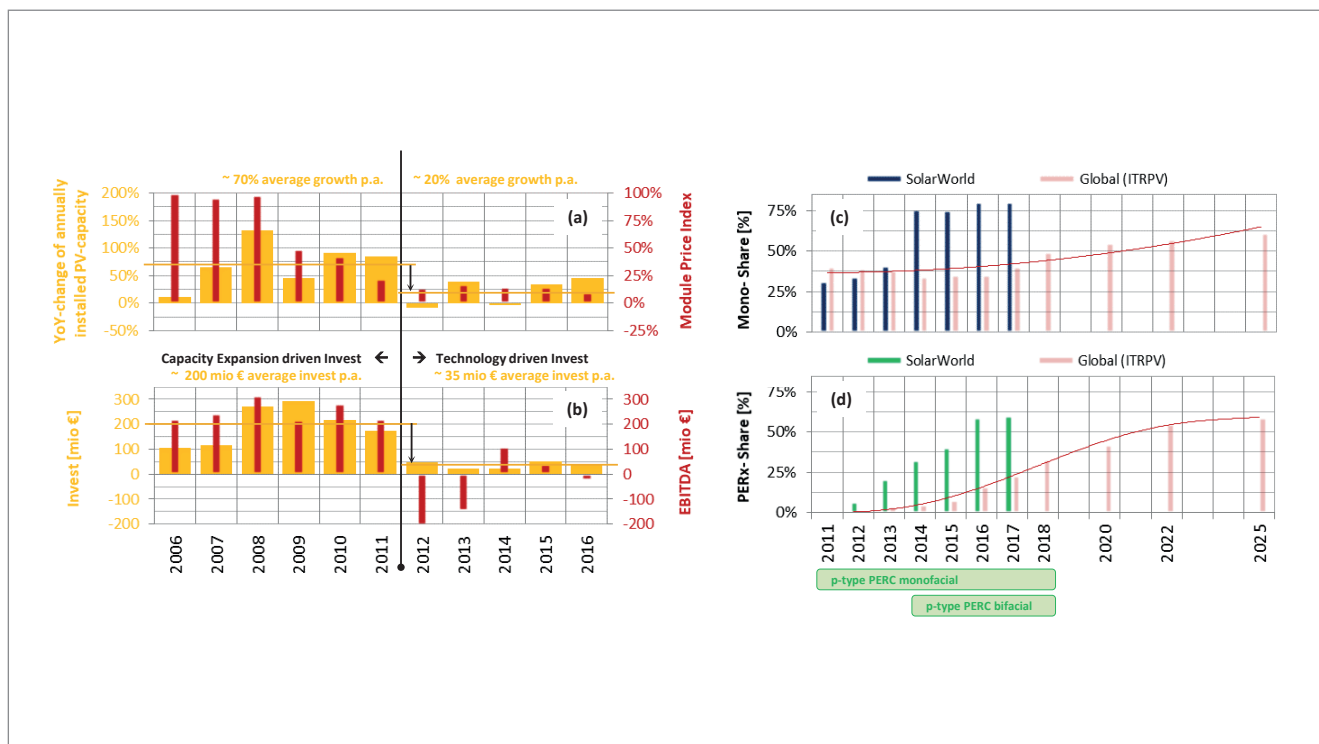


Figure 1. Pioneering the industrialization of PERC technology under adverse market and business conditions. (a) PV market growth: year-on-year (YoY) change of annually installed PV system capacity [1–2] and PV module price index as derived from BNEF [3] (Chinese c-Si modules [\$/Wp, 2018 real], [ref. year: 2006]). (b) Evolution of annual investment volume and EBITDA at SolarWorld (annual reports). (c) Evolution of monocrystalline cell capacity share at SolarWorld vs. global evolution. (d) Evolution of p-type PERC capacity share at SolarWorld vs. global evolution of p/n-type PERx technology share. (Note: historical data of the global evolution in (c) and (d) are taken from the ITRPV roadmap editions of the respective years. Projected data for 2020 and onwards are taken from ITRPV 9th ed. (03/2018) [4].)

With EBITDA slipping into the negative, SolarWorld's investment budget (which up until then had mainly been allocated to production capacity expansions) dropped significantly by 2012, at a time when capital expenditures (CapEx) for technology-driven investments were needed to sustainably differentiate on a technological level. However, and despite persisting CapEx constraints as well as R&D quota just above 2%, PERC capacity was continuously ramped up at all three SolarWorld production sites in the 2012–2017 time frame, at a rate far exceeding that of the industry, as shown in Fig. 1(d). Increasingly adverse business conditions, however, put a halt to SolarWorld's PERC production capacity fraction at around 60% by the end of 2016. Further line conversions planned for 2017 and the following years had to be cancelled. With monocrystalline wafers leveraging the technological advantages of PERC to the fullest, the shift towards PERC technology within SolarWorld was also accompanied by a dedicated technological-strategic shift towards *monocrystalline* solar cells. This measure was supported by the acquisition of Bosch Solar Energy as a pure play, p-type monocrystalline Al-BSF cell manufacturer at the end of 2013. By 2016, all SolarWorld PERC lines were operating with monocrystalline wafers, whereas the final remaining production capacity share of multicrystalline cell lines operating with Al-BSF had dropped to below 20%.

In summary, SolarWorld not only helped to introduce PERC technology to the PV market, but also anticipated the shift towards monocrystalline technology well ahead of the industry, with PERC and diamond-wire (DW) wafering setting up the game-changing triggers. Furthermore, SolarWorld developed and launched a highly cost-effective PERC bifacial solar cell variant which has led to unprecedented hype regarding bifacial technology. In the end, SolarWorld was not able to implement a full conversion to PERC, given the increasingly adverse business conditions leading to company insolvency. Credit is due to the former SolarWorld R&D and engineering staff responsible for the pioneering work on industrializing PERC technology at SolarWorld, as well as to the universities, R&D institutes and key equipment and material manufacturers for their instrumental contributions along this path.

PERC technology implementation at SolarWorld

Today, the dominant implementation of PERC technology with over 90% technology share is based on plasma-enhanced chemical vapour deposition (PECVD) of aluminium oxide (AlO_x)/silicon nitride (SiN_x) stacks for rear-side passivation and increased rear reflection (light trapping) [4,6,7]. Even though SolarWorld did ramp up PERC AlO_x using *remote* plasma technology on one of its production lines, and developed

PERC AlO_x using *direct* plasma technology on its R&D pilot line, the initial industrialization of PERC technology at SolarWorld, as well as the successive conversion of Al-BSF to PERC lines, was based on PECVD deposition of $\text{SiO}_x\text{N}_y/\text{SiN}_z$ rear-side stacks [8]. Independently of the passivation stack employed, local contact opening (LCO) of the rear-side dielectric via laser ablation is used [9,10] to enable rear-side contacting and local Al-BSF formation employing full-area Al screen printing and making use of local Al-Si alloying during fast firing [11]. Before opting for LCO and Al screen printing as the preferred technology for implementing local rear contacts, SolarWorld had been working up until 2011 on an industrial PERC implementation based on thick thermal oxide as the rear-side passivation layer, Al evaporation or Al screen printing for metallization, and laser-fired contacts (LFC) for rear-side contact formation [12]. The approach was abandoned mainly for technological reasons, i.e. excessive contact recombination inherent in the LFC approach limiting cell efficiency [13].

Fig. 2 reiterates the generic advantages of PERC technology. The distinctive features, representing the best-known methods (BKM) of SolarWorld's industrial PERC baseline process as of 05/2018, are highlighted below:

- Base material: Ga-Czochralski (Cz) wafers.
- Process flow: rear-side polishing and passivation before front-side texturing and diffusion [8].
- Single processes:
 - Rear-side passivation: $\text{SiO}_x\text{N}_y/\text{SiN}_z$ using direct PECVD (adapted stack for bifacial).
 - Emitter: selective emitter (SE) using laser doping from phosphorus silicate glass (PSG).
 - Emitter passivation: thermal oxidation using tube furnaces.
 - 5BB metallization rear: floating silver (Ag) pads. Aluminium grid (for bifacial).
 - 5BB metallization front: single print, *actively* aligned on SE.

For completeness, the well-known benefits of the SE and rear-side passivation with respect to increasing solar cell performance are shown in Fig. 2(c): the SE leads to an improved blue response when compared with a homogeneous emitter, while the rear-side passivation shows an improved infrared (IR) response when compared with an Al-BSF solar cell as a result of improved passivation and light trapping. The improved spectral response (internal quantum efficiency in Fig. 2(c)) gives rise to a short-circuit current gain, whereas improved emitter and rear-side passivation both contribute to a gain in open-circuit voltage as shown in Fig. 2(b).

The following sections highlight the main technological measures which have allowed an increase in *median* solar cell efficiency of *industrial*

monocrystalline PERC SiO_xN_y solar cells from 20.0% to 22.0% in the 01/2015–05/2018 time frame on the R&D PERC cell pilot line in Freiberg, Germany.

PERC $\text{SiO}_x\text{N}_y/\text{SiN}_z$ monofacial: evolution of the industrial PERC baseline process on the R&D pilot line

This section provides a review of the main PERC solar cell R&D activities at SolarWorld carried out within the 01/2015–05/2018 time frame, enabling the performance improvements shown in Fig. 3 of the industrial PERC $\text{SiO}_x\text{N}_y/\text{SiN}_z$ baseline process on the R&D cell pilot line at SolarWorld.

Emitter/emitter passivation

At the beginning of 2015, the overall share of solar cell line capacity at SolarWorld running SE technology already stood at almost 70%, far exceeding the corresponding global share of ~5% for SE technology at that time (ITRPV 7th edn). The homogeneous emitter (HE) technology on the remaining cell production lines was based on a POCl_3 process which had been successfully developed by the University of Konstanz. Aimed at reducing emitter saturation currents at sheet resistances of the order of 80–100 Ω/sq , the underlying approach was chosen to reduce the amount of phosphorus precipitates, and thus the amount of inactive phosphorus present in the emitter, mainly by adjusting the $\text{POCl}_3\text{-N}_2$ gas flow during the deposition phase [14]. The thus-formed HE places stringent requirements not only on the POCl_3 -diffusion process itself, but also on the front-side silver (Ag) paste selection as well as the firing conditions to ensure acceptable contact formation. Before being transferred to SolarWorld, the POCl_3 process was optimized using a design-of-experiment (DoE)-based approach. Final open-circuit-voltage levels reached 660mV on the R&D pilot line at the beginning of 2015 using direct plasma deposited SiN_z as the emitter passivation and anti-reflection coating (ARC). Up until then, the R&D PERC monofacial baseline process served to ensure a stable operation of this emitter type on the remaining HE cell lines in production.

With simulation-guided optimization [15] still identifying the HE as the largest recombination channel, further measures for emitter optimization were implemented in 2015 on the R&D pilot line. First, the PERC baseline was switched to SE technology [16], already available on the R&D pilot line. Second, dry thermal oxidation for improved emitter passivation, which had been investigated at SolarWorld starting in 2012 [17], was introduced with support from the process engineers of the Arnstadt site (former Bosch Solar Energy). Reduced emitter saturation currents well below 50 fA/cm^2 were thus achieved via improved surface passivation, phosphorus activation and phosphorus drive-in

– all simultaneously occurring during the tube furnace process [17,18]. The successive introduction of SE and thermal oxidation can be identified as step-like improvements in open-circuit voltage. Both measures were part of a device optimization strategy primarily guided by the suppression of recombination channels, thus increasing open-circuit voltage.

Base passivation

Representing the passivation technology of choice for PERC implementation at SolarWorld, the R&D pilot line baseline data shown in Fig. 3 exclusively reflect the performance of the monofacial PERC process using $\text{SiO}_x\text{N}_y/\text{SiN}_z$ rear-side stacks and direct PECVD tube furnaces for deposition of the dielectric layers [8]. One important activity, which had already started in Q2 2014, was the design and the corresponding process development of a $\text{SiO}_x\text{N}_y/\text{SiN}_z$ rear-side stack adapted and optimized

for bifacial operation (not shown). In parallel, a PERC AlO_x process based on direct PECVD tube furnaces was also developed, investigating whether a thus-deposited stack does indeed show superior performance over $\text{SiO}_x\text{N}_y/\text{SiN}_z$ [19,20]. Furthermore, a PERC AlO_x process sequence based on remote PECVD [7] as the current mainstream technology was developed and ramped up on one production line.

Regardless of the PERC $\text{AlO}_x/\text{SiN}_z$ process used, the main challenge from a process integration point of view – which was successfully resolved – was to integrate emitter passivation via thermal oxidation in a PERC AlO_x process flow. Ultimately, with the $\text{SiO}_x\text{N}_y/\text{SiN}_z$ stack exhibiting effective surface recombination velocities (S_{eff}) as low as 15cm/s [18], SolarWorld kept with PERC SiO_xN_y as the (passivation) technology of choice for further line conversions throughout its PERC ramp-up activities.

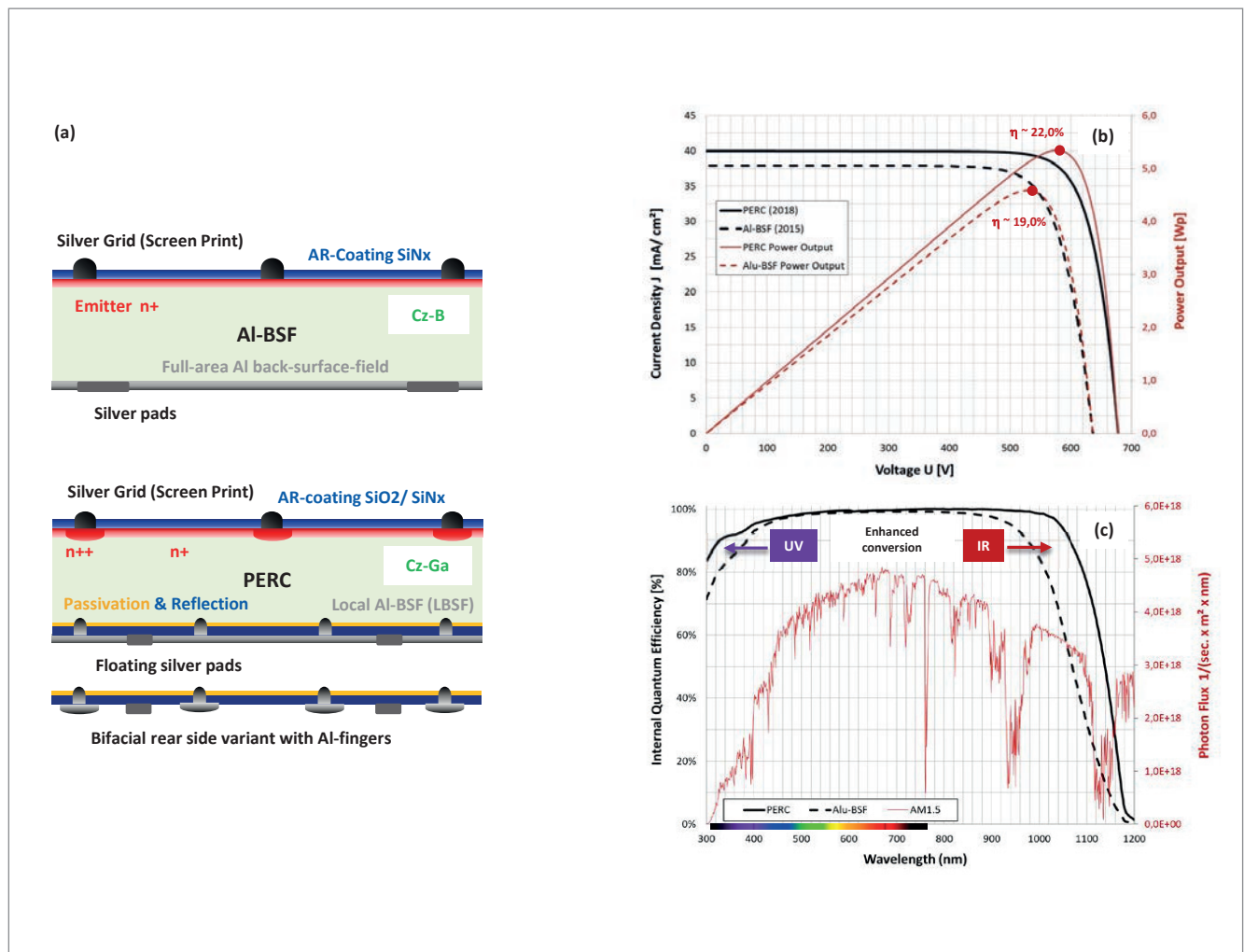
Figure 2. Transitioning from Al-BSF to PERC at SolarWorld.

(a) Design and process changes:

- Rear side: Rear-side passivation: $\text{SiO}_x\text{N}_y/\text{SiN}_z$ using PECVD direct plasma.
- Rear side: Local contact opening (LCO): laser ablation @ 532 or 1064nm.
- Front side: Selective emitter (SE): laser doping from PSG @ 532nm.
- Front side: Emitter passivation: dry thermal oxidation using tube furnace.

(b) Comparison of current–voltage characteristics.

(c) Comparison of internal quantum efficiency: enhanced internal photon conversion in the UV as a result of SE, and in the IR as a result of rear-side passivation.



DKEM® Metallization / Interconnection Solutions for Advanced Solar Cells and Modules



High Performance Silver Pastes for Advanced Solar Cells

- BSF Solar Cells
- Black-silicon PERC Solar Cells*
- Mono PERC SE Solar Cells*
- Dual Printing Technology
- Double Printing Technology
- N-type TOPCon Solar Cells



High Performance Metallization and ECAs for Advanced Solar Modules

- Integrated Metallization Solutions for Multi-busbar / Shingled Modules
- Electrically Conductive Adhesives (ECAs) for Interconnection of Shingled Modules

** Including single-side AlOx passivation and double-side AlOx passivation technologies*

DK Electronic Materials, Inc (DKEM®) is an advanced materials firm dedicated to the development and application of performance electronic materials, and committed to the product philosophy of When Performance Matters®.

As the top brand of China PV silver pastes and one of the industry leading suppliers of electrically conductive silver pastes, DKEM® is serving PV industry through high intensity of R&D investment, high quality products and prompt marketing & sales engagement. Meanwhile, DKEM® is proactively investing and developing products and solutions in display / lighting and semiconductor industries.



Contacting and metallization

Within the dedicated recombination-suppressing device optimization strategy, contact features were consequently and continuously miniaturized:

- Front side: reduction of the selective emitter regions to 130µm finger width. Continuous reduction of screen-printed Ag fingers, reaching 30µm finger width with state-of-the-art meshes and Ag pastes.
- Rear side: switch from a line to a dashed layout, reaching LCO area fractions well below 2%.

With the early introduction of 5BB technology at SolarWorld starting in 2015 and the outlook towards zero-busbar technology (oBB), SolarWorld's extensive efforts to develop an extrusion printing technology for high-aspect-ratio fine-line printing were finally abandoned at the beginning of 2015 [21] in order to fully focus on single screen printing as the technology of choice. Anticipating the necessity for active alignment at ever-decreasing contact feature sizes, SolarWorld installed a novel screen printer on the R&D pilot line in 2016, featuring in situ recognition of the patterns to be metallized, allowing:

- Active positioning of front-side Ag screens on SE-patterns.
- Active positioning of rear-side Al screens on LCO patterns for PERC bifacial.

Metallization layouts for oBB technology were developed and tested on SolarWorld's proprietary multiwire stringer built by USK Karl Utz Sondermaschinen GmbH. The machine combined a laser to produce *half-cut cells*, a wire field, contact soldering and laser separation of the wires to form the entire 120-half-cell matrix in a continuous process with a throughput of 3,600 full cells per hour [22]. In addition, multiwire modules with *full cells* were built with the help of Meyer Burger Germany GmbH using their SmartWire Connection Technology (SWCT), reaching 320Wp for a 60-cell glass-backsheet module employing an industrial module bill of materials (BOM) only.

Base recombination

As part of PERC development, bulk properties were studied intensively at theoretical [23] and experimental levels at SolarWorld, with recognition that for the efficiency potential of PERC to unfold, low *and* stable material recombination currents ($j_{0,mat}$) are required. Consequently, several highly innovative crystallization technologies were developed at SolarWorld by the crystal R&D team as well as by production engineers. Both approaches followed the strategy of reducing interstitial oxygen [Oi] in the crystal analogously to magnetic Czochralski (MCz) and float zone (FZ), yet keeping it economically viable:

“With the $\text{SiO}_x\text{N}_y/\text{SiN}_z$ stack exhibiting effective surface recombination velocities (S_{eff}) as low as 15cm/s, SolarWorld kept with PERC SiO_xN_y as the (passivation) technology of choice.”

- Cast monosilicon (or quasimono): with the use of appropriately oriented Cz crystal slabs as well as full-area seeds, a proprietary variant of quasimono technology was extensively developed and transferred to production. Already by the end of 2014, a world-record p-type cast monosilicon PERC solar cell from the R&D pilot line exhibiting >21.4% cell efficiency [21] demonstrated the excellent bulk crystal quality of SolarWorld's cast monosilicon material. Bulk lifetimes for cast monosilicon wafers exceeding those in Cz-grown silicon were demonstrated [24] thanks to the low interstitial oxygen content $[O_i] \sim 1-2 \times 10^{17} \text{at/cm}^3$ inherent in crystal casting technology and to a deep understanding of dislocation density control during seeding [25].
- NeoGrowth: another proprietary crystal growth technique, termed *NeoGrowth*, which uses a contactless bulk crystal growth method for producing single crystal ingots, was developed at SolarWorld, aimed at providing monocrystalline wafers at lower cost than Cz-grown wafers [26]. This being a contactless technology, the oxygen content can be kept to below $[O_i] \sim 1-2 \times 10^{17} \text{at/cm}^3$. With liquid silicon being continuously fed onto a crystalline silicon seed layer, the otherwise segregation-driven resistivity span over the crystal height can be significantly reduced, allowing low resistivity wafers ($\sim 1.0 \Omega \text{cm}$) to be tailored at a tight resistivity distribution in favour of PERC solar cells, which require low base/spreading resistance.

Not having reached technological maturity and chasing after ‘moving’ cost targets, the development of both crystal technologies was overtaken by the rapid price decline of Cz-grown wafers as the incumbent technology. With the demonstration of world-record PERC efficiencies of 21.7% (07/2015) and 22.0% (12/2015) on the R&D PERC pilot line at SolarWorld using Ga-doped Cz-grown monocrystalline wafers [27,28], the decision was thus made in 2016 to pilot Ga-doped Cz crystals at SolarWorld to further increase the efficiency of PERC solar cells, despite the lack of in-house continuous Cz (CCz) technology for achieving tight resistivity control.

While the R&D pilot line served to sample and assess the quality of the above-mentioned crystals as well as other substrate types, the baseline as shown in Fig. 3 strictly reflects the performance

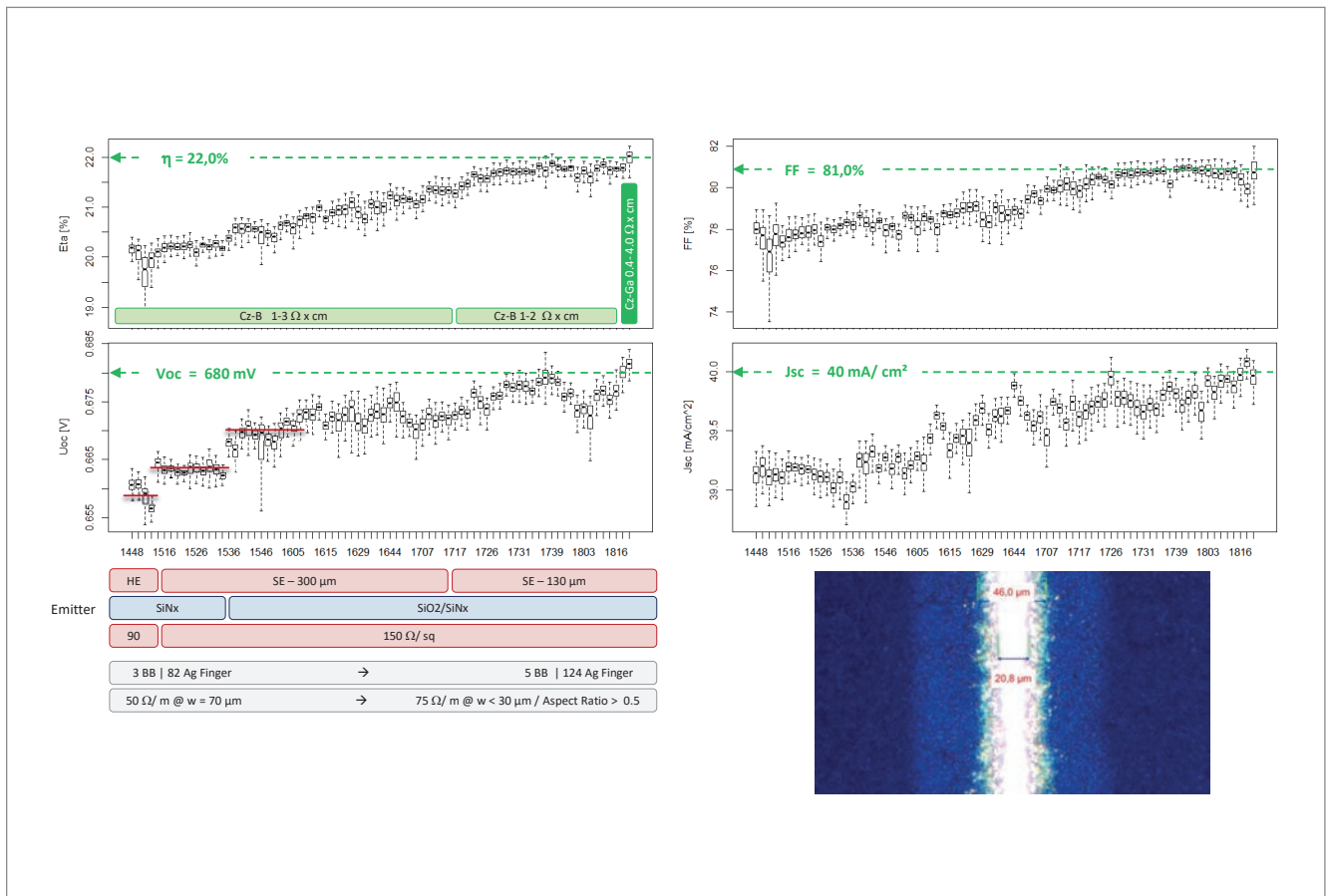


Figure 3. Evolution of the industrial PERC monofacial baseline process on the R&D PERC cell line at SolarWorld. The I – V measurement is calibrated against CalLab-certified reference cells, which were continuously updated upon significant design/process changes. The baseline ID is indexed as YYww. The best-known method 05/2018 exceeds 22.0% median cell efficiency and 680mV open-circuit voltage. The open-circuit voltage reveals stepwise improvements in emitter (passivation) technology. The early transition from 3BB to 5BB allowed the limits of screen printing to be continuously pushed towards finger widths (as printed) <30μm. The introduction of a novel SE laser process with a focal width of 130μm, in combination with a novel front-side printer using in situ pattern recognition for active print alignment in 2016, allowed further and continuous reduction of contact-related V_{oc} losses. The inset bottom right shows an optical microscope image of a front-side Ag-finger. The n^{++} region of the SE underneath can also be seen in the contrast. The Ag finger is well centred as a result of active alignment.

based on commercially available Cz-B wafers (internally or externally sourced), with the only measure being the tightening of the resistivity specification. The final baseline run was carried out using Cz-Ga material from an in-house Cz pull, to achieve a median cell efficiency exceeding 22.0% for an industrially relevant process. The best cell from a sister run yielded an ISE-CalLab-certified open-circuit voltage of $V_{oc} = 688.5\text{mV}$ and a cell efficiency of $\eta = 22.5\%$ for a fully industrial 5BB Cz-Ga PERC cell, demonstrating the excellent recombination properties of Cz-Ga bulk as well as $\text{SiO}_x\text{N}_y/\text{SiN}_z$ rear-side passivation.

Base material choice – Cz-Ga vs. Cz-B

Sticking with p-type technology, the alternative strategy for achieving high initial, and above all stable, bulk lifetime – other than reducing $[\text{O}_i]$ content in the crystal – is the switch from boron to gallium as the p-type dopant [29–31]. The main technological barrier of entry for the industrialization of Cz-Ga crystals and wafers for crystalline silicon solar cells is the low segregation coefficient of Ga ($k = 0.008$), which results in a wide resistivity span over the ingot height.

Crystallization technologies based on a continuous feeding of silicon (such as CCz or NeoGrowth), however, can overcome this issue and produce essentially flat resistivity profiles over the ingot height [32].

In the following, the results of a dedicated material study benchmarking Cz-Ga against Cz-B crystals/wafers are summarized. Practically relevant benchmark metrics contained in the extended I – V dataset of Cz-B/Cz-Ga PERC solar cells at efficiency levels/ V_{oc} levels of 22.0%/680mV respectively are applied. Initial, degraded and regenerated bulk lifetimes for Cz-B/Cz-Ga base materials in *post-cell-process* conditions are also presented, underlining the corresponding I – V parameter evolution for Cz-B/Cz-Ga PERC solar cells exposed to illumination at elevated temperatures. Since in-house CCz-puller capability was lacking, the crystals were grown in-house using semi-continuous (or recharge) RCz technology available at SolarWorld. It is shown that, despite the segregation-inherent resistivity span, RCz grown Cz-Ga wafers can offer a superior substrate choice over RCz-grown Cz-B wafers, despite the strong segregation of gallium.

Additional equipment for cell regeneration is not needed, given the robustness of Cz-Ga base material against illumination at elevated temperatures.

Cz-Ga vs. Cz-B – Part 1: Initial (as-flashed) I – V data

In Fig. 4 the as-flashed I – V data of an experimental cell run that was simultaneously carried out on two Cz-B wafer reference batches and one Cz-Ga wafer batch are shown. The Cz-B wafer batches were randomly chosen from the deliveries of two external Tier 1 wafer suppliers (S-1, S-2), both exhibiting base resistivities in the range 1.0–2.0 Ωcm . The Cz-Ga wafer batch originated from an in-house Cz crystal run (2016) and was split into four sub-batches, with wafers from each sub-batch originating from four ingot sections (Sec 1 = tail, Sec 2 = tail-centre, Sec 3 = top-centre, Sec 4 = top) making up the full crystal (where *top* denotes the seed end). The segregation-inherent resistivity range for the Ga-doping level chosen corresponds to 0.4–4.0 Ωcm . All wafers have M2 format and are diamond-wire cut. To ensure consistent cell-processing conditions, all wafer batches were homogenized into one single batch prior to processing. The cell process employed reflects the baseline BKM 05/2018 of the final run shown in Fig. 3. The I – V data for the Cz-Ga sub-batches are shown separately for each ingot section to illustrate the dependence on crystal height. The data of all four sections are consolidated in the box termed *Cz-Ga-all* to benchmark the overall performance of the complete, ingot-representative, Cz-Ga wafer ensemble with the Cz-B reference batches.

The as-flashed and hysteresis-free I – V measurement reveals superior performance of the Cz-Ga PERC cell batch, with a median cell efficiency exceeding that of the still undegraded Cz-B PERC reference batches by $\Delta\eta > 0.10\%_{\text{abs}}$. The broad base-resistivity range manifests itself within the broad lumped cell series resistance (S_{ser}), and correspondingly the fill factor (FF) distribution. S_{ser} (FF) increases (decreases) from tail (Sec 1) to top (Sec 4) in line with expectation. It is mainly the spread in FF that determines the broader efficiency distribution of the Cz-Ga batch. Whereas V_{oc} is constant over the crystal height for the PERC cell design chosen, the short-circuit current density starts to drop in the tail region of the Cz-Ga crystal, indicating decreased carrier lifetimes for resistivities below 0.5 Ωcm . The S_{ser} data confirm a similar base resistivity (1.0–2.0 Ωcm) of the Cz-B reference batches and Sec 2 of the Cz-Ga batch, as expected, from the resistivity profile of the Cz-Ga ingot. Most interestingly, a higher pseudoFF (pFF) can still be observed for the Cz-Ga PERC cells, implying higher bulk carrier lifetimes at similar doping levels as well as a generally superior injection dependence

of the carrier lifetime for Cz-Ga base material in the initial state. Superior bulk properties are also reflected within a V_{oc} gain of the order of 3 mV, and correspondingly lower saturation currents J_{oi} of the Cz-Ga PERC cells, with J_{oi} decreasing from tail (100 fA/cm²) to top (85 fA/cm²).

In the next two sections, the degradation/regeneration behaviour of the different wafer types is presented.

Cz-Ga vs. Cz-B – Part 2: Evolution of I – V data under illumination at elevated temperatures

For each of the six wafer batches (two Cz-B reference batches and four Cz-Ga sub-batches), ten cells were randomly picked and subjected to illumination at elevated temperatures (0.5 Suns/75°C) for 180 h. The evolution of the I – V parameters, after normalization to their initial state prior to degradation, is shown in Fig. 5. Since the evolution of the normalized pFF matches that of the normalized FF for all samples, pFF is not shown separately. Note that no major differences in the degradation behaviour of Cz-Ga PERC cells originating from different crystal sections are observed; the data of all Ga batches (Sec 1–4) are therefore consolidated in the graphs. Distinctively different behaviours within the time frame of the measurement are observed for:

- **Cz-B | S-1.** This sample shows a degradation and regeneration behaviour which is typical of BO-related light-induced degradation (LID). At the lowest power point (LPP), a substantial relative efficiency loss of the order of 6% is monitored. All I – V parameters shown regenerate to their initial values to within 1%, within the time frame of the measurement.
- **Cz-B | S-2.** This sample not only shows a more severe degradation, with over 8% relative efficiency loss at LPP, but also a more persistent degradation, with only some initial signs of regeneration within the time frame of the measurement. This behaviour, which is characteristic of light and elevated-temperature induced degradation (LeTID) observed in multicrystalline PERC cells, has been reported by Hanwha Q CELLS to also occur in p-type Cz PERC cells [33] and is herein confirmed.

Note that, for both Cz-B PERC reference batches investigated, the magnitude of the observed degradation is of similar order for the I – V parameters $FF / V_{\text{oc}} / J_{\text{sc}}$, with only a slight trend in decreasing contribution from FF (highest relative degradation) $\rightarrow V_{\text{oc}} \rightarrow J_{\text{sc}}$ (lowest relative degradation) to the overall relative efficiency degradation.

- **Cz-Ga all.** In contrast to both Cz-B PERC cell batches, Cz-Ga PERC solar cells exhibit a significantly lower relative efficiency loss

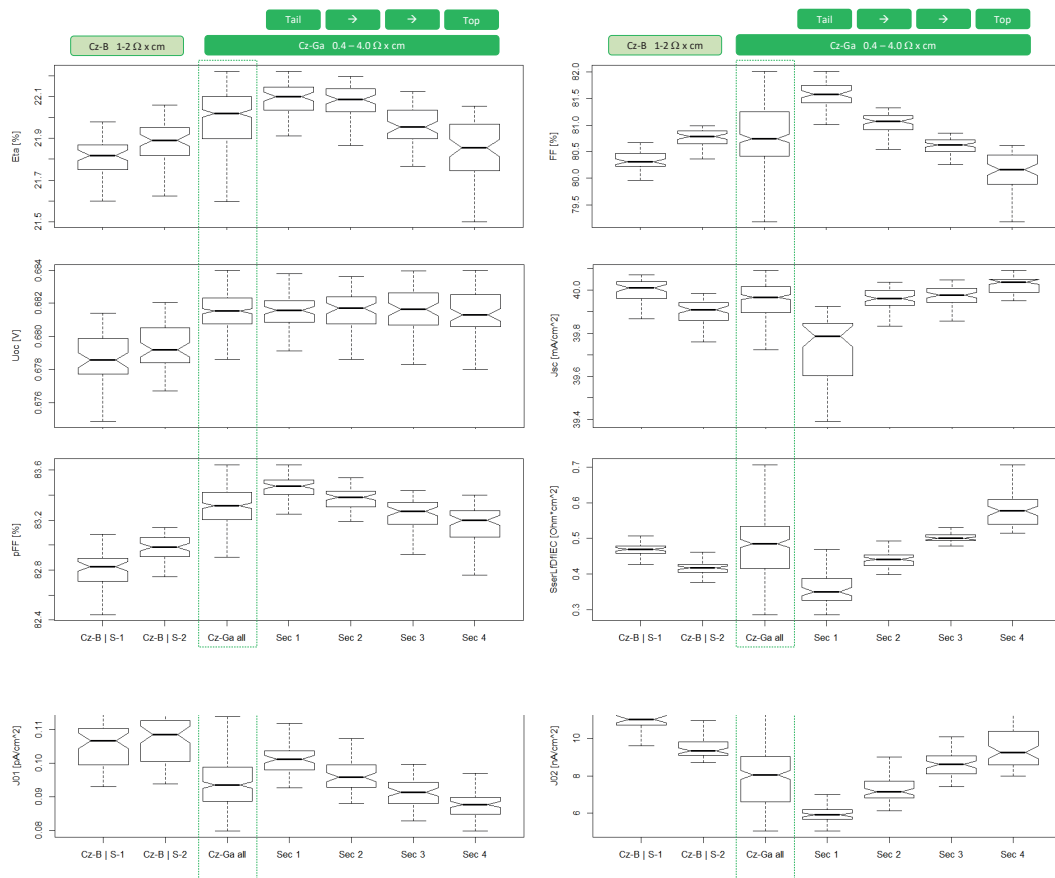


Figure 4. As-flashed, hysteresis-free I - V data for Cz-B and Cz-Ga PERC Cells. Two Cz-B reference batches (S-1 and S-2) are included. To illustrate the effect of the large resistivity span for Cz-Ga, the Cz-Ga batch is split into four sub-batches, corresponding to the four ingot sections (Sec 1: tail, Sec 4: top).

of the order of 1.5% within the time frame of the measurement, irrespective of longitudinal position within the crystal. As opposed to the Cz-B reference batches, J_{sc} and V_{oc} show almost no signs of deterioration. In particular, the slight efficiency loss observed is solely driven by a slight loss in pFF . As in the case of batch Cz-B | S-2, a persistent component can be observed in the pFF , reflecting a deterioration of the injection dependence of the bulk carrier lifetime, which is strongly suppressed, however, for Ga-doped Cz PERC cells. Within the two-diode fitting procedure underlying the I - V dataset, a persistent degradation also appears in the saturation current of the second diode (J_{02}). Reflecting changes in (the injection dependence of) bulk carrier lifetime, pFF and J_{02} should be closely monitored when signatures of LeTID are observed in the I - V parameters of, for example, Cz-B- or Cz-Ga-based PERC solar cells.

“No major differences in the degradation behaviour of Cz-Ga PERC cells originating from different crystal sections are observed.”

To summarize, superior bulk performance of Cz-Ga wafers over Cz-B wafers is observed on the basis of the I - V parameters in the initial state and after illumination at elevated temperatures for high-efficiency industrial PERC solar cells at an efficiency level of 22.0%. Consistency of this result with the evolution of initial, degraded and regenerated bulk lifetime data of *post-process* Cz-B and Cz-Ga base materials is presented in the next section.

Cz-Ga vs. Cz-B – Part 3: Evolution of bulk carrier lifetime: initial – degraded – regenerated state

In order to obtain a better understanding of carrier lifetime-limiting defects for Cz-B and Cz-Ga base materials in fully processed PERC solar cells, and in order to correlate experimentally determined bulk carrier lifetimes in a *post-process condition* with corresponding I - V parameters, lifetime measurements have been carried out on different materials subjected to two different cell processing conditions (R&D pilot line vs. production line).

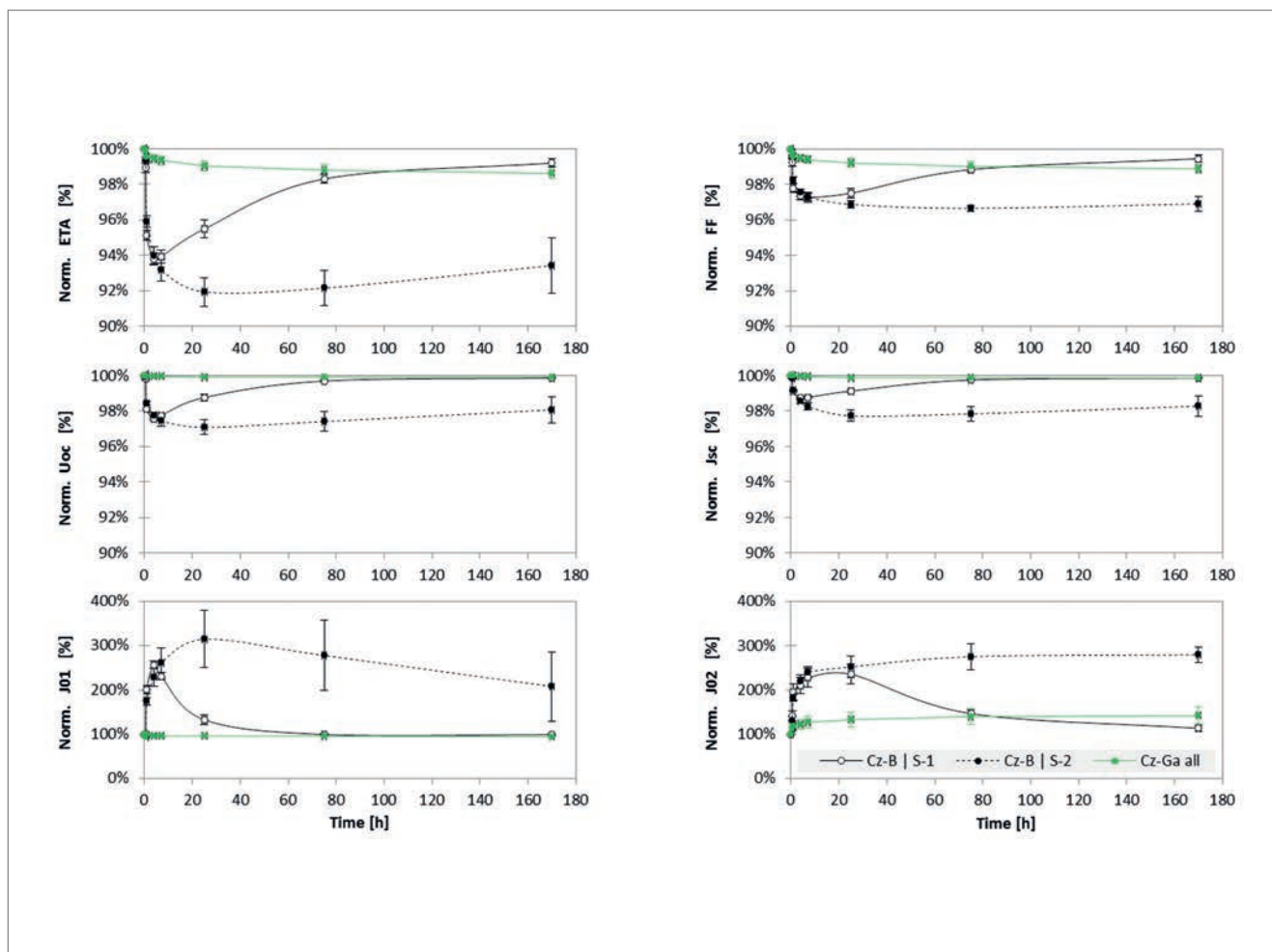


Figure 5. Degradation under illumination at elevated temperatures (0.5 Suns @ 75°C). For Cz-Ga, all ingot sections 1–4 are consolidated in one graph (40 cells total). Batch Cz-B | S-1 exhibits typical BO-driven LID behaviour, while Cz-B | S-2 exhibits an additional LeTID component. In contrast to the Cz-B reference batches, degradation is strongly suppressed in the Cz-Ga PERC cell batch.

Fig. 6 shows photoconductance decay (PCD) lifetime measurements recorded with a WCT-120 Sinton tool for Cz-B and Cz-Ga base materials. Rather than testing ‘typical’ lifetime samples, as (for example) prepared in Walter et al. [34], it was chosen to investigate the bulk carrier lifetime in wafers which have undergone full PERC processing in order to include within the measured bulk carrier lifetimes the impact of 1) the thermal budget/history of the particular cell process, and 2) potential contamination sources of the particular cell process affecting the base material. Metallization and dielectric layers were thus chemically removed from fully processed PERC solar cells by the analytic laboratory at SolarWorld in order to recover the bare bulk wafer and to determine *post-cell-process bulk carrier lifetimes at injection levels corresponding to the maximum power point (mpp)* [23]. In a similar way to the procedure described in Walter et al. [34], the recovered bare wafers were both-side passivated (ALD- AlO_x /PECVD- SiN_x) and fired (note that the substrates were *not* diffused, since they had already undergone diffusion during cell processing). PCD measurements were carried out 1) in the initial state, 2) after degradation (0.1 Sun

@ 30°C for 72h), and 3) after regeneration (1.0 Sun @ 185°C for 15 min.). Lifetime sample passivation, firing, conditioning and PCD measurements were performed at the Institute for Solar Energy Research in Hamelin (ISFH).

Independently of the crystal growth process (‘Crystal 1/2’) and the cell process employed (‘R&D Pilot Line’/‘Production Line’), the Cz-Ga substrates show similar bulk carrier lifetimes. Note that, given the excellent passivation quality of the ALD- AlO_x /PECVD- SiN_x passivation with recombination velocities $<1\text{cm/s}$ [34], the carrier lifetimes measured correspond to bulk defect recombination. Bulk carrier lifetimes in Cz-Ga base materials do not change when subjected to typical degradation and regeneration procedures. In contrast, the Cz-B lifetime samples (the original cells of which had been simultaneously processed with sample ‘Cz-Ga Crystal 2 – Production Line’), show severe bulk carrier lifetime degradation, which can, however, be recovered within a regeneration process. On the basis of these carrier lifetime data, the impact of interstitial iron Fe_i as a potential bulk carrier lifetime-limiting defect in Cz-Ga is discussed, following a simple Shockley-Read-Hall (SRH) analysis.



EU PVSEC 2019

**36th European
Photovoltaic Solar Energy
Conference and Exhibition**

The Innovation Platform for the global PV Solar Sector



09 - 13 September 2019

**Marseille Chanot
Convention and Exhibition Centre**

Marseille, France



www.photovoltaiic-conference.com • www.photovoltaiic-exhibition.com

Cz-Ga vs. Cz-B – Part 4: FeGa vs. FeB defects – SRH analysis

With iron being one of the most critical contaminants in crystalline silicon [35], the question arises whether the experimentally determined bulk carrier lifetimes in Fig. 6 are in line with –and potentially limited by – an Fe-related defect in the Ga/B-doped Cz-crystals. It is well known that electrically active iron-acceptor (FeX) pairs are formed in p-type crystalline silicon as a result of Coulomb attraction between highly mobile, positively charged interstitial iron Fe_i and negatively charged substitutional acceptors ($X = B, Al, Ga, In$) [36,37]. The characteristic of such FeX defects is that they can be dissociated via light stimulation within minutes [38]. Re-association kinetics are found to be independent of the dopant species (X). Timescales for re-association in the dark are higher than dissociation timescales and vary, depending on dopant concentration $[X]$, from several minutes ($\rho_{base} \sim 0.5 \Omega cm$) to over one hour ($\rho_{base} \sim 4.0 \Omega cm$) [39]. With the Fe_i defect showing a strong injection dependence in the fully dissociated state, and the associated FeX

“Despite careful sample conditioning, the degree of iron-acceptor association/dissociation is difficult to determine experimentally.”

defects showing a weak injection dependence, a dopant-characteristic crossover point of the SRH lifetimes is observed. This feature is at the base of a highly sensitive iron detection method, which was first developed for boron-doped silicon [38] and later extended to Ga-doped silicon [40]. In Schmidt & Macdonald [40], SRH parameters have been determined for the dominating FeGa defect in intentionally Fe-contaminated Cz-Ga samples, assuming that the lifetime in the associated state is solely determined by the deeper level FeGa defect which corresponds to the trigonal configuration of the FeGa pair [37,40].

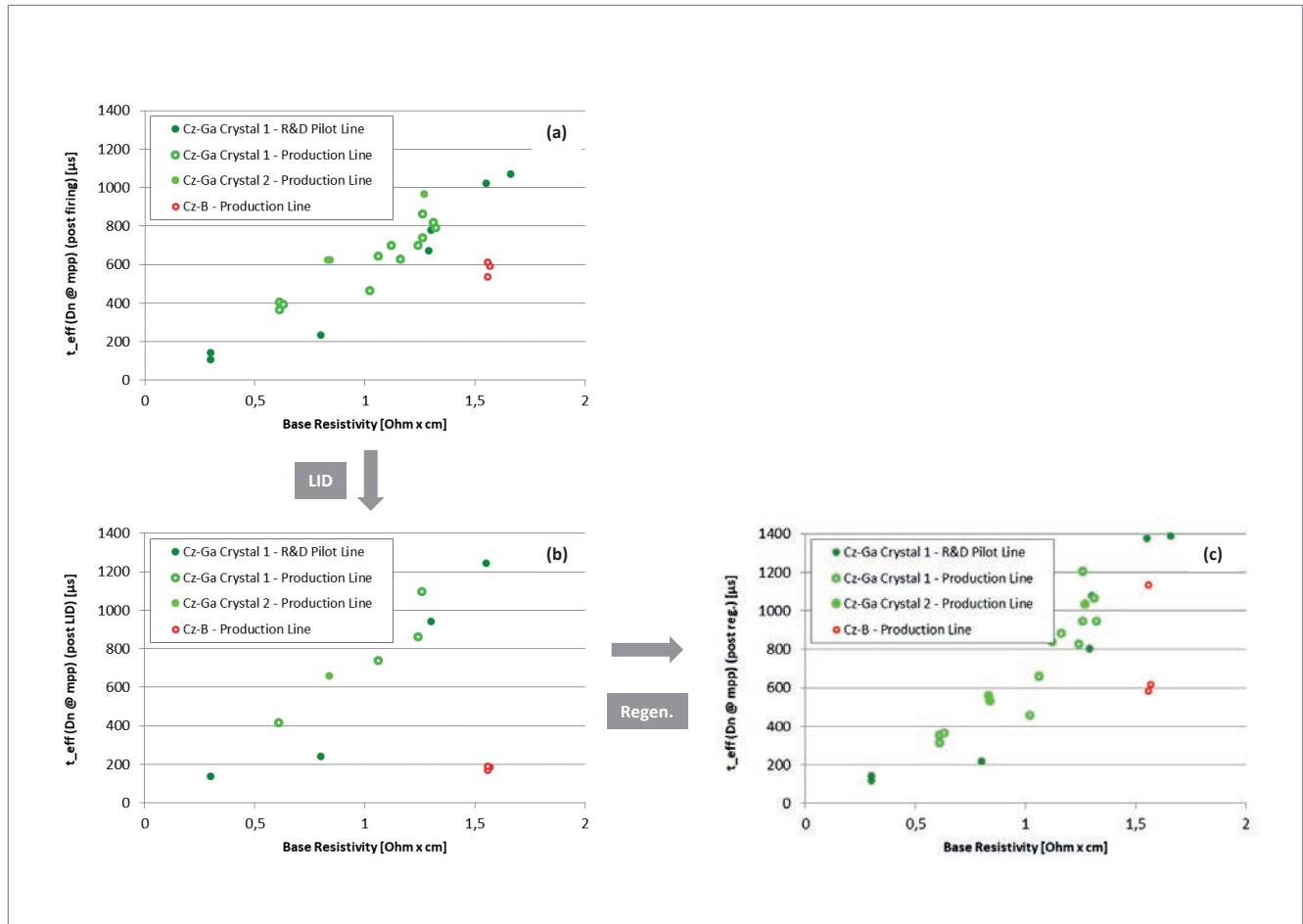
Fig. 7 shows the analytical results for the SRH lifetime and the material saturation current density $j_{0,mat}$ as a function of base resistivity and at carrier injection levels corresponding to mpp conditions [23]. The iron level is set to $[Fe_i] = 1.5 \times 10^{10} \text{ at/cm}^3$. The SRH parameters for Fe_i , FeB

Figure 6. PCD carrier lifetimes (Δn @ mpp) on wafers recovered from fully processed solar cells, thus reflecting post-process bulk properties. The carrier lifetime study was part of a Cz-Ga pilot and was meant to assess the potential impact of crystal growth- and cell process-related contamination sources (2016). Metallization and dielectric layers were chemically removed to recover the bulk wafer and determine the post-process carrier lifetime at mpp injection levels. Wafers were both-side passivated (ALD- AlO_x /PECVD- SiN_x) and fired:

(a) Lifetimes post-firing.

(b) Lifetimes post-LID (0.1 Sun @ 30°C for 72h).

(c) Lifetimes post-regeneration (1.0 Sun @ 185°C for 15 min.).



and FeGa as given in Schmidt & Macdonald [40] are employed. It is stressed here that, despite careful sample conditioning, the degree of iron-acceptor association/dissociation is difficult to determine experimentally, with unwanted dissociation/association occurring during sample handling. The results of the SRH analysis were thus parameterized with respect to the degree of dissociation, assuming that the two defects Fe_i and FeX are coexisting (100% corresponds to full dissociation) [42]. Given that dissociation timescales are fairly short (within minutes), and association timescales comparably long (minutes to hours), it can be assumed that samples are dominated by the dissociated Fe_i defect if handled under ambient conditions.

Postulating Fe_i to be the lifetime-limiting defect in Cz-Ga, the iron level, as a free parameter, was adjusted to $[Fe_i] = 1.5 \times 10^{10} \text{ at/cm}^3$. At this iron level, consistency can be established for the Cz-Ga samples with respect to:

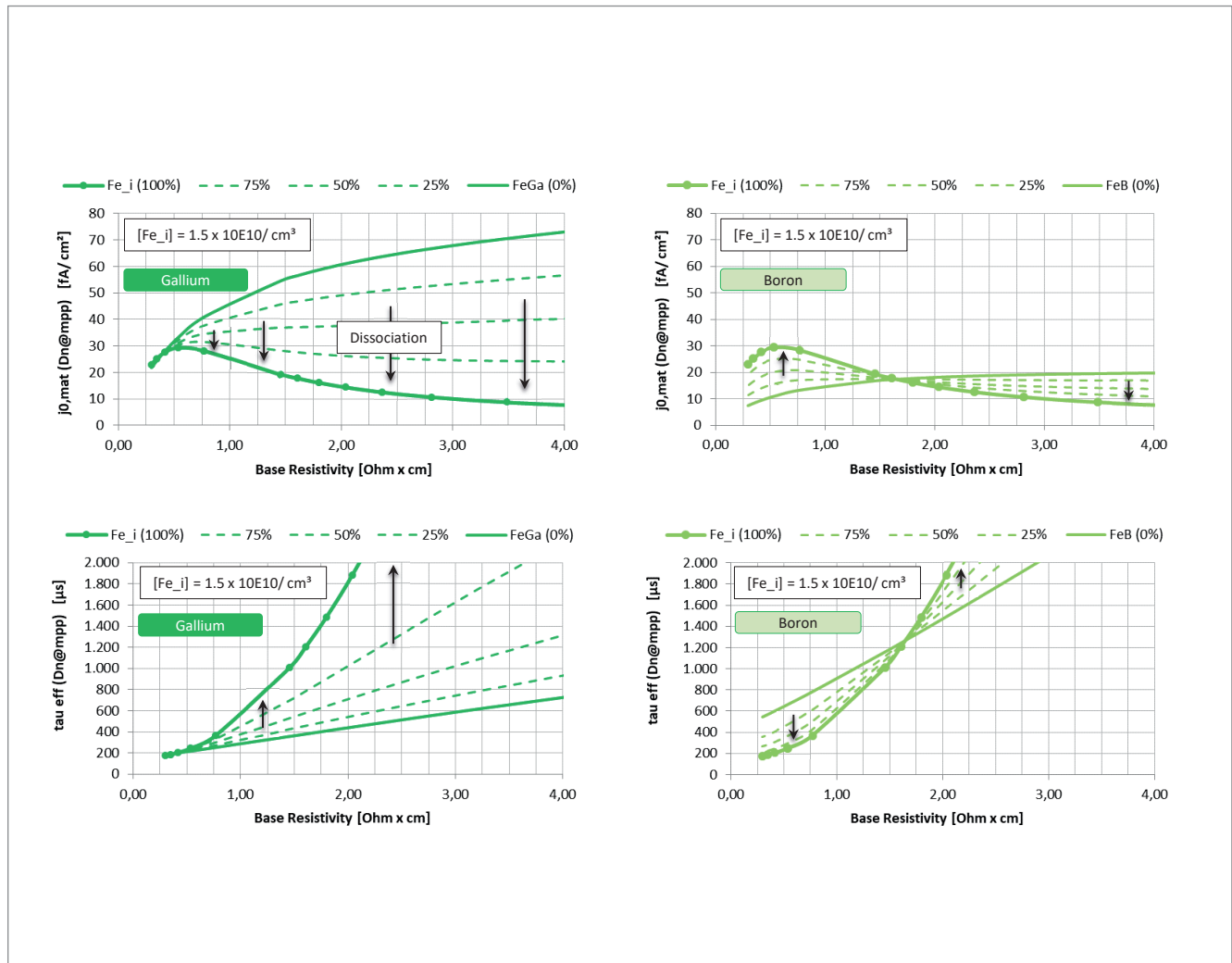
- The experimentally determined carrier lifetimes shown in Fig. 6, assuming the Fe_i defect, i.e. the

dissociated state, to be dominating in those measurements.

- The experimentally determined total saturation currents J_{oi} in Fig. 4 after subtracting $j_{oe, tot} \sim 50 \text{ fA/cm}^2$ and $j_{oe, tot} \sim 20 \text{ fA/cm}^2$ (refer to the loss analysis in Müller et al. [18]) from J_{oi} in order to obtain an estimated $j_{o, mat}$. Note, in particular, that the simulated decrease in material saturation current $j_{o, mat}$ with increasing base resistivity from tail to top follows the measured J_{oi} dependence on base resistivity in Fig. 4, again assuming the Fe_i defect to be dominating.

With the Cz-B PERC reference batches having been processed under exactly the same conditions, the same iron level of $[Fe_i] = 1.5 \times 10^{10} \text{ at/cm}^3$, as an adjustable parameter, was applied in the SRH analysis for B-doped silicon. Comparing the SRH analysis with the experimentally obtained lifetime data (Fig. 6) and I - V data (Fig. 4) for the Cz-B samples, an additional background defect must be assumed to be present in the Cz-B

Figure 7. Analytical results for the SRH lifetime and material saturation current at mpp injection levels. The SRH parameters for Fe_i , FeB and $FeGa$ as given in Schmidt & Macdonald [40], and an iron contamination level of $[Fe_i] = 1.5 \times 10^{10} \text{ at/cm}^3$, are used. With the degree of iron-acceptor dissociation being hard to determine experimentally, the results are parameterized with respect to the degree of dissociation.



samples, which is limiting the bulk lifetime in Cz-B to lower than Fe_i -limited values, even after regeneration.

Cz-Ga vs. Cz-B – Part 5: FeGa vs. FeB defects – I – V data before/after light soaking

Further *qualitative* consistency can be obtained when looking at the relative change in the I – V parameters before and after light soaking, despite the fact that the initial and final degrees of FeX dissociation are not known precisely. In this experiment, the regenerated sample set, as shown in Fig. 6, i.e. after 180h exposure to illumination at elevated temperatures, was stored in the dark for 24h and then exposed to the first I – V measurement. FeX pairs within the samples were then (partially) dissociated during light soaking at 1 Sun for 10 sec. before the second I – V measurement. Fig. 8 shows the resulting observed relative change in $\%_{\text{rel}}$ for selected I – V parameters (note that the original units of the I – V parameters are indicated in the axis labels, although the relative change is shown). Even though the relative changes are small and well within $1\%_{\text{rel}}$, the ‘controls’ show that the observed effects are real. The differences between the Cz-B and Cz-Ga PERC samples upon (partial) dissociation of the associated initial state before light soaking can, in principle, be explained by the fact that the FeGa defect presents a much stronger recombination centre than the FeB defect [40]. Consequently, the crossover point in Ga-doped silicon ($\Delta n_{\text{co}}(\text{Ga}) \sim 0.25 \times 10^{14}/\text{cm}^3$) occurs at a lower injection level than in B-doped silicon ($\Delta n_{\text{co}}(\text{B}) \sim 1.4 \times 10^{14}/\text{cm}^3$).

As a result, a higher V_{oc} increase/ J_{oi} decrease is observed upon (partial) dissociation in Cz-Ga than in Cz-B. The V_{oc} effect is dominating in Cz-Ga-doped silicon. Light soaking for as short as 10 sec. already leads to an overall cell efficiency increase, whereas a slight decrease in cell efficiency is observed for Cz-B-doped silicon, in line with previous studies [41]. Again, a qualitative agreement is obtained for the J_{oi} behaviour of the Cz-Ga samples, showing a relative (absolute) decrease of 5% ($\sim 5 \text{ fA}/\text{cm}^2$) to 10% ($\sim 10 \text{ fA}/\text{cm}^2$) with increasing resistivity from tail (Sec 1) to top (Sec 4). This trend is consistent with the SRH analysis for Cz-Ga in Fig. 7, which shows an increase in the reduction in material saturation current $j_{\text{o,mat}}$ with increasing base resistivity upon (partial) dissociation.

In summary, it is inferred from experimental I – V data (before and after light soaking), as well as from lifetime data, that bulk recombination in Cz-Ga-doped PERC cells under normal operating conditions (i.e. exposure to light) is strongly influenced by interstitial iron in its dissociated state. In the case of Cz-B, an even more dominating, additional background defect limits the bulk lifetime in Cz-B-doped PERC cells to levels below the Fe_i -limited lifetime – even

after regeneration. As a result, the experimental findings suggest superior bulk properties in Cz-Ga over Cz-B in a regenerated state, assuming sufficient Fe-gettering efficiency and sufficiently low Fe_i contamination arising from industrial solar cell production lines.

Given the oversimplified interpretation of the observed results, postulating Fe_i to be the lifetime-limiting SRH defect in our Cz-Ga PERC solar cells, it is suggested that future experimental studies follow (for *practically relevant* experimental investigations of carrier lifetime-limiting defects in Cz-B/Cz-Ga base materials) the methodology outlined in this section. In other words, the I – V parameters as well as correlated bulk carrier lifetimes as measured in a post-cell-process condition including regeneration should be investigated, rather than lifetime samples which have not been exposed to the thermal budget and the contamination load associated with a full cell process sequence. In addition, for an improved interpretation of the experimental I – V results and the impact of $j_{\text{o,mat}}$, numerical simulations should be applied in order to accurately single out the contribution of $j_{\text{o,mat}}$ to $V_{\text{oc}}/J_{\text{oi}}$.

PERC $\text{SiO}_x\text{N}_y/\text{SiN}_x$ – bifacial: overall performance assessment and joint optimization of front/rear side

Following the industrialization of PERC solar cells in 2012 and onwards, well ahead of the industry, SolarWorld conceived and industrialized another innovative product technology, namely a PERC-based bifacial solar cell, recognizing PERC to be a potential door opener for a highly cost-effective bifacial solar cell. Technology development and business case assessment of the PERC bifacial variant was initiated by the R&D unit at SolarWorld at the beginning of 2014 [43], and has since been adopted by research institutes and several Tier 1 solar cell manufacturers alike [44,45].

Design modifications

Three simple design modifications of the cell rear side are needed in order to derive a PERC bifacial solar cell from the PERC monofacial variant. First, the rear-side dielectric layer stack is adapted for improved rear-side optics (depending on the stack design of the monofacial reference, this may be an optional measure). Second, the full-area rear Al metallization is replaced by a screen-printed Al grid. Third, the LCO pattern is adjusted for optimum overall bifacial performance, since the LCO/Al-finger pitch defines rear-side shading, and the LCO dimensions affect Al-BSF formation at the contact.

As a potential fourth design change, texturing of the rear side can be applied; this is prohibitive for $\text{SiO}_x\text{N}_y/\text{SiN}_x$ rear passivation, which requires a polished surface to ensure good passivation. Similarly, for $\text{AlO}_x/\text{SiN}_x$ rear passivation deposited

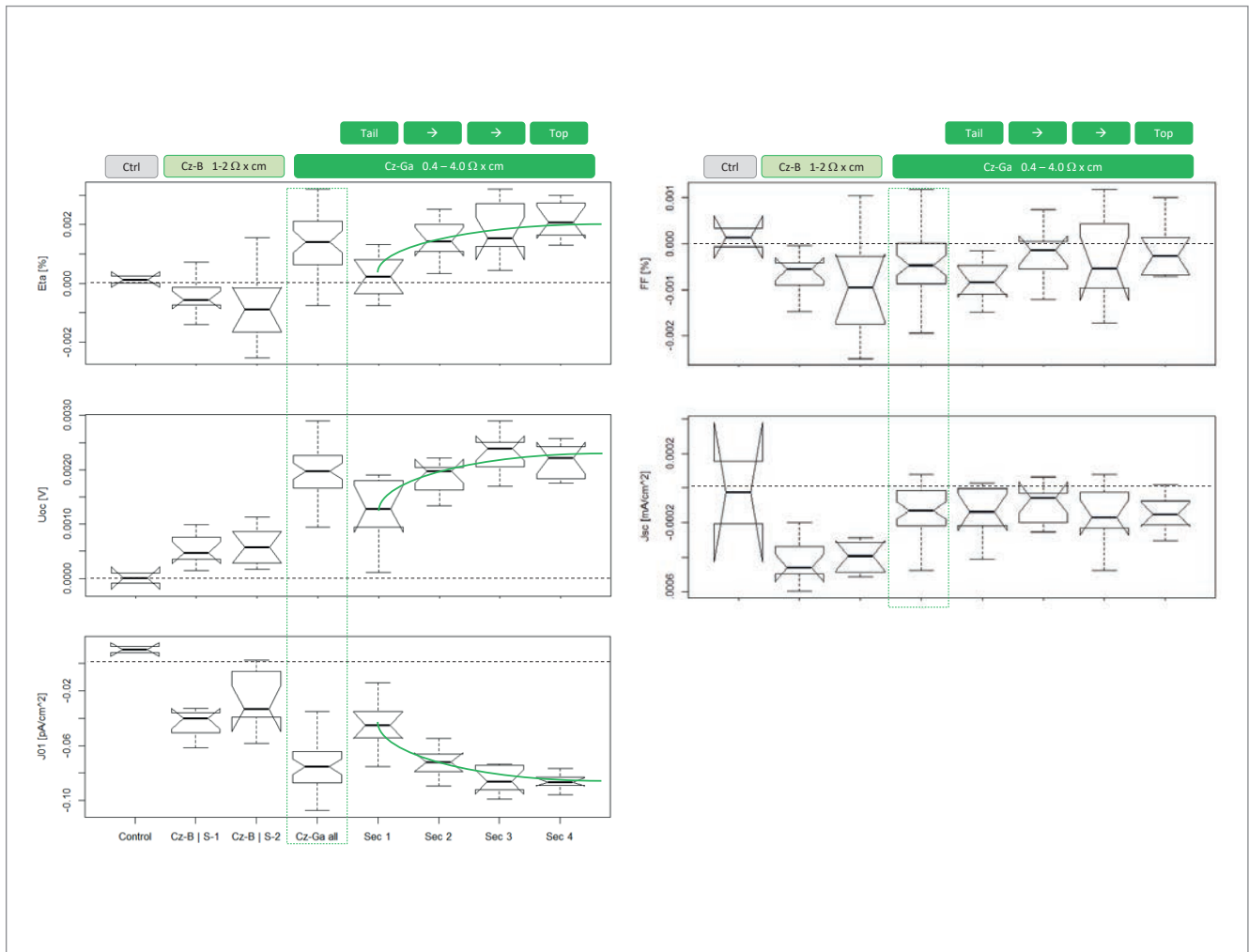


Figure 8. Relative changes in selected I - V parameters after light soaking under 1 Sun for 10 sec., leading to *partial* dissociation of Fe-acceptor pairs (note that the original units of the I - V parameters are indicated in the axis labels, although the relative change $\%_{rel}$ is shown). Controls are used to ensure that the small observed effects are real.

by remote PECVD, experimental investigations (carried out on SolarWorld's PERC AlO_x production line in collaboration with Fraunhofer ISE, comparing polished and textured rear surfaces) have shown that a textured rear side significantly decreases the front-side efficiency of a PERC $\text{AlO}_x/\text{SiN}_x$ bifacial solar cell because of increased light escape from the rear ($J_{sc} \downarrow$) and deteriorating rear passivation ($V_{oc} \downarrow$). As a result, texturing of the rear side for PERC bifacial cells is only suited to high-albedo applications [46].

Metrology

While the above-mentioned design changes are fairly straightforward to implement without additional equipment, the assessment and comparability of bifacial cell I - V performance remains up until now non-trivial: measurement techniques and normative rules are still under development [47], and individually chosen I - V measurement hardware hinders apple-to-apple comparisons. Particularly misleading – yet still unfortunately in use – are I - V measurements using a reflective brass chuck [44]. The use of a reflective chuck leads to an increased short-

circuit current (as compared to the use of an absorbent black chuck) and increased fill factors (as compared to the use of contacting bars), since the ohmic resistance of the Al grid (GridRes) is essentially nulled. The main loss channels of a bifacial cell design – transmission losses as well as additional ohmic losses – are (over-)compensated in such a cell I - V measurement, which is thus not suitable for bifacial cell design optimization.

Furthermore, in an effort to publish record front- or rear-side efficiencies, bifacial cell designs which are optimized for either front- or rear-side performance and only front- or rear-side efficiency – but not both simultaneously – are reported [44]. Yet, a practically relevant bifacial solar cell design requires joint optimization of front- and rear-side cell efficiencies, which is ideally developed on the basis of an I - V measurement setup that:

1. simultaneously applies front-side (1.0 kW/m^2) and adjustable rear-side ($0.X\text{ kW/m}^2$) illumination in a double-side measurement, mimicking defined carrier injection levels under bifacial cell operating conditions [46,48];

2. employs a contacting scheme that mimics the resistive cell losses as imposed by a given cell interconnection technology (e.g. five contacting bars for tabbing and stringing of 5BB cells).

Single front-side I - V measurements with a black/absorbing background for simplified inline applications are suggested within the ' G_E method', which employs a front-side irradiance of $G_E = 1,000 \text{ W/m}^2 + \phi_{j_{sc}} \times G_R$. Here, G_R is typically chosen within 0 to 200 W/m^2 and $\phi_{j_{sc}}$ denotes the bifaciality coefficient for the short-circuit current $\phi_{j_{sc}} = J_{sc}^{\text{rear}} / J_{sc}^{\text{front}}$. Deviations of the G_E method from a more extensive and accurate two-side measurement are mainly due to cell-to-cell bifaciality variations (since a fixed $\phi_{j_{sc}}$ is assumed). The impact of potential nonlinearity of the cell's irradiance/injection dependence has also been considered [49]. It is recommended that two-side measurements are applied in order to validate and thus qualify the G_E method for a given cell type and manufacturing process.

Bifacial cell design rules

As bifacial cell, module and system applications become more sophisticated, future design rules will be developed at the cell, module [45] and system levels as a function of the expected albedo of the particular PV system under consideration. At the cell level, reflection of the rear-side stack and metal shading are clearly the relevant design parameters for rear-side performance tuning; these parameters can be adjusted via rear stack layer thicknesses, LCO pitch and Al-finger width. Optimizing rear-side efficiency is, in general, contrary to front-side optimization, and so a design compromise needs to be made, ideally depending on the expected albedo.

On the basis of the final mono- and bifacial PERC $\text{SiO}_x\text{N}_y/\text{SiN}_z$ design chosen in the R&D baseline process at SolarWorld (design/process BKM 05/2018), the limitations of 5BB p-type PERC bifacial solar cells are addressed with regard to 1) inevitable front-side efficiency losses compared with 5BB p-type PERC monofacial, and 2) rear-side efficiency, and thus bifaciality limitations, as imposed by the optical properties of the rear side.

Front-side efficiency losses: 5BB PERC $\text{SiO}_x\text{N}_y/\text{SiN}_z$ bifacial vs. 5BB PERC $\text{SiO}_x\text{N}_y/\text{SiN}_z$ monofacial

In order to separate the impact of the above-mentioned design modifications on front-side efficiency losses, an experimental run was carried out including three cell types: 1) PERC monofacial reference; 2) PERC bifacial-1, exhibiting the same rear-side stack as the PERC monofacial reference; and 3) PERC bifacial-2, exhibiting a rear-side $\text{SiO}_x\text{N}_y/\text{SiN}_z$ stack optimized for bifacial performance for which the SiN_z capping was

"A practically relevant bifacial solar cell design requires joint optimization of front- and rear-side cell efficiencies."

significantly reduced. Compared with the monofacial reference, a different, more viscous, Al paste was applied for printing the Al grid on both PERC bifacial-1 and PERC bifacial-2. All other single processes not mentioned are the same for all three cell batches; in particular, the same dashed LCO layout was used for all three cell types.

Fig. 9 depicts the resulting pareto analysis of front-side efficiency losses for the 5BB PERC bifacial solar cells with respect to the 5BB PERC monofacial reference solar cell. I - V measurements are carried out using contacting bars (pins) on the front and rear sides. The rear side is fully absorbent (black cloth). CalLab certified reference cells are used for separate calibration of the I - V measurements on monofacial and bifacial solar cells. FF losses are split into purely resistive losses (FF_{R_s}) and pure pFF losses; the sum of both corresponds to the overall FF loss.

As can be seen in Fig. 9, an overall relative loss of $1.5\%_{\text{rel}}$ front-side efficiency already occurs with the printing of an Al grid instead of a full-area Al rear. The relative FF_{R_s} loss is in good correspondence with the increase in the rear (grid) resistance in the I - V measurement. An analytical estimate of the Al rear (grid) resistance based on measured Al finger cross sections is well in line with the observed FF_{R_s} loss.

Losses are also present for $V_{oc} / J_{sc} / pFF$, which increase with decreasing thickness of the SiN_z capping. The comparison of PERC bifacial-1 and PERC bifacial-2 reveals a reduction in rear-passivation quality and in increased light escape as the SiN_z -capping thickness is reduced. The pFF losses are not understood in detail, although it is assumed that inferior local Al-BSF formation when printing an Al grid instead of a full-area Al rear is the driving source. Contrary to the findings in Kranz et al. [50], an inferior quality of the Al-BSF formed in the case of an Al grid print is conjectured from the I - V data in the SolarWorld experiments. This is supported by PL V_{oc} images, which show higher recombination activity of the local Al-BSF when compared with a full-area Al metallization. Note that, in contrast to Kranz et al. [50], a different rear-side dielectric ($\text{SiO}_x\text{N}_y/\text{SiN}_z$) and LCO (dash) design was applied in SolarWorld's implementation. The intricate interplay between rear-side dielectric, LCO-process and LCO-feature size, Al paste and Al laydown, as well as firing conditions, critically affects the Al-Si alloying process and thus the quality of the formed local Al-BSF. This topic will remain crucial to further development of local Al-BSF formation in the PERC bifacial concept based on LCO and Al grid screen printing.

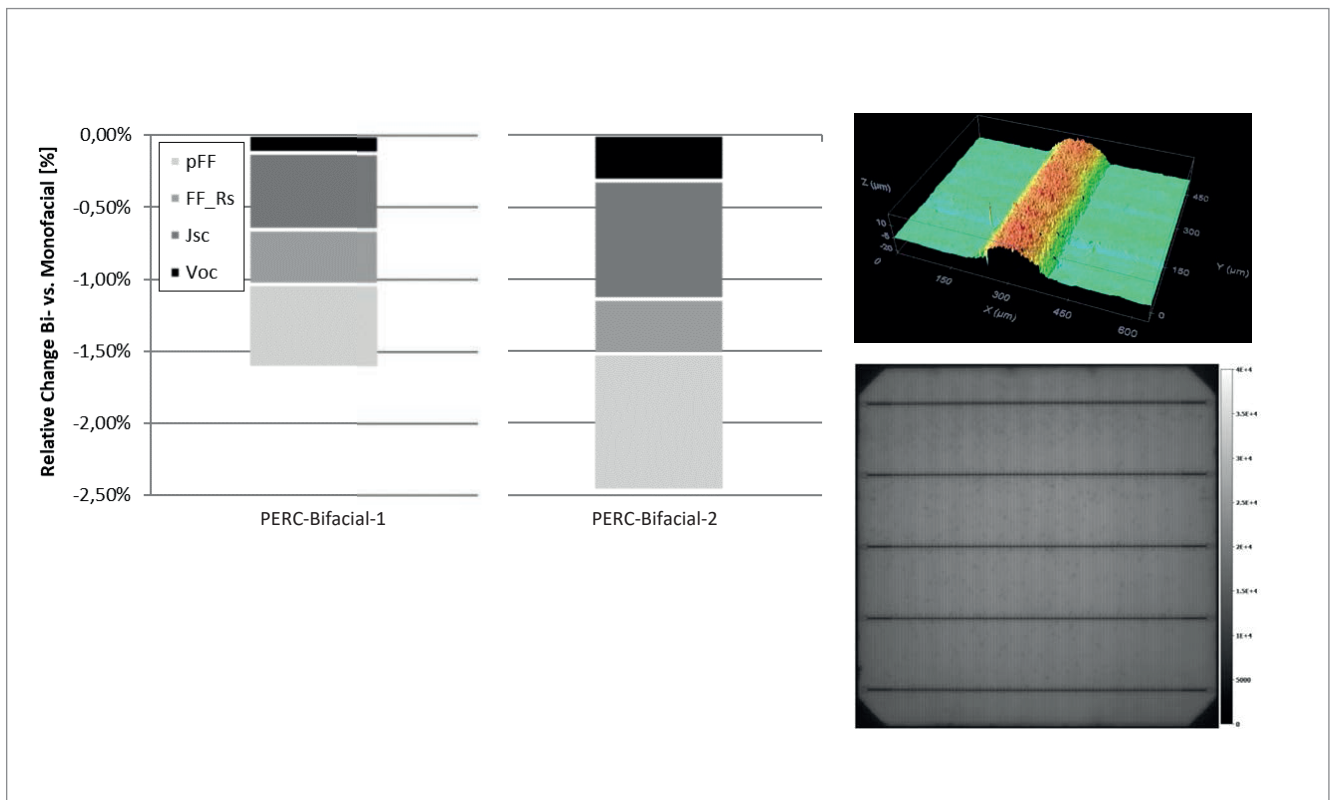


Figure 9. Pareto analysis of front-side efficiency losses for 5BB PERC bifacial solar cells with respect to 5BB PERC monofacial solar cells (BKM 05/2018)]. *I-V* measurements are carried out using contacting bars (pins) on the front and rear sides. The rear side is fully absorbent (black cloth). Callab-certified reference cells are used for separate calibration of the *I-V* measurements on monofacial and bifacial solar cells.

- Rear Stack – 1 applied for PERC Bifacial-1 is identical to the rear-side stack of the PERC monofacial reference.
- Rear Stack – 2 applied for PERC Bifacial-2 is an adapted rear-side stack optimized for bifacial performance.
- LCO-Layouts are identical to the PERC monofacial reference.

The insets show a 3D scan of an Al finger using a confocal microscope and a PL V_{oc} image of a bifacial solar cell exhibiting black dots (increased non-radiative recombination) in the LCO regions. Note that this feature is not observed for PERC monofacial reference cells.

Rear-side efficiency/bifaciality limitations of PERC $\text{SiO}_x\text{N}_y/\text{SiN}_2$ bifacial solar cells

‘Classical’ implementations of bifacial solar cells – for example, n-type heterojunction (HJT) pioneered by Sanyo, or n/p-type passivated emitter and rear totally diffused (PERT) cells first brought into mass production by Yingli [45] – feature a full-area BSF (for a front-junction cell) or emitter (for a rear-junction cell) on the rear side; in both cases, this allows passivation functionality to be decoupled from optical functionality (anti-reflection) for the rear-side dielectric to a larger extent. Furthermore, a pyramidal texture can be applied to the rear side in these cell concepts, which allows a high bifaciality in excess of 90%.

In the case of the p-type PERC bifacial cell concept, the rear dielectric needs to simultaneously fulfil passivation and optical requirements. Consequently, a design compromise needs to be made. First and foremost, since texturing of the rear side significantly deteriorates rear-side passivation and internal light reflection in p-type PERC bifacial solar cells, *planar rear* sides are typically in use. Furthermore, since passivation quality deteriorates with decreasing thickness of the SiN_2 capping, the optical thickness of the rear stack is not fully optimized for rear light

absorption. Consequently, light-capturing from the rear is inherently limited in PERC bifacial.

Another limitation of p-type PERC bifacial is imposed by the use of Al pastes for screen printing instead of Ag pastes, as in the above-mentioned bifacial cell concepts. Given the inferior fine-line printing capability and the increased resistivity of screen-printed Al fingers (finger width $\sim 100\mu\text{m}$; resistivity $\sim 20\mu\Omega\text{cm}$) when compared with state-of-the-art Ag paste screen printing (finger width $\sim 30\mu\text{m}$; resistivity $\sim 3\mu\Omega\text{cm}$), the rear Al metallization fraction, and thus metal shading, in p-type PERC bifacial is comparably high.

Fig. 10 shows the bifaciality limits as imposed by 1) the reflection-limited external quantum efficiency (EQE) of the planar rear side (stack analogous to PERC bifacial-2), and 2) the Al metallization. Note that the reflection spectrum of a typical $\text{AlO}_x/\text{SiN}_2$ stack (10nm/100nm) on a planar rear side exhibits a very similar profile to that of the $\text{SiO}_x\text{N}_y/\text{SiN}_2$ stack shown.

A 5BB Al layout with a $\sim 1.0/1.3\text{mm}$ pitch (corresponding to 156/120 Al fingers) and roughly 8.5% Al coverage from the busbars gives rise to a bifaciality of 65%/70% at $200\mu\text{m}$ as-printed finger width. The high Al coverage/width associated with the busbars was necessary in order to

account for the very low tab-positioning accuracy on the cell rear side of the stringers available at SolarWorld's module manufacturing. Clearly, measurements of the efficiency for bifacial cells using a reflective brass chuck eliminate the resistive losses of the rear Al grid, and finer Al fingers can, in principle, be printed to showcase increased bifaciality using such a measurement configuration without significant FF losses in the measurement.

Of practical relevance is the switch to multiwire technology, as it allows the elimination of the rear busbars [45] and thinner Al fingers without sacrificing FF as in the 5BB case; this leads to bifacialities exceeding 80% as shown in Fig. 10. As outlined in Dullweber et al. [44] and Nussbaumer et al. [45], the switch to half cells is even more advantageous for bifacial solar cells than for monofacial ones, given the higher operating cell currents, and consequently the increased ohmic losses, for bifacial solar cells. It is therefore clear that PERC bifacial will promote the use of multiwire interconnection and half-cell technology. Even though bifaciality will remain

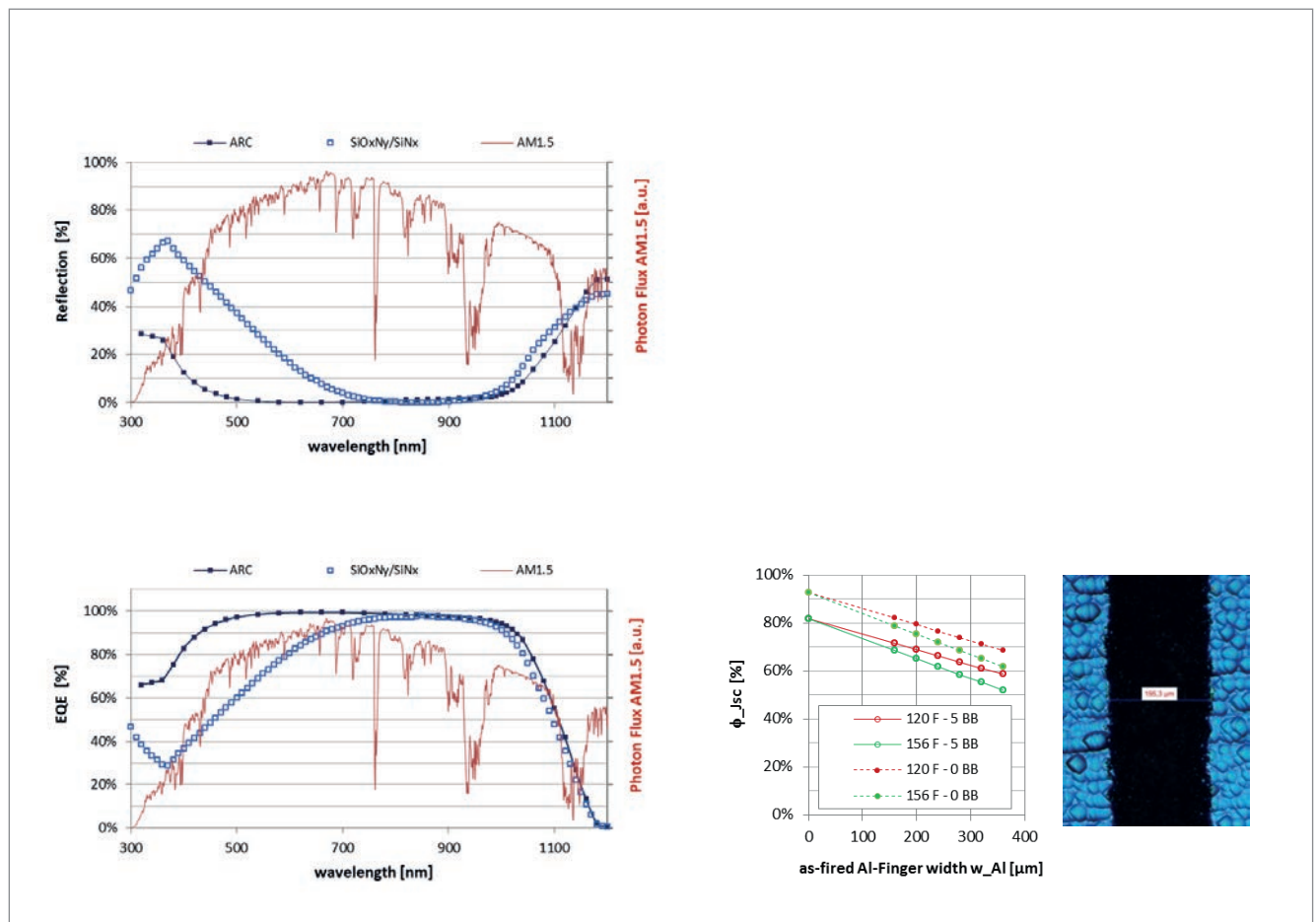
comparably low at 80–85%, the authors believe that PERC bifacial will continue to outperform as a low-cost bifacial solution for typical albedo values in the mid-term.

Summary and outlook

It took more than 20 years to transfer the PERC cell concept from lab to fab [51]. The PERC cell has only been able to enter mass production thanks to 1) equipment suppliers providing the necessary key technologies for *industrially viable* process implementation (most importantly PECVD for rear-side passivation [7,8]), and 2) material suppliers developing Al screen-printing pastes designed for effective local Al-BSF formation. Only as a result of these developments has a simple and cost-effective implementation of PERC solar cells been possible. As an integrated PV module manufacturer, SolarWorld anticipated and significantly contributed to three technology trends which have been guiding the industrial solar cell roadmap since 2012:

- Introduction and process integration of PERC technology in mass production.

Figure 10. Bifaciality limiting factors. Reflection and external quantum efficiency (EQE) spectra for a planar rear side and a $\text{SiO}_2\text{N}_y/\text{SiN}_x$ stack optimized for bifacial performance. For reference, the corresponding spectra are also shown for the front-side ARC on a pyramidal texture ($\text{SiO}_2/\text{SiN}_x$). Compared with the monofacial $\text{SiO}_2\text{N}_y/\text{SiN}_x$ stack, the SiN_x capping for the bifacial cell is significantly thinner to allow improved light capture. Short-circuit currents for the front and rear sides are calculated from the EQE spectra to obtain a 'metallization free' bifaciality with an optical limit of $\phi_{\text{Jsc, optical}} \sim 86\text{--}88\%$. Adding metallization on the front ($f_{\text{met}} \sim 4.0\%$) and rear ($f_{\text{met 5BB}} \sim 8.5\%$) allows the calculation of cell bifaciality as a function of as-printed Al finger width for 5BB and OBB configurations. Note that 'effective' metal finger widths need to be applied after cell encapsulation, accounting for light-trapping effects in the module.



- Introduction of a highly cost-effective PERC-based bifacial solar cell in mass production.
- Conversion from multi- towards monocrystalline wafers, to fully leverage the efficiency potential of PERC [52].

With regard to further increasing the efficiency of p-type PERC solar cells and modules in the short term, the authors foresee the following.

Crystal: gallium – the preferred dopant

On the basis of SolarWorld's investigations of Cz-Ga wafers, further material benchmarks are recommended by comparing CCz-Ga/RCz-Ga and CCz-B/RCz-B technologies with respect to lifetime-limiting defects in *regenerated* solar cells. Monocrystalline Ga, e.g. ideally based on CCz technology, is considered to be a leap in technology that will finally enter mass production.

Cell: selective emitter – certainly, but which technical implementation?

The necessity for introducing selective emitter technology is the general consensus in the context of the 24% PERC roadmap [53]. The more pressing question relates to the preferred technical implementation of SE, and the respective trade-off between efficiency potential and process complexity. Selective etch-back exhibits an inherent advantage over laser doping from PSG with regard to reduced emitter saturation currents in the n^+ region (given the efficient removal of inactive phosphorus), as well as the n^{++} regions (given the avoidance of potential laser damage) [54]. Nevertheless, the process complexity of selective etch-back is higher. The authors consider the choice of SE implementation to be still an open topic and expect technology selection to take place.

Cell: emitter passivation – $\text{SiO}_2/\text{SiN}_x$

Thermal oxidation for n^+ -type emitters will become widespread.

Cell: rear passivation – cannot beat CVD

With rear passivation representing the smallest loss channel in current 22.0%-efficient p-type Cz PERC solar cells, there is little motivation at the moment to abandon well-established PECVD-based

$\text{AlO}_x/\text{SiN}_2$ deposition and to shift towards, for example, atomic layer deposition (ALD) for Al_2O_3 deposition. On the contrary, CVD offers the flexibility 1) to be used in n-type solar cells using adapted $\text{AlO}_x/\text{SiN}_2$ stacks for the

passivation of p^+ -type emitters, or 2) to deposit doped a-Si (PECVD) or poly-Si (LPCVD) layers for the implementation of passivating contacts. The potential option to derive classical n-type PERC cells or p/n-type PERT-like cells employing passivating contacts with the use of existing equipment from current p-type PERC solar cell lines makes PECVD the preferred and compelling process choice for the time being.

Cell: Metallization – active alignment will become standard

With 1) SE becoming the standard and 2) PERC bifacial shares predicted to increase, screen printers with in situ recognition of contact features (e.g. highly-doped regions or local contact openings) and active alignment capability will become standard.

Module: PERC bifacial = accelerating catalyst for multiwire and half-cell module technology

Multiwire technology alleviates the problem of increased ohmic losses in PERC bifacial cells which result from increased Al grid resistance; multiwire therefore enables decreased FF losses at increased bifaciality. Half-cell technology, on the other hand, helps to reduce ohmic losses occurring within the interconnecting tabs/wires, and will be even more beneficial for bifacial modules, given their generally higher operating currents. As a result, PERC bifacial will act as a catalyst and push for an accelerated near-term adoption of multiwire, half-cell technology as well as glass-glass encapsulation, i.e. module technologies which SolarWorld has been pursuing since 2013 [22,55]. In addition, the multiwire approach will enable significant further reductions in front finger width and Ag paste consumption.

Before upcoming solar cell technology cycles in crystalline silicon PV (e.g. based on passivating contacts, including HJT as an industrially proven variant) and tandem solar cells later on are in full swing, PERC still holds incremental improvements up its sleeve in crystal, cell and module production technologies which will allow cell efficiencies *in mass production* to be pushed towards 24% [53].

Acknowledgements

The authors would like to give credit to the former SolarWorld staff from R&D, engineering, production, quality assurance, procurement and management responsible for the pioneering work on industrializing PERC technology at SolarWorld, as well as the universities, R&D institutes, key equipment and material manufacturers for their support on this path. We would like to acknowledge our former colleagues in R&D and production transfer: G. Erfurt, E. Schneiderlöchner, A. Münzer, K.-H. Stegemann, M. Wagner, P. Müller, L. Sylla, U. Kirpal, B. Bitnar, R.

“PERC still holds incremental improvements up its sleeve in crystal, cell and module technologies which will allow cell efficiencies *in mass production* to be pushed towards 24%.”

Schiepe, P. Richter, S. Gatz, H. Sträter, G. Citarella, C. Merkwitz, A. Fülle, M. Kutzer, M. Georgi, N. Stoddard, E. Good, G. Grupp-Müller, S. Yamanaka, D. Palko, S. Pecis, M. Dulani, A. Rolle, C. Bellmann, U. Mareck, D. Stichtenoth, M. Kipping, T. Roth, A. Froitzheim, K. Kubitz, H. Reetz, L. Oberbeck and the entire team operating the R&D cell pilot line in Freiberg. We would like to thank and give credit to our former R&D partners at the Fraunhofer Institute for Solar Energy Systems ISE, University of Konstanz, Institute for Solar Energy Research in Hamelin (ISFH) as well as our equipment (Centrotherm, Meyer & Burger Germany, Gebr. Schmid, Rena, InnoLas, Asys) and material (Heraeus, Toyo, GigaSolar, Namics, h.a.l.m., USK and 3D Micromac) suppliers, all having done their part in pushing the limits of industrially viable PERC technology. Last, but not least, we would like to thank the Federal Ministry of Economic Affairs and Energy (BMWi) for the funding of PERC solar cell development within the SONNE (FKZ: 0325277A), HELENE (FKZ: 0325777A) and LAURA (FKZ: 0325716A) research projects.

References

- [1] IRENA 2015, "Renewable capacity statistics 2015", International Renewable Energy Agency (IRENA), Abu Dhabi.
- [2] IRENA 2018, "Renewable capacity statistics 2018", International Renewable Energy Agency (IRENA), Abu Dhabi.
- [3] BNEF 2018, "New Energy Outlook 2018: BNEF experience curve for crystalline-silicon PV module prices".
- [4] ITRPV 2018, "International technology roadmap for photovoltaic (ITRPV): 2017 results", 9th edn (Mar.) [<http://www.itrpv.net/Reports/Downloads/>].
- [5] Weber, T. et al. 2013, "High volume pilot production of high efficiency PERC solar cells – Analysis based on device simulation", *Energy Procedia*, Vol. 38, pp. 474–481.
- [6] Chunduri, S.K. et al. 2018, "PERC solar cell technology 2018 edition, PERC+: How to improve high efficiency crystalline solar cells", TaiyangNews.
- [7] Sperlich, H.-P. et al. 2010, "High productive solar cell passivation on Roth&Rau MAiA[®] MW-PECVD inline machine – A comparison of Al₂O₃, SiO₂ and SiN_x-H process conditions and performance", *Proc. 25th EU PVSEC*, Valencia, Spain.
- [8] Münzer, K.A. et al. 2012, "Technical performance and industrial implementation in favour of centaurus technology", *Energy Procedia*, Vol. 27, pp. 631–637.
- [9] Preu, R. et al. 2000, "Laser ablation – A new low-cost approach for passivated rear contact formation in crystalline silicon solar cell technology", *Proc. 16th EU PVSEC*, Glasgow, Scotland.
- [10] Agostinelli, G. et al. 2005, "Local contact structures for industrial PERC-type solar cells", *Proc. 20th EU PVSEC*, Barcelona, Spain.
- [11] Agostinelli, G. et al. 2005, "Screen printed large area crystalline silicon solar cells on thin substrates", *Proc. 20th EU PVSEC*, Barcelona, Spain.
- [12] Schneiderlöchner, E. et al. 2002, "Laser-fired rear contacts for crystalline silicon solar cells", *Prog. Photovolt: Res. Appl.*, Vol. 10, pp. 29–34.
- [13] Boschke, T. et al. 2011, "Fully screen-printed PERC cells with laser-fired contacts – An industrial cell concept with 19,5% efficiency", *Proc. 37th IEEE PVSC*, Seattle, Washington, USA, pp. 3663–3666.
- [14] Dastgheib-Shirazi, A. et al. 2013, "Relationships between diffusion parameters and phosphorus precipitation during the POCl₃ diffusion process", *Energy Procedia*, Vol. 38, pp. 254–262.
- [15] Fischer, G. et al. 2015, "Model based continuous improvement of industrial p-type PERC technology beyond 21% efficiency", *Energy Procedia*, Vol. 77, pp. 515–519.
- [16] Röder, T.C. et al. 2010, "Add-on laser tailored selective emitter solar cells", *Prog. Photovolt: Res. Appl.*, Vol. 18, pp. 505–510.
- [17] Yamanaka, S. et al. 2012, "Optical transparency and surface recombination considerations for high sheet resistance emitter passivation on silicon solar cells", *Proc. 38th IEEE PVSC*, Austin, Texas, USA, pp. 001166–001171.
- [18] Müller, M. et al. 2017, "Loss analysis of 22% efficient industrial PERC solar cells", *Energy Procedia*, Vol. 124, pp. 131–137.
- [19] HELENE research project, under Contract No. 0325777.
- [20] Zhou, T. et al. 2016, "Different dielectrics deposited by PECVD for the industrial manufacturing of PERC solar cells", *Proc. 31st EU PVSEC*, Hamburg, Germany.
- [21] Richter, P.L. et al. 2015, "Progress in fine-line metallization by co-extrusion printing on cast monosilicon PERC solar cells", *Sol. Energy Mater. Sol. Cells*, Vol. 142, pp. 18–23.
- [22] Schaarschmidt, M. et al. 2011, "Method for contacting and connecting solar cells and solar cell combination produced by means of said method", Patent WO/2011/147388.
- [23] Müller, M. 2016, "Reporting effective lifetimes at solar cell relevant injection densities", *Energy Procedia*, Vol. 92, pp. 138–144.
- [24] Wolny, F. et al. 2017, "Study of the bulk lifetime and material saturation current density of different p-type monocrystalline silicon materials", *Energy Procedia*, Vol. 124, pp. 235–239.
- [25] Krause, A. et al. 2016, "Plastic deformation as an origin of dislocations in cast mono", *Energy Procedia*, Vol. 92, pp. 833–838.
- [26] Stoddard, N. et al. 2018, "NeoGrowth Silicon: A new high purity, low-oxygen crystal growth

- technique for photovoltaic substrates", *Prog. Photovoltaics: Res. Appl.*, Vol 26, pp. 324–331.
- [27] PV-Tech 2015, "SolarWorld touts 21.7% PERC world record efficiency", News Report, [https://www.pv-tech.org/news/solarworld_touts_21.7_perc_world_record_efficiency].
- [28] PV-Tech 2016, "SolarWorld reaches 22% efficiency in p-type PERC cell", News Report [https://www.pv-tech.org/news/solarworld-reaches-22-efficiency-in-p-type-perc-cell].
- [29] Schmidt, J. et al. 1997, "Investigation of carrier lifetime instabilities in Cz-grown silicon", *Proc. 26th IEEE PVSC*, Anaheim, California, USA, pp. 13–18.
- [30] Glunz, S.W. et al. 1999, "Comparison of boron-doped and gallium-doped p-type Czochralski silicon for photovoltaic application", *Prog. Photovoltaics: Res. Appl.*, Vol 7, pp. 463–469.
- [31] Tadashi, S. et al. 2000, "Overview of light degradation research on crystalline silicon solar cells", *Prog. Photovoltaics: Res. Appl.*, Vol 8, pp. 537–547.
- [32] Lauermaier, T. et al. 2010, "Large area solar cells made from degradation-free, low resistivity gallium doped Cz wafers", *Proc. 25th EU PVSEC*, Valencia, Spain.
- [33] Fertig, F. et al. 2017, "Mass production of p-type Cz silicon solar cells approaching average stable conversion efficiencies of 22 %", *Energy Procedia*, Vol. 124, pp. 338–345.
- [34] Walter, D. et al. 2016, "Realistic efficiency potential of next-generation industrial Czochralski-grown silicon solar cells after deactivation of the boron-oxygen-related defect center", *Prog. Photovoltaics: Res. Appl.*, Vol 24, pp. 920–928.
- [35] Weber, E.R. 1983, "Transition metals in silicon", *Appl. Phys. A*, Vol. 30, No. 1, pp. 1–22 [https://doi.org/10.1007/BF00617708].
- [36] Ludwig, G.W. & Woodbury, H.H. 1962, "Electron spin resonance in semiconductors", *Solid State Phys.*, Vol. 13, pp. 223–304.
- [37] Istratov, A., Hieslmair, H. & Weber, E. 1999, "Iron and its complexes in silicon", *Appl. Phys. A*, Vol. 69, No. 1, pp. 13–44 [https://doi.org/10.1007/s003390050968].
- [38] Macdonald, D. et al. 2004, "Iron detection in crystalline silicon by carrier lifetime measurements for arbitrary injection and doping", *J. Appl. Phys.*, Vol. 95, 1021.
- [39] Macdonald, D. et al. 2005, "Formation of iron-acceptor pairs in crystalline silicon", *J. Appl. Phys.*, Vol. 98, 083509.
- [40] Schmidt, J. & Macdonald, D. 2005, "Recombination activity of iron-gallium and iron-indium pairs in silicon", *J. Appl. Phys.*, Vol. 97, 113712.
- [41] Schmidt, J. 2005, "Effect of dissociation of iron-boron pairs in crystalline silicon on solar cell properties", *Prog. Photovoltaics: Res. Appl.*, Vol 13, pp. 325–331.
- [42] Naerland, T. et al. 2017, "On the recombination centers of iron-gallium pairs in Ga-doped silicon", *J. Appl. Phys.*, Vol. 122, 085703.
- [43] Handelsblatt 2014, "Asbeck versucht Neustart: Ex-Sonnenkönig kündigt neue Modultechnik an", Press Release [http://www.genios.de/presse-archiv/artikel/HB/20141215/asbeck-versucht-neustart/6E27CF9D-B436-48EF-9CEA-EFC3080CD8F5.html].
- [44] Dullweber, T. et al. 2018, "Industrial implementation of bifacial PERC+ solar cells and modules: Present status and future opportunities", *Photovoltaics International*, 38th edn, pp. 46–55.
- [45] Nussbaumer, H. et al. 2018, "State-of-the-art bifacial module technology", *PV Tech Power*, Vol. 16, pp. 60–80.
- [46] Wöhrle, N. et al. 2017, "Understanding the rear-side layout of p-doped bifacial PERC solar cells with simulation driven experiments", *Energy Procedia*, Vol. 124, pp. 225–234.
- [47] Fakhfour, V. 2016, "IEC 60904-1-2: Measurement of current-voltage characteristics of bifacial photovoltaic devices", 3rd Bifi PV Workshop, Miyazaki, Japan.
- [48] Ramspeck, K. et al. 2017, "Measurement techniques for bifacial solar cells", 4th Bifi PV Workshop, Konstanz, Germany.
- [49] Rauer, M. et al. 2017, "Bifacial solar cells under single- and double-sided illumination: Effect of non-linearity in short-circuit current", 4th Bifi PV Workshop, Konstanz, Germany.
- [50] Kranz, C. et al. 2016, "Analysis of local aluminum rear contacts of bifacial PERC+ solar cells", *IEEE J. Photovolt.*, Vol. 6, No. 4, pp. 830–836.
- [51] Blakers, A.W. 1989, "22.8% efficient silicon solar cell", *Appl. Phys. Lett.*, Vol. 55, No. 13, pp. 1363–1365.
- [52] Colville, F. 2018, "China-531 to accelerate demise of multi; polysilicon consumption decline to 3g/W by 2022", PV Tech News Report (Sep).
- [53] Min, B. et al. 2017, "A roadmap toward 24% efficient PERC solar cells in industrial mass production", *IEEE J. Photovolt.*, Vol. 7, pp. 1541–1550.
- [54] Ye, F. et al. 2016, "22.13% efficient industrial p-type mono PERC solar cell", DOI: 10.1109/PVSC.2016.7750289.
- [55] BINE-Projektinfo 10/2013, ISSN 0937-8367, "Development of high-efficiency solar cells and modules" [http://www.bine.info/fileadmin/content/Presse/Projektinfos_2013/PM_10_2013/ProjektInfo_1013_engl_internetx.pdf].

About the Authors



Phedon Palinginis joined SolarWorld in 2006 and has led the solar cell development group since 2015, with a focus on monocrystalline p-type PERC technology. Prior to that, he was in charge of technology assessment and selection over the entire c-Si PV value chain. Phedon holds

a diploma degree in physics from the University of Karlsruhe and has worked as a doctoral and postdoctoral researcher at the University of Oregon and the University of California Berkeley respectively, on nonlinear optical properties of compound semiconductor nanostructures.



Christian Kusterer received his doctorate in 2006 from the University of Bonn, with a thesis in solid state chemistry. He joined SolarWorld in 2007, and since 2011 he has been responsible for the development and improvement of wet chemistry processes for solar cell processing, including the suppression of process-related contamination sources. Christian has been heavily involved in assessing alternative etching technologies, equipment and processes within feasibility, prototyping and technology transfer, as well as production ramp-up projects.



Stefan Steckemetz received his diploma degree in technical physics from the University of Applied Sciences Aachen in 1993. He then worked on crystalline silicon solar cells at ISFH and Sunways AG, before joining SolarWorld in 2006, where he has been focusing on screen-printing metallization for high-efficiency solar cells in production and R&D. In parallel, Stefan has been investigating and assessing dual/double screen printing as well as extrusion and stencil printing as metallization technology alternatives.

René Köhler joined SolarWorld in 2010. Working within the solar cell development group at SolarWorld, he was responsible for the process development of thin-film coatings and high-temperature processes. Before he joined SolarWorld, he worked in the field of amorphous silicon/crystalline silicon heterojunction solar cells. He holds a diploma degree in technical physics from the Technical University of Ilmenau.

René Härtwig joined SolarWorld in 2002. As an industrial specialist in the field of mechatronics, he first worked as shift supervisor at the solar cell manufacturing site in Freiberg from 2003 until 2012, before taking over the lead of solar cell pilot line operations within R&D in 2012. René and his team ensured stable baseline operation and highly reliable execution of experiments on the R&D pilot line.



Torsten Weber received his diploma degree in physics from the University of Hanover in 2006. He then joined SolarWorld as a senior R&D engineer and project manager, and was responsible for the transfer and integration of high-efficiency cell concepts from feasibility studies to high-volume manufacturing. He is now with Heliatek GmbH, where he focuses on process integration and yield enhancement of OPV.



Matthias Müller received his diploma degree in physics from Leipzig University in 2009, followed by his Ph.D. from Leibniz University Hannover in 2014. From 2007 he worked for Q-Cells SE, GP Inspect GmbH, Magdeburg-Stendal University of Applied Sciences and SolarWorld Innovations GmbH, before joining TU Bergakademie Freiberg in 2017 as the PV group leader at the Institute of Applied Physics. His field of research combines numerical device simulation with solar cell reliability and energy yield calculations.



Gerd Fischer received his Ph.D. in chemistry from TU Dresden. Prior to joining SolarWorld, he worked at Infineon and Qimonda. He joined SolarWorld Innovation in 2008 and worked as a project manager for PERC optimization. Gerd has been instrumental in introducing numerical device simulation for multi- and monocrystalline solar cells at SolarWorld. Since 2017 he has been a professor of inorganic chemistry at the University of Applied Sciences Zittau/Goerlitz.



Dirk Holger Neuhaus holds a Ph.D. from the University of New South Wales. He was a development engineer at Pacific Solar Pty Ltd., and worked for more than 15 years at SolarWorld, where he initially was responsible for quality assurance and technology in cell production, and later headed the global R&D activities along the entire value chain. Holger joined Fraunhofer ISE in 2018 and is in charge of module technology.

Enquiries

Phedon Palinginis
Email: phedon_pv@yahoo.com

Dirk Holger Neuhaus
Email: holger.neuhaus@ise.fraunhofer.de



June 16 - 21, 2019 | Chicago, IL

The PVSC brings together researchers, scientists, and technology leaders from industry, academia and government in an interactive environment conducive to strengthening collaborations and sharing knowledge across the field of photovoltaics. With a technical program focused on the leading advances in PV materials, devices and systems in conjunction with its industry exhibition, the PVSC provides an ideal forum to advance the scientific, technological, educational and business base of the international PV community. Topics include:

Area 1: Fundamentals and New Concepts for Future Technologies

Area 2: Chalcogenide Thin Film Solar Cells

Area 3: Multijunction and Concentrator Technologies

Area 4: Silicon Photovoltaic Materials and Devices

Area 5: Characterization Methods

Area 6: Perovskite and Organic Solar Cells

Area 7: Space and Specialty Technologies

Area 8: PV Modules Manufacturing and Applications

Area 9: PV Modules and System Reliability

Area 10: Power Electronics and Grid Integration

Area 11: Solar Resource and Forecasting

Area 12: PV Deployment, Policy and Sustainability

**OVER 900 TECHNICAL PRESENTATIONS
ARE EXPECTED, BE SURE TO JOIN US!**

**VISIT IEEE-PVSC.ORG
FOR MORE INFORMATION**

PVSC 46 WILL HOST A **VIBRANT
EXHIBITS FLOOR FOCUSED ON
TOOLS FOR THE PV SPECIALIST**



Low-cost standard nPERT solar cells towards 23% efficiency and 700mV voltage using Al paste technology

Radovan Kopecek¹, Zih-Wei Peng¹, Thomas Buck¹, Corrado Comparotto¹, Valentin D. Mihailetschi¹, Lejo J. Koduvelikulathu¹, Joris Libal¹, Jan Lossen¹, Masahiro Nakahara², Kosuke Tsuji², Marwan Dhamrin² & Wolfgang Jooss³

¹International Solar Energy Research Center (ISC) Konstanz, Germany; ²Hino Solar Laboratory, Core Technology Center, Toyo Aluminium K.K., Hino-cho, Japan; ³RCT Solutions GmbH, Konstanz, Germany

Abstract

Stable high voltages in solar cells and modules are becoming increasingly important as large PV systems are being set up in desert regions and are therefore exposed to high temperatures. High-voltage solar cells have lower temperature coefficients and thus produce a higher energy yield for such PV systems. Standard passivated emitter rear cell (PERC) devices have moderate voltages below 680mV, and also have the risk of degrading in such regions, because of light and elevated-temperature induced degradation (LeTID) effects and, in more recent observations, passivation degradation. This paper presents a solution for PERC producers to easily make the switch to n-type passivated emitter, rear totally diffused (nPERT) solar cells, which are capable of stable efficiencies above 22% and voltages close to 700mV, at almost no additional cost. This technology, called *MoSoN* (**Monocrystalline Solar cell on N-type**), merges the aluminium metallization technology from PERC with diffusion technology from nPERT (BiSoN). The adaptation of Al point contacts using the advanced Al-technology from Toyal for the rear side of the MoSoN cell leads to a rear point contact selective emitter and device voltages of around 695mV using n-type LONGi wafers. Further optimizations could even lead to voltages above 700mV. The cost of ownership (COO) is in the same range as that of standard PERC solar cells, even before the degradation in PERC has been taken into account, as the rear AlO_x (passivation) is replaced by BBr_3 diffusion (simultaneous diffusion and passivation by an in situ grown SiO_2 layer). In addition, no degradation of the passivating layers is observed in MoSoN cells, in contrast to PERC solar cells, where such effects have been recently observed.

on standard mc-Si Al-BSF technology. Fig. 1(a) shows the cell technology market share in 2018 and forecasts, indicating that in the next five years the future belongs to PERC technologies on p-type Cz-Si material.

One of the great things to come out of the first crisis was the rapid entry of new innovations into the PV market, such as PERC and n-type passivated emitter, rear totally diffused (nPERT) technologies. On the other hand, the speed of implementation of PERC technology has been so quick that not every PERC producer has keen insights into the actual challenges connected with this technology, such as light and elevated-temperature induced degradation (LeTID) [3,4] and, more recently, passivation degradation of the PERC rear side, observed by the University of Konstanz [5]. Whereas light-induced degradation (LID) is based on the formation of boron–oxygen complexes and can be suppressed by, for example, low oxygen material or by regeneration [6], LeTID is suspected to be the consequence of too much hydrogen in PERC being introduced to the Si-bulk from two-sided plasma-enhanced chemical vapour deposited (PECVD) SiN_x passivation layers [7].

Several solutions have already been proposed for reducing LeTID – for example, the use of low-hydrogen-content SiN_x layers, or the reduction of the metal contact firing temperatures in order to minimize the amount of hydrogen released into the bulk material [7]. Some PERC producers, with deeper insights into their products, use a combination of both the above, and select Si materials that are less affected. However, a certain amount of degradation can still be observed, even in such adapted solar cells, as the degradation mechanisms in PERC remain very complex.

In the authors' opinion, one of the best and simplest options for non-degrading solar cell design is to switch directly to MoSoN (**Monocrystalline Solar cell on N-type**). This type of device is very similar to the existing PERC structure, with just two major feature differences: 1) a switch to n-type material; and 2) the addition of a BBr_3 -diffusion step, instead of the more commonly

Introduction

PV solar cell and module manufacturers are again finding themselves in a deep crisis. As in the case of the crisis that started in 2011, there is huge overcapacity, since the demand has not been growing as expected. At the end of 2018 a total production capacity of 160–170GW with a 60–70GW passivated emitter rear cell (PERC) capacity is forecast [1]; this will be about 60–70% above the actual demand in 2018. The shake-up continues, but now in Asia, as there are hardly any large manufacturers left in the EU or USA. The most-affected companies are those which focus

“The degradation mechanisms in PERC remain very complex.”

used AlO_x passivation. N-type wafers are nowadays only 5% more expensive than p-type ones, but have the advantage of being more stable to the above-mentioned degradation mechanisms. This paper describes very briefly ISC Konstanz's MoSoN solar cell concept, summarizes the solar cell parameters achieved, compares the costs with standard PERC, and sketches out what such a switch from PERC to MoSoN could look like.

Fig. 2 shows the cross section of a MoSoN cell; it consists of an n-type PERT solar cell with a boron rear junction and Al metallization (similarly to PERC technology) on the rear side. By recrystallization of aluminium-doped silicon, a selective emitter is created locally beneath the rear-side contacts. The advantages of this solar cell concept will be described in the following sections.

Many scientists are saying nowadays that the 'next big thing' after the introduction of PERC and bifaciality will be TOPCon [8], by which they mean carrier-selective passivated contacts and a heavily doped silicon layer between the contacts and the wafer. Such passivated contacts can be processed in many ways, as summarized (for example) at EU PVSEC 2018 by Cuevas [9]. As PV is more an evolutionary industry than a revolutionary one, in the authors' opinion there is

still at least one step in between, namely the low-cost and stable n-type Al paste technology, with efficiencies reaching 23% (nPERT) and above (IBC) and voltages of around 700mV.

Fig. 3 shows a summary of ISC Konstanz's status, along with a roadmap, for the dominating c-Si technologies.

Standard Al-BSF technology, shown in Fig. 1 in the lower left corner, is losing market share in favour of PERC solar cells. Not only that, Al-BSF standard solar cells are limited to efficiencies of around 20%, and Al-BSF technology cannot even be adapted to bifacial application. In contrast, PERC solar cells can be produced for bifacial application and will boost the bifacial market, as bifacial PERC modules can be offered at almost the same price as monofacial ones. Going bifacial will save Al paste; however, the front-side efficiency will consequently be partly cannibalized by 0.2–0.4%_{abs}, depending on the bifaciality factor, which is typically between 65 and 80% [10]. Standard front-emitter nPERT technology (BiSoN in ISC's case) produced by, for example, Yingli, Jolywood, REC, Adani, Linyang and others, can yield the same efficiencies as bifacial PERC but at higher bifaciality factors, ranging from 85 to 95%. The highest and most stable efficiencies with diffused junctions can be achieved with rear-

ESTABLISHED SUPPLIER OF WET PROCESSING EQUIPMENT FOR HIGH EFFICIENCY CELLS

About 20 years ago a team of engineers started designing batch wet benches for solar cell manufacturing. The first large high efficiency mono cell plant relied on wet benches with ozone based processes, which were essential at various stages of the cell process. This team continued to be a leader in developing and manufacturing of batch wet benches. In 2015, it joined the newly founded exateq GmbH near Nuremberg, Germany where it continues to develop and manufacture top performing wet benches for high efficiency cell processing.

In Taiwan, Korea and China customers rely on more than 20 of exateq's wet benches when establishing high efficiency lines for mono p-PERC, n-type and IBC technology. Various research institutes value the capabilities of exateq's extremely compact and flexible lab wet benches. exateq has become the market leader in range, flexibility and features:

- basic manual lab wet bench for 25 wafers per batch,
- fully automatic lab/pilot wet benches,
- production systems up to 12,000 wafers/hour
- builds shorter than almost all other manufacturers'
- most auxiliary devices integrated maintaining footprint
- provided for any etching or cleaning process
- ozone based cleaning is integral part of high efficiency technologies
- Process support is provided through partners

exateq has also been qualified by Meyer Burger to provide suitable wet benches for their heterojunction technology. On this basis exateq has succeeded in participating in an HJT project in Asia. The majority of projects in Asia have this far been handled through a Korean partner providing local support; direct projects can be offered subject to agreement.



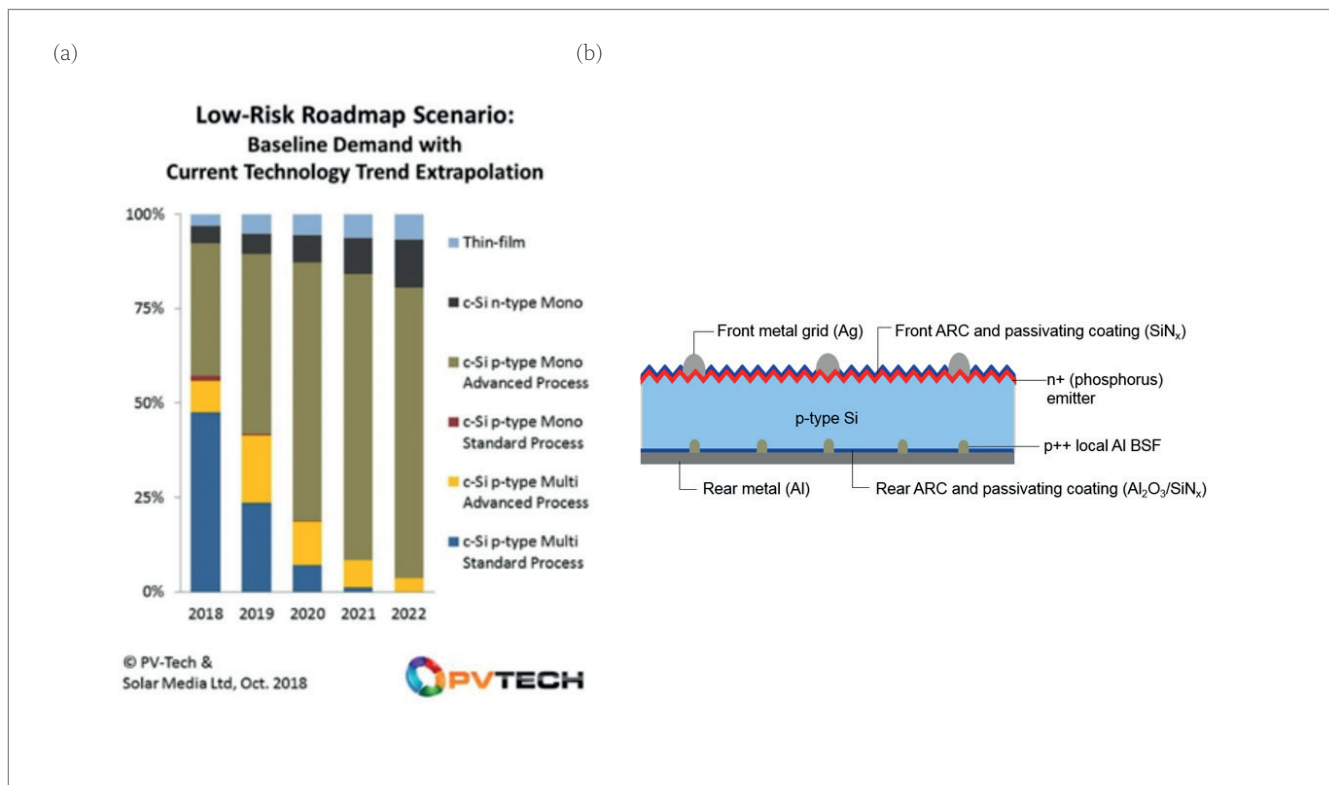


Figure 1. (a) Forecasts of technology shares (from PV Tech [2]); (b) a typical cross section of a p-type PERC solar cell.

emitter Al paste nPERT technology (MoSoN) and IBC technology (ZEBRA).

Efficiencies with MoSoN currently stand at 22.2% (22.98 with oBB) – and with ZEBRA at 23.2%. In addition, Al paste technology will be introduced to ZEBRA and BiSoN in the coming months, and the V_{oc} is expected to be boosted to around 700mV. In the case of BiSoN, this will be a bigger challenge, as the Al paste will be used for the front side, where thinner contacts need to be printed, something that is not trivial for Al paste technology at the moment. Dielectrics laser opening technology as well as advanced Al paste from Toyal will be used, in addition to Toyal's optimized firing-through Al paste.

Status of PERC solar cells and possible degradation mechanisms

PERC solar cells are rapidly becoming the new standard – the question is whether this is happening too quickly in some cases.

Status of PERC

PERC is a mature technology with a relatively simple process, and therefore also with a low cost of ownership (COO) attached. With PERC technology, a record efficiency (at the time) of 23.6% was achieved by LONGi [11] (March 2018) with a busbar-less metal contact design, which was later surpassed by JinKo with 23.95% [12] (May 2018). Record efficiencies are nice; however, what counts is the average values in production and the stabilities over time. For the big players (Hanwha Q CELLS, JA Solar, LONGi, TRINA, JinKo,

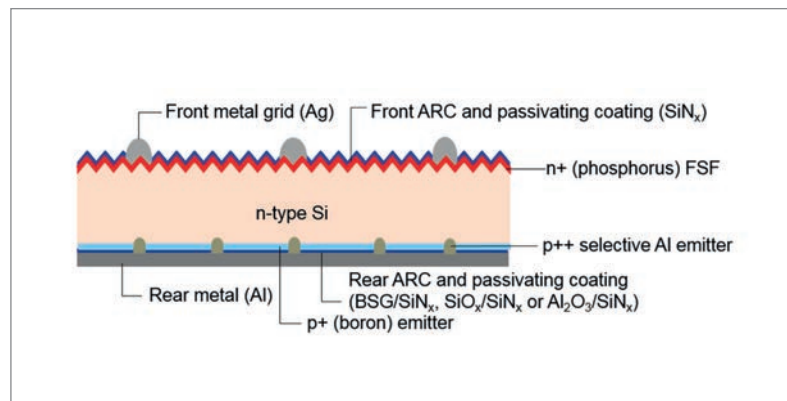


Figure 2. Cross section of a MoSoN solar cell.

Canadian Solar, etc.), average efficiencies these days in production are between 21.5% and 22%; this is outstanding compared with standard Al-BSF technology, which has dominated the market for decades and for which the best average efficiencies hardly exceeded 20%. With regard to degradation, however, it is not certain if all PERC producers have understood the challenges of coping with all these types of effect that this device can additionally suffer from.

Degradation of PERC

When visiting conferences and manufacturers, it is often surprising to see how many people responsible for PERC modules have never even heard about the severe degradation problems that can affect PERC devices – in particular when talking about LeTID (alias 'carrier-induced degradation' – CID). Even at the 4th PERC Solar

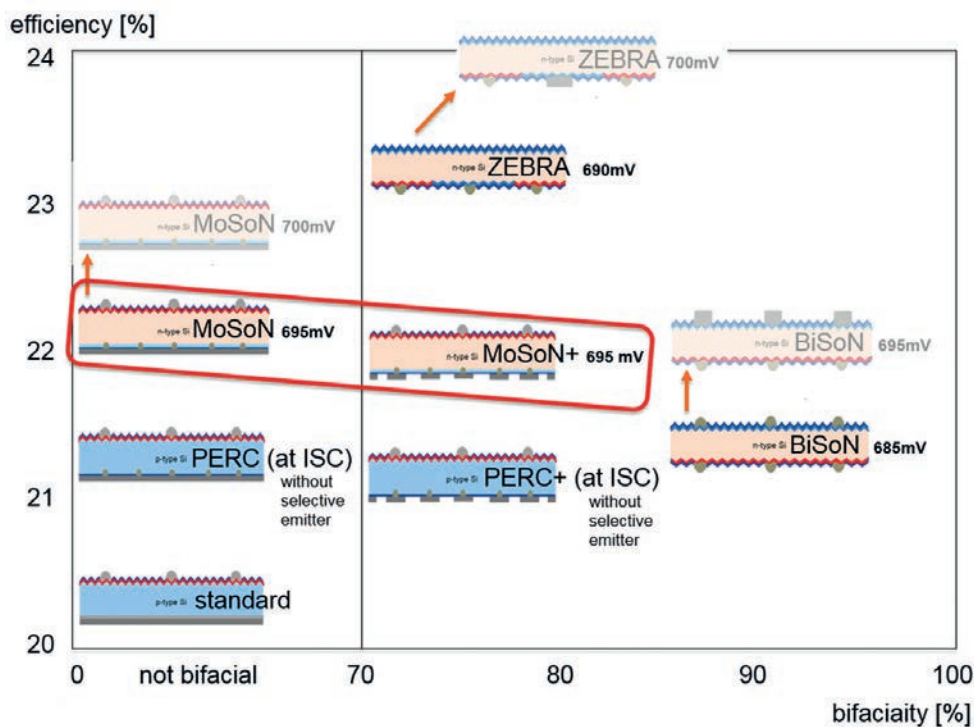


Figure 3. ISC Konstanz's status and roadmap for standard diffused cell technologies.

Cell and Bifacial Module Forum 2018 [13], LeTID was not really one of the topics. A common response to LeTID that can be heard is: "LeTID? No – we have no LID: we are stabilizing." Or, some – who are more informed – say: "LeTID only impacts mc-Si PERC – we produce Cz-Si PERC." Neither of these statements is true. Even if LeTID was first observed on mc-Si PERC cells [3], the effect is also visible and detrimental in the case of Cz-Si PERC modules [4], where it can be very severe. In this regard, PI Berlin has tested (and continues to test) for LeTID in many of the PERC modules available in the market. After six weeks of exposure to accelerated degradation, all the tested modules (around 10 so far) had degraded by 5% relative or more in terms of power – and the degradation curve did not appear to have reached saturation. Furthermore, there are stories of PERC PV systems 'out there' where the modules have degraded to close to 20% after 2–3 years' operation, which is simply a tragedy.

Status of PERT solar cells and degradation mechanisms

Status of PERT

There are two different PERT approaches, of which currently only the Afront-side emitter approach is commercially produced (e.g. by Jolywood, REC, Yingli, Adani, Linyang and others). A good summary presentation at EUPVSEC 2018 was

given by Tous from imec [14] on the lab results for both technologies, from which a selection of the achieved efficiencies is cited in Fig. 4 (in the paper, all groups are referenced). The efficiencies marked with * are those certified by calibration labs.

The highest efficiencies were achieved with the rear-emitter nPERT concept, with 23% achieved by imec. It has to be noted that many different techniques are used in both technologies – even passivated contacts as of now, with plating procedures and zero-busbar technology measured by Grid^{TOUCH}. ISC Konstanz's strategy is to use only processes which are currently employed in industry. At the time of the presentation by Tous [14], with ISC Konstanz's MoSoN concept an efficiency of 21.8% [15] had been achieved, which was confirmed by FhG ISE CalLab (shown later in this paper, in Fig. 8). Recently, 22% has been surpassed and 693mV achieved with a homogeneous front-surface field (FSF) and standard screen-printing technology (see later, Table 1). Details of this technology will be discussed later.

Degradation of PERT

Much less degradation occurs in n-type devices; however, some scientists have claimed that LeTID can also impact nPERT and IBC solar cells. Such studies are currently being carried out at ISC Konstanz: no noticeable decreases in the cell parameters have been observed. In the past, scientists have also seen UV degradation

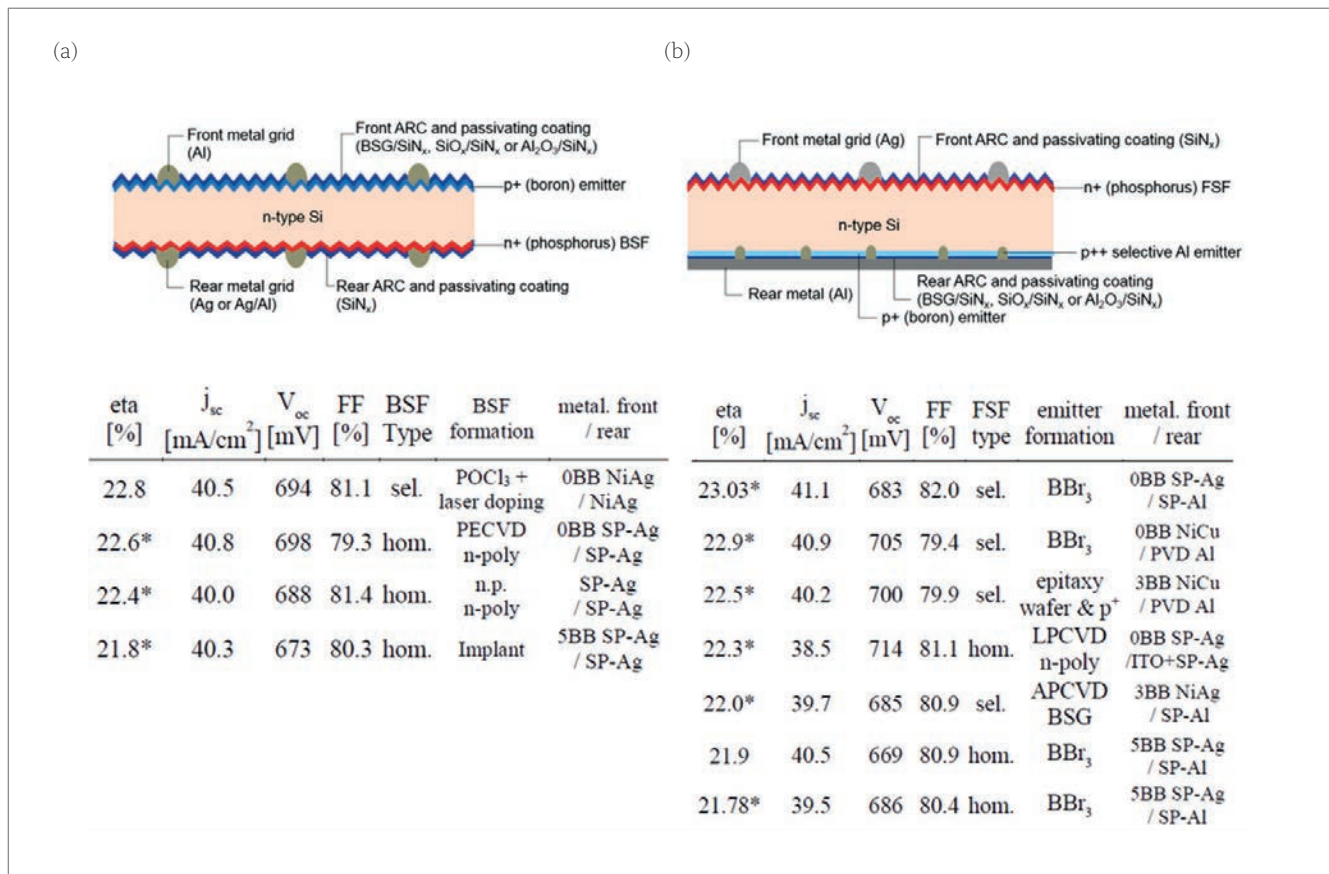


Figure 4. Solar cell parameters for two different nPERT technologies: (a) front emitter; (b) rear emitter (tables from Tous [14]).

in oxide-passivated B-emitter solar cells, which was based on the migration of B dopants into the oxide, creating a stronger depletion layer [16]. In all ISC Konstanz's cell concepts, however, an in situ grown SiO₂ passivation layer is used on the B emitter during the BBr₃ diffusion [17]; therefore, this layer is already saturated with boron, and the depletion regions at the Si surface are not increased. No such degradation has been observed so far in all the cell concepts, such as BiSoN, MoSoN and ZEBRA.

Advanced aluminium paste technology

The idea behind MoSoN (and other rear-junction nPERT technologies) is to combine n-type, which offers high and stable efficiencies, with Al paste contacting technology. In this technology, for nPERT rear-junction devices, selective emitters are created during Al recrystallization and the η is increased. If the contact area is minimized to a region of small dots, one can get very close to the passivated contacts by minimizing the total contact area to less than 1% (see Fig. 5). Such small contacts can, in principle, be easily contacted by aluminium, provided proper alloying is realized by adjusting the paste chemistry, including the glass frit and boron content in the paste. Additionally, the smaller the size of the laser contact opening (LCO), the stronger the out-diffusion of silicon from the wafer to the paste during alloying, and the lower the rate of the out-diffused silicon returning to the wafer

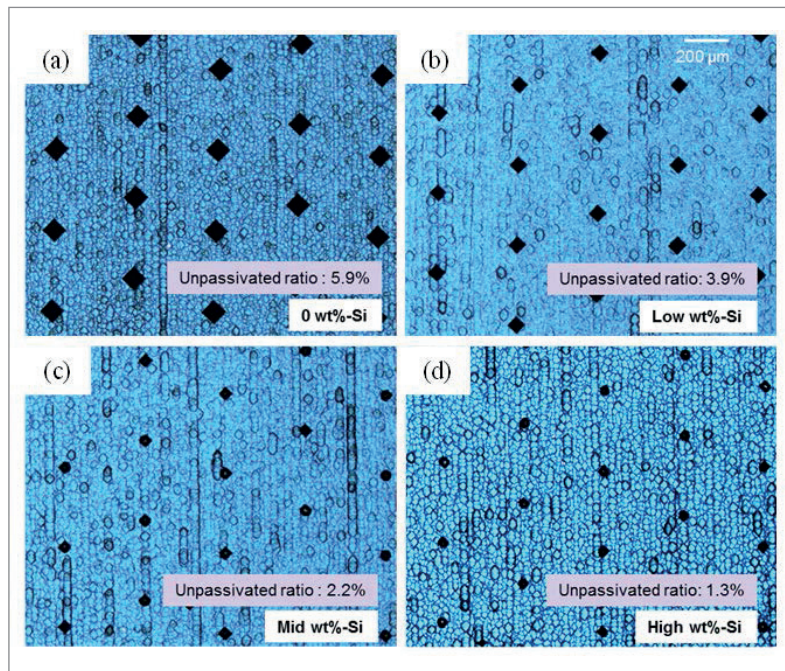


Figure 5. Creation of small point contacts as a function of the Si content in Toyal's Al paste [15].

during the cooling-down, to form the required locally alloyed emitter. Toyal have developed an Al paste which can be used for the generation of small local emitter points and contacts by adjusting special Al-Si alloy and Al powders in the paste, opening up new horizons in low-cost metallization of MoSoN solar cells.

“The idea behind MoSoN is to combine n-type, which offers high and stable efficiencies, with Al paste contacting technology.”

Aluminium-contacted homogeneous and selective rear-emitter PERT solar cells

The aim of MoSoN is to reap two advantages:

1. The lower degradation sensitivity of n-type material.
2. The low-cost and high-voltage contacting properties of Al paste.

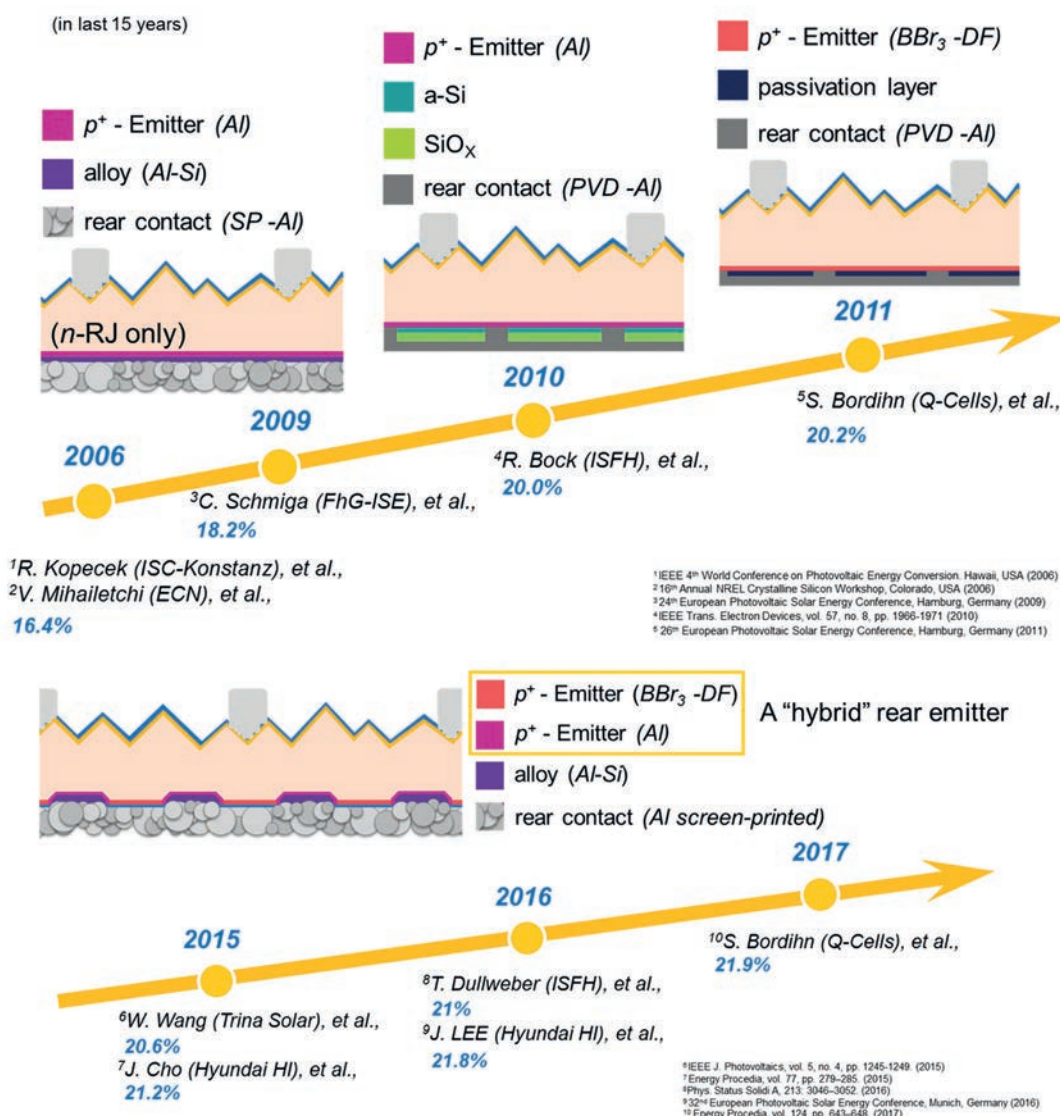
The history of rear-junction nPERT technology extends over more than 10 years, as illustrated in Fig. 6.

At the beginning, in the case of the so-called ‘Phos-Top concept’ at the time, the emitter formation was performed using Al paste only, but very soon this became a combination of boron

diffusion with Al paste technology, which was investigated in detail by Hanwha Q CELLS. The potential of these solar cell concepts is still very high, as the process is extremely simple and results in stable and high efficiencies. ISC Konstanz has therefore been working on such a concept – namely MoSoN – for a long time, within the scope of several national and industrial projects.

Fig. 7 shows the process and the cross section of MoSoN technology. The process begins with saw-damage etching. This is followed by both-side boron diffusion, during which the rear surface is already passivated by an in situ grown SiO_2 interface layer, and so no AlO_x passivation is required. SiN_x is then deposited on the rear side, and the wafers are textured on the front side. After a POCl_3 diffusion process, the front-side SiN_x is PECVD deposited, and the rear SiN_x opened by a fast laser. Subsequent to metallization and firing, the finished devices are edge isolated. Currently, work is also under way on wet-chemical edge isolation, which will be implemented in the near future.

Figure 6. History of rear-junction nPERT technology [15].



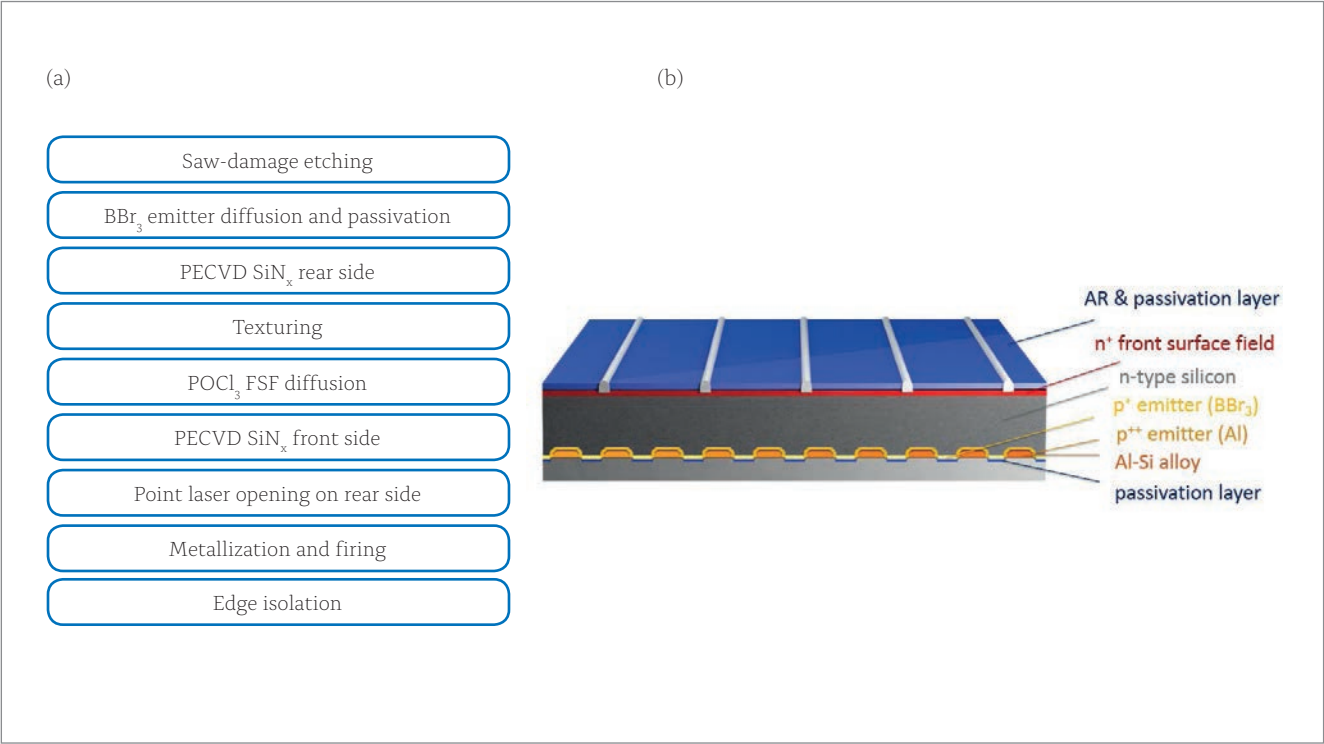


Figure 7. MoSoN solar cell: (a) process flow chart; (b) cross section.

It has to be noted that the rear PECVD SiN_x layer is included in a high-temperature diffusion process, resulting in a very low hydrogen content, which might explain why no LeTID is observed for MoSoN cells. Fig. 8 shows the *I*–*V* measurement of a 21.8% cell, certified by FhG ISE CalLab.

The high efficiency is excellent, but what is remarkable here is the very high voltage of 686 mV without a selective FSF and without passivated contacts. The MoSoN development at ISC Konstanz is focused on achieving high voltages with very simple ‘close to standard’ processes. The most recent cell parameters resulting from the development with optimized point contacts, which resulted in an efficiency of 22.2% and an outstanding voltage of 693 mV, are summarized in Table 1.

The bifacial cells, with (so far) a moderate bifaciality factor of 60%, resulted in efficiencies of 22%; experiments are under way in an attempt to achieve 700 mV and 22.5%. MoSoN solar cells with zero busbars (oBB) yielding 22.98%, measured by Grid^{TOUCH}, were recently processed (*J*_{sc}=40.7 mA/cm², *V*_{oc}=693 mV, *FF*=81.5%); this efficiency corresponds to the highest achieved by imec from the table in Fig. 4(b). The MoSoN concept will be presented at the centrotherm booth and during an invited talk at the 2019 SNEC PV Power Expo.

Table 2 summarizes the advantages of the MoSoN solar cell compared with standard PERC devices.

The process for MoSoN does not include selective FSF, and so the front-side process is simpler than that for many PERC record cells. The efficiency potential in production is higher for MoSoN, as a result of the n-type material used

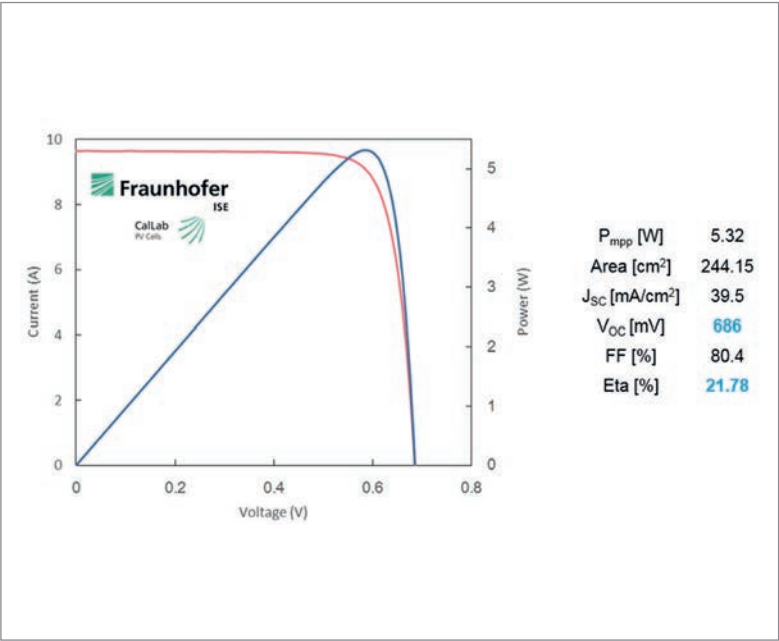
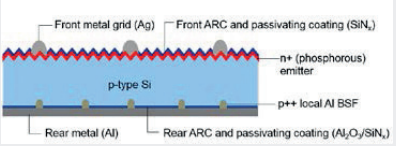
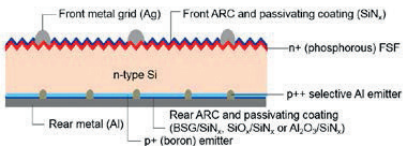


Figure 8. *I*–*V* measurement of a five-busbar MoSoN solar cell, certified by FhG ISE CalLab [15].

	FF [%]	<i>V</i> _{oc} [mV]	<i>J</i> _{sc} [mA/cm ²]	<i>η</i> [%]
MoSoN _{best}	80.1	693	40.0	22.2
MoSoN _{bifi}	79.4	692	40.0	22.0

Table 1. Latest MoSoN results for best mono- and bifacial devices with optimized point contacts.

as well as the totally diffused surfaces; moreover, these two factors guarantee not only high but also stable efficiencies. In the MoSoN process the AlO_x passivation tool can be replaced by a highly productive LP-BBr₃ diffusion furnace from

	PERC	MoSoN
		
Technology	P-type front junction Selective emitter	N-type rear junction Homogeneous FSF
Efficiency in production	21.5–22% 22–22.5% (potential) <680mV	22% 22.5–23% (potential) >690mV
Wafer	Low resistivity wafers required	Wide range of resistivities possible
Ag use	100%	90% (10% front-side Ag reduction)
Bifaciality	70–80%	75–85% (rear junction)
Degradation	Up to 20% in 3 years' LeTID (possible)	Not yet observed
Different machines	AlO _x passivation	BBr ₃ diffusion (with BSG passivation)
COO cell	US\$16.4/Wp	US\$16.7/Wp*
Solar cell transformation costs (excl. wafer costs)	US\$8.3/Wp	US\$8.0/Wp
LCOE	US\$4.84/kWh** US\$4.21/kWh*** US\$4.050/kWh****	US\$4.57/kWh** US\$4.06/kWh*** US\$3.91/kWh****

** September 2018; ** Fixed-tilt monofacial; *** Fixed-tilt bifacial; **** HSAT bifacial*

Table 2. Comparison of standard PERC and MoSoN.

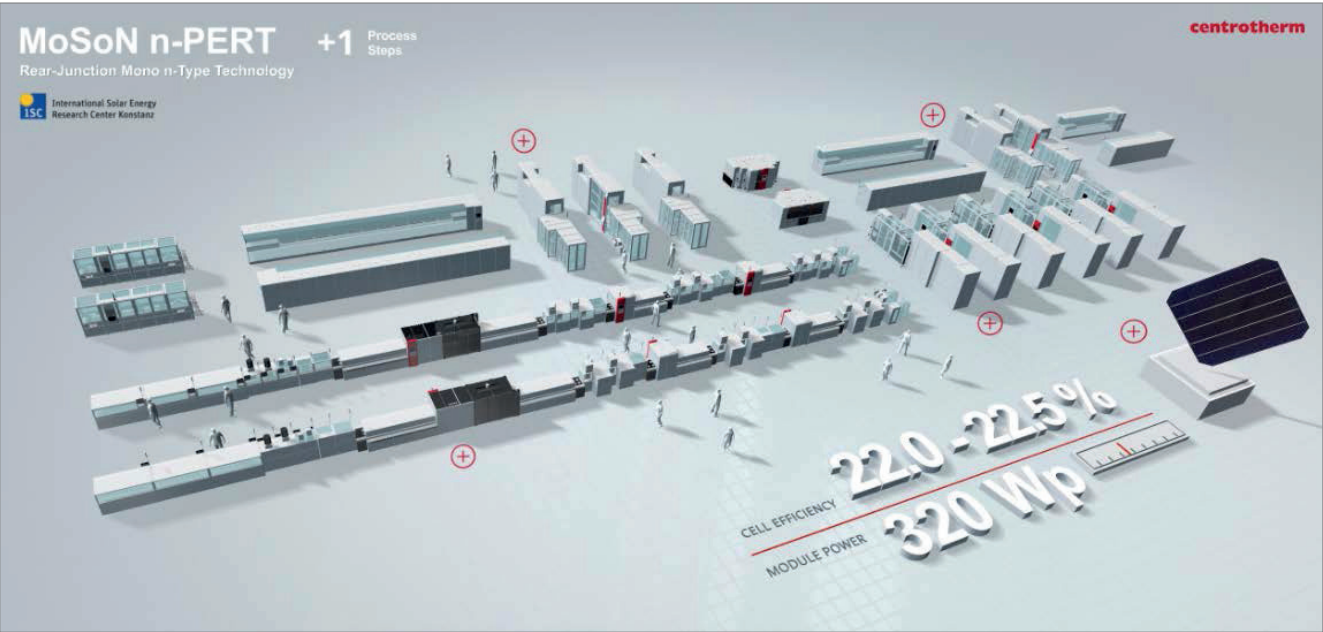


Figure 9. Lay-out of a possible MoSoN production line from centrotherm (from SNEC 2017).

centrotherm, which provides diffusion of the rear emitter and in situ passivation with good homogeneity [17]. Another advantage of this cell architecture is that the bulk conductivity of the wafer contributes to the lateral conductivity in parallel to the FSF. As a result, the rear-junction nPERT concept requires fewer Ag fingers than a PERC cell, thus saving Ag costs [18].

Fig. 9 shows a MoSoN production line proposed by ISC Konstanz and centrotherm. The COO will

be discussed in the next paragraph, and a summary is presented in Table 2. Because the wafer price of n-type is still higher than n-type, the MoSoN cell is slightly more expensive. Nevertheless, the higher cost of a MoSoN module in a system environment is already offset by the advantages of higher efficiency, better stability and slightly higher bifaciality. For bifacial horizontal single-axis tracking (HSAT) MoSoN systems, a leveled cost of electricity (LCOE) of US\$3.9/kWh can be achieved

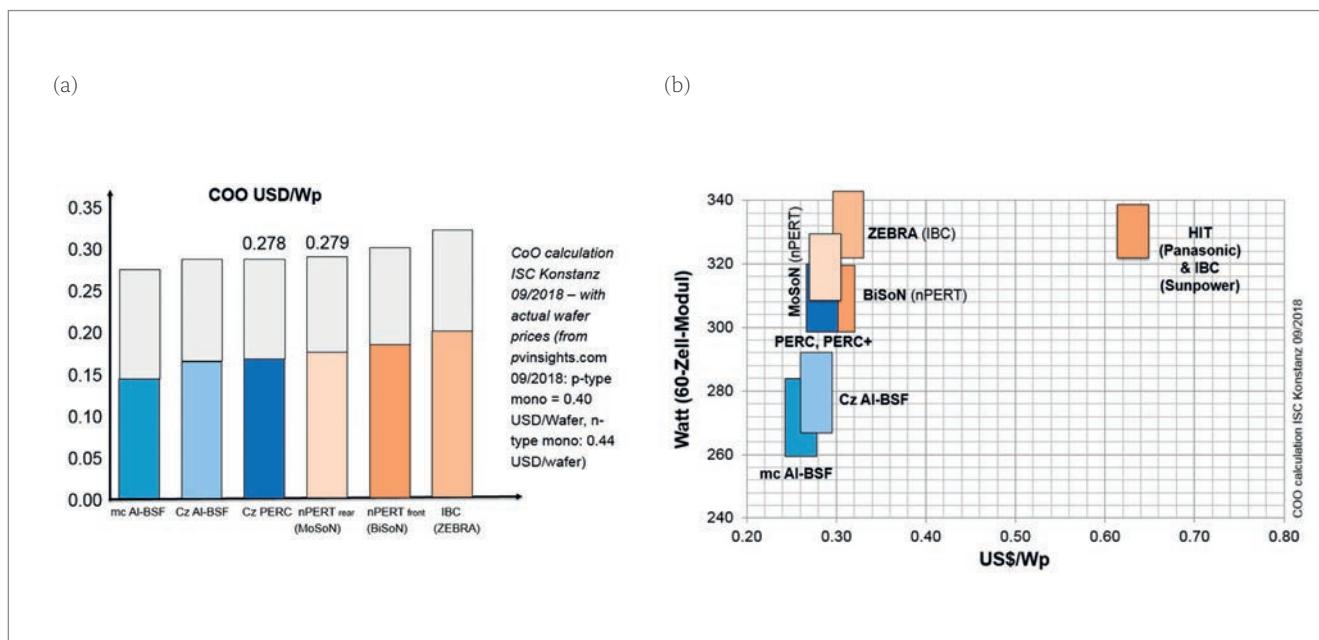


Figure 10. COO for different solar cell concepts: (a) broken down into solar cell and module costs; (b) as a function of the module power of a 60-cell module.

in locations with 1,875kWh/kWp/year irradiation and an albedo of 35% (typical for desert sand).

“The higher cost of a MoSoN module in a system environment is already offset by the advantages of higher efficiency, better stability and slightly higher bifaciality.”

COO for PERC and PERT solar cells

N-type solar cells do not have to be expensive when the processes are based on standard p-type processes. Fig. 10 depicts the COO for standard solar cell products on the PV market. Since wafer price is very dynamic and still represents a large portion of a solar cell cost, the differences between processes are very dependent on the current wafer market. It is clearly visible, however, that current advanced solar cell processes, compared with those in the past, are getting very close to producing the lowest-cost mc-Si module. At the system level, it is nowadays important to select high-power modules in order to minimize the LCOE.

Since the MoSoN COO is low and the achievable module power high and stable, the authors considered it the best concept to go with.

Summary and outlook

After the long-term market monopoly of Al-BSF solar cells, PERC solar cells are becoming standard in solar cell production lines. This is good for PV, as higher efficiencies help to reduce the balance of system (BOS) cost of PV systems.

The authors believe that the next step following on from PERC is a switch to n-type material and rear-emitter standard nPERT concepts, because of the lower degradation potential and the higher efficiency potential, while keeping the process sequence simple. This next step does not yet include passivated contacts, since with a very cost-effective advanced Al paste technology, efficiencies of close to 23% and voltages of 700mV are also realizable in a simple way.

This paper has presented ISC Konstanz's rear-junction nPERT concept MoSoN, on n-type material from LONGi, achieving an efficiency of 22.2% and a high voltage of 693mV. This very low-cost advanced Al paste point-contact technology from Toyal offers the potential to achieve 23% using a simple process, with solar cell transformation costs of around US\$7/Wp (excluding wafers costs). This technology will, in addition, be used in the future to test and further develop ISC Konstanz's ZEBRA IBC solar cell concept, with the aim of reaching 24%.

Acknowledgements

The authors thank all the people at ISC Konstanz involved in the processing of MoSoNs. This work was partly funded by German BMWi projects Kosmos (0325822E) and Ideal (0325889A).

References

- [1] <https://www.pv-magazine.com/2018/09/07/perc-market-to-reach-158-gw-by-2022/>.
- [2] PV Module Tech, Malaysia 2018.
- [3] Ramspeck, K. et al. 2012, “Light induced degradation of rear passivated mc-Si solar cells”, *Proc. 27th EU PVSEC*, Frankfurt, Germany, pp. 861–865.

- [4] Fertig, F. et al. 2017, "Mass production of p-type Cz silicon solar cells approaching average stable conversion efficiencies of 22%", *Energy Procedia*, Vol. 124, pp. 338–345.
- [5] Herguth, A. et al. 2018, "A detailed study on light-induced degradation of Cz-Si PERC-type solar cells: Evidence of rear surface-related degradation", *IEEE J. Photovolt.*, Vol. 8, No. 5, pp. 1190–1201, DOI: 10.1109/JPHOTOV.2018.2850521.
- [6] Schmidt, J. et al. 1997, "Investigation of carrier lifetime instabilities in Cz-grown silicon", *Proc. 26th IEEE PVSC*, Anaheim, California, USA, pp. 13–18.
- [7] [<https://www.pv-tech.org/guest-blog/is-letid-degradation-in-perc-cells-another-degradation-crisis-even-worse-th>].
- [8] [<https://www.pv-magazine.com/2018/10/08/topcon-the-next-big-thing-after-perc/>].
- [9] Cuevas, A. et al. 2018, "Solar cells by 'Desijn'", *Proc. 35th EU PVSEC*, Brussels, Belgium.
- [10] Dullweber, T. et al. 2017, "Bifacial PERC+ solar cells and modules: An overview", *Proc. 33rd EU PVSEC*, Amsterdam, The Netherlands, pp. 649–656.
- [11] [<https://www.pv-tech.org/news/longi-hits-record-23.6-conversion-efficiency-for-mono-perc-solar-cells>].
- [12] [<https://www.pv-magazine.com/2018/05/09/jinkosolar-achieves-23.95-efficiency-for-p-type-mono-cell/>].
- [13] [<https://de.enfsolar.com/directory/service/002639/4th-perc-solar-cell-and-bifacial-module-forum-2018>].
- [14] Tous, L. et al. 2018, "Large area monofacial screen-printed rear emitter nPERT cells approaching 23% efficiency", *Proc. 35th EU PVSEC*, Brussels, Belgium.
- [15] Peng, Z.-W. et al. 2018, "Towards 22% efficiency n-PERT rear junction solar cells with screen printed Al point back contact", *Proc. 8th SiliconPV*, Lausanne, Switzerland.
- [16] Zhao, J. et al. 2003, "Performance instability in n-type PERT silicon solar cells", *Proc. 3rd WCPEC*, Osaka, Japan.
- [17] Mihailetchi, V.D. et al. 2018, "Surface passivation of boron-diffused junctions by a borosilicate glass and in situ grown silicon dioxide interface layer", *IEEE J. Photovolt.*, Vol. 8, No. 2, 435–440.
- [18] Comparotto, C., Lossen, J. & Mihailetchi, V.D. 2018, "Bifacial screen-printed n-type passivated emitter rear totally diffused rear junction solar cells", *AIP Conf. Proc.*, Vol. 1999, No. 1, 100001.

About the Authors



Dr. Radovan Kopecek obtained a Dipl. Phys. degree from the University of Stuttgart in 1998, and completed his Ph.D. dissertation in the field of c-Si thin-film silicon solar cells at the University of Konstanz in 2002. One of the founders of ISC

Konstanz, Dr. Kopecek has been head of the advanced solar cells department since 2007; the department deals with several European and national research projects and technology transfers focusing on high-efficiency n-type devices and bifacial technology. Since 2016 he has been on the board of directors at EUREC – the European association for research centres involved in renewable R&D.



Zih-Wei Peng received his master's in 2012. He then worked for a Taiwanese PV industrial company, where he was involved in R&D on nPERT bifacial cell technology, later transferring to the area of mass production technology in 2015. He joined ISC Konstanz in 2016 to pursue his doctoral degree at the University of Tübingen; his research topic is Al metallization and nPERT rear-junction solar cell technology.



Thomas Buck graduated from the University of Konstanz with a degree in physics; for his thesis, he investigated the characterization of PEM fuel cells at Daimler-Chrysler. He is currently pursuing his doctoral degree at the University of Konstanz, where he is conducting research on multicrystalline n-type industrial solar cells. He is one of the founding members of ISC Konstanz, and has been employed at the research institute since March 2008. His other research interests lie in the fields of metallization and bifacial solar cells.



Corrado Comparotto obtained his M.Sc. in electronic engineering in 2008 from the Università degli Studi di Brescia, Italy. After graduation, he worked as a volunteer on several projects in Bulgaria and Denmark, where he acquired further qualification in the fields of ecological sustainability and nature protection. Since 2011 he has been working on n-type solar cells in the advanced solar cells department at ISC Konstanz.



Dr. Valentin D. Mihailetchi received his B.Sc. in physics from the West University of Timisoara, Romania, in 2000, and his Ph.D. (cum laude) in device physics of organic solar cells from the University of Groningen, The Netherlands, in 2005. From November 2005 to June 2008, he was a research scientist working on crystalline silicon with ECN Solar Energy, The Netherlands, where he developed n-type-based solar cell processes. In July 2008 he joined ISC Konstanz, where he is currently a senior scientist and leads the n-type solar cells group in the advanced cell concepts department.



Lejo J. Koduvelikulathu received his B. Tech. in electronics and telecommunication engineering from Dr. Babasaheb Ambedkar Technological University, India, in May 2005. From July 2005 to July 2007, he worked with M/s Siemens Ltd, India, as a commissioning engineer. In October 2009 he received a master's in telecommunication engineering, and in November 2010 a professional master's degree in the field of nano-micro systems, both from the University of Trento, Italy. Since November 2010 he has been working with ISC Konstanz, where his research encompasses simulation studies of solar cell structures and metallization-induced recombination losses. Since 2018 he has been part of the industrial solar cells department and is in charge of mapping customers' requirements and the subsequent experiments and laboratory planning. He is also a member of the ISC technology transfer team, responsible for transferring thermal processes into industrial production lines.



Dr. Joris Libal received his diploma in physics from the University of Tübingen in 2000, after which he began his career as a quality engineer in the area of PCB assembly. In 2003 he took employment at the University of Konstanz, where he finished his Ph.D. on multicrystalline n-type silicon solar cells in 2006; he subsequently conducted postdoctoral research at the Università di Milano-Bicocca, Italy, in the field of solar-grade silicon. In 2008 he began working as an R&D manager for the Italian company Silfab, where he was involved in the planning of a polysilicon plant and responsible for the company's R&D projects in the fields of cells and modules as well as module certification. Since October 2012 he has been employed at ISC Konstanz, working in the field of n-type cells, energy yield simulations, and COO and LCOE calculations.



Jan Lossen studied physics at the University of Freiburg, Freiburg im Breisgau, Germany, and at the University of Cologne, Germany. He graduated in 2003 with a thesis on the hot-wire chemical vapour deposition of microcrystalline silicon layers. For more than ten years he worked in different positions in the production and development of crystalline silicon solar cells with ErSol/Bosch Solar Energy AG. Since 2014 he has been a senior scientist and project manager for process transfers with ISC Konstanz.



Masahiro Nakahara joined Toyo Aluminium K.K in 2010 and has been working at ISC Konstanz since 2017. He is responsible for the development of the metallization paste for solar cell applications.



Kosuke Tsuji studied material science at Tokyo University of Science in Japan, graduating in 2011. He joined Toyo Aluminium K.K in 2011 and has been working at ISC Konstanz since 2018. He is responsible for the development of metallization paste, not only for solar cell applications but also for electronic materials.



Dr. Marwan Dhamrin graduated from the physics department at Sana'a University, Yemen, in 1998, and obtained his M.Sc. and Dr. Eng. degrees from Tokyo University of Agriculture and Technology in 2004.

His doctorate thesis topic concerned the suppression of LID in multicrystalline silicon wafers by Ga doping. After graduation he worked on developing mc-Si n-type heterojunction solar cells under a JSPS fellowship, and as an industrial collaborator/assistant professor at Tokyo University on many NEDO projects, including the recycling of kerf-loss silicon powders retrieved from diamond-wire slicing machines. In 2011 he joined Toyo Aluminium K.K and led R&D activities in metallization pastes and backsheet development, and in the introduction of high-quality aluminium pastes, especially for PERC full-area and bifacial solar cells.



Dr. Wolfgang Jooss received his Ph.D. from the University of Konstanz in 2002 for his work on multicrystalline and rear-contact buried-contact solar cells; the major outcome of the experimental work

was a world record 17.5% for a large-area multicrystalline solar cell. Between 2002 and 2009 he worked at sunways AG as an R&D engineer and became head of solar cell R&D. He joined centrotherm in 2009, where initially he was the director of integrated factory technologies, looking at the complete c-Si value chain, and subsequently the director of PV technology, responsible for the technology development of solar cell equipment. Since April 2016 he has been the director of R&D at RCT Solutions GmbH in Konstanz, Germany.

Enquiries

Email: radovan.kopecek@isc-konstanz.de

Solving all bottlenecks for silicon heterojunction technology

Christophe Ballif², Mathieu Boccard¹, Antoine Descoeudres², Christophe Allebé², Antonin Faes², Olivier Dupré¹, Jan Haschke¹, Pierre-Jean Ribeyron³ & Matthieu Despeisse²

¹Ecole Polytechnique Fédérale de Lausanne (EPFL), Neuchâtel, Switzerland; ²CSEM, PV-Center, Neuchâtel, Switzerland; ³CEA-INES, LITEN, Le Bourget-du-Lac, France

Abstract

Silicon heterojunction (SHJ) solar cells are the archetypes of ‘full-surface passivating contact’ solar cells; such contacts are required in order to achieve typical open-circuit voltages of up to 730–750 mV. Although SHJ technology has fewer manufacturing steps and enables higher efficiencies than standard passivated emitter and rear cell (PERC) technology, the market has been slow in taking it up. This paper discusses some of the obstacles that have been overcome in the last 10 years, and shows why the technology is now readier than ever for a competitive mass-market launch. The reasoning behind this is based on: 1) improvements at the solar cell level, leading to >24–25% efficiencies in R&D, with screen-printed contacts; 2) the availability of high-quality, low-cost, thin n-type c-Si wafers; 3) improvements in metallization and interconnection solutions; and 4) the availability of cost-effective mass-production tools. Many research groups and industries currently demonstrate R&D 6" cells that typically reach 23–24% efficiency. Several new manufacturing or demonstration lines with production tools are in operation, running on average 24-hour production of 6" cells with an efficiency level of 23% (five busbars). When the excellent temperature coefficient and bifaciality of the modules are taken into account (leading to more kWh per nominal W), SHJ has the potential to outperform traditional technologies in terms of electricity cost. However, the CAPEX is still significantly higher than that for PERC lines and creates a hurdle when growth in capacity (MW/year) is favoured for a given capital. This paper indicates how it should be possible to further reduce manufacturing costs once a true volume learning curve is started, by acting both on the CAPEX and on the costs of consumables, in particular silver and indium, on which today's popular transparent electrodes are based. Finally, there will be a brief discussion of how the technology could be upgraded, either to full back-contacted approaches or to multijunction structures, forming a natural extension to the PV learning curve.

Introduction

Silicon heterojunction (SHJ) cell technology is based on the simple structure and typical processes illustrated in Fig. 1; it aims to take the best of both the c-Si world (perfect absorber) and the thin-film world (coatings on large area). After initial developments by various research groups, Sanyo (now Panasonic) introduced the heterojunction concept for the a-Si:H(i/p)/TCO front stack and

rear n⁺/Al back side [1,2]. A few years later, IMT Neuchâtel's PV-Lab introduced a rear side with a-SiH(i/n) and transparent conductive oxide (TCO) [3]. Sanyo was the first to push the concept to large-scale manufacturing, and demonstrate high-efficiency solar cells. A review of the key elements of the technology can be found in recent papers [1,4].

In the last decade, an increasing number of research groups and companies have been working at industrializing various versions of the technologies [5–10]. In line with expectations, in terms of production cost for current manufacturing [11] several obstacles remained, precluding a full mass introduction. Some of these are described below, along with how they have been overcome just recently, which explains the high number of new players in the field of SHJ cell manufacturing.

Material quality

For a long time, access to high-quality n-type wafers was costly. In consequence, additional processing – such as gettering, thermal donor killing or hydrogenation – was required in order to obtain sufficient material quality for high-efficiency solar cell production. Today, however, the situation is different. In step with the improvement in quality of p-type wafers, the quality of n-type wafers pulled using the standard Czochralski (Cz) method has significantly improved over the last five years. This advance has stemmed from better control of the oxygen content as well as from optimized pulling techniques, with faster cooling allowing a reduction in thermal donor concentration. As a result, state-of-the-art n-type c-Si wafers no longer require gettering or thermal donor killing to enable high-efficiency cells to be fabricated. This has been demonstrated by values of the lifetime/resistivity ratio (typical quality criteria with lifetime expressed in ms and resistivity in Ωcm) greater than unity along the entire ingot [12].

For a thickness of 180 μm, such n-type wafers are now typically 5–8% more expensive than p-type [13]. The difference compared with p-type essentially arises from the limited number of pullings (e.g. three instead of five) using the same crucible; fewer pullings can be made to avoid

“State-of-the-art n-type c-Si wafers no longer require gettering or thermal donor killing to enable high-efficiency cells to be fabricated.”

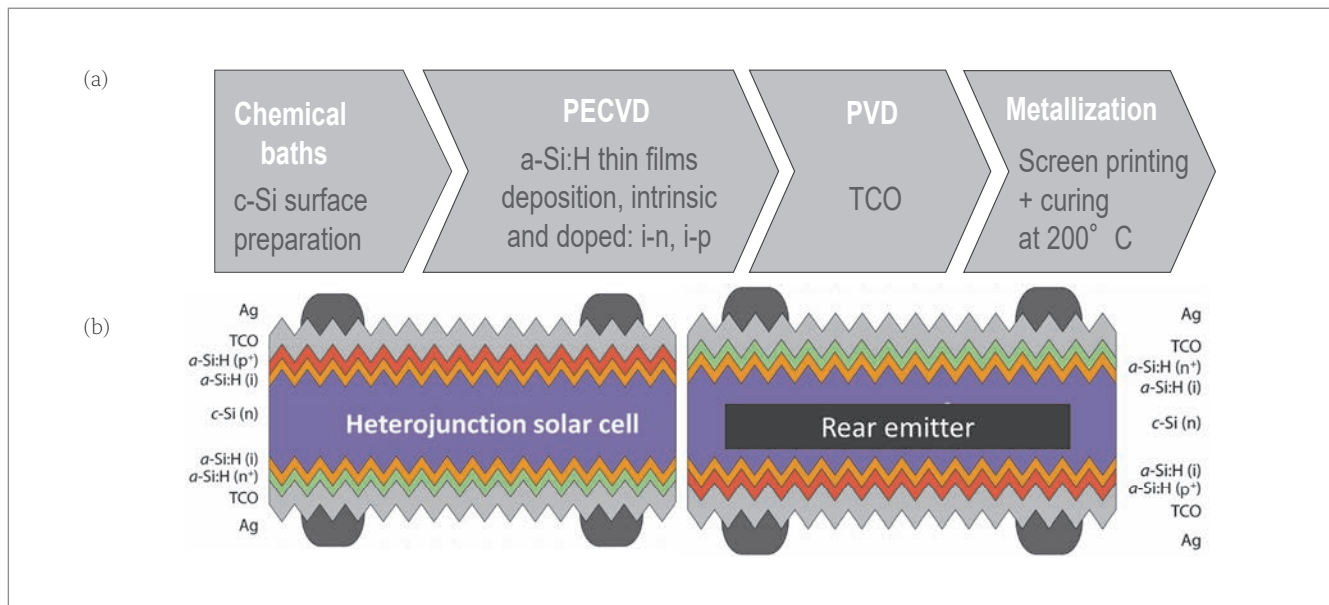


Figure 1. (a) A typical process flow for standard SHJ. The plasma-enhanced chemical vapour deposition (PECVD) and physical vapour deposition (PVD) steps on both sides can each be performed in a single tool. Alternatively, catalytic (CAT)-CVD and plasma-assisted evaporation (PAE) can be used for the deposition of a-Si:H and TCO layers respectively. **(b) Schematics of the front-junction (left) and rear-junction (right) configurations.** Note that in both cases, providing that high-quality surface passivation and low local contact resistance are obtained, the sheet resistance of the TCO is not as crucial as in, for example, thin-film modules, because of the high injection of charge carriers under operating conditions that contribute to lateral charge transport.

excess (metallic) impurities which accumulate in the melt, and which cannot be gettered during the low-temperature SHJ process.

In the case of SHJ technology, on the other hand, the low-temperature and stress-free processing make it easier to handle thinner wafers than with standard silicon technology. Moreover, the efficiency is independent of the wafer thickness down to around 100µm: the short-circuit current (J_{sc}) loss due to the thinner wafer is compensated by an open-circuit voltage (V_{oc}) gain, enabled by the ultralow surface recombination. This characteristic is illustrated in Fig. 2, which shows the efficiencies of SHJ solar cells from the CEA-INES pilot line. Note that for ‘standard’ technologies with lower V_{oc} , due to a poorer surface passivation, the situation is different, as current losses are not compensated by V_{oc} gains. At the moment, wafer producers are able to offer a price reduction of 1.2–1.5€/wafer per 10µm of thickness reduction [13]. A 130–140µm high-quality n-type wafer is therefore available at the *same price as (or an even lower price than)* 170–180µm high-quality monocrystalline p-type wafers used for passivated emitter and rear cell (PERC) production.

Metallization and interconnection

Two reviews of metallization and interconnections for heterojunction technology were given by Geissbühler et al. [14] and Faes et al. [15]; some of the key elements are summarized here.

- Ten years ago, the first low-temperature pastes (annealed at typically 200°C) had limited conductivity (resistivity as high as 20µΩcm), and two- or three-busbar cells needed high volumes

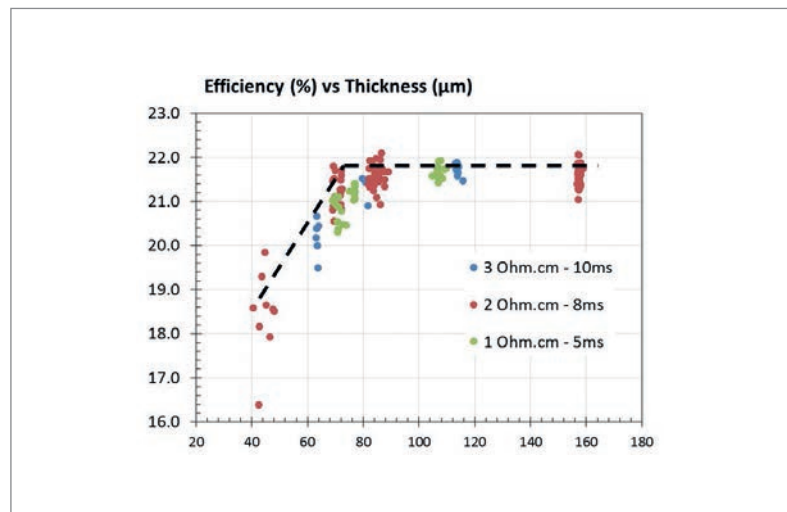


Figure 2. Illustration of SHJ cell efficiency as a function of the wafer thickness for devices made on the CEA-INES pilot line. There is no efficiency loss for wafer thicknesses down to 100µm. The efficiency reduction at a lower thickness is linked to surface and handling processing issues for thinner wafers (which could still be optimized).

of Ag paste. Thanks to the developments by paste manufacturers, there has been a big improvement in low-temperature Ag pastes, with resistivity down to 5–6µΩcm, bridging the gap with high-temperature pastes (demonstrating a typical resistivity of 3µΩcm).

- Additionally, SHJ benefits markedly from the multi-busbar approach (five busbars as a first step, but ideally eight or more), which can be implemented by either gluing or soldering the ribbons. In respect of more advanced solutions, multiwire (equivalent to >15 ‘busbars’) approaches are highly attractive (Fig. 3(a)), as they allow even lower Ag paste consumption, with effective finger lengths shorter than 5mm.

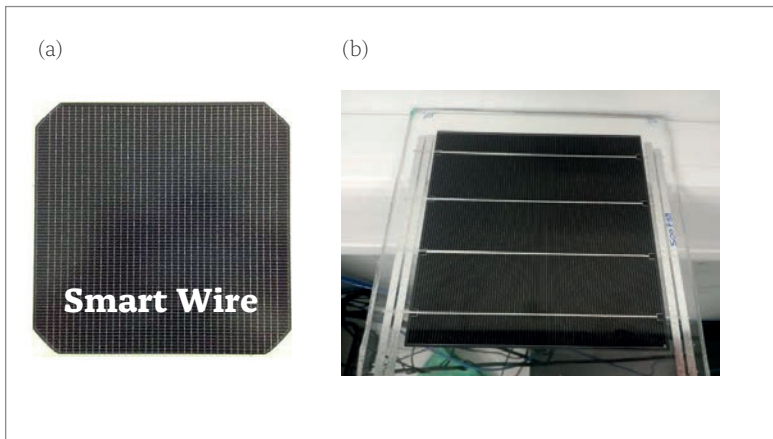


Figure 3. (a) New-generation Smart Wire Connection Technology (SWCT), enabling effective finger lengths of <5mm. (b) Cu-plated four-busbar SHJ solar cell produced at CSEM, with a certified efficiency of 24.15% (designated area efficiency, for an area of 225cm²).

“SHJ technology has the lowest number of process steps.”

- Alternatively, one can replace Ag by copper plating; several groups and companies have reported excellent results with plating [14,16–18], as illustrated in Fig. 3(b). Such approaches can be combined with shingling approaches with

a limited number of cuts (one to three cuts per cell), noting that the front TCO acts as an excellent barrier to copper.

As an example, the smart-wire approach (Fig. 3(a)) is typically based on 18 to 24 wires, with a diameter range of 250–300µm, attached to a thin, highly transparent carrier foil [19]. This geometry allows a minimum amount of printed Ag paste for the front and rear metallization (25–45mg per side, with the possibility of reducing this to 10mg [20]). This ‘soft’ process does not lead to microcrack generation, even with thin wafers. Modules based on this technique have frequently passed all accreditation tests [21]. Remarkably high module fill factors in the range of 80% (Fig. 4) are made possible, and the technique should currently allow the lowest total cost for the metallization and interconnection of SHJs [15].

In conclusion, certified and reliable metallization and interconnection approaches with inexpensive materials are now available. Further advantages are discussed later in this paper.

Heterojunction process simplicity

The SHJ process has had the reputation in the past of being difficult to control, as it is based on equipment and processes that are not familiar to

Meco Plating Equipment

Copper metalization for high efficiency solar cells

- HJT, IBC, bifacial, PERC
- HJT plating: > 24.0%
- > 65% reduction of metalization costs
- Inline process up to 30 - 100 MW tool capacity
- IEC61215 certified
- Eco-friendly processes with maximum material recycling
- 40 years of plating experience
- More than 800 plating tools installed
- Installed base at leading PV manufacturers

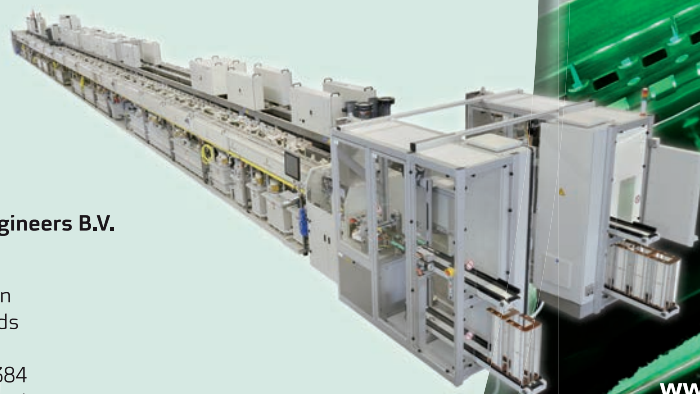


Besi

Meco Equipment Engineers B.V.

Marconilaan 2
5151 DR Drunen
The Netherlands

T: +31 416 384 384
meco.sales@besi.com



Meet us at
SNEC PV Power Expo
Shanghai, June 4-6
Hall N3 - Booth 820-821

www.besi.com

the traditional c-Si community. The mindset is changing, however, since there are many arguments to demonstrate the simplicity and ease of control of this process. The following points are worth noting:

- From the thin-film solar, flat-panel display and glass-coating industries, low-cost coatings per m² have been achieved for PECVD (e.g. from industrial parallel-plate reactors handling, in parallel, 10 plates of 1.4m² [22], or of even up to 5.6m² [23]), as well as for sputtering (PVD), e.g. through more and wider-band magnetrons.
- SHJ technology has the lowest number of process steps – five to seven, depending on the tools and processes.
- It is possible to precisely control the homogeneity

of the thin layers with good tool design, and the process can be made robust against, for example, layer thickness variations [24].

- There are now at least 20 research institutes and pilot or production lines demonstrating efficiencies above 23% as baseline efficiencies for cells on 6" wafers. Lab records reaching 25.1% for two-side-contacted devices have been reported, and up to 26.7% for interdigitated back contact (IBC) configurations [25,26]. Some reference values are given in Table 1.

In the authors' experience, a well-configured set of tools can already produce efficiencies above 22% in the initial processed cells, and a continuous process improvement taking advantage of the

Figure 4. A 72-cell (M2 wafers) module with 412W. The measured FF is 80.18%, with a front-side aperture area efficiency of 20.88%.

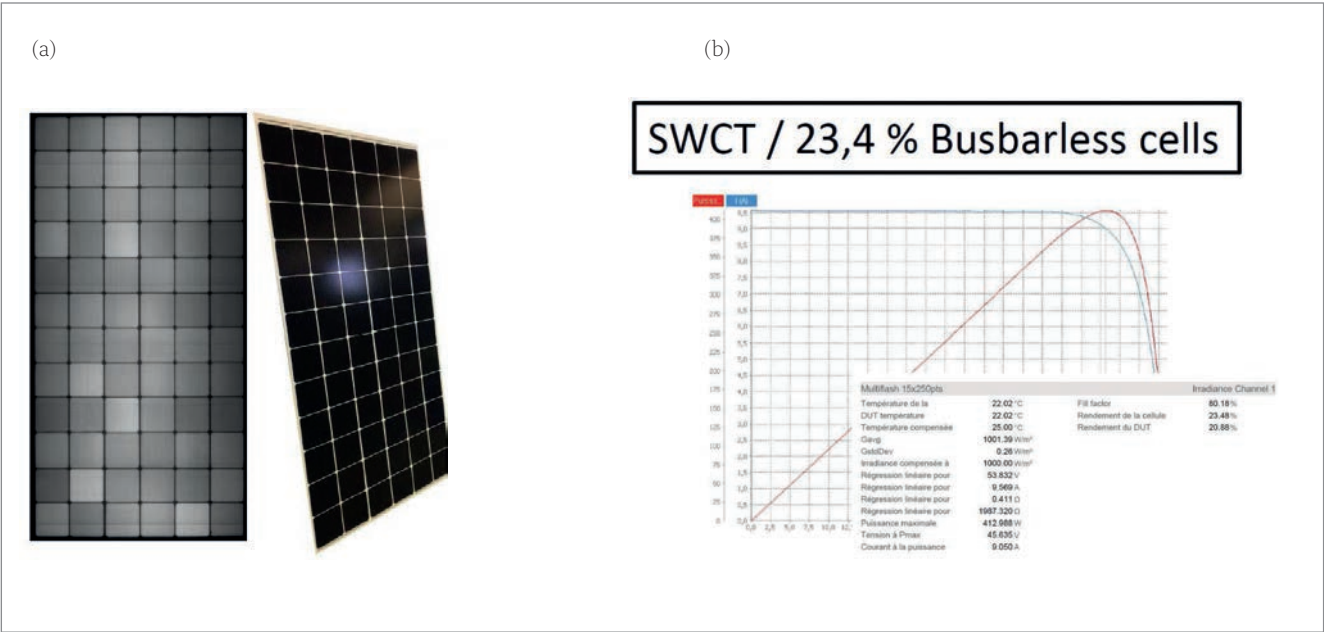


Table 1. Examples of high-efficiency SHJs from various players. The top six are laboratory devices, whereas the bottom six are produced in industrial production/pilot lines. ('BBx' denotes x number of busbars, and 'BBo' denotes busbar-less, i.e. with no current losses from the busbars.)

Efficiency [%]	Company/Institute	Cell type/Specs	Reference
26.7	Kaneka	IBC, 79cm ² , n-type, certified	[27]
25.6	Panasonic	IBC, 144cm ² , n-type, certified	[28]
25.1	Kaneka	100cm ² , n-type, certified	[25]
24.7	Panasonic	102cm ² , n-type, 98μm, certified	[29]
24.2	CSEM/EPFL	4cm ² , n-type, SP, certified	[30]
23.8	CSEM/EPFL	4cm ² , p-type, SP, certified	[30]
24.1	CSEM/CIC	220cm ² , n-type, BB4, Cu-plated, certified	[10]
24.0	Meyer Burger	244cm ² , n-type, BBo, SP, certified	[30]
23.9	CEA-INES	244cm ² , n-type, BB5, SP, certified	[31]
23.7	CIE	244cm ² , n-type, BB5, SP	
23.4	Hanergy	244cm ² , n-type, BB5, SP	
23.4	SIMIT	n-type, plated	



Figure 5. Meyer Burger's HELiA PECVD tool, which uses reactors based on the 'plasma box' concept. This guarantees perfect layer homogeneity, reducing contamination, and facilitates reactor cleaning [35]. Wafer carriers see only one deposition chamber, ensuring that no contamination is introduced by the carriers. (SP = screen printed.)

numerous published results will rapidly lead to efficiencies greater than 23%.

Manufacturing equipment

More and more sets of equipment are now available for production, such as the HELiA PECVD tool from Meyer Burger, shown in Fig. 5.

"An efficiency gain at the cell level and an energy yield gain at the system level *should more than offset the extra CAPEX* for achieving a low cost of solar electricity."

The amorphous silicon layers can be deposited by PECVD with different reactor designs or by CAT-CVD (hotwire), whereas the TCO layers can be deposited by PVD (sputtering) or plasma-assisted evaporation (PAE, otherwise known as RPD, denoting rapid plasma deposition). These techniques have all been proved in production. Even though CAT-CVD and PAE are known to reduce bombardment from high-energy ions, PECVD and PVD layers lead to equally good cell results with proper processes. Other coating techniques, however, have not yet been proved in production. Two other critical elements are:

Advertisement



GENERIS PVD – Inline Sputtering System for Heterojunction Solar Cells

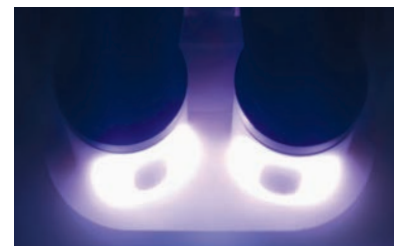
SINGULUS Sputtering Competence at a Glance

SINGULUS has delivered in excess of 8000 vacuum sputtering machines worldwide over the past 20 years. The machines range from standard sputtering systems to ultra-high vacuum deposition machines applying extremely thin layers with capabilities down to 0.2 nm.

The SINGULUS GENERIS PVD machine is a horizontal inline sputter tool designed for the special requirements of Heterojunction cell production with coatings on both sides. By using rotatable sputtering

magnetrons, the highest target utilization is achieved and offers some of the lowest production costs in the industry:

- For transparent conductive oxide layers like ITO and AZO, e.g. for HJT
- Parallel processing of several substrates (Si wafers)
- Low cost of ownership and high uptime
- Top down and bottom up sputtering
- Full temperature control throughout the whole process



- Target utilization about 80 % for rotatable cathodes compared with only 30 % for planar cathodes
- Sputtering materials: ITO, AZO and metals like Ag, NiV, Cu, Al etc.



Figure 6. INDEOtec’s R&D OCTOPUS II, incorporating with the mirror reactor concept. The wafers are placed once on a carrier and receive front and rear a-Si:H coatings while remaining on the same carrier.

- **Wet chemistry**, which is now well under control. The introduction of ozone cleaning can significantly reduce the cost of consumables [32,33].
- **Automation**, which is often underestimated, with many first lines having suffered from issues linked to wafer handling, queue time and sometimes low process control. Experience and production solutions suited to fully exploit these kinds of surface-sensitive device are hence needed. These are not available from all equipment vendors, but as demand grows, new solutions are being introduced [34].

Equipment pricing

In an emerging market, several equipment vendors are reluctant to release official numbers. Currently, the total of core production equipment (wet, PECVD, PVD solutions) should be in the range \$7–13m/100MW, depending on the line suppliers, to which \$3–5m must be added for the remainder of the tools (entrance control, automation, printing, annealing, measurement and sorting). Once the market develops, a significant price drop should take place, as well as simplifications to automation. Even at the current stage, it is worth considering the following elements:

- An extra CAPEX of \$5m/100MW (for cell + module) compared with, for example, a PERC line would lead to about 1¢/W extra cost, when depreciated over five years, which ought to be the case in a sustainable business (i.e. if capital is available and if the market has been in existence for at least five years).
- An efficiency gain at the cell level and an energy yield gain at the system level *should more than offset the extra CAPEX* for achieving a low cost of solar electricity, as will be shown in the next section.

Various approaches to reducing CAPEX, beyond purely manufacturing volumes of tools, include:

SHJ producers	Ramping-up	Piloting	Equipment suppliers
CIE	Ecosolifier	CEA-INES	Applied Materials ^{1,2}
Hanergy	Enel/3sun	Kaneka	Ideal Energy ¹
Hevel	GS Solar	Meyer Burger	Indeotec ¹
Panasonic	Jinergy		Jusung ¹
Solar City	Neo Solar Power		Meyer Burger ^{1,2,3}
Sunpreme	Tongwei		Ulvac ^{1,2}
			Von Ardenne ²
			Singulus ^{4,2}

¹PECVD or CAT-CVD; ²PVD; ³Modules; ⁴Wet chemistry.

Table 2. Overview of some industries involved in the field of SHJ technology.

parallelization of processing reactors, single-carrier processes for PECVD and PVD, in-line processing, and shorter cycling times through suitable system design. For instance, in INDEOtec’s approach, a single hollow carrier allows the deposition of the front and rear a-Si:H, by keeping the wafer on the same carrier, saving on space and automation (Fig. 6).

Table 2 gives an overview of the activities of some of the companies and institutes involved in SHJ technology.

Consumables

The three major cell consumable costs are related to the wet etching and cleaning (currently reported by Singulus at <0.5–0.6¢/W with ozone cleaning [32]), the Ag paste and the TCOs. Ag paste typically comes at a similar price per kg to that of conventional paste, with a conductivity that is lower by a factor of around 0.6–0.7. For a screen-printing pattern equivalent to (for example) a front PERC, a bifacial SHJ (which operates at higher V_{oc} and slightly lower current) will require around twice as much paste, because of differences in paste conductivity. In the case of a six-busbar bifacial configuration, ~180mg Ag/cell is required, equating to ~1.5¢/W (for a paste cost of \$600/kg). This would fall to 0.95¢/W for a multiwire configuration [15], and to almost zero with improved printing patterns for multiwires (10mg/side [20]). With regard to the TCO target

costs, manufacturers typically charge \$520–900/kg for In-based target processing, including the price of In (currently at ~\$220/kg); for 3.5g of target usage for TCO on both sides, this corresponds to 0.80–1.25¢/Wp.

Potential advantages and requirements

On the assumption of a 40µm thinner wafer and a 1%_{abs.} higher efficiency, when the indicative prices given earlier are used, the wafer price would be 6.26¢/W for n-type SHJ (130µm), as opposed to 6.9¢/W for p-type wafers (170µm), i.e. 0.64¢ less per W.

With improvement to the cleaning technology, it can be assumed that cleaning costs will come in line with those for standard technology. Little effort has been made so far to benefit from the low-temperature process for the metallization of SHJ. With a growing market, pastes with lower Ag content, such as Cu-based paste [36], should quickly improve, and could lead to significant price decreases and advantages over high-temperature metallization, where Cu, for example, is particularly not acceptable.

Finally, the TCO costs can be further cut by taking different approaches, such as lowering the target manufacturing cost (–20%), reducing the rear-side TCO thickness (–25%), and possibly substituting

one TCO by ZnO (–30%). In the long run, the TCO costs would be offset by the reduction in cost of the metallization, and the technology will fully benefit from the reduced wafer thickness.

At the module level, a glass–glass configuration is favoured for bifacial modules. To ensure a long lifetime, some manufacturers propose the use of an edge sealant. Depending on the type of screen-printing paste, it is possible to use soldering, gluing or a multiwire assembly for cell interconnection. Compared with a standard busbar soldering and EVA encapsulation material, alternative schemes (e.g. polyolefin – PO – encapsulation material) can ensure higher reliability, usually costing \$2–3 more per m² for the encapsulation material, edge sealant and conductive adhesive or contacting wires. Already at the \$/W level, the extra cost will be fully offset by the efficiency gain if a 1% higher efficiency is assumed, corresponding to an increase in module wattage of 10W/m², which is already typically observed nowadays.

Levelized cost of electricity (LCOE)

Table 3 illustrates some of the effects expected and measured for SHJ modules. The better temperature coefficient can lead to 2–6% additional energy gain compared with a PERC module with –0.38%/°C,

THE
WET PROCESSING
COMPANY

R | E | N | A | .



www.rena.com

RENA BatchTex SHJ

Wet chemical texturization and cleaning
for silicon heterojunction application

- For high throughput mass production of high efficiency SHJ solar cells
- Alkaline texturing with IPA-free RENA monoTEX® process technology
- Low operating costs

Visit us!
SNEC 2019
N3-355



and 6% being an estimation for bifacial one-axis tracking solar parks in a hot climate. Comparing the best datasheet guarantees for SHJ (Panasonic) and PERC (LONGi) over 20 years would yield a gain of 1%_{rel.} in energy. Notably, as for all technologies, some sets of modules can show greater degradation, as is also being reported for PERC modules, which can suffer from various light-induced degradation mechanisms [37]. On the other hand, SHJ modules with properly processed cells show a slight increase in fill factor and V_{oc} under light soaking [38]. Because of their high bifaciality of up to 93%, an additional 2% more energy can be collected compared with standard modules with 82% bifaciality [39]. Finally, with the SHJ's higher voltage, and absence of metal impurities in the junction (leading to a better diode ideality factor), contrary to a diffused screen-printed junction, the low-illumination behaviour should allow 0.3–1% more energy (because of a lower relative voltage drop), depending on the climate. Note that this last factor can be influenced by the edge losses of SHJ cells, which, if not properly addressed, will tend to be higher than for devices with a diffused junction. With regard to this last aspect, a selection of the right coating sequence, carrier opening (e.g. in sputtering) and process parameters (e.g. coating of the edge of the wafer) should be optimized to reduce the edge losses to a minimum. Note that efficiencies of 24% or thereabouts have already been demonstrated on full wafers.

Depending on the mounting configuration, high-quality SHJ modules could therefore deliver 5.5–10% more energy per rated watt over 20 years; in the case of an equivalent module design with 6" cells, this gain should be supplemented by a 10W power gain per m². For large parks, assuming total system costs of 70¢/W and module costs of 25¢/W, there is a further gain to be had on the area- and engineering-related cost (here estimated at \$50/m²). If a conservative 7% increase in energy yield is assumed on the basis of Table 3, this means that the SHJ modules could be 6¢/W more expensive but still lead to the same LCOE. The above-mentioned gain, discussed in Haschke et al. [40], is illustrated in Fig. 7, where passivated emitter, rear totally diffused (PERT) bifacial modules and SHJ bifacial modules are compared in the United Arab Emirates (UAE) [33].

From lab to fab

Some recent results on SHJ cells were shown in Table 1; these include some of the most recent 2cm × 2cm screen-printed devices made by CSEM/EPFL. Certified efficiencies of 24.24% and 23.76% for n- and p-type wafers respectively have been achieved (designated area – da – measurements) using the process flow in Fig. 1. For n-type, similar results have been obtained on Cz-Wafers. Table 1 also indicates various results on industrial cell sizes with similar process flows to those described in this paper, as well as the figures for back-contacted record cells.

Parameter	Expected EY gain vs PERC	Remarks
Impact of TC- P_{MPP} (-0.20 to -0.27%/°C)	2-6%	2% cold climate, 4% hot climate, 5-6% for 1 axis track bifacial or for BIPV
No PID or other degradation	1.2-3%	Based on best data sheets from manufacturers -0.3%/year from year 2 vs. 0.45%/year for best PERC
Bifaciality (f_{bifi})	2%	Assuming 20% rear illumination f_{bifi} SHJ = 93%, f_{bifi} PERC = 82%
Low illumination	0.3-1.0%	Estimates for V_{oc} of 740mV (SHJ), 680mV (PERC) for resp. high, low average irradiance
Total	5.5-10%	

Table 3. Potential percentage gain in energy yield (EY) by SHJ technology relative to PERC. ('BIPV' denotes building-integrated photovoltaics.)



Figure 7. Field data collected from PERT bifacial modules and SHJ SWCT bifacial modules.

Cells in pilot and production lines

There are now more and more players in the field, and several 50–200MW lines have been deployed, several of which are operating on a 24/7 basis, as shown in Table 2. Besides Panasonic, plans for GW lines have been announced by several manufacturers, some with first-phase constructions. There will be a need for volume, as with all c-Si technologies, in order to compete with the absolute lowest manufacturing costs in terms of \$/W. At an intermediate production level (100–500MW),

Source: Courtesy A. Richter, Meyer Burger [41].

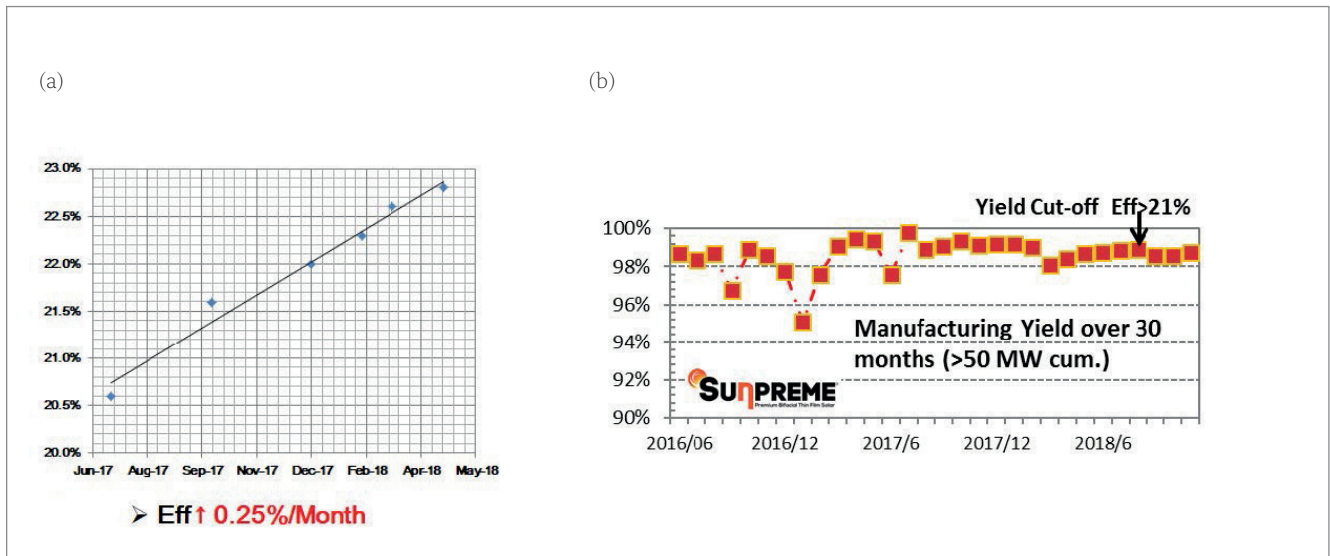


Figure 8. (a) Ramping-up of production at CIE (China), showing the significant efficiency increase (BB5 SHJ solar cells) over the first year (courtesy CIE). (b) Production yield for over 50MW produced cells, with a yield of around 99% in 2018 (for >21%, average 22.2%, five busbars).

there is still room for a competitive market entry in terms of cost of energy, by considering energy yield benefits.

At the 6"-cell level, several pilot lines have achieved efficiencies in the range 22.5–24%; for instance, Fig. 3(b) shows cells with 24.15% after plating (four-busbar measurements). In its demo line in Germany, Meyer Burger has demonstrated runs yielding an average efficiency of 23.65%,

and certified 24.17%-efficiency best cells in the busbarless (BBo) mode (a popular industry standard, taking no account of either the shading from busbars or some of the resistive losses in the fingers, corresponding to ~0.5–0.6% efficiency gain compared with a five-busbar cell) [12]. Note that these are pilot-line cell results, whereas some of the high-efficiency PERC cell results rely on localized passivating contacts not representative of

VON ARDENNE

www.vonardenne.biz

GW

IGA ATT

FUTURE-PROOF COATING EQUIPMENT

MAXIMUM PERFORMANCE FOR MINIMUM CAPEX PER GIGAWATT

Are you looking for coating equipment with a low cost of ownership for crystalline or thin-film photovoltaics and for technologies such as HJT, PERC, CIGS, perovskite or tandem cells? We can provide you with future-proof technology and system solutions in all scales.

Visit our booth at the SNEC (N3-520) and the Intersolar Europe (C1-438)

XENIA

width: up to 3 m

XEA|nova®

8000 wafers/h

XENIA

width: up to 3 m

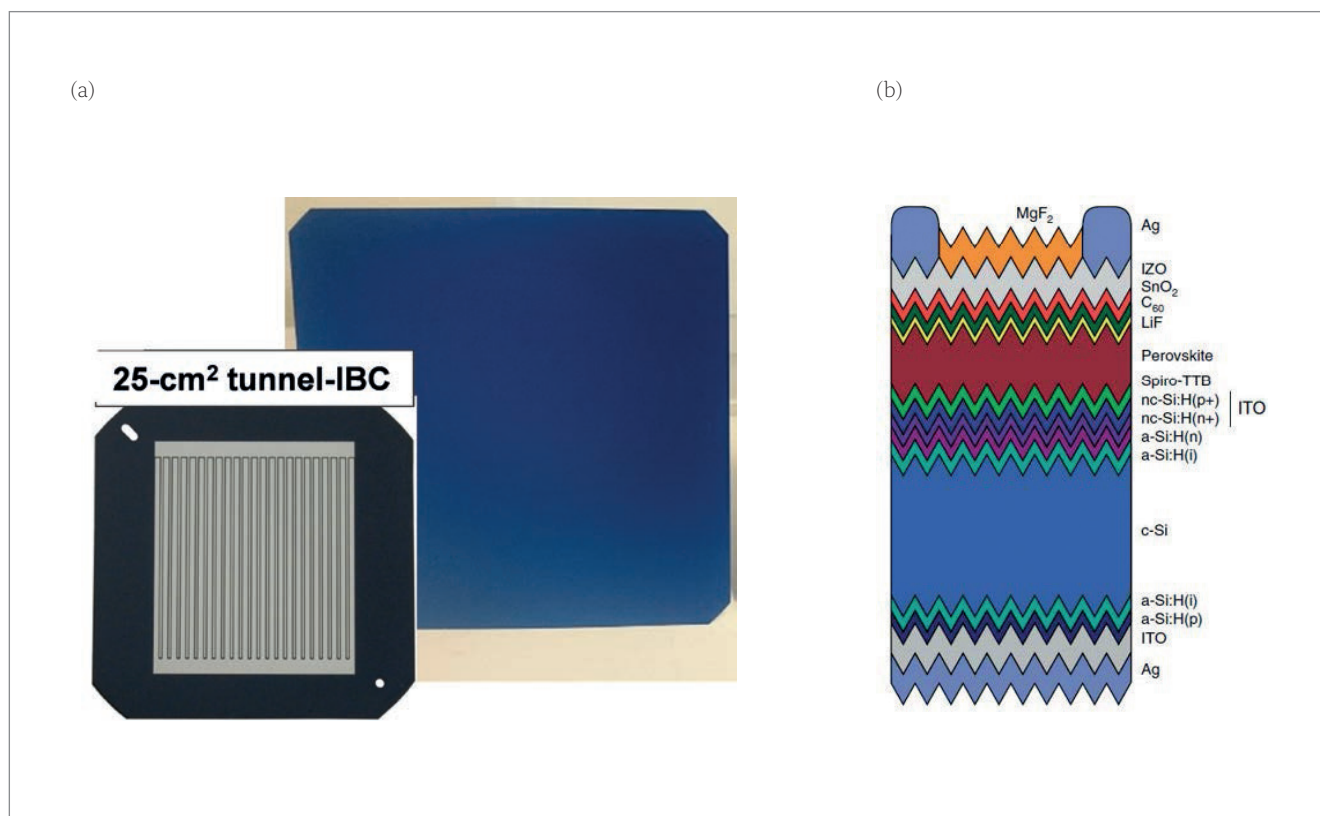


Figure 9. (a) New-generation IBC-SHJ, created at CSEM [42] using the tunnel process, yielding an efficiency of 24.8%. (b) Schematic of the perovskite on textured SHJ cell concept [45].

production status, and not necessarily compatible with low production costs. On the basis of continuous process improvements, CEA was able to demonstrate a 23.9%-certified five-busbar SHJ using Meyer Burger production tools. With line optimization and further improvement in printing and TCO, efficiencies in the range 24–24.5% should be targetable.

Table 1 illustrates that lab results can readily be transferred to production tools; for instance, using multiwire technology, certified modules with 341W (60 cells) and 412W (72 cells) of standard-size wafers (M2) have been obtained, with FFs reaching 79.7% and >80% respectively – remarkable values, illustrating the maturity of the technology. More recently, CEA and Meyer Burger produced a 348W standard 60-cell module with high efficiency by using half cells. As well as Panasonic, Sunpreme and Hevel, several production lines are now running with 6" cells, achieving high efficiencies, such as Hanergy at 22.2–22.3% and CIE at 23% average (all values reported in October 2018). All these companies are still on the efficiency learning curve: Fig. 8(a) shows the improvement in average cell efficiency from 20.5% to 22.8% in 10 months during 2017/18. After an adaptation of some equipment, average efficiencies are surpassing 23% (Oct 2018). The production yields have been reported by manufacturers or by pilot lines to be at high levels, coming close to 99%, as indicated, for example, by Sunpreme (Fig. 8(b)).

“SHJ is set to become one of the most attractive PV technologies.”

Extending the learning curve

On the basis of the lab and pilot-line results, it can be expected that screen-printed, multi-busbar devices will reach, with full optimization, efficiencies in the range 24–24.5%.

Extending the efficiency curve

There are two ways SHJ could, in a next step, evolve towards a higher-efficiency product.

First, one can add a set of tools to realize back-contacted cells with a 5–8%_{rel.} efficiency increase. Such a device structure holds the world record for c-Si-based PV, including 26.7% by Kaneka [26]. Although the processing steps required to achieve such an impressive efficiency result are probably not straightforward to industrialize, Fig. 9(a) shows an image of a 25cm² cell created using the tunnel junction approach, which drastically simplifies the processing of IBC devices [42]. It notably requires only one in situ patterned contact layer, and one alignment step for the metallization. Certified results of 24.45% [43], and more recent in-house results of 24.8% (25cm²), have already been obtained.

Second, SHJ solar cells are ideal as a bottom cell in multijunction devices; they were used in the record-breaking four-terminal III-V on Si (32.8% for two junctions, and 35.9% for three junctions) [44]. These cells also serve as an ideal bottom

“At the 6" cell level, several pilot lines have achieved efficiencies in the range 22.5–24%.”

cell for perovskite/silicon tandem devices (Fig. 9(b)), with a recently certified efficiency of 25.24% [45]. Even more recently, Oxford PV announced a 27.3% efficiency, and even 28.0%, presumably with an SHJ bottom cell [46]. These approaches could lead to >30% efficiency 6" solar cells, even though there are still cost and reliability hurdles to overcome in order to achieve the status of a bankable product.

Conclusions

Over the last 10 years, there have been a number of significant improvements in the field of SHJ technologies. These include:

- The development of processes compatible with low-cost industrial production.
- The technology becoming widespread, with more and more groups achieving efficiencies above 23%.
- The development of advanced metallization and interconnections technologies.
- The improvement of n-type wafer material quality.
- The achievement of high efficiency on production tools.
- The availability of comprehensive production solutions.

If and when capital is available, SHJ is set to become one of the most attractive PV technologies. One can therefore assume that it is now ready for a true mass-production launch.

Acknowledgements

The authors acknowledge funding from the European Union's Horizon 2020 research and innovation programmes under Grant Agreement Nos. 745601 (Ampere), 727529 (Disc) and 727523 (NextBase), from the Swiss Federal Office for Energy, from Innosuisse, from SNF, PNR70, Bridge and Nanotera, and from industrial partners, including Meyer Burger, 3Sun and INDEOtec. A special thanks goes to all members at EPFL PV-lab, CSEM PV-center and CEA-Ines, as well as to all academic partners, RTOs and companies who provided us with data or information for this paper.

References

- [1] De Wolf, S. et al. 2012, “High-efficiency silicon heterojunction solar cells: A review”, *Green*, Vol. 2, No. 1, pp. 7–24.
- [2] Tanaka, M. et al. 1992, “Development of new a-Si/c-Si heterojunction solar cells: ACJ-HIT (Artificially Constructed Junction-Heterojunction with Intrinsic Thin-Layer)”, *Jpn. J. Appl. Phys.*, Vol. 31, No. 11, pp. 3518–3522.

- [3] Keppner, H. et al. 1994, “Passivation properties of amorphous and microcrystalline silicon layers deposited by VHF-GD for crystalline silicon solar cells”, *Sol. Energy Mater. Sol. Cells*, Vol. 34, No. 1–4, pp. 201–209.
- [4] Haschke, J. et al. 2018, “Silicon heterojunction solar cells: Recent technological development and practical aspects – from lab to industry”, *Sol. Energy Mater. Sol. Cells*, Vol. 187, pp. 140–153.
- [5] Bivour, M. et al. 2014, “Doped layer optimization for silicon heterojunctions by injection-level-dependent open-circuit voltage measurements”, *IEEE J. Photovolt.*, Vol. 4, No. 2, pp. 566–574.
- [6] Mazzarella, L. et al. 2015, “p-type microcrystalline silicon oxide emitter for silicon heterojunction solar cells allowing current densities above 40 mA/cm²”, *Appl. Phys. Lett.*, Vol. 106, p. 023902.
- [7] Jay, F. et al. 2014, “Advanced process for n-type mono-like silicon a-Si:H/c-Si heterojunction solar cells with 21.5% efficiency”, *Sol. Energy Mater. Sol. Cells*, Vol. 130, pp. 690–695.
- [8] Kobayashi, E., Watabe, Y. & Yamamoto, T. 2015, “High-mobility transparent conductive thin films of cerium-doped hydrogenated indium oxide”, *Appl. Phys. Express*, Vol. 8, No. 1.
- [9] Herasimenka, S.Y. et al. 2016, “ITO/SiO_x:H stacks for silicon heterojunction solar cells”, *Sol. Energy Mater. Sol. Cells*, Vol. 158, pp. 98–101.
- [10] Descoeudres, A. et al. 2018, “Low-temperature processes for passivation and metallization of high-efficiency crystalline silicon solar cells”, *Sol. Energy*, Vol. 175, pp. 54–59.
- [11] Louwen, A. et al. 2016, “A cost roadmap for silicon heterojunction solar cells”, *Sol. Energy Mater. Sol. Cells*, Vol. 147, pp. 295–314.
- [12] Zhao, J. et al. 2018, “>24% silicon heterojunction solar cells on Meyer Burger's mass production tools and how wafer material impacts cell parameters”, *Proc. 7th WCPEC, Waikoloa, Hawaii, USA (Joint Conf. 45th IEEE PVSC, 28th PVSEC & 34th EU PVSEC)*, 2018, pp. 1514–1519.
- [13] Wang, Y.C. 2018, “Mass production high quality and cost effective n type wafer supply”, Shanghai.
- [14] Geissbühler, J. 2017, “Metallization techniques and interconnection schemes for high efficiency silicon heterojunction PV”, *Photovoltaics International*, 37th edn, p. 67.
- [15] Faes, A. et al. 2018, “Metallization and interconnection for high-efficiency bifacial silicon heterojunction solar cells | PV Tech”, *Photovoltaics International*, Vol. 41, p. 65.
- [16] Li, B. 2016, “Industrial bifacial silicon heterojunction technology that improves system LCOE”, HERCULES Workshop, Berlin, Germany.
- [17] Yamamoto, K. et al. 2015, “High-efficiency heterojunction crystalline Si solar cell and optical splitting structure fabricated by applying thin-film Si technology”, *Jpn. J. Appl. Phys.*, Vol. 54, No. 8S1, p. 08KD15.
- [18] Yu, J. et al. 2015, “Tungsten doped indium oxide

- film: Ready for bifacial copper metallization of silicon heterojunction solar cell", *Sol. Energy Mater. Sol. Cells*, Vol. 144, pp. 359–363.
- [19] Papet, P. et al. 2015, "New cell metallization patterns for heterojunction solar cells interconnected by the Smart Wire Connection Technology", *Energy Procedia*, Vol. 67, pp. 203–209.
- [20] Brok, W. et al. 2014, "Advanced metallization concepts by inkjet printing", *Proc. 29th EU PVSEC*, Amsterdam, The Netherlands.
- [21] Bonnet-Eymard, B. et al. 2018, "New generation SmartWire Modules Technology", 8th nPV Worksh., Lausanne, Switzerland.
- [22] Meier, J. et al. 2005, "Progress in up-scaling of thin film silicon solar cells by large-area PECVD KAI systems", *Proc. 31st IEEE PVSC*, Lake Buena Vista, Florida, USA, pp. 1464–1467.
- [23] Applied Materials 2019, "Applied PECVD 5.7" [<http://www.appliedmaterials.com/products/applied-pecvd-57>].
- [24] Zimmermann, T. et al. 2014, "Deposition of intrinsic hydrogenated amorphous silicon for thin-film solar cells – A comparative study for layers grown statically by RF-PECVD and dynamically by VHF-PECVD", *Prog. Photovolt: Res. Appl.*, Vol. 22, No. 2, pp. 198–207.
- [25] Adachi, D., Hernández, J.L. & Yamamoto, K. 2015, "Impact of carrier recombination on fill factor for large area heterojunction crystalline silicon solar cell with 25.1% efficiency", *Appl. Phys. Lett.*, Vol. 107, No. 23, p. 233506.
- [26] Yamamoto, K. et al. 2018, "High-efficiency heterojunction crystalline Si solar cells", *Jpn. J. Appl. Phys.*
- [27] Green, M.A. et al. 2018, "Solar cell efficiency tables (version 51)", *Prog. Photovolt: Res. Appl.*, Vol. 26, No. 1, pp. 3–12.
- [28] Masuko, K. et al. 2014, "Achievement of more than 25% conversion efficiency with crystalline silicon heterojunction solar cell", *IEEE J. Photovolt.*, Vol. 4, No. 6, pp. 1433–1435.
- [29] Taguchi, M. et al. 2014, "24.7% record efficiency HIT solar cell on thin silicon wafer", *IEEE J. Photovolt.*, Vol. 4, No. 1, pp. 96–99.
- [30] Ballif, C., Boccard, M. & Despeisse, M. 2018, "From wafers to modules to mass production: Solving all bottlenecks in silicon heterojunction technology", *Proc. 35th EU PVSEC*, Brussels, Belgium.
- [31] CEA Liten 2018, "New record for heterojunction technology" [<http://liten.cea.fr/cea-tech/liten/Pages/actualites/Hétérojonction--record-de-rendement-.aspx>].
- [32] Zhang, Z. 2018, "Starting the era of HJT solar cells – Technical insight into advanced ozone cleaning based on SINGOZON Technology and optimized magnetron sputtering for damage-free processing of TCO layers", *Proc. 1st Int. Worksh. Sil. Heterojunc. Sol. Cells: Sci. Ind. Technol.*
- [33] Richter, A. 2018, "System design & optimization and performance energy yield of bifacial module technologies and yield estimation methods by rule of thumb", *Proc. 7th WCPEC*, Waikoloa, Hawaii, USA (Joint Conf. 45th IEEE PVSC, 28th PVSEC & 34th EU PVSEC).
- [34] Izzi, M. et al. 2018, "AMPERE: A European project aimed to decrease the levelized cost of energy with innovative heterojunction bifacial module solution ready for the market", *Proc. 7th WCPEC*, Waikoloa, Hawaii, USA (Joint Conf. 45th IEEE PVSC, 28th PVSEC & 34th EU PVSEC), pp. 569–572.
- [35] Bubenzer, A. & Schmitt, J.P.M. 1990, "Plasma processes under vacuum conditions", *Vacuum*, Vol. 41, No. 7–9, pp. 1957–1961.
- [36] Faes, A. et al. 2018, "Direct contact to TCO with SmartWire Connection Technology", *Proc. 7th WCPEC*, Waikoloa, Hawaii, USA (Joint Conf. 45th IEEE PVSC, 28th PVSEC & 34th EU PVSEC), pp. 1998–2001.
- [37] Kopecek, R. 2018, "Is LeTID degradation in PERC cells another degradation crisis even worse than PID?", PV-Tech Guest Blog [<https://www.pv-tech.org/guest-blog/is-letid-degradation-in-perc-cells-another-degradation-crisis-even-worse-th>].
- [38] Kobayashi, E. et al. 2017, "Increasing the efficiency of silicon heterojunction solar cells and modules by light soaking", *Sol. Energy Mater. Sol. Cells*, Vol. 173, pp. 43–49.
- [39] Kopecek, R. & Libal, J. 2018, *Bifacial Photovoltaics: Technology, applications and economics*, London: Institution of Engineering and Technology (IET).
- [40] Haschke, J. et al. 2017, "The impact of silicon solar cell architecture and cell interconnection on energy yield in hot & sunny climates", *Energy Environ. Sci.*, Vol. 10, No. 5, pp. 1196–1206.
- [41] Richter, A. 2018, "An approach to quantify benefits & risks of bifacial PV systems based on energy yield", 5th Bifi PV Workshop, Denver, Colorado, USA.
- [42] Tomasi, A. et al. 2017, "Simple processing of back-contacted silicon heterojunction solar cells using selective-area crystalline growth", *Nat. Energy*, Vol. 2, No. 5, p. 17062.
- [43] Despeisse, M. et al. 2018, "Engineering of thin-film silicon materials for high efficiency crystalline silicon solar cells", *Proc. 7th WCPEC*, Waikoloa, Hawaii, USA (Joint Conf. 45th IEEE PVSC, 28th PVSEC & 34th EU PVSEC), pp. 3888–3889.
- [44] Essig, S. et al. 2017, "Raising the one-sun conversion efficiency of III–V/Si solar cells to 32.8% for two junctions and 35.9% for three junctions", *Nat. Energy*, Vol. 2, No. 9, p. 17144.
- [45] Sahli, F. et al. 2018, "Fully textured monolithic perovskite/silicon tandem solar cells with 25.2% power conversion efficiency", *Nat. Mater.*, Vol. 17, No. 9, pp. 820–826.
- [46] NREL 2019, "Best research-cell efficiencies" [<https://www.nrel.gov/pv/assets/pdfs/pv-efficiency-chart.20190103.pdf>].

About the Authors



Christophe Ballif received his Ph.D. from EPFL in 1998. In 2004 he became a full professor with the Institute of Microengineering at the University of Neuchâtel, Switzerland, where he directs the Photovoltaics and Thin-Film Electronics Laboratory, which is now part of EPFL. Since 2013 he has also been the director of the CSEM PV-center. His research interests include materials for PV, high-efficiency c-Si solar cells, module technology, BIPV and energy systems.



Mathieu Boccard received his Ph.D. from EPFL in 2012 for his work on thin-film-silicon tandem solar cells at the PV-Lab. He then joined ASU in Tempe, USA, as a postdoc, specializing in high-efficiency crystalline silicon, CdTe-based and perovskite/silicon tandem solar cells. Since 2017 he has led the silicon heterojunction activities at PV-Lab, working on fundamentals and novel materials for carrier-selective contacts, multijunction devices and location-dependent solar cell design.



Antoine Descoedres received his M.Sc. and Ph.D. in physics from EPFL in 2001 and 2006 respectively. He was a postdoctoral researcher at CERN, Geneva, from 2007 to 2009, and at the PV-Lab in Neuchâtel, from 2009 to 2013. In 2013 he joined the PV-center at CSEM, where he is responsible for the development of silicon heterojunction solar cells.



Christophe Allebé received his master's in physics from the Université Catholique de Louvain. From 2000 to 2011 he was at the Interuniversity Microelectronics Center, Leuven, and then at its spin-off company Photovoltech, focusing on crystalline-silicon-based homojunction solar cells. He subsequently switched to Si-based heterojunction solar cells while working for Kaneka in Japan. In 2013 he joined the CSEM PV-center, where he works on processes and approaches for enabling high solar cell performance.



Antonin Faes received his Ph.D. in 2010 for his work on solid oxide fuel cells at the Interdisciplinary Center for Electron Microscopy (CIME) and the Industrial Energy System Laboratory (LENI) at EPFL. In 2012 he joined the CSEM PV-center in Neuchâtel, where he is responsible for c-Si solar cell metallization and interconnection activities, with a particular focus on silicon heterojunction solar cells.



Olivier Dupré received his Ph.D. in 2015 from INSA-Lyon (France) for his work on the thermal behaviour of photovoltaic devices. He is now a researcher at the PV-Lab, EPFL, working on silicon heterojunction and perovskite/silicon tandem solar cells. His research interests include the development of solutions at the cell and module levels to maximize PV energy output for specific locations and operating conditions.



Jan Haschke received his Ph.D. in electrical engineering from the Technical University Berlin in 2014. He is currently working as a postdoctoral research engineer with EPFL at the PV-Lab in Neuchâtel. His research interests include development and understanding of high-efficiency silicon heterojunction solar cell devices and fabrication processes.



Pierre-Jean Ribeyron received his Ph.D. on the crystallization of multicrystalline silicon for PV applications in 1998 from the University of Grenoble-Alps (France). In 2000 he joined CEA to build the first R&D platform for silicon solar cell technology. After the creation of INES in 2005, he focused on high-efficiency solar cells, especially silicon heterojunctions. He now works on the entire value chain, from silicon material through modules to PV systems.



Matthieu Despeisse received his Ph.D. in 2006 for his work on advanced detectors at CERN in Geneva. He then joined EPFL in 2009 as head of the thin-film silicon photovoltaics research team. Since 2013 he has led research activities at CSEM concerning crystalline silicon photovoltaics and metallization, with a special focus on silicon heterojunction technology, passivating contacts, silicon-based multi-junction cells, metallization and interconnection.

Enquiries

Mathieu Boccard
Ecole Polytechnique Fédérale de Lausanne (EPFL)
Institute of Microengineering (IMT)
Photovoltaics and Thin-Film Electronics Laboratory (PV-Lab)
Rue de la Maladière 71b
2002 Neuchâtel, Switzerland

Email: mathieu.boccard@epfl.ch

Beyond boron–oxygen deactivation: Industrially feasible LID-free p-type Czochralski silicon

Bianca Lim¹, Agnes Merkle¹, Robby Peibst^{1,2}, Thorsten Dullweber¹, Yichun Wang³ & Rui Zhou³

¹Institute for Solar Energy Research Hamelin (ISFH), Emmerthal, Germany

²Institute of Electronic Materials and Devices, Leibniz Universität Hannover, Hanover, Germany

³LONGi Clean Energy Technology Co., Ltd., Xi'an City, China

Abstract

Today's industry-standard B-doped monocrystalline silicon still suffers from light-induced degradation (LID) of the carrier lifetime. Illumination at elevated temperatures leads to a so-called *regeneration*, i.e. a recovery of both the carrier lifetime and the solar cell efficiency. However, even though the carrier lifetime on test wafers increases from about 1ms after processing to 3ms after regeneration, the corresponding PERC+ cell efficiencies in both states are identical; possible reasons for this discrepancy are discussed in this paper. Additionally, B-doped Czochralski silicon wafers with an ultralow oxygen content of 2.6 ppma are evaluated, as well as industrial Ga-doped wafers. Both wafer materials are completely LID free, as demonstrated in lifetime measurements and PERC+ cell efficiencies, and enable up to 0.4%_{abs.} higher efficiencies than current industry-typical boron-doped wafers.

Introduction

About 35% of current global PV production uses B-doped monocrystalline silicon (c-Si) [1]. Advances in the Czochralski (Cz) process, i.e. the crystal growth technique, have resulted in ever-better material quality and ever-lower prices. This in turn supports the roll-out of high-efficiency passivated emitter and rear cells (PERCs), which already yield efficiencies of up to 21.5–22.0% in mass production when using Cz-Si [2–5].

Yet, despite all advances, industrial B-doped Cz-Si still contains significant amounts of interstitial oxygen. This, in combination with the boron doping, results in light-induced degradation (LID) of the carrier lifetime and, in turn, the solar cell efficiency.

Boron–oxygen (BO)-related LID was first reported in 1973 [6] and was studied in detail in the late 1990s and early 2000s. As this degradation is firmly linked to the simultaneous presence of both boron and oxygen [7,8], two straightforward ways to avoid it are to either reduce the interstitial oxygen content or replace boron as a dopant (e.g. with Ga for p-type or with P for n-type wafers) [7,9].

One way to produce low-oxygen Cz-Si is to employ a strong magnetic field during the silicon crystal growth process [10]; however, this technology

has not entered mass production, probably because production costs are too high. Replacing boron with gallium is not as straightforward as it sounds either; using standard Czochralski processes for Ga-doped ingots results in a very large increase in doping concentration along the ingot.

A third option to mitigate LID due to BO-related defects is the permanent deactivation of these defects, which can be done by generating excess carriers at elevated temperatures, e.g. by illumination. The resulting regeneration of the solar cell characteristics and the carrier lifetime was first reported in 2006 [11]. The process can be employed with all B-doped Cz-Si materials and solar cells; however, the effectiveness of regeneration depends on a variety of material and process parameters.

In work reported in this paper, the carrier lifetime, as well as the solar cell efficiency potential of current industry-standard B-doped Cz-Si, is evaluated. For this, dedicated test samples are used for lifetime measurements, along with an in-house PERC+ solar cell baseline process which typically yields energy conversion efficiencies of around 21.5% [12].

Lifetime and efficiency are measured after full LID due to BO-related defects, and after applying an optimized, lab-type regeneration treatment.

The performance of industry-standard B-doped Cz-Si is compared with that of industrial Ga-doped Cz-Si as well as with that of B-doped Cz-Si wafers with ultralow oxygen content. The latter wafers result from an advanced pulling technology that is being developed by LONGi as a potential candidate for future mass production of high-quality and low-cost Cz-Si wafers.

The lifetimes measured on dedicated test samples are used as an input parameter for device simulations, and the results are compared with the measured solar cell characteristics. In particular, lifetime and solar cell efficiency are measured in three different states: 1) directly after processing; 2) after 24h of illumination at room temperature (which results in complete LID for the industry-standard B-doped Cz-Si); and 3) after applying the regeneration treatment.

“Despite all advances, industrial B-doped Cz-Si still contains significant amounts of interstitial oxygen.”

By means of this sequence of measurements, an assessment of the effectiveness of the permanent deactivation of BO-related defects is essentially made, as well as of the extent of LID (if any) in the advanced Cz-Si wafers with Ga doping or ultralow oxygen content. Also investigated is whether there are any other lifetime-limiting defects present in industry-standard B-doped Cz-Si that are not observed in Ga-doped or oxygen-lean B-doped Cz-Si.

Bulk lifetimes of the different Cz-Si wafer materials

Four different Czochralski-grown (Cz) silicon materials from LONGi Clean Energy Technology Co. are studied in terms of stability of the bulk lifetimes. Two of the materials are industrial B-doped Cz-Si with 'standard' interstitial oxygen concentrations of 12 and 16 ppma respectively. The other two materials are assessed as industrial-scale LID-free options; the first is B-doped Cz-Si with an extremely low interstitial oxygen concentration of 2.6 ppma, and the second is Ga-doped Cz-Si from an industrial-type puller. The ultralow oxygen concentration of 2.6 ppma was achieved by using an advanced Cz pulling technology developed by LONGi, which reduces the oxygen dissolution into the silicon melt during crystallization.

Table 1 summarizes the resistivities and interstitial oxygen concentrations (measured by

Fourier-transform infrared spectroscopy – FTIR – using the ASTM F121-83 standard) of the four materials. The wafers are of dimension 156.75mm × 156.75mm (M2) and have an initial thickness of around 180µm.

To measure the bulk lifetime, symmetrical test structures are processed. First, the saw damage is removed and the wafers cleaned. The wafers then go through the same POCl_3 diffusion that is used for the baseline PERC+ solar cell process. On the one hand, this acts as a gettering step; on the other, it adds to the thermal history of the wafers and keeps it close to that of the PERC+ solar cells. Subsequently, the resulting n^+ regions on both surfaces are etched off and the wafers cleaned, and an $\text{AlO}_x/\text{SiN}_x$ stack is deposited on the front and the rear for optimal surface passivation.

Finally, the lifetime samples are fired in a belt-firing furnace. Note that there are two groups, which are fired at two different belt speeds: 5.6m/min, which is the speed at which the solar cells are fired, and 6.8m/min, in order to obtain optimum lifetimes after regeneration [13].

After firing, the lifetime samples are in the 'as-processed' state. The carrier lifetimes are then measured with a WCT-120 Lifetime Tester from Sinton Instruments, both in quasi-steady state and in photoconductance decay mode.



SENTECH

SENperc PV

QC for solar cell manufacturing



The innovative solution for quality control of coatings on PERC cells

- QC for multi- and c-Si based solar cell manufacturing
- Thickness measurement of AR coatings and passivation layers
- Long-term stability monitoring of deposition process
- Easy recipe based push button operation
- Software interface for data transfer
- Compact design

www.sentech.com
mail: marketing@sentech.de
phone: +49 30 63 92 55 20

Next, the samples are illuminated for 24h at around 0.1 Suns and at room temperature to activate the BO-related defects. With regard to the bulk resistivity values of up to 2.1Ωcm, 24h was chosen in order to reach saturation of LID [14]; at this point, the lifetime is measured again.

Finally, the regeneration treatment is applied, and the lifetime measured for a third time. The lab-type regeneration process consists of annealing on a hotplate set to 185°C and simultaneously illuminating with a halogen lamp at a light intensity of around 1 Sun for 15 min. It is important to note that it was verified that no further increase in lifetime is observed when annealing under illumination for longer times.

The lifetimes of the four different materials in the three different states are plotted in Figs. 1 and 2. Figs. 1(a) and 2(a) depict the effective lifetimes of inherently LID-free Cz-Si materials, while Figs. 1(b) and 2(b) show the significant changes that happen in B-doped Cz-Si with an industrially typical interstitial oxygen concentration.

Note that Fig. 1 contains the materials with slightly higher resistivities (1.7 and 2.1Ωcm), while Fig. 2 depicts the materials with lower resistivities (1.1 and 1.0Ωcm). The materials are grouped like this because material quality, or rather solar cell potential with regard to material quality, is determined by lifetime as well as resistivity. One can therefore only easily compare lifetimes of materials with similar doping concentrations.

The blue triangles in the graphs correspond to the measured lifetimes after the fast-firing step (as-processed). The red circles give the lifetimes after illumination at room temperature for 24h, i.e. in the case of the B-doped samples after LID. The green diamonds refer to the lifetimes after applying the regeneration treatment (annealing under illumination at 185°C for 15 min). In addition, all graphs contain the respective intrinsic lifetime according to the model of Richter et al. [15] (solid black line).

Fig. 1(a) depicts the effective lifetimes of the 2.1Ωcm B-doped material with ultralow interstitial oxygen concentration of 2.6 ppma. As expected, no LID of the bulk carrier lifetime is observed between the as-processed and the degraded state [16]. However, applying the regeneration treatment improves the lifetime from around 2ms to around 3.8ms at an excess carrier concentration $\Delta n = 10^{15} \text{ cm}^{-3}$.

For the B-doped 1.7Ωcm sample, the lifetimes measured after firing at different belt speeds are plotted in Fig. 1(b). The open symbols correspond to the effective lifetimes measured after firing at a belt speed of 5.6m/min, and the filled symbols correspond to a belt speed of 6.8m/min. For the slower belt speed, the as-processed lifetime (open blue triangles) at an excess carrier concentration of $\Delta n = 10^{15} \text{ cm}^{-3}$ is around 650μs. After 24h of illumination at

No.	Dopant species	Resistivity [Ωcm]	[O] _i [ppma]
1	B	1.7	~16
2	B	1.1	~12
3	B	2.1	2.6
4	Ga	1.0	~16

Table 1. Dopant species, resistivity ρ and interstitial oxygen concentration [O]_i for each of the four different Cz-Si materials investigated.

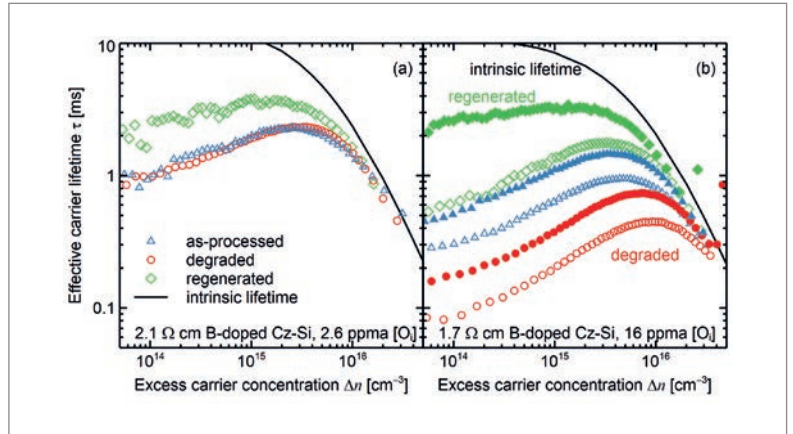


Figure 1. Effective lifetimes as a function of excess carrier concentration: (a) 2.1Ωcm, ultralow [O]_i B-doped Cz-Si; (b) 1.7Ωcm industry-standard B-doped Cz-Si. The blue triangles represent the as-processed state, the red circles the degraded state, and the green diamonds the regenerated state. The open symbols denote a belt speed during fast-firing of 5.6m/min, while the filled symbols indicate a belt speed of 6.8m/min. The solid black line marks the intrinsic lifetime limit according to Richter et al. [15] for the given resistivity.

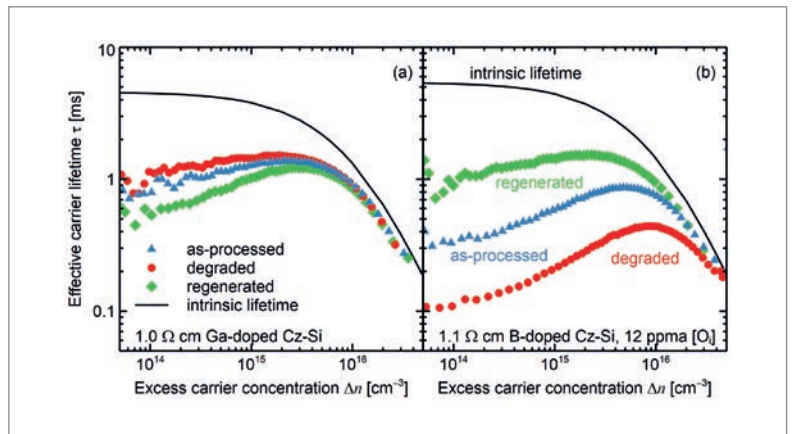


Figure 2. Effective lifetimes as a function of excess carrier concentration: (a) 1.0Ωcm Ga-doped Cz-Si; (b) 1.1Ωcm industry-standard B-doped Cz-Si. The wafers are fired at a belt speed of 6.8m/min. The blue triangles signify the as-processed state, the red circles the degraded state, and the green diamonds the regenerated state. The solid black line marks the intrinsic lifetime limit according to Richter et al. [15] for the given resistivity.

room temperature, the lifetime drops to around 200μs (degraded state, open red circles), and after application of the regeneration treatment, the lifetime increases to around 1.4ms (regenerated state, open green diamonds).

Using a faster belt speed during the fast-firing process notably increases the effective lifetimes in all three states. An as-processed (filled blue triangles) lifetime of 1.1ms at $\Delta n = 10^{15} \text{ cm}^{-3}$ is measured. In the degraded state (filled red circles), the lifetime is

“Industry-standard B-doped Cz-Si wafers perform as well as the inherently LID-free materials with similar doping concentrations.”

around 390 μ s, and regeneration results in an effective lifetime of 3.2ms at

$\Delta n = 10^{15}\text{cm}^{-3}$ (filled green diamonds), which is comparable to the lifetime measured on the ultralow [O]_i Cz-Si.

While such a dependence of the lifetime on the belt speed during fast firing was already shown in Walter et al. [17], it should be noted that this was not observed at ISFH for all B-doped Cz-Si materials. The ultralow [O]_i Cz-Si, for example, yields similar lifetimes after firing at 5.6m/min and 6.8m/min (not shown here).

The fact that even the regenerated lifetime curves are below the intrinsic lifetime published by Richter et al. [15] (solid black line) can be attributed to surface recombination. Assuming a surface recombination velocity of just 2cm/s per side already closes the gap between measured lifetime and intrinsic model; this is a reasonable value for the AlO_x/SiN_y stack used.

On inspection of the measured lifetimes of the Ga-doped Cz-Si (Fig. 2(a)), only small changes are seen, as might be expected. A period of 24h of illumination at room temperature (red circles) actually results in slightly higher lifetimes than those measured in the as-processed state (blue triangles). After the regeneration treatment, however, a slight decrease in the lifetime is seen, especially at excess carrier densities below $5 \times 10^{15}\text{cm}^{-3}$ (green diamonds). This might be a bulk effect, but could also be related to a degradation in the surface passivation quality. However, it needs to be proved with larger wafer numbers whether or not the slight lifetime degradation after regeneration is statistically significant.

In contrast, for the industrial 1.1 Ω cm Cz-Si with an interstitial oxygen concentration of 12 ppma (Fig. 2(b)), the lifetime changes significantly. Approximately 600 μ s was measured in the as-processed state at $\Delta n = 10^{15}\text{cm}^{-3}$, 210 μ s after LID, and around 1.4ms after regeneration.

When the injection-dependent bulk lifetimes measured after applying the regeneration treatment are compared, it is seen that the industry-standard B-doped Cz-Si wafers perform as well as the inherently LID-free materials with similar doping concentrations. One would therefore also expect a similar solar cell performance after permanent deactivation of the BO defect.

Higher PERC+ conversion efficiencies on completely LID-free Cz-Si wafer materials

The four above-mentioned Cz-Si materials were used to process bifacial PERC+ solar cells. The PERC+ process sequence is described in detail in Dullweber et al. [18]; however, here, just the basic process flow will be highlighted.

The PERC+ process starts with saw-damage removal and wafer cleaning. A rear protection layer is then applied to act as an etching and diffusion barrier during the subsequent front-surface texturing and phosphorus diffusion steps. After this, the PSG and protection layer are removed, and a stack of aluminium oxide (AlO_x) and plasma-enhanced chemical vapour deposited (PECVD) silicon nitride (SiN_y) is applied to passivate the rear side. PECVD-SiN_y is also deposited on the front to passivate the P-doped emitter and act as an anti-reflection coating.

To enable contact formation on the rear side, the AlO_x/SiN_y stack is locally removed using a picosecond laser with a wavelength of 532nm, before Al fingers are screen printed on the rear side and Ag fingers on the front. At the end of the sequence, the metal pastes are co-fired in a belt-firing furnace with a belt speed of 5.6m/min. A schematic of the final solar cell structure is shown in Fig. 3.

The *I*-*V* curves of the solar cells are measured using a LOANA system from pvtools. As in the case of the dedicated lifetime samples, the solar cells are measured: 1) directly after processing; 2) after illumination at room temperature for 24h; and 3) after applying the regeneration treatment.

The results of the measurements are shown in Fig. 4; the solar cell efficiencies have been plotted for the different materials in the as-processed state relative to the efficiency of the industrial 1.7 Ω cm B-doped Cz-Si with 16 ppma [O]_i (green diamonds). The change due to illumination at room temperature and the change after applying the regeneration treatment are plotted relative to the respective as-processed efficiencies.

After processing, the efficiency of the PERC+ solar cells with 2.6 ppma [O]_i (blue squares) is 0.4%_{abs.} higher than that of the cells using the industrial 16 ppma [O]_i Cz-Si. Similarly, the solar cells from the Ga-doped Cz-Si (open red circles) perform 0.3%_{abs.} better than the industry-standard B-doped Cz-Si with similar doping concentrations (purple triangles). On an absolute scale, the PERC+ conversion efficiencies range between 21.0 and 21.5% in a five-busbar design. With a busbar-less design and R&D-type Ga wafers similar to material 4 in Table 1, the best PERC+ efficiency is 22.1% [16].

As expected from the lifetime measurements, the solar cell efficiency of the ultralow [O]_i B-doped as well as the Ga-doped cells is not affected by either illumination at room temperature or illumination at elevated temperature (within the measurement uncertainty), and hence the cells are completely LID free [16].

In contrast, the PERC+ solar cells from industrial B-doped Cz-Si degrade by 0.5–0.7%_{abs.} after 24h of illumination at room temperature, widening the gap to the LID-free materials to 0.8–1.1%_{abs.}. After the regeneration treatment is applied, the measured efficiencies improve, but only to a similar level to that before LID, and no higher.

The efficiency gap between the inherently LID-free materials and the industrial B-doped Cz-Si after regeneration seems to be in disagreement with the lifetime measurements: here, the lifetime of the industrial B-doped materials after regeneration was similar to that of the ultralow $[O_i]$ and the Ga-doped Cz-Si.

Device simulations: Translating bulk lifetimes to solar cell efficiencies

In order to understand the discrepancy discussed in the previous section, a device simulation was set up using the conductive boundary model [19], as implemented by the Quokka 2 computer simulation program in Fell [20]. The input parameters, which are based on an extensive characterization of ISFH's baseline PERC+ solar cell process, are summarized in Table 2. The injection-dependent lifetimes of the B-doped Cz-Si wafers, as measured on the lifetime test structures, can be described by a Shockley-Read-Hall (SRH) defect at mid-gap, with a factor of 10 between τ_{no} and τ_{po} . The table lists the defect lifetimes for the as-processed state of the $1.7\Omega\text{cm}$ B-doped sample with 16 ppma $[O_i]$ (material 1). Note that the lifetime measured on the designated test sample that was fired at the same belt speed as the solar cells, i.e. 5.6m/min, was used.

The front-contact shadowing is calculated from the optical finger width and the layout of the front grid. The saturation current density of the emitter J_{oc} is determined on symmetrical test wafers using the Kane and Swanson method. Transmission line model (TLM) measurements were taken to determine the specific contact resistances at the front and rear. The saturation current densities J_o at the contacts are based on lifetime measurements performed on test samples with various metallization fractions, both for the emitter and for the base contact. The depth-dependent generation profile is calculated by parameterizing the measured reflectance of a PERC+ solar cell according to Brendel et al. [21].

The simulation set-up was verified by inserting the effective lifetime measured in the as-processed state for material 1 ($1.7\Omega\text{cm}$ B-doped with 16 ppma $[O_i]$) and comparing the result with measured I - V parameters in the as-processed state. The results are summarized in Table 3.

The efficiency η , open-circuit voltage V_{oc} and short-circuit current density J_{sc} are in good agreement with the simulated values, while the measured fill factor FF is 0.45% higher. This is partly the result of a higher pseudo fill factor pFF (0.3%) as well as a lower series resistance ($\sim 0.05\Omega\text{cm}^2$), but it is nevertheless a fairly good match.

Once the simulation set-up has been verified, the lifetimes measured after process, after illumination at room temperature and after applying the regeneration treatment are inserted. Thus, the efficiency changes that one would expect from the observed lifetime changes can be compared with the actual changes observed on the solar cells. This

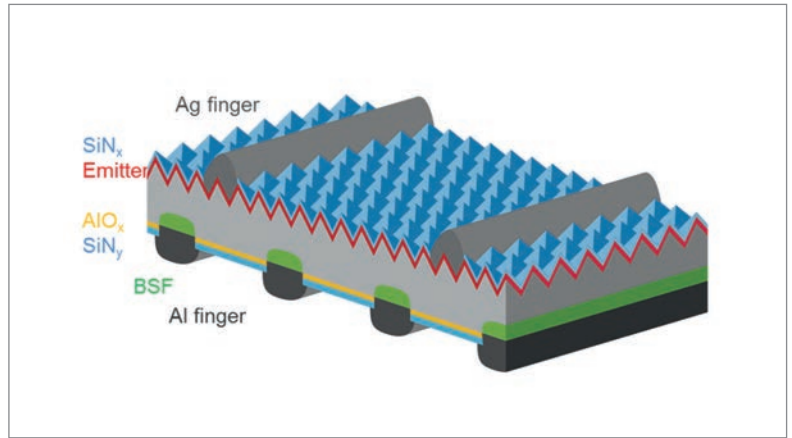


Figure 3. Schematic of a bifacial PERC+ solar cell.

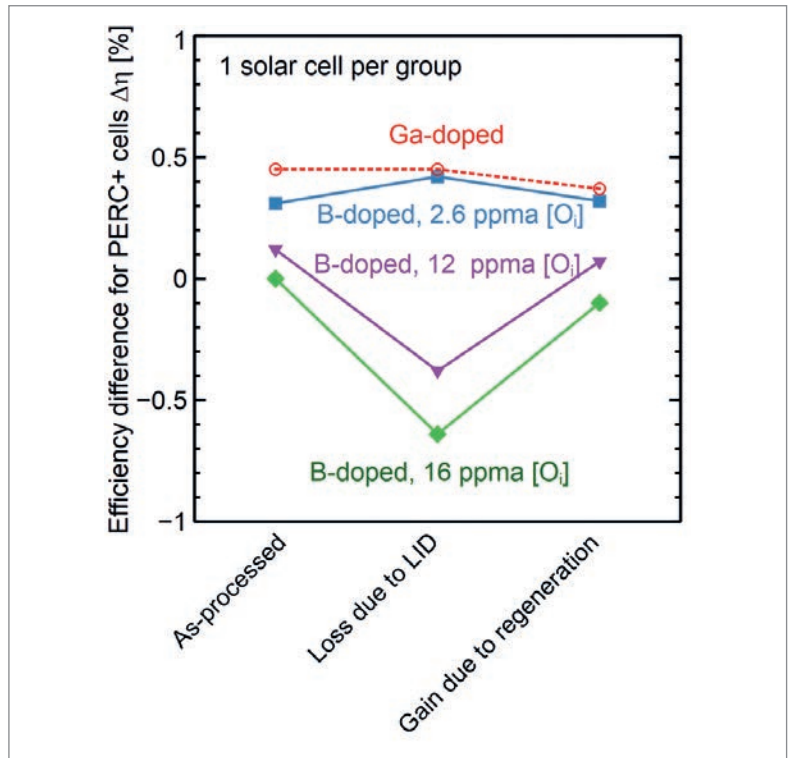


Figure 4. Efficiency differences for the PERC+ solar cells fabricated from the four different Cz-Si materials in the as-processed state, as well as after illumination at room temperature and after applying the regeneration treatment.

comparison is performed for materials 1 and 3, i.e. the industry-standard $1.7\Omega\text{cm}$ B-doped Cz-Si and the B-doped Cz-Si with extremely low interstitial oxygen concentration.

The results are shown in Fig. 5. For the as-processed state, the efficiency of the industrial $1.7\Omega\text{cm}$ B-doped Cz-Si with 16 ppma $[O_i]$ (green diamonds) is used as the baseline value. The change due to illumination at room temperature and the change after applying the regeneration treatment are plotted relative to the respective as-processed efficiencies. Values corresponding to measured solar cell efficiencies are represented by filled symbols, while the results from the simulation are depicted by open symbols.

As mentioned above, the actual ultralow $[O_i]$ solar cells (orange circles) yield 0.3% higher efficiencies than the solar cells fabricated on industrial B-doped

Parameter	Value
Wafer resistivity	1.7Ωcm
Wafer thickness	170μm
τ_{no} for mid-gap SRH centre	292μs
τ_{po} for mid-gap SRH centre	2,920μs
Front-contact shadowing	4.5%
Emitter sheet resistance R_{sh}	95Ω/sq.
J_{oe} of SiN _y -passivated emitter	100fA/cm ²
J_{oe} below Ag finger contacts	1,000fA/cm ²
Specific contact resistance, front	1.5mΩcm ²
J_o at the passivated rear side	12fA/cm ²
J_o at the Al rear contact	350fA/cm ²
Specific contact resistance, rear	3mΩcm ²

Table 2. Input parameters for the device simulations of PERC+ solar cells using the lifetime data of the B-doped Cz-Si with 16 ppma [O_i] in the as-processed state.

Parameter	Simulation	Measurement
Efficiency η [%]	21.49	21.53
V_{oc} [mV]	669.8	667.3
J_{sc} [mA/cm ²]	39.54	39.53
FF [%]	81.16	81.62
R_s [Ωcm ²]	0.468	0.420
pFF [%]	83.37	83.68

Table 3. Simulated and measured I - V parameters for the baseline PERC+ solar cell process and the 1.7Ωcm B-doped Cz-Si with 16 ppma [O_i].

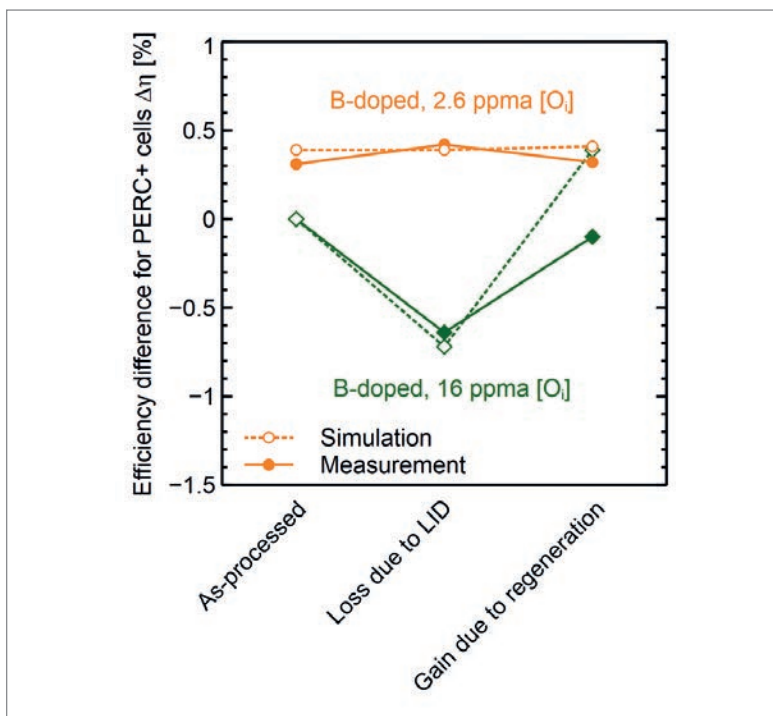


Figure 5. Measured (filled symbols, solid lines) and simulated (open symbols, dashed lines) differences in PERC+ cell efficiency $\Delta\eta$ after illumination at room temperature and after applying the regeneration treatment.

Cz-Si (green diamonds) directly after processing. This difference is also predicted by the simulation when the respective effective lifetimes measured in the as-processed state are entered.

Illumination at room temperature notably decreases the lifetime in the 16 ppma [O_i] B-doped Cz-Si. Inserting this degraded lifetime into the simulation yields a 0.7%_{abs.} loss compared with the as-processed state (open green diamonds). This is in good agreement with the degradation observed on actual PERC+ solar cells (filled green diamonds). After regeneration, the measured PERC+ efficiency of the industrial B-doped Cz-Si improves to a similar level to that before LID, whereas the device simulation with the regenerated lifetime predicts an increase by 0.4%_{abs.} compared with before LID.

The measured PERC+ efficiency of the 2.6 ppma [O_i] B-doped material, on the other hand, is stable, during both the degradation and the regeneration treatment (within the measurement uncertainty). This is in accordance with the measured bulk lifetimes, which do not decrease after illumination at room temperature (see Fig. 1(b)). While an increase in bulk lifetime is observed for the 2.6 ppma B-doped Cz-Si after applying the regeneration treatment, this increase only translates to an efficiency gain of 0.02% in the device simulation, as the other recombination channels are much more dominant.

The comparison between measured solar cell efficiencies and efficiencies simulated on the basis of measured bulk lifetimes reveals a notable discrepancy for the regenerated state of the industrial B-doped Cz-Si. The difference in the measured bulk lifetimes in the degraded and the regenerated states should translate to an efficiency gain of 1.1%_{abs.} after regeneration. For the actual solar cells, however, an increase by only 0.7%_{abs.} was observed.

Hence, in contrast to the experimental results, according to the simulation the regenerated industrial B-doped wafer material should enable identical PERC+ efficiencies to those for the ultralow [O_i] wafer material. This suggests that in the case of the industrial B-doped Cz-Si, there is a difference in the regenerated bulk lifetime of the test wafers and the PERC+ solar cells. Since the lifetime test wafers were processed in parallel to the solar cells – as far as possible – this raises the question as to where this difference might stem from.

Possible reasons for lower-than-expected efficiency after regeneration of industry-typical Cz-Si

A look at the detailed processing sequence used in this work reveals three major differences between lifetime test structures and PERC+ solar cells: 1) the solar cells have a rear protection layer during the P-diffusion step; 2) during the fast-firing process, the solar cells have an emitter on the front side; and 3) the solar cells are fired with metal pastes on both surfaces. In contrast, for the lifetime test wafers: 1) the n⁺ emitter first forms on both wafer sides;

subsequently, 2) the emitter is removed from both wafer surfaces, which are then passivated with an $\text{AlO}_x/\text{SiN}_y$ stack; and 3) metal pastes are obviously not applied to the lifetime samples.

With regard to the rear protection layer during P diffusion, experimental results obtained from a different study make it seem unlikely that this has any significant impact. In that study's experiment, the solar cells as well as the lifetime samples were diffused on both surfaces, and the n^+ emitter on the rear was then removed by a rear polishing step. Also in that experiment, the PERC+ cell efficiencies after processing and after regeneration were identical, in contrast to the carrier lifetimes, measured on lifetime samples, which were higher after regeneration.

In respect of the presence of the n^+ emitter during the fast-firing step, the effective lifetimes of non-metallized implied- V_{oc} (iV_{oc}) solar cell precursors were measured and simulated. These are identical to PERC+ solar cells except for the laser contact opening and the screen-printing steps. For the simulation, the front metal recombination was set to be equal to that of the passivated emitter, and the rear metal recombination to be equal to that of the passivated rear side. All other parameters were the same as for the solar cell simulation.

Fig. 6 shows the effective lifetime of such an iV_{oc} precursor. The blue triangles correspond to the as-processed state, and the green diamonds to the regenerated state. The lines indicated the simulated effective lifetimes, i.e. the result of simulating an implied- V_{oc} structure, on the assumption of the bulk lifetime measured in the as-processed (solid blue line) and in the regenerated state (dashed green line).

In the as-processed state, the measured effective lifetime (blue triangles) matches the simulated effective lifetime (solid blue line) very well. The measured effective lifetime on the non-metallized precursor after regeneration (green diamonds), however, is notably lower than the simulated effective lifetime (dashed green line). It therefore seems as if the presence of the n^+ emitter during the fast-firing step negatively affects the bulk lifetime.

A possible reason for the above effect could be related to hydrogen, which interacts with various defects in the silicon bulk. A major source of hydrogen is the SiN_x layer combined with the fast-firing step [22]. The presence of an n^+ emitter, however, affects the transport of hydrogen from the SiN_x into the bulk [23], which could result in different bulk lifetimes in the lifetime test wafers and the solar cell precursors. This aspect is currently undergoing further investigation.

References

- [1] ITRPV 2018, "International technology roadmap for photovoltaic (ITRPV): 2017 results", 9th edn (Mar.) [<http://www.itrpv.net/Reports/Downloads/>].
- [2] [<https://www.pv-magazine.com/2018/01/19/longi->

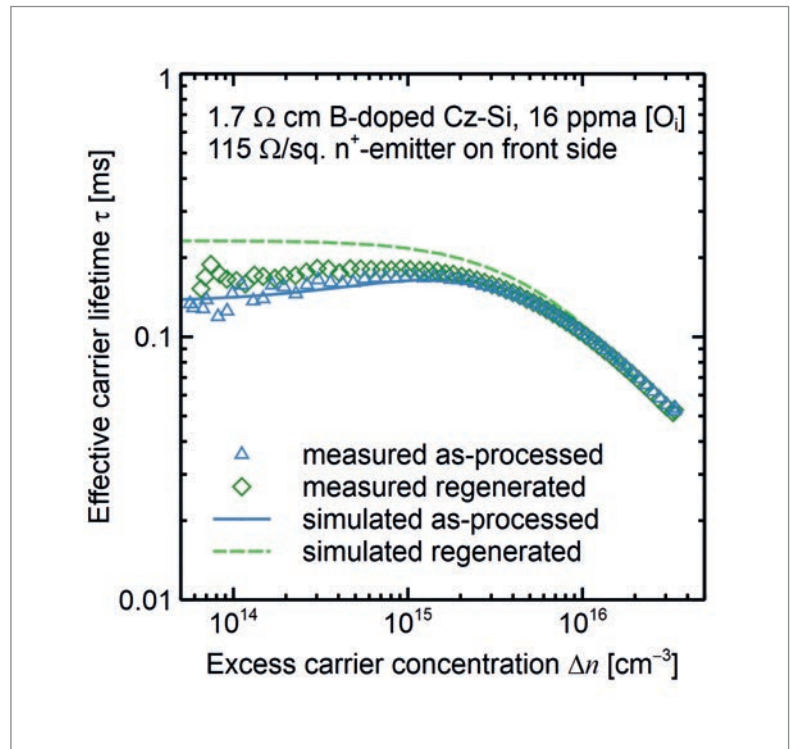


Figure 6. Measured (symbols) and simulated (lines) injection-dependent effective lifetimes of industry-standard 1.7 $\Omega \text{ cm}$ B-doped Cz-Si with a SiN_x -passivated 115 $\Omega/\text{sq.}$ n^+ emitter on the front side. The blue triangles and solid blue line correspond to the as-processed state, and the green diamonds and dashed green line to the regenerated state.

achieves-record-conversion-rate-of-20-41-for-perc-modules/].

[3] JinkoSolar Holding Co., Ltd. 2017, Annual Report.

[4] [<https://www.pv-tech.org/news/aiko-solar-enters-volume-production-of-mono-perc-cell-with-22-conversion-ef/>].

[5] Lee, B.G. et al. 2018, "Development of p-Cz PERC solar cells approaching 23% efficiency for gigawatt-level production", *Proc. 35th EU PVSEC*, Brussels, Belgium, pp. 308–400

[6] Fischer, H. & Pschunder, W. 1973, "Investigation of photon and thermal induced changes in silicon solar cells", *Proc. 10th IEEE PVSC*, Palo Alto, California, USA, p. 404.

[7] Schmidt, J., Aberle, A. & Hezel, R. 1997, "Investigation of carrier lifetime instabilities in Cz-grown silicon", *Proc. 26th IEEE PVSC*, Anaheim, California, USA, pp. 13–18.

[8] Glunz, S.W. et al. 1998, "On the degradation of Cz-silicon solar cells", *Proc. 2nd World Conf. PV Solar Energy Conv.*, Vienna, Austria, p. 1343.

[9] Glunz, S.W. et al. 1999 "Comparison of boron and gallium doped p type Czochralski silicon for photovoltaic application", *Prog. Photovolt. Res. Appl.*, Vol. 7, No. 6, pp. 463–469.

[10] Mosel, F. et al. 2012, "Growth of high quality silicon mono ingots by the application of a magnetic CUSP field in Cz-puller", *Proc. 27th EU PVSEC*, Frankfurt, Germany, p. 933.

[11] Herguth, A. et al. 2006, "Avoiding boron-oxygen related degradation in highly boron doped Cz silicon",

"It seems as if the presence of the n^+ emitter during the fast-firing step negatively affects the bulk lifetime."

Proc. 21st EU PVSEC, Dresden, Germany, p. 530.

[12] Dullweber, T. et al. 2017, "Bifacial PERC+ solar cells and modules: An overview", *Proc. 33rd EU PVSEC*, Amsterdam, The Netherlands, pp. 649–656.

[13] Walter, D., Lim, B. & Schmidt, J. 2016 "Realistic efficiency potential of next-generation industrial Czochralski-grown silicon solar cells after deactivation of the boron–oxygen-related defect center", *Prog. Photovolt: Res. Appl.*, Vol. 24, No. 7, pp. 920–928.

[14] Palmer, D.W., Bothe, K. & Schmidt, J. 2007, "Kinetics of the electronically stimulated formation of a boron–oxygen complex in crystalline silicon", *Phys. Rev. B*, Vol. 76, p. 035210.

[15] Richter, A. et al. 2012, "Improved quantitative description of Auger recombination in crystalline silicon", *Phys. Rev. B*, Vol. 86, p. 165202.

[16] Lim, B. et al. 2018, "LID-Free PERC + solar cells with stable efficiencies up to 22.1%", *Proc. 35th EU PVSEC*, Brussels, Belgium, pp. 359–365.

[17] Walter, D.C. et al. 2014, "Lifetimes exceeding 1ms in 1- Ω cm boron-doped Cz-silicon", *Sol. Energy Mater. Sol. Cells*, Vol. 131, pp. 51–57.

[18] Dullweber, T. et al. 2016, "PERC+: Industrial PERC solar cells with rear Al grid enabling bifaciality and reduced Al paste consumption", *Prog. Photovolt: Res. Appl.*, Vol. 24, No. 12, pp. 1487–1498.

[19] Brendel, R. 2012, "Modeling solar cells with the dopant diffused layers treated as conductive boundaries", *Prog. Photovolt: Res. Appl.*, Vol. 20, No. 1, pp. 31–43.

[20] Fell, A. 2012, "A free and fast three-dimensional/two-dimensional solar cell simulator featuring conductive boundary and quasi-neutrality approximations", *IEEE Trans. Electron Dev.*, Vol. 60, No. 2, pp. 733–738.

[21] Brendel, R. et al. 2016, "Breakdown of the efficiency gap to 29% based on experimental input data and modeling", *Prog. Photovolt: Res. Appl.*, Vol. 24, No. 12, pp. 1475–1486.

[22] Kleekajai, S. et al. 2006, "Concentration and penetration depth of H introduced into crystalline Si by hydrogenation methods used to fabricate solar cells", *J. Appl. Phys.*, Vol. 100, No. 9, p. 093517.

[23] Hamer, P. et al. 2018, "Modelling of hydrogen transport in silicon solar cell structures under equilibrium conditions", *J. Appl. Phys.*, Vol. 123, No. 4, p. 043108.

to ISFH in 2017 and is currently working on p-PERC solar cells as well as on BIPV.



Agnes Merkle studied physics at the University of Bucharest, Romania, where she specialized in biophysics. She joined ISFH in 1996, carrying out R&D work on several high-efficiency solar cell concepts. Her

current research focuses on the drop-in implementation of passivating contacts in the current PERC process flow.



Prof. Dr. Robby Peibst is head of the emerging solar cell technologies R&D group at ISFH, and holds a professorship at the MBE institute at Leibniz University Hanover. His current research work focuses on

passivating contacts based on doped polycrystalline silicon layers deposited on thin passivating interface oxides (POLO, poly-Si on oxide), including process development, principle studies and implementation in Si single-junction and Si bottom cells for tandem structures.



Dr. Thorsten Dullweber is head of the industrial solar cells R&D group at ISFH. His research work focuses on high-efficiency industrial-type PERC and bifacial PERC+ silicon solar cells.

Before joining ISFH in 2009, Thorsten worked as a project leader for DRAM memory chips at Infineon Technologies AG. He received his Ph.D. in 2002 for research on Cu(In,Ga)Se₂ thin-film solar cells. He is a member of the scientific committees of the EU PVSEC and SNEC conferences, and of the editorial advisory board of Photovoltaics International.

Yichun Wang received an M.S. in electrical engineering in 2010 from the University of Kentucky, USA, and a B.S. in electrical engineering in 2007 from Northwestern University, China. She joined LONGi Green Energy Technology Co., Ltd. in 2014, and is currently the director of application engineering and key customer service in the Silicon Wafer Business Unit, where her responsibilities include technical/product quality support and supervising technical collaboration projects with global institutes and R&D corporations.

About the Authors



Dr. Bianca Lim joined ISFH in 2007 to work on boron–oxygen-related recombination centres. After receiving her Ph.D. in 2011, she was a project leader at ISFH. In 2015 she joined the Solar Energy Research

Institute of Singapore (SERIS) to develop ion-implanted p- and n-type Si solar cells. She returned

Enquiries

Bianca Lim
Institute for Solar Energy Research Hamelin (ISFH)
Am Ohrberg 1, D-31860 Emmerthal
Germany

Tel: +49-5151-999-403
Email: b.lim@isfh.de

LED solar simulators and new test approaches for high-efficiency solar cells

Marko Turek, Kai Sporleder & Christian Hagendorf, Fraunhofer Center for Silicon Photovoltaics CSP, Halle (Saale), Germany

Abstract

Solar simulators are among the most important and fundamental measurement tools in photovoltaic production facilities as well as in R&D labs. Two major solar simulator technologies can be distinguished: xenon light sources and, more recently, light sources using light-emitting diodes (LEDs). While xenon solar simulators are a well-established technology, LED-based systems appear to be promising candidates for future applications, as they provide a higher flexibility with regard to the flash times, spectral light composition and intensity. Measurement recipes for power quantification under standard test conditions (STC) can be adapted to high-efficiency cells, which require longer flash times. Furthermore, fast inline spectral testing, such as a rapid external quantum efficiency (EQE) test or a rapid reflectivity test, becomes feasible. However, the development of LED-based systems requires well-designed optical and electronic components to ensure high-precision measurements on the basis of a laterally uniform and temporally stable light field.

standards [1]. In accordance with these standards, solar simulators are classified according to their spectral match, the lateral uniformity and the temporal stability of the irradiance.

Currently, there are two major solar simulator technologies available. First, there are the well-established *xenon-based solar simulators*, which are operated in either a flash mode or a steady-state mode, depending on the light source and field of application. Xenon lamps come with an irradiance spectrum that exhibits several sharp peaks on a broad background (see Fig. 1), which can be modified using optical elements such as filters. The light source itself is point-like, and shaping the lateral intensity requires lenses, apertures or light-guiding elements.

Second, there are the *solar simulators using light-emitting diodes (LEDs)*, which have been gaining market share in recent years. Introduced around five years ago with the first commercial in-line LED lighting units, about hundred systems from different manufacturers are in operation today. The spectrum of the irradiated light is composed of the individual spectra of each LED type, and can be controlled by an electronic adjustment of the individual LED's power. The light engines are area-like, requiring a careful positioning of the individual LEDs, possibly combined with some special optical elements.

Either simulator technology must comply with the solar simulator standard, while different technical realizations exist, depending on the intended usage [2]. Typical spectra from a filtered xenon-based flasher and a 21-channel-LED solar simulator are presented in Fig. 1. The xenon spectrum shows good agreement with the norm spectrum for wavelengths below 800nm, whereas the contribution to the longer wavelengths is characterized by several sharp spectral peaks. The LED solar simulator spectrum, however, can be tailored to produce a fairly smooth representation of the AM1.5G reference spectrum defined in the norm, depending on the number of implemented LED colours.

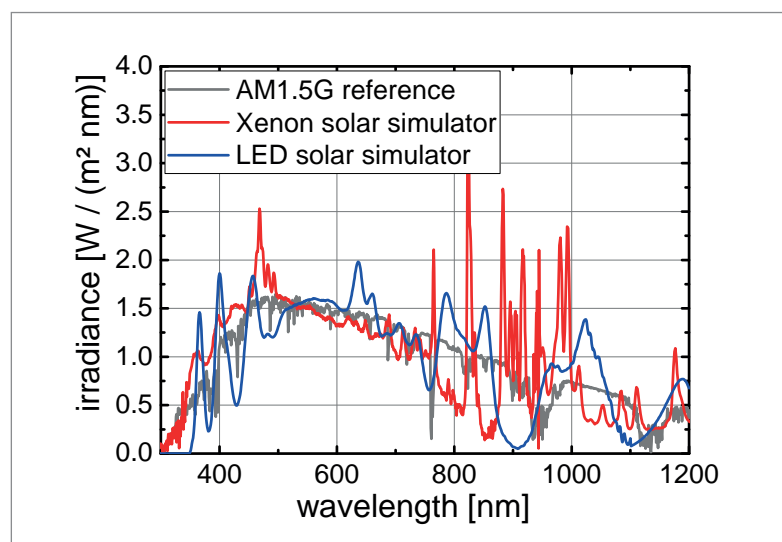
Fields of application and requirements for solar simulators

In general, three fields of application for solar simulators can be distinguished.

Introduction

The most important solar cell or module characteristic is its output power, obtained by a current–voltage measurement under illumination. These measurements are performed, both in PV production and research labs, using artificial light with properties close to natural sunlight. In industry, virtually 100% of all cells and modules are characterized using solar simulators. The sorting of cells into various efficiency bins, and the pricing of the modules, rely on this data. For this reason, the requirements on the measurement procedure, as well as on the solar simulators as measurement devices, are described in several IEC

Figure 1. Spectra of a LED solar simulator and a xenon-based flasher, in comparison to the AM1.5G reference spectrum.



LEDs COPY THE SUN



Measure PV cells with perfect LED solar simulation, and you enhance every aspect of production. What's more, quality control costs are lower than with conventional Xenon simulators. From cell and module quality to nominal ratings and reliability, everything improves with a WAVELABS SINUS-220 solar simulator. And a better product for less means higher margins. No wonder institutes and manufacturers alike are all riding the LED wave with us. Take a closer look at the SINUS-220 today — you may be next to see the light. www.wavelabs.de



First, solar simulators are designed to provide high-quality data on the performance of solar cells and modules under standard test conditions (STC); here, a single fixed-measurement procedure is required which relies on a device to give precise and repeatable measurements. From a technical point of view, the focus therefore lies on a light source with minimal spectral mismatch when compared with the norm spectrum, and with a high temporal stability. All production tools and most R&D tools have to be designed to meet these requirements.

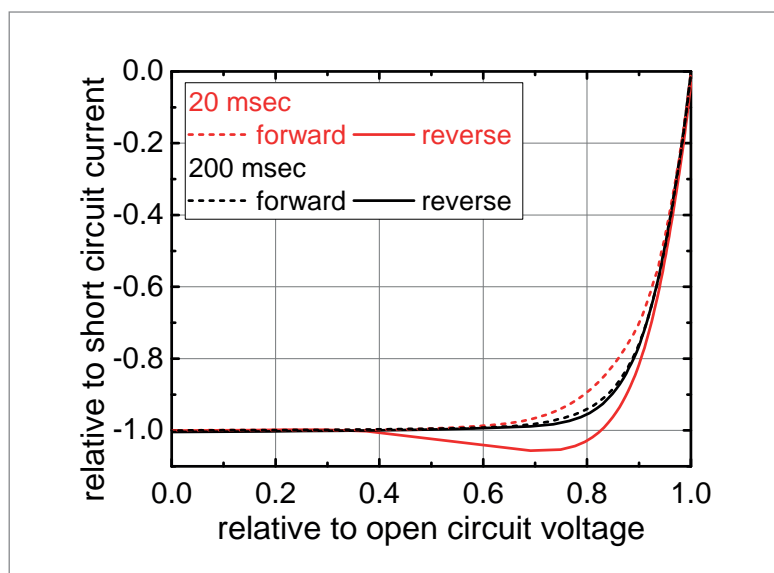
Second, solar simulators can be used for advanced quality control and loss analysis measurements; in this case, the solar simulator should provide the technical basis for more-flexible measurements beyond STC. This can include variations in intensity for series-resistance analysis, variations in the spectrum for spectral analysis, or variations in the measurement time for an analysis of capacity effects.

Third, extended solar simulator measurements can be employed for yield estimations and energy ratings, as well as supplying the data for a quantitative estimation of the levelized cost of electricity (LCOE) of PV power plants. For this solar simulator application, the measurement system has to provide specific measurement procedures adapted to non-standard spectra, and

to measurements at different temperatures or with modifications to the angle of incidence.

In PV production, the emphasis is on fast and reproducible measurements, robust and reliable contacting solutions, short downtimes and low maintenance costs. R&D labs or calibration laboratories, on the other hand, usually focus on the realization of a much better-defined measurement

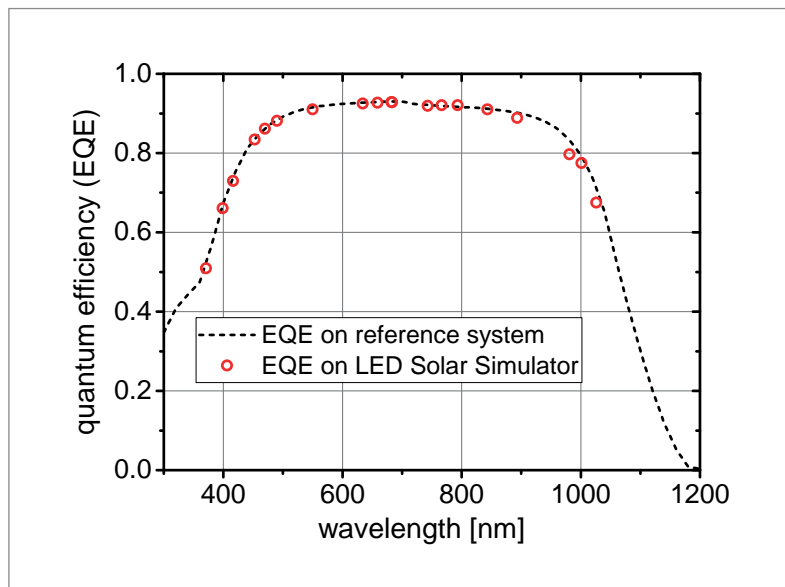
Figure 2. Hysteresis effect occurring between forward and reverse measurement directions, for a high-performance solar cell.



environment, such as temperature uniformity and stability, irradiance uniformity, and spectral accuracy and traceability. A second aspect in R&D labs concerns the flexibility of the measurement tools with regard to parameters such as the measurement times, the spectrum, the intensity of the irradiance, or the sample size.

Measurements under STC

Research labs usually have the means to repeatedly check the technical parameters of their solar simulators. A production tool, on the other hand, has to perform in a continuous operation mode for several weeks or months without the frequent application of more-sophisticated crosschecks on the measurement system. The ageing of the light sources is one example of an issue that might arise in this context: xenon-based systems show some shift in the spectrum and lose some of their intensity [3]. With a production cycle time of 1 sec per cell, the light sources are required to perform millions of flashes in a month; therefore, an exchange of the light source has to be performed on a regular basis when the flash bulb ageing has advanced too far. Similarly, xenon flash lamps exhibit a certain amount of spectral shift in the spectral match during a single flash [3]. From a technological point of view, these short- and long-time spectral shifts can be compensated in LED solar simulators if an appropriate feedback loop that controls the LED colours individually is implemented, ensuring stable spectral properties of the irradiance. Additionally, the lifetime of LEDs is significantly longer than that of xenon bulbs, although this depends somewhat on the wavelength of the particular LED. On the other hand, an exchange of individual LEDs is usually



not possible in a short time, and so a very high level of quality control has to be ensured in the production of LED solar simulators. Hence, a well-designed LED solar simulator with an intrinsic control and feedback loop could lead to a reduction in maintenance and operation activities in PV production lines.

The better imitation of the AM1.5G reference spectrum by the LED solar simulator also results in a lower spectral mismatch correction factor for the short-circuit current. This is not just beneficial in R&D, where the spectral response (SR) of newly developed cell technologies differs from the spectral

Figure 3. Typical EQE curve of a silicon solar cell, measured on a lab-based tool with a spectral resolution of 20nm over a three-minute measurement period, compared with the EQE based on an LED solar simulator, measured over 200ms.

“The LED solar simulator spectrum can be tailored to produce a fairly smooth representation of the AM1.5G reference spectrum.”

Revolutionary, Flexible, Precise.
With double LED light source.

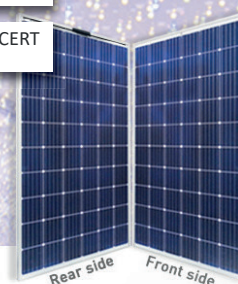
THE NEW LED SUN SIMULATOR FOR BIFACIAL SOLAR PANELS

ECOSUN BIFACIAL

SUITABLE FOR ALL THE NEW
HIGH EFFICIENCY SOLAR CELLS

- CERTIFIED BY TÜV INTERCERT
- COMPLIANT TO IEC ED.3

ECOPROGETTI
SPECIALIST IN PHOTOVOLTAIC
PRODUCTION PROCESS



COME VISIT US!



Middle East Electricity
5-7 March; Booth: Z2.F39



The Solar Show Africa
26-27 March; Booth: B74



Discover more:

www.ecoprogetti.com | sales@ecoprogetti.com

Contact us:

sales@ecoprogetti.com



response of the available reference cells. It is also advantageous in production, where reference cells with a spectral response similar to that of produced cells *are* available, in which case the variations in spectral mismatch due to process variations are lower than for xenon-based systems [4].

New cell technologies and advanced quality control

Besides the maintenance and operation costs, a second aspect has recently come to light. More-advanced high-efficiency cell concepts, such as PERC/PERT or heterojunction cells, are increasingly coming onto the market; it is predicted that more than 50% of all cells will be comprised of these new technologies by 2020 [5]. Because of the longer charge-carrier lifetimes and the modified cell designs, these cell technologies are characterized by a higher internal capacitance. This effect can have some severe implications for the power measurement when performed over short time periods, as the resulting I - V curves exhibit some hysteresis effects, in dependence on the direction of measurement (Fig. 2).

The most straightforward approach to resolving the hysteresis issue is to slow down the measurements by increasing the sweep times; this also involves sufficiently long flash times, in some cases (such as for heterojunction cells) up to more than 100ms. While some xenon-based flash light measurement systems are capable of satisfying this requirement, this class of solar simulator is generally limited by the technical implementation of the flash bulbs. Consequently, a number of more-advanced measurement procedures have been developed for systems with limited flash times. The proposed solutions include:

- Implementation of adapted voltage ramps, e.g. Pasan's DragonBack® approach [6].
- Dynamic I - V curve measurements with adapted measurement times for each single point on the I - V curve, e.g. TÜV Rheinland's approach [7].
- Multiple I - V curve measurements, e.g. Halm's advanced hysteresis approach [8], Endea's capacitance compensation method (CAC) [9], and Fraunhofer CSP's approach [10].

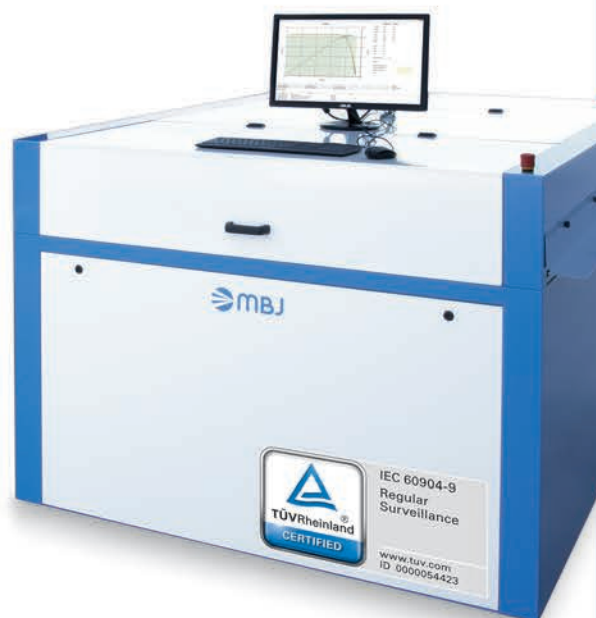
In contrast, LED-based solar systems are highly flexible in terms of flash times, which can be electronically controlled and adjusted without any hardware changes if the system has an appropriate implementation of temperature control of the LEDs. This advantage can not only make more-sophisticated measurement approaches obsolete, but also allow new measurement approaches that provide the capacitance of a solar cell as an additional quality control parameter [10].

The new cell technologies mentioned earlier are accompanied by more-advanced front- and rear-side surface layers; for example, the major advantage of PERC solar cells results from the improved passivation of the rear side. Thus, fast and reliable inline-capable measurement approaches are needed in order to enable an adequate quality monitoring of individual cell components in modern production lines. Such a quality control

“LED-based solar systems are highly flexible in terms of flash times.”



LED Sun Simulator



Future ready innovative LED technology for your module production

- IEC 60904-9 Edition 3 ready
- Electronic load
- For highly efficient modules
- Up to 200ms pulse duration
- 200 - 1200 W/m² irradiance

MBJ Solutions GmbH

www.mbj-solutions.com
+49 40 22 6162 300

can be established by a depth-resolved loss analysis using spectral measurements, as developed by Fraunhofer CSP. This type of loss analysis can be performed by means of a rapid external quantum efficiency (rapid EQE, see Fig. 3) test, yielding insights into the electronic losses on the surfaces, in comparison to the bulk losses [11]. Some solar simulators are combined with imaging units, such as electroluminescence or infrared cameras, in which case a spatially resolved spectral measurement of the reflectivity (rapid REFL) can also be implemented [12]. On the basis of this rapid REFL measurement, a quantitative assessment and quality control of the passivation layer thickness and uniformity is feasible. Finally, the analysis of a multi-intensity measurement leads to very detailed information on the series resistance of a solar cell [13].

Cell-to-system approach: quantifying the yield for LCOE prediction

Power measurements of solar cells and modules under STC yield some indication of quality based on very well-defined conditions of operation. One cannot directly infer from this data, however, the performance of a module in a PV power plant under realistic operating conditions. Such a yield prediction under realistic conditions is nevertheless required in order to obtain a quantitative estimate of the LCOE for a given cell and module technology. In particular, a quantitative cell-to-system key figure requires power measurements of a module under various spectral conditions that go beyond the AM1.5G spectrum [14], at different temperatures, and with modifications to the angle of incidence. From a technological point of view, such an energy-rating tool could be realized by combining a series of measurements in an LED-based solar simulator for modules. This additionally requires a software algorithm that combines and weights these data to generate a yield prediction for a module installed in a specific region. Work towards this goal is being carried out within some ongoing research projects at Fraunhofer CSP.

Ensuring the quality of solar simulator measurements

In order to ensure a high quality of the measurement results, a solar simulator should be checked frequently with respect to its light intensity, the uniformity of its light field, the spectral composition of the irradiance, and the temporal stability. In production, where many samples of identical design are measured, the major quality assurance measure is the use of calibrated reference cells or modules. While this approach works well for identical samples, yielding power values with minimal errors, it does not ensure the basic requirements for the light source as defined in the standard. For example,

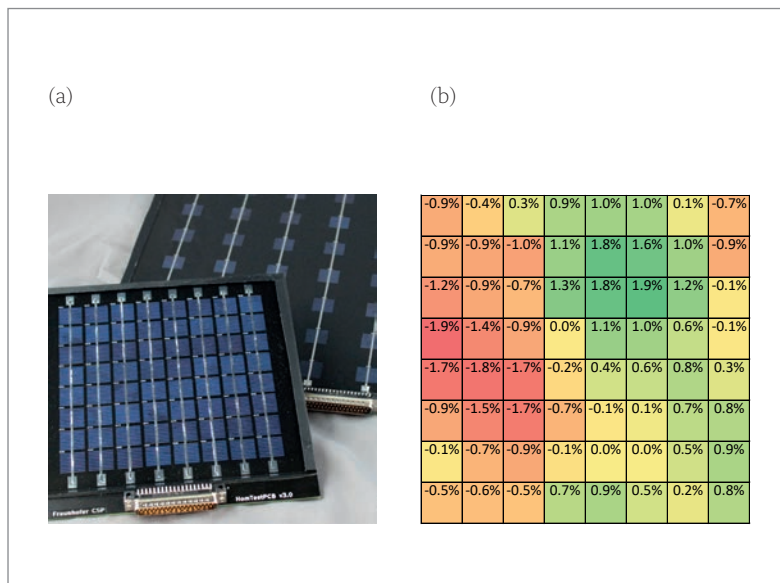


Figure 4. (a) Fraunhofer CSP's 'reference cell +' in different sizes, adapted to the solar simulator under investigation. (b) Example of the irradiance non-uniformity of the AM1.5G spectrum, showing a slightly reduced irradiance at the left edge of the test plane.

“LED solar simulators are gaining market share because of their potential for better-controlled light field properties and their higher flexibility in terms of measurement recipes that go beyond taking power measurements under STC.”

calibration using a reference cell does not give any information on the uniformity, the spectral composition, or the temporal stability.

Most of the aforementioned properties, however, can be quantified using a 'reference cell +', as developed by Fraunhofer CSP (see Fig. 4). For example, an assessment of five different solar simulators has shown that there are major differences in the lateral uniformity of the light fields [15]. This sensor system has been designed for easy use in any kind of solar simulator, yielding data on the lateral uniformity and temporal stability of light sources. The system is currently available for cell-size solar simulators, but a larger version for module-size simulators is in development.

Conclusions

The solar simulator is one of the most important devices for measurement purposes in photovoltaic production facilities and research laboratories. There are two major technologies commercially available: xenon-based solar simulators and LED-based measurement systems. Xenon-based systems currently dominate the market simply because of the maturity of the technology; however, LED solar simulators are gaining market share because of their potential for better-controlled light field properties and their higher flexibility in terms of measurement recipes that go beyond taking power measurements under STC.

New high-efficiency cell technologies are accompanied by higher cell capacities, which require adaptations to the I - V measurements with regard to the measurement times. To this end, special solutions for xenon-based systems have been developed, while LED-based systems can compensate for these effects by adapting the measurement times. The development of new advanced measurement applications, such as rapid EQE or reflectivity testing, is a field of ongoing active research at Fraunhofer CSP. Furthermore, new sensor concepts are being developed to ensure the quality of the solar simulators while minimizing the downtimes of the measurement tools.

References

- [1] IEC 60904:2007, "Photovoltaic devices".
- [2] Sinton, R.A. et al. 2018, "Critical evaluation of the foundations of solar simulator standards", *Proc. 7th WCPEC (and 45th IEEE PVSC)*, Waikoloa, Hawaii, USA.
- [3] Herrmann, W. et al. 2012, "Uncertainty of solar simulator spectral irradiance data and problems with spectral match classification.", *Proc. 27th EU PVSEC*, Frankfurt, Germany.
- [4] Scherff, M.L.D. et. al. 2017, "Spectral mismatch and solar simulator quality factor in advanced LED solar simulators", *Jpn. J. Appl. Phys.*, Vol. 56.
- [5] ITRPV 2018, "International technology roadmap for photovoltaic (ITRPV): 2017 results", 9th edn (Mar.) [<http://www.itrpv.net/Reports/Downloads/>].
- [6] Ferretti, N. et al. 2013, "Performance testing of high-efficient PV modules using single 10 ms flash pulses", *Proc. 28th EU PVSEC*, Paris, France.
- [7] Monokroussos, C. et al. 2012, "Accurate power measurements of high capacitance PV modules with short pulse simulators in a single flash", *Proc. 27th EU PVSEC*, Frankfurt, Germany.
- [8] Ramspeck, K. et al. 2014, "Accurate efficiency measurements on very high efficiency silicon solar cells using pulsed light sources", *Proc. 29th EU PVSEC*, Amsterdam, The Netherlands.
- [9] Vahlman, H. et al. 2018, "Capacitive effects in high-efficiency solar cells during I - V -curve measurement: Consideration on error of correction and extraction of minority carrier lifetime", *Proc. 35th EU PVSEC*, Brussels, Belgium.
- [10] Sporleder, K. et al. 2018, "Fast I - V and capacitance measurements using LED solar simulators for in-line applications", Oral presentation, 8th SiliconPV, Lausanne, Switzerland.
- [11] Luka, T. et al. 2015, "Rapid testing of external quantum efficiency using LED solar simulators", *Energy Procedia*, Vol. 77, p. 113.
- [12] Sporleder, K. et al. 2017, "Rapid testing of spectrally resolved optical cell quality using LED solar simulators", *Proc. 33rd EU PVSEC*, Amsterdam,

The Netherlands.

- [13] Turek, M. 2014, "Current and illumination dependent series resistance of solar cells", *J. Appl. Phys.*, Vol. 115, p. 114503.
- [14] Brammer, T. 2015, "Modified AM1.5 spectra for inline measurement of cell-to-module effects by using an LED solar simulator", Poster presentation, SNEC 2015, Shanghai, China.
- [15] Turek, M. et al. 2018, "Evaluation of the lateral uniformity of solar simulator light fields", *Proc. 35th EU PVSEC*, Brussels, Belgium.

About the Authors



Dr. Marko Turek studied physics at Dresden University, and received his Ph.D. in the field of condensed matter theory from the University of Regensburg. At Fraunhofer CSP he leads the team involved with

electrical characterization of solar cells and modules. His research focuses on loss analysis of solar cells, advanced characterization methods and development of new test methods and devices.



Kai Sporleder studied medical physics at Martin Luther University Halle-Wittenberg, Germany. In 2015 he joined Fraunhofer CSP and worked in the field of defect diagnostics and electrical

characterization of silicon solar cells. Since 2017 he has been working on his Ph.D., focusing on loss mechanisms at the rear side of bifacial solar cells.



Dr. Christian Hagendorf is head of the diagnostics and metrology research group at Fraunhofer CSP. He obtained his Ph.D. from Martin Luther University Halle-Wittenberg in the field of surface and interface

analysis of semiconductor materials. Joining Fraunhofer CSP in 2007, he established a research group that focuses on defect diagnostics and metrology in crystalline and thin-film PV.

Enquiries

Kai Sporleder
Fraunhofer Center for Silicon Photovoltaics CSP
Otto Eissfeldt Strasse 12
06120 Halle (Saale)
Germany

Tel: 49 345 5589555
Email: kai.sporleder@csp.fraunhofer.de

Efficiency and cost effectiveness of large-area perovskite-based tandem solar cells

Manoj Jaysankar & Tom Aernouts, imec, Genk, Belgium

Abstract

Tandem solar cells combine several solar cells with different photoabsorbers, stacked in a descending order of bandgap energies. They come in many flavours, but one promising combination is a bottom cell of c-Si or copper indium gallium selenide (CIGS) and a top cell of perovskite. Perovskite solar cells are thin-film solar cells with many advantages, such as a low-cost, high-throughput sheet-to-sheet and roll-to-roll production, and a tuneable bandgap. Their long-term instability, however, is a challenge that needs to be overcome in order to make these cells a success. In this paper it is demonstrated that, by combining comprehensive loss-reduction strategies with effective large-area fabrication, perovskite-based tandem solar modules have the potential to yield power conversion efficiencies (PCEs) that are significantly higher (PCE of up to 45%) than those of established PV technologies, and can be manufactured on an industrial scale.

Tandem solar cells

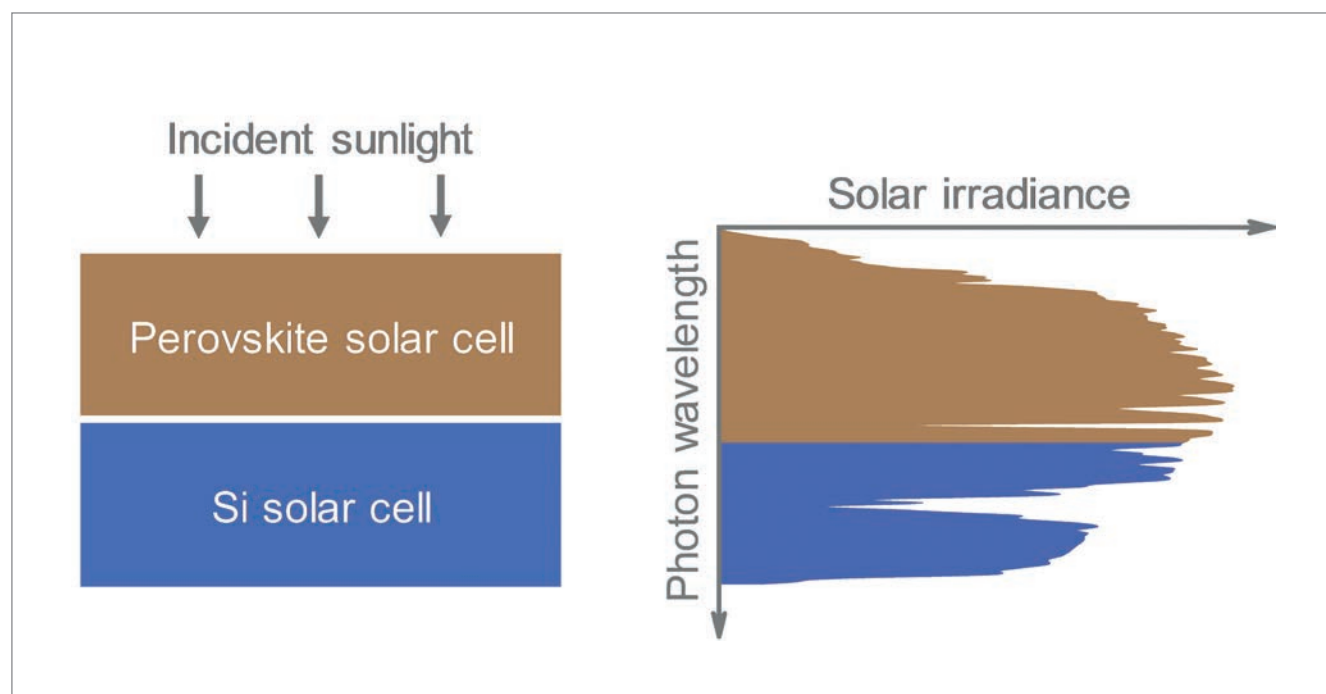
Tandem solar cells comprise several solar cells with different bandgaps coupled with each other, enabling more-efficient harvesting of solar irradiation. In tandem solar cells, cells with different photoabsorbers are stacked in a descending order of bandgap energies (Fig. 1).

Since solar cells with wider-bandgap photoabsorbers generate higher voltages, thermalization losses are significantly reduced in tandem solar cells, compared with single-junction solar cells that absorb the same number of photons; this results in a higher PCE for tandem solar cells.

Tandem solar cells have been widely used for space applications. Such tandem solar cells comprise up to five subcells based on III-V semiconductors, and exhibit PCEs of up to 38.8% under 1 Sun illumination. However, these tandem solar cells have a high degree of complexity and are expensive to manufacture on a large scale. The use of III-V based tandem solar cells is therefore restricted to niche applications, such as powering spacecraft.

For terrestrial applications, manufacturing costs profoundly influence the extent of deployment. Since the terrestrial PV market is dominated by c-Si solar cells, adding a low-cost absorber on top of the c-Si, resulting in high-efficiency tandem solar cells, will be a more promising

Figure 1. Schematic of a tandem solar cell comprising two solar cells with descending bandgap energies. Incident photons with energies above the bandgap of the top solar cell are harvested at a higher voltage by the wider-bandgap top solar cell. The lower-energy (longer-wavelength) photons transmitted by the top solar cell are harvested by the bottom solar cell.



“Thermalization losses are significantly reduced in tandem solar cells.”

route to lowering the levelized cost of electricity (LCOE). Until a few years ago, there was a lack of efficient, low-cost solar cells that could be used in a tandem configuration with the PV technologies established in the market. However, the advent of perovskite solar cells and their rapid progress has changed the status quo. Additionally, the feasibility of fabricating perovskite solar cells through solution processing enables low-cost, high-throughput sheet-to-sheet, and in the longer term roll-to-roll, production.

The advantages and challenges of perovskite solar cells

Perovskite, a mineral containing calcium titanate (CaTiO_3), was discovered in 1839 and named after the Russian mineralogist Lev Perovski. Today, the term *perovskite* is used to denote all the compounds that have a crystal structure similar to CaTiO_3 . The generic chemical formula of perovskites is ABX_3 , where A and B are positively charged ions of different sizes and X is a negatively charged ion.

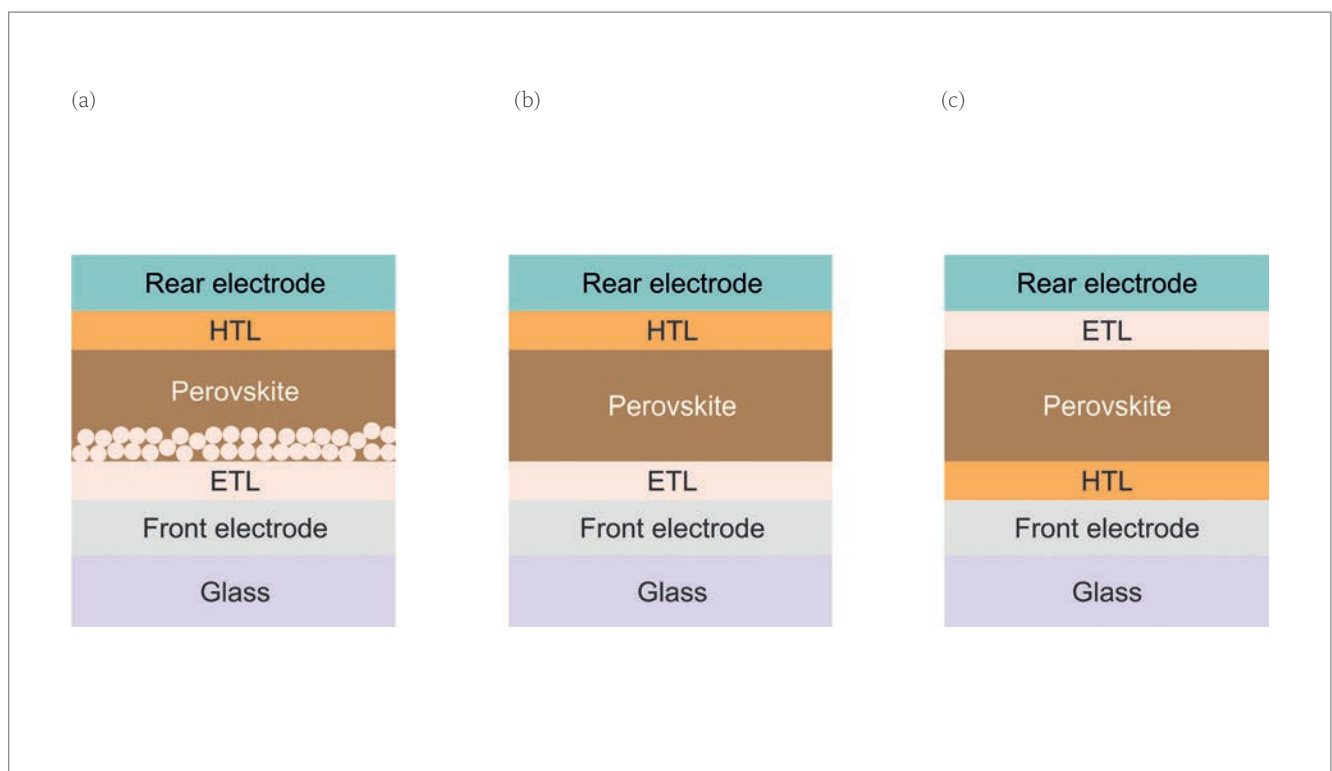
Depending on the choices of A, B and X ions, perovskites can be insulators, semiconductors, conductors or superconductors. Perovskites used in solar cells are crystalline semiconductors and are called *hybrid metal halide perovskites*. In such perovskites, the A site is usually occupied by monovalent methylammonium CH_3NH_3^+ (MA) or

formamidinium $\text{CH}(\text{NH}_2)_2^+$ (FA) or caesium (Cs^+), or a combination of these. The B site is taken up by bivalent lead (Pb_2^+) or tin (Sn_2^+), or a mixture of both. The X site is reserved for halides, such as iodide (I^-), bromide (Br^-) or chloride (Cl^-), or a mixture of these.

The most widely researched perovskites for solar cells are lead halide perovskites; they are also the most efficient owing to their remarkable optoelectronic properties. They have a direct optical bandgap, making them promising materials for solar cells as well as for light-emitting diodes and photodetectors. In particular, they offer the following advantages:

- Perovskites have high absorption coefficients of the order of 10^5cm^{-1} in the visible spectral range. Consequently, a perovskite layer of several hundred nanometres is enough to absorb most of the incident light. Besides leading to lower material cost, such thin layers are beneficial for efficient extraction of photo-generated charge carriers.
- Perovskites have sharp absorption edges that translate to low Urbach energies around 15meV, which is comparable to that of gallium arsenide, a direct bandgap crystalline semiconductor of very high optoelectrical quality. The low Urbach energy implies a low degree of structural disorder in the perovskite.
- Perovskites have a very low concentration of deep-level defects. Because of the combination of low Urbach energy and low concentration of

Figure 2. Schematic of the different architectures of perovskite solar cells: (a) mesoporous, (b) planar n-i-p, and (c) planar p-i-n.



deep-level defects, perovskite solar cells exhibit high open-circuit voltages (V_{oc}) in relation to their bandgap (E_g). The V_{oc} deficit ($E_g - qV_{oc}$) in perovskite solar cells is one of the lowest among all solar cell technologies.

Another noteworthy property of perovskites that makes them attractive for solar cells is the long diffusion length of charge carriers. A charge-carrier diffusion length exceeding 1 μm has been demonstrated in polycrystalline perovskite films, while in perovskite single crystal the value is around 175 μm . Such long diffusion lengths are made possible by the combined effect of high mobility and long lifetime of charge carriers, primarily because of a low concentration of deep-level trap states in the perovskite. The long charge-carrier diffusion length, coupled with the small thickness of the perovskite layer (thanks to the high absorption coefficient), leads to a high charge-carrier collection efficiency in perovskite solar cells.

Despite the remarkable properties and excellent performance of perovskite solar cells, their prospects of commercialization have been dampened by their long-term instability. However, extensive research into this key aspect has recently resulted in solar cells with improved stability over a period of several thousand hours.

Architecture of the perovskite solar cell

Most perovskite solar cells are fabricated on glass substrates, although fabrication on flexible plastic substrates is also feasible. The primary layers in a typical perovskite solar cell include a *front electrode*, which is usually a transparent conductive oxide (TCO) deposited on the substrate, an *electron transport layer* (ETL), a *photoactive perovskite layer*, a *hole transport layer* (HTL), and a *rear electrode*, which can be a metal or a TCO.

Perovskite solar cells belong to the so-called thin-film photovoltaics (TFPV) and are classified into three categories on the basis of their architecture: mesoporous, planar n-i-p, and planar p-i-n (Fig. 2).

The *mesoporous architecture* is derived from dye-sensitized solar cells, where a mesoporous scaffold is used for better extraction of charge carriers. As perovskite solar cells evolved from dye-sensitized solar cells, the mesoporous architecture was maintained during their early development. The architecture typically uses a mesoporous structure of TiO_2 made of nanoparticles, on top of a compact TiO_2 layer as the ETL. The perovskite is then deposited on the mesoporous scaffold, filling the vacant spaces up to the compact TiO_2 layer. With such a design, the interfacial surface area between the ETL and the perovskite is substantially increased, thus increasing the efficiency of electron extraction. As the understanding of the

“The use of certain mixed cations can remedy the phase segregation of perovskites and thus lead to photostable behaviour.”

fundamental properties of perovskites improved, and with the discovery of their ambipolar conductivity and long charge-carrier diffusion lengths, the mesoporous device architecture gave way to the less complex planar architectures.

In the *planar architectures*, the mesoporous scaffold is replaced by a planar ETL. Planar perovskite solar cells come in two flavours: n-i-p and p-i-n. In the case of the n-i-p architecture, the ETL is first deposited on the TCO/glass substrates followed by the perovskite and then the HTL. In n-i-p perovskite solar cells, the *ETL* is in front of the perovskite, facing the incident light, while in p-i-n perovskite solar cells, the *HTL* is in front of the perovskite, facing the incident light. Planar architectures are simpler to fabricate than the mesoporous architecture and allow a wide range of material choices for the transport layers. Although the current record perovskite solar cell with a PCE of 23.3% has a mesoporous architecture, the majority of high-efficiency planar perovskite solar cells, including the ones discussed in this work, use the n-i-p architecture.

A tuneable bandgap

Despite the challenges, high-efficiency perovskite solar cells are currently the most promising low-cost candidates for tandem solar cells with established PV technologies, for terrestrial applications. An interesting property of perovskites, particularly attractive from a tandem perspective, is the ease of bandgap tuneability. The bandgap of most perovskites can be tuned simply by varying their chemical composition, most commonly the anion; the replacement of ions alters the size of the perovskite crystal lattice, thus changing the bandgap. This interesting property enables the fabrication of perovskites with bandgaps ranging from 1.1 eV to 3.2 eV.

The most commonly used perovskites for high-efficiency solar cells have a bandgap of ~1.6 eV. For tandem applications with c-Si and copper indium gallium selenide (CIGS), perovskite bandgaps between 1.7 eV and 1.8 eV are of particular interest. However, the PCE of such wide-bandgap perovskite (1.7–1.8 eV) solar cells are lower than expected.

One of the reasons for the low performance of wide-bandgap perovskite solar cells is related to their photo-instability. Under continuous illumination, the perovskites tend to phase segregate, leading to degradation; this phenomenon has been shown to occur in certain wide-bandgap perovskites that have mixed halides (I^- and Br^-) as anions. The phase segregation

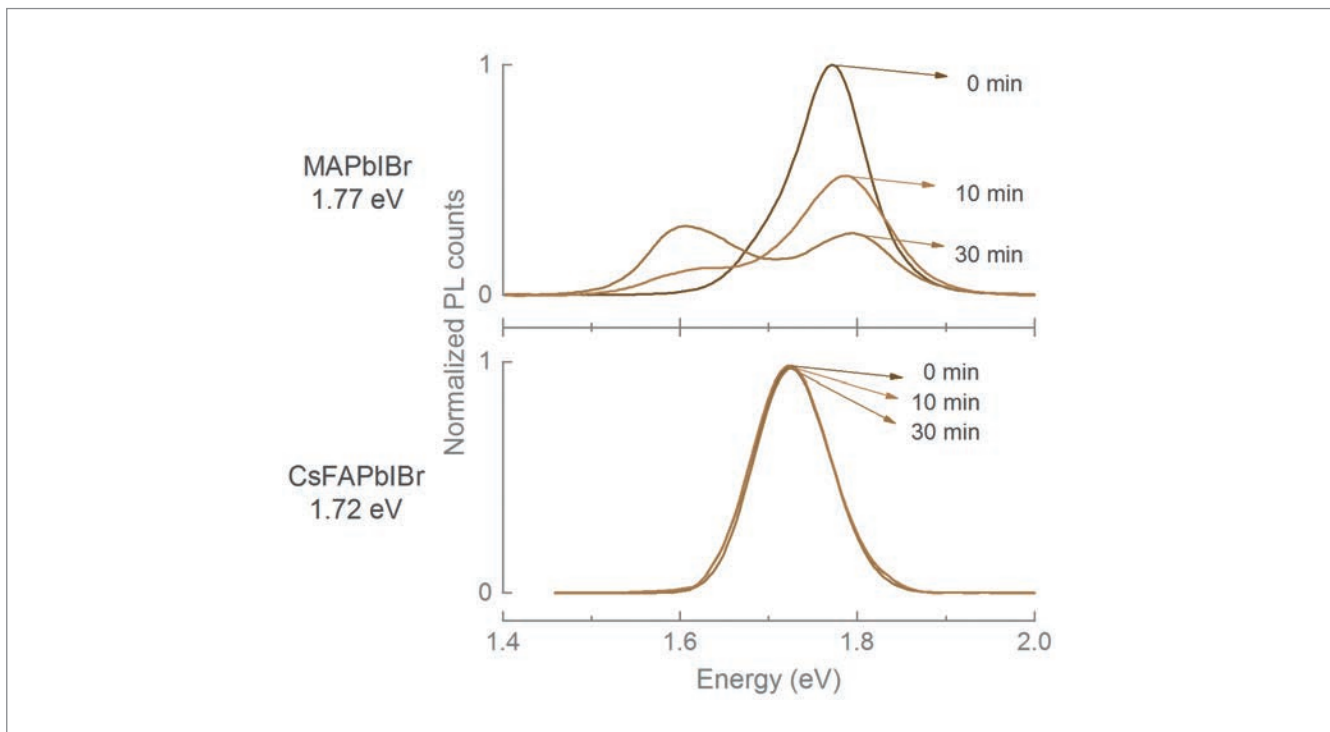


Figure 3. PL spectra of MAPbIBr and CsFAPbIBr thin films under continuous AM1.5G irradiation.

has a significant effect on the performance of such wide-bandgap solar cells, reducing their effectiveness as a top solar cell in tandem solar cells. It has been shown at imec that the use of certain mixed cations can remedy the phase segregation of perovskites and thus lead to photostable behaviour.

How to address the photo-instability of perovskite cells

The photostability of two different mixed-halide perovskites, namely methylammonium lead iodide–bromide, $\text{CH}_3\text{NH}_3\text{Pb}(\text{I}_{0.6}\text{Br}_{0.4})_3$ (MAPbIBr) with a bandgap of 1.77 eV, and caesium formamidinium lead iodide–bromide, $\text{Cs}_{0.15}(\text{CH}_5\text{N}_2)_{0.85}\text{Pb}(\text{I}_{0.71}\text{Br}_{0.29})_3$ (CsFAPbIBr) with a bandgap of 1.72 eV, is investigated. The phase stability of both perovskites, light soaked under continuous AM1.5G illumination, was characterized by photoluminescence (PL) measurements.

The PL response of MAPbIBr thin films changes over time, with the PL peak corresponding to the pristine MAPbIBr perovskite phase splitting into two separate peaks over time (Fig. 3). The splitting of the PL peak indicates the segregation of the pristine MAPbIBr perovskite phase into iodide-rich and bromide-rich phases under illumination. The iodide-rich phase (indicated by the PL peak at

~1.6 eV) limits the electrical performance, resulting in a reduction in V_{oc} of the MAPbIBr solar cells over time.

On the other hand, CsFAPbIBr mixed-halide perovskite does not exhibit photoinduced phase segregation. The CsFAPbIBr thin films show a similar PL response, with no peak splitting, even after 30 min of light soaking, suggesting that CsFAPbIBr perovskite is phase stable under illumination. Additionally, long-term light stability tests reveal no undue degradation of the 1.72 eV CsFAPbIBr solar cells, compared with standard 1.56 eV perovskite solar cells. The phase stability is also reflected in a stable V_{oc} of the CsFAPbIBr solar cells over time. Although these solar cells exhibit stable voltage output, their V_{oc} deficit is 0.62 V; such a large V_{oc} deficit is unfavourable for tandem applications, considering the low current output of wide-bandgap perovskite solar cells.

Addressing the large V_{oc} deficit in wide-bandgap perovskite cells

Wide-bandgap perovskite solar cells also generate less current than the standard perovskite (1.6 eV) solar cells owing to their bandgap. Nevertheless, the lower current is expected to be compensated by a higher voltage output in the wide-bandgap perovskite solar cells. However, the V_{oc} of wide-bandgap perovskite solar cells has so far been lower than expected, with a V_{oc} deficit greater than 0.6 eV. Interestingly, the V_{oc} deficit in standard perovskite solar cells is just 0.4 eV, and their PCE is considerably higher than with wide-bandgap perovskite solar cells. This has led to

“The constraints on the optimal bandgap of the top and bottom solar cells are more relaxed for the four-terminal configuration.”

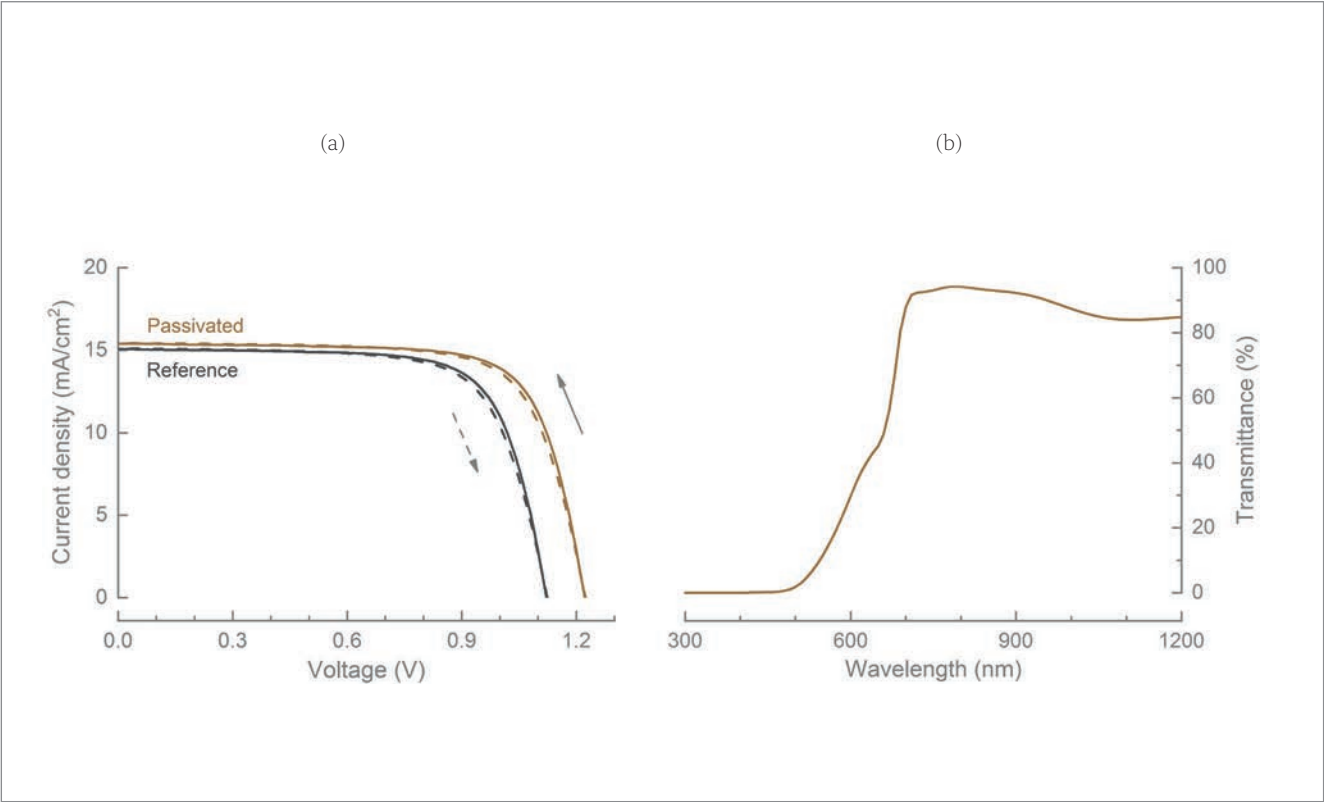


Figure 4. (a) Current density–voltage characteristics of semi-transparent CsFAPbI₂Br solar cells with interfacial passivation layer ('Passivated') and without ('Reference'), measured in forward and reverse directions. (b) Transmittance spectra of a passivated semi-transparent CsFAPbI₂Br solar cell.

Device	J_{sc} [mA/cm ²]	V_{oc} [V]	Fill factor [%]	Aperture PCE _{SPO} [%]
Reference CsFAPbI ₂ Br	15.1 ± 0.13	1.11 ± 0.03	70.1 ± 0.7	11.7 ± 0.1
Passivated CsFAPbI ₂ Br	15.4 ± 0.11	1.22 ± 0.02	73.4 ± 0.4	13.8 ± 0.1
c-Si stand-alone	41.3 ± 0.02	0.691 ± 0.002	80.6 ± 0.1	23.0 ± 0.01
c-Si in tandem	24.1 ± 0.03	0.678 ± 0.002	81.2 ± 0.1	13.3 ± 0.03
CsFAPbI ₂ Br–Si tandem				27.1 ± 0.1

Table 1. PV parameters of semi-transparent CsFAPbI₂Br perovskite and c-Si solar cells, measured under 1,000W/m² AM 1.5G irradiance. The reported power conversion efficiency PCE_{SPO} is the stabilized power output of the solar cells tracked at the maximum power point for 10 min

many research groups using standard perovskites for top solar cells in tandem with c-Si and CIGS solar cells, although the bandgap combination is not optimum. Through effective interface passivation, 1.72eV mixed-halide perovskite solar cells with a V_{oc} deficit of just 0.5V have been demonstrated; this is the lowest reported value for a mixed-halide perovskite system with a bandgap wider than 1.7eV (see also Fig. 4(a)).

Better optimization of the cells in the stack

Perovskite-based tandem solar cells are commonly fabricated in two configurations: two-terminal and four-terminal.

In *two-terminal* tandem solar cells, the top solar cell is processed directly on the bottom solar cell, and the two cells are connected in series. This configuration requires only one transparent electrode, and thus has potentially

lower parasitic absorption. For efficient operation of two-terminal tandem solar cells, however, the currents generated by the top and bottom solar cells must be similar. As a result, the overall current output of the tandem solar cell will be limited by the lower of the currents generated by the individual subcells. Additionally, seasonal and angular variations in the solar irradiance significantly impact the overall performance of two-terminal tandem solar cells. Consequently, the constraints on the optimal bandgaps of top and bottom solar cells are stricter for the two-terminal configuration. The influence of angular variations of the solar irradiance can be mitigated by employing solar tracker systems, but the use of such systems leads to increased costs.

In the case of *four-terminal* tandem solar cells, the top and bottom cells are electrically isolated from each other, and the output power is extracted separately. This configuration does not

Device	Aperture area [cm ²]	I_{sc} [mA]	J_{sc} [mA/cm ²]	V_{oc} [V]	Fill factor [%]	Aperture PCE _{SPO} [%]
Perovskite	0.13		21.1 ± 0.15	1.07 ± 0.04	72.3 ± 0.9	16.7 ± 0.1
	4	11.1 ± 0.1	19.4 ± 0.1	7.595 ± 0.001	70.1 ± 1.1	14.8 ± 0.1
CIGS	3.8	13.1 ± 0.08		2.692 ± 0.009	75.6 ± 1.0	7.1 ± 0.05
Perovskite–CIGS tandem	0.13					23.8 ± 0.1
	3.8					21.3 ± 0.1

Table 2. PV parameters of semi-transparent perovskite and CIGS solar cells and modules in a four-terminal configuration, measured under 1,000W/m² AM1.5G irradiance; the response of CIGS device is measured with the incident light filtered through a semi-transparent perovskite solar module. The reported power conversion efficiency PCE_{SPO} is the stabilized power output tracked at the maximum power point for 10 min. The J_{sc} values reported for the perovskite module are normalized to a single cell, for easier comparison with 0.13cm² cells.

require current matching of the two solar cells, and therefore enables independent optimization of the subcells and modular fabrication. For the final assembly, both solar cells are simply mechanically stacked; this configuration requires more than one transparent electrode, leading to increased parasitic absorption. Moreover, on a system level, additional inverters/converters are required to drive the top and bottom solar cells individually, thus increasing the balance-of-system cost. Nevertheless, as a result of the independent power extraction from the top and bottom solar cells, the output of four-terminal multijunction devices is less affected by seasonal and angular variations in solar irradiance, thereby potentially resulting in greater energy yield than for two-terminal tandem solar cells.

Consequently, the constraints on the optimal bandgap of the top and bottom solar cells are more relaxed for the four-terminal configuration, providing additional flexibility in design over the two-terminal configuration. The work reported in this paper focuses on the four-terminal configuration of perovskite-based (perovskite–Si and perovskite–CIGS) tandem solar cells. As discussed above, photostable, wide-bandgap, mixed-halide perovskite solar cells were fabricated, and high V_{oc} was achieved by careful control of the perovskite–HTL interface.

The current–voltage characteristics of reference and passivated CsFAPbIBr solar cells are shown in Fig. 4(a). The passivation significantly improves the V_{oc} and fill factor of the solar cells, boosting the PCE from 11.7% to 13.8%. Furthermore, the CsFAPbIBr solar cells exhibit an average transmittance of 90% in the wavelength range 700–1,200nm (Fig. 4(b)). The high transmittance, coupled with a high V_{oc} , makes the passivated CsFAPbIBr solar cells attractive for highly efficient tandem solar cells.

Four-terminal tandem solar cells were then fabricated by combining the passivated CsFAPbIBr solar cells with c-Si solar cells. The wider bandgap of CsFAPbIBr compared with standard 1.56eV perovskites allows additional light to reach the bottom Si solar cell, enabling efficient harvesting of solar irradiation. The resulting CsFAPbIBr–Si tandem solar cells exhibit a PCE of 27.1% – the highest reported for a perovskite-based four-terminal tandem solar cell, exceeding the record PCE of single-junction Si solar cells (Table 1).

The scalability of perovskite-based tandem cells

Besides high efficiency on small sizes, the scalability of such perovskite-based multijunction devices needs to be addressed for commercial viability of this technology. To that end, perovskite–CIGS multijunction solar modules of up to two orders of magnitude larger than the small-area cells were fabricated. The key issue with the fabrication of large-area multijunction solar modules lies with the scalability of the perovskite device.

The losses in aperture PCE when scaling up the semi-transparent perovskite device from 0.13cm² cells to 4cm² modules were investigated. The design of perovskite modules and the choice of subcell lengths (3mm) are discussed in the authors' earlier work [1]. Three loss factors can be identified:

- *Resistance losses* include the loss in aperture PCE due to sheet resistance of the transparent electrodes and the losses at the interconnections of individual cell stripes in a module.
- *Dead area losses* are a consequence of the monolithic module design, where part of the active material is removed through scribes to allow interconnection of individual cell stripes. Dead area is the difference between aperture area and active area of a module.
- *Inhomogeneity losses* account for the variation in uniformity of the layers deposited on different sizes.

“By combining comprehensive loss reduction strategies with effective large-area fabrication, perovskite-based tandem solar modules with a PCE surpassing that of established PV technologies can be realized on an industrial scale.”

The reduction in aperture PCE of the semi-transparent perovskite device when going from a 0.13cm^2 cell to a 4cm^2 module is due to a combined effect of all three loss factors. A SPICE-based analogue electronic-circuit simulator was used to estimate the perovskite efficiency when scaling up from a 0.13cm^2 cell to a 4cm^2 mini-module comprising seven subcells, each $\sim 2.9\text{mm}$ long [2]. The estimate indicates that dead area loss accounts for $\sim 58\%$ of the difference in aperture PCE, while resistance loss constitutes $\sim 31\%$. The perovskite modules have a geometric fill factor of 0.91; in other words, 9% of the module aperture area is dead area, which justifiably makes dead area the major loss factor for aperture PCE when going from 0.13cm^2 cell to 4cm^2 module.

The width of individual cell stripes in the perovskite solar module is optimized for the sheet resistance of indium tin oxide (ITO) electrodes, as described in the authors' previous work [1], thus minimizing the resistance loss when scaling up from cell to module. The 0.13cm^2 perovskite cell and the 4cm^2 perovskite mini-module were fabricated identically on substrates with the same dimensions; therefore, the loss in aperture PCE due to layer inhomogeneity when going from 0.13cm^2 cell to 4cm^2 module accounts for just 11% of the total losses.

An all thin-film perovskite/CIGS multijunction module of similar size was fabricated, yielding an overall PCE that substantially outperformed the single-junction PCE of the CIGS single module. For this, a 3.8cm^2 aperture area module with PCE of 16.7%, provided by the Center for Solar Energy and Hydrogen Research (ZSW), was later used as the bottom cell. When the perovskite module was placed on top, a PCE of 7.1% was still recorded for the CIGS module. The 4cm^2 perovskite module had an aperture PCE of 14.8%, bringing the total PCE of the perovskite/CIGS multijunction stack to a remarkable 21.3%, on an overall 3.8cm^2 aperture area (Table 2).

Outlook

Scalable perovskite solar modules have strong potential for low-cost, high-efficiency tandem photovoltaics. Although the demonstrated tandem module design is scalable to commercial dimensions, various factors affect the aperture PCE of such large-area modules. Resistive losses caused by transparent electrodes can be reduced to a certain extent by using better conductive transparent electrodes, such as hydrogen-doped indium oxide and indium zinc oxide. Losses to aperture PCE due to the dead area formed during patterning of the modules can be minimized by advanced laser patterning, which improves the geometric fill factor.

For industrial-level upscaling, large-area linear coating techniques must be employed for the fabrication of perovskite solar modules. Note

that while scaling up to industrial-scale modules, inhomogeneity will be the key loss factor limiting the aperture PCE of the perovskite solar module, and consequently the aperture PCE of the tandem solar module. Homogeneous, large-area perovskite coating and deposition techniques are therefore essential for maintaining the high aperture PCE on large sizes. By combining comprehensive loss reduction strategies with effective large-area fabrication, perovskite-based tandem solar modules with a PCE surpassing that of established PV technologies can be realized on an industrial scale.

References

[1] Jaysankar, M. et al. 2017, "Four-terminal perovskite/silicon multijunction solar modules", *Adv. Energy Mater.*, Vol. 7, p. 1602807 (doi:10.1002/aenm.201602807).

[2] Eidelloth, S., Haase, F. & Brendel, R. 2012, "Simulation tool for equivalent circuit modeling of photovoltaic devices", *IEEE J. Photovolt.*, Vol. 2, pp. 572–579 (doi:10.1109/JPHOTOV.2012.2187774).

About the authors

Dr. Manoj Jaysankar holds a Ph.D. in electrical engineering from KU Leuven, Belgium. He is a graduate of the Erasmus Mundus Master in Nanoscience and Nanotechnology programme, for which he specialised in nanoelectronics to earn a joint M.Sc. from KU Leuven and Chalmers University of Technology, Sweden. His research at imec focuses on design and development of high-efficiency, perovskite-based tandem solar cells.

Dr. Tom Aernouts is an R&D manager at imec. He received his M.Sc. in semiconductor physics from KU Leuven in 1998, and his Ph.D. in science in 2006 from the same university. Since 2006 he has been the group leader of imec's thin-film PV group, steering imec's thin-film PV research activities, with an initial infrastructure upgrade in 2009 enabling the processing of devices up to $15\text{cm} \times 15\text{cm}$, and a subsequent upgrade in 2018 to extend the device size to $35\text{cm} \times 35\text{cm}$.

Enquiries

Tom Aernouts
imec
Thor park 8320
B-3600 Genk, Belgium

Tel: +32-16 281689
Email: aernouts@imec.be
Website: www.imec-int.com

Taking the temperature of bifacial modules: Are they warmer or cooler than monofacial modules?

Bas Van Aken & Gaby Janssen, ECN.TNO – Solar Energy, Petten, The Netherlands

Abstract

Bifacial cells and modules collect light falling not only on the front side of the panels but also on the rear; this additional collection of light increases the total absorbed irradiance, and accordingly the generated current. One of the remaining questions is: what temperature do bifacial solar panels operate at compared with monofacial panels? The extra light absorption at the rear will heat up the modules more, but at the same time, the parasitic heating by the absorption of infrared light is reduced, because infrared light is mostly transmitted through the glass–glass panels. In this paper, different bifacial and monofacial cell and module architectures are considered for the calculation of the energy spectra for all heat loss and absorption processes and the effective heat input. The heat transfer coefficients and the heat capacities of modules with different rear panels are given. Actual module temperatures for different layouts are presented and discussed for low- and high-irradiance (diffuse/direct) conditions in the Netherlands.

Introduction

That temperature plays an important role in the module power and cell efficiency is well known – hence the importance of controlling module and cell temperatures under standard test conditions (STC). For example, PV panels with silicon-based cells have a temperature coefficient of the order of $-0.5\%_{\text{rel}}$ per °C. PV panels that are installed in the field or on a roof, however, have no temperature control; their temperature is determined by the ambient temperature, wind and irradiance conditions, but also by the thermal properties of all module materials. Extensive research has been carried out to predict or model the temperature of regular monofacial PV panels under ‘real’ conditions, either on the basis of complicated mathematical or physical models [1] or by using numerical approximations [2].

The temperature of bifacial modules is also a topic of research interest [3,4], and an important parameter in determining the (additional) energy yield of bifacial PV systems. Soria and colleagues from CEA-INES [5] showed, for a vertical facade-integrated system with a diffuse reflector on the inner wall, that with increasing front irradiance, the temperature of bifacial modules decreases relative to that of monofacial modules. Recently, Lopez-Garcia and colleagues from JRC-ISPRA [6] published an extensive work on the temperature coefficients of bifacial crystalline silicon modules, determined using solar simulators and natural sunlight; they found that the temperature coefficients were not affected by reflecting or absorbing rear covers. For

bifacial modules, a clear relation between module parameters, light/heat absorption in the silicon wafer and bifacial irradiance has so far not been published.

Bifacial photovoltaic systems also utilize the light that reaches the rear side of the PV modules to generate electricity. The rear incident light either originates from diffuse or indirect light from the sky, or from reflected light from the ground (so-called *albedo light*). The combined irradiance on the PV module will consequently be greater, leading to an increase in the generated photocurrent. This brings about the question as to whether the additional incident light also generates an increase in the actual operating temperature of these bifacial solar panels, compared with the operating temperature of monofacial modules. Since an increase in operating temperature will lead to a reduction in the output voltage of a module [7,8], this would partly offset the gain due to the bifaciality.

There are three possible responses to the question whether bifacial modules are warmer or cooler than monofacial modules:

1. **Warmer:** the module temperature rises because of the additional absorption of light on the rear side of bifacial PV panels, and consequently the output of the bifacial modules will be lower than expected from an optical analysis alone.
2. **Cooler:** the bifacial modules are not warmer, because the transmission of light through bifacial panels is also greater than in the case of monofacial PV panels.
3. **Neither warmer or cooler:** there is no difference in operating temperatures.

To answer this question correctly, it is necessary to analyse the full energy balance of the PV module by taking into account not only the additional light absorption and electricity generation by the rear side of the solar cells, but also the heat transfer to the environment and the heat capacity of the different modules.

First, the energy balance will be covered in detail, and all relevant optical, electrical and thermal processes will be highlighted. The differences in the absorption, generation and loss energy spectra of monofacial and bifacial solar cells will be shown.

The way in which the heat input of these samples increases with additional rear irradiance is then derived from these spectra. Next, the heat output term is evaluated from experimental heating curves. Finally, outdoor data are presented for the different single-cell devices and full-size monofacial and bifacial modules, showing the influence of the rear irradiance fraction and the albedo on the different device temperatures.

Energy balance and theory

The energy balance of an operating (bifacial) PV system is sketched in Fig. 1. The energy input is determined by the sum of the irradiance on all surfaces of the PV module, which is a combination of: 1) direct irradiance, i.e. the beam of light directly from the sun; 2) indirect irradiance from the sky; and 3) indirect irradiance from reflected (albedo) light from the ground, caused by either sun beam or sky light. For the energy balance, the optical losses due to reflection and transmission need to be subtracted from the energy input.

All the incident light that is not reflected or transmitted is, by definition, absorbed somewhere in the solar panel. The major portion is absorbed by the absorber material, in this case the Si wafer, generating electron-hole pairs that are to be collected and generate the solar electricity. Generated electricity extracted at the maximum power point is one source of energy transfer from the module. Although ~90% of incident light is absorbed in the Si wafer, only ~20% of the energy is converted to electricity. A significant part of the absorbed energy leads to conversion losses in the Si wafer, such as thermalization, entropy generation and recombination, or is parasitically absorbed [9,10] in heavily doped emitters or surface fields or in the metallization and module materials. All these conversion and parasitic absorption losses are converted to heat, as a result of which the system heats up, resulting in heat transfer to the environment. Heat transfer to the environment occurs by convection to the ambient air, enhanced by wind, and by radiation to the sky and ground. A *steady state* (constant temperature) is achieved when the heat generated in the system equals the heat transfer to the environment.

The energy balance thus consists of:

- A heat input, determined by the bifacial irradiance and many electro-optical processes in the solar panel.
- A heat transfer, determined by the heat transfer coefficient(s) and the difference in module and ambient temperatures.
- The heat capacity of the module.

In the next section, the formula describing the relation between these parameters will be introduced.

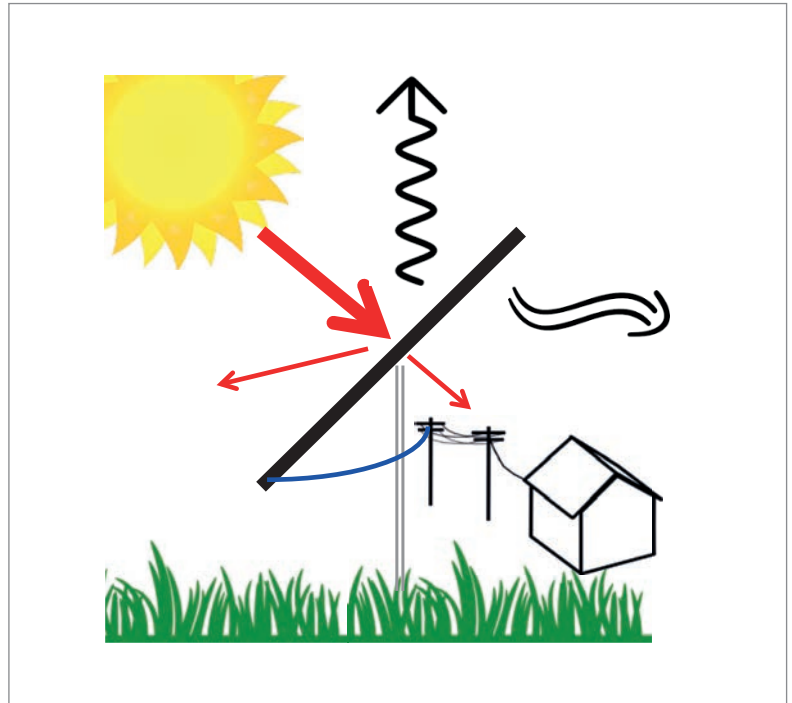


Figure 1. Sketch of the thermal balance of a PV module. The heat input to the module is represented by the thick red arrow, corrected for reflected and transmitted light losses (indicated by thin red arrows). Energy is removed from the module by: 1) grid connection of the produced electricity (blue line); 2) radiation of heat to the sky and ground (wavy black arrow); and 3) convection of heat by the air (curved black double arrow).

Energy balance formula

Consider a solar device that is to be exposed to a constant irradiance. The temperature of the device is then given by an exponential heating curve as a function of time:

$$T(t) = T_{\text{amb}} + \frac{Q_{\text{eff}}}{U} \left(1 - \exp\left(-\frac{U}{C_p} t\right) \right) \quad (1)$$

where

$T(t)$	= module temperature as a function of time
T_{amb}	= ambient temperature
Q_{eff}	= the heat input
U	= heat transfer coefficient
C_p	= heat capacity of the panel

In this simple model, the heat transfer is assumed to be proportional to the temperature difference $\Delta T = T(t) - T_{\text{amb}}$, with an effective heat transfer coefficient U , which combines the effects of radiative and convective heat transfer.

Equation 1 shows that the ratio of the heat transfer coefficient U and the heat capacity C_p will determine how fast the panel heats up. The timescale of the exponential curve is characterized by a half time $t_{1/2}$ (the time to reach one-half the steady-state value) equal to $\ln(2) / b$ where b is given by the ratio U / C_p . The ratio Q_{eff} / U determines

“Conversion and parasitic absorption losses are converted to heat, as a result of which the system heats up.”

Bifacial Workshop 2019

6th edition of bifiPV

Come and create the PV future with us!

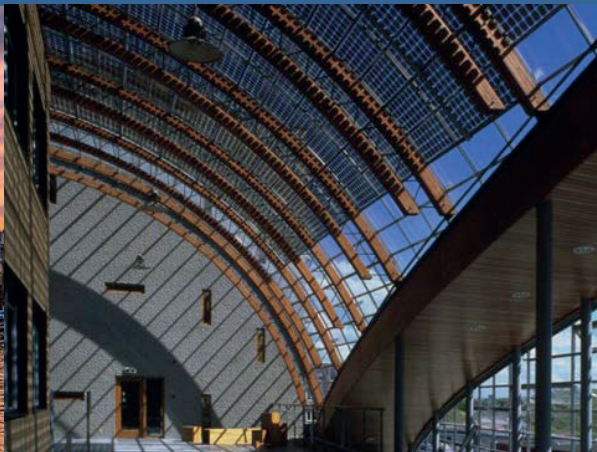
REGISTER SOON!
www.bifiPV-workshop.com



September 16-17, 2019 | Amsterdam | NL

- ❖ Sessions on: systems and bankability, cell and module technology, standardization, simulation
- ❖ Experts from academy and industry discuss the latest developments
- ❖ Podium discussions and networking activities in great atmosphere

Bankability and bifacial modeling will be in the focus of bifiPV2019



sponsors



media partners



how much the temperature will increase. At steady state, the temperature T_{ss} is given by:

$$T_{ss} = T_{amb} + \frac{Q_{eff}}{U} \quad (2)$$

The heat transfer out of the device is given by:

$$Q_{out} = U \Delta T \quad (3)$$

Thus, from a heating/cooling curve under constant irradiance, the ratio Q_{eff} / U can be determined from $T_{ss} - T_{amb}$, and the ratio U / C_p determined from the half time of the exponential fit. In the case where Q_{eff} is known, e.g. from the analysis that will be presented in the next section, the heat transfer coefficient and the heat capacity can be deduced.

Indoor measurements

Two types of solar cell and two rear panel materials are considered in this study. The conventional, monofacial Al-BSF solar cell is compared with the bifacial n-PERT solar cell. The Al-BSF cell has a highly doped back-surface field (BSF), which is created by screen printing Al paste on the full rear surface; this paste forms an opaque Al-Si alloy. In contrast, the n-PERT solar cell's rear BSF is formed by diffusion of phosphorus [11], and this transparent BSF is contacted with an Ag metallization grid.

Both cell types were employed in monofacial single-cell mini-modules with a white backsheet (WBS) as a back reflector, and in bifacial mini-modules in a glass-glass configuration. Furthermore, two 60-cell modules were assembled with the bifacial n-PERT solar cells – one with a WBS and the other with a glass rear panel.

Cell spectral measurements

In this section, the discussion will be about where the energy ends up when light falls on a solar device. Since the fraction of the incoming irradiance that heats the solar device needs to be determined, measurements are performed to determine what fractions of the light end up as optical losses and photovoltaic energy output, or contribute to the heating of the solar cells.

First, the optical losses. The fraction of light reflected off the solar cells or transmitted through the solar cells is measured using an integrating sphere. By convolution of these measurements with the reference AM1.5G spectrum, the absolute transmission and reflection spectra are calculated. The remaining fraction, the absorption spectrum, is calculated from the difference between the AM1.5G spectrum and the reflection and transmission spectra.

The spectral response measurement determines the spectrally resolved current contribution, in short-circuit conditions. From the spectral response measurement, the internal quantum efficiency

(IQE) is then derived. Convoluting the absorption spectrum with the IQE curve gives the sum of the electrical power and the losses due to thermalization, recombination, resistance and entropy generation, while the convolution of the absorption spectrum with the $(1 - \text{IQE})$ curve gives the parasitic heating. Multiplication of this spectrum by various ratios yields the electrical power spectrum, the thermalization spectrum and the remaining loss spectrum:

- *Electrical power spectrum*: multiplication by the ratio $qV_{oc} * FF / E(\lambda)$, where V_{oc} and FF are the short-circuit voltage and the fill factor of the cell, q is the elementary charge and $E(\lambda)$ is the energy of a photon with wavelength λ .
- *Thermalization spectrum*: multiplication by the ratio $(E(\lambda) - E_g) / E(\lambda)$, where E_g is the band gap energy of Si.
- *Remaining loss spectrum*: multiplication by the ratio $(E_g - qV_{oc} * FF) / E(\lambda)$.

Fig. 2 shows these power and loss spectra for the two cell technologies. Note that the y axes – the absolute power spectral density – have different ranges in each graph in order to show more detail. In this figure, the standard monofacial Al-BSF cell, with 18.6% efficiency, is compared with an n-PERT bifacial solar cell, with 21.0% efficiency. As the Al-BSF solar cell has a lower conversion efficiency than the n-PERT solar cell, the electrical power spectrum is lower (Fig. 2(a)). Notwithstanding the difference in efficiency, there is hardly any difference ($-0.6\%_{abs}$) in the sum of the thermalization, recombination and entropy generation losses between the n-PERT and the Al-BSF solar cells (Fig. 2(c)).

Larger differences are observed in the optical losses (Fig. 2(b)). The reflection is highest, but similar in magnitude, at short wavelengths, below 500nm, and at wavelengths above the band gap. In comparison, the Al-BSF cell exhibits a larger reflection than the n-PERT solar cell in the 500–900nm wavelength range. The bifacial n-PERT solar cell has a non-zero transmission (green line), especially for wavelengths around and above the bandgap of Si. The Al-BSF solar cell obviously has no transmission losses.

The parasitic absorption losses (Fig. 2(d)) see an initial peak at low UV wavelengths, and significant absorption around, and especially above, the Si bandgap. The parasitic losses are significantly higher for the Al-BSF solar cell. Of course, the Al layer at the rear of the solar cell will absorb all IR radiation that is transmitted through the Si wafer. In the n-PERT solar cell, while there is some parasitic absorption in the metallization grid and some free-carrier absorption in the highly doped regions of the emitter and the BSF, a significant portion of the IR light is also transmitted through the solar cell.

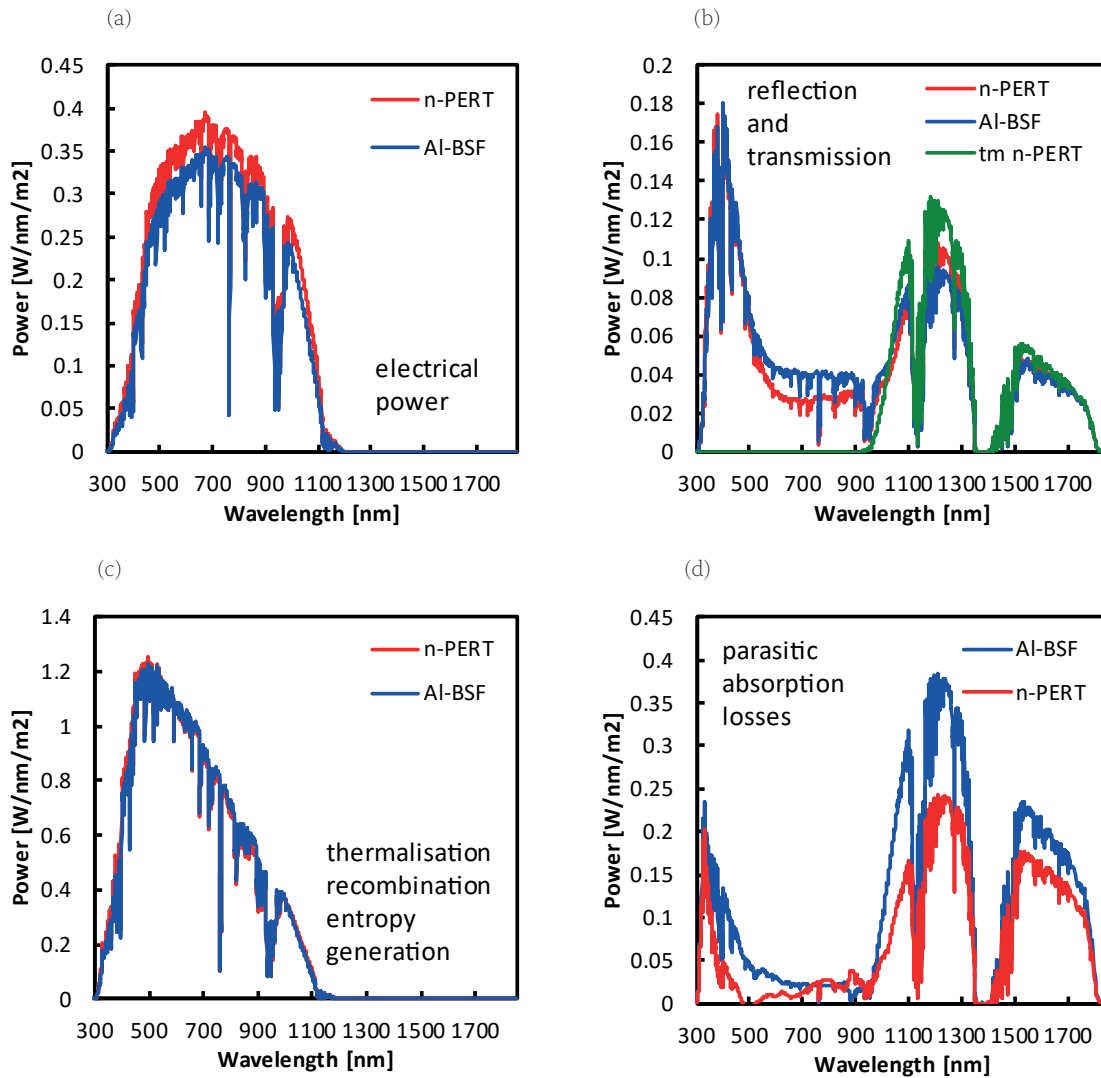


Figure 2. The different spectra for an Al-BSF (red) and an n-PERT (blue) solar cell: (a) electrical power; (b) optical losses, with transmission of n-PERT in green; (c) losses associated with photocurrent generation, such as thermalization, recombination and entropy generation; (d) parasitic absorption losses in metal and polymer layers.

Effective heat input of solar cells and modules

The effective heat input Q_{eff} of a cell or module results from the front and rear irradiation received:

$$Q_{\text{eff}} = \alpha_f G_f + \alpha_r G_r \quad (4)$$

where α_i ($i = f, r$) is the fraction of the incident irradiance transformed to heat, G_i ($i = f, r$) is the in-plane irradiance, and the subscripts f and r stand for front and rear respectively.

In Fig. 3 the total energy of each spectrum in Fig. 2 have been integrated and their fraction plotted in the bar diagrams for both bare solar cells and cells after encapsulation in either a (monofacial) module with a WBS, or a (bifacial) module in a glass-glass configuration. Most bars show that ~55% are generation losses, ~20% is the electrical power, ~15% is due to parasitic absorption and ~5–10% are optical losses. Obvious differences with the general behaviour are observed for rear-side measurements

on WBS devices and the rear-side results for the Al-BSF solar cell in a glass-glass module. In the former samples, reflection of rear incident light by the WBS makes up the major proportion, and the remaining part, ~30%, is absorbed as heat by the backsheet. In the glass-glass module with monofacial Al-BSF solar cells, up to 80% of the light is absorbed as heat in the Al-alloy layer at the rear of the solar cell.

From the graphs in Fig. 3, the fraction α_i (see Equation 4) of the incident energy that is converted to heat can be deduced by adding the conversion losses and the parasitic absorption (the red striped and solid blue regions in the graphs). Clearly, the laminates with Al-BSF cells have generally higher heating terms, specifically +3% to +8%, than in the case of laminates with n-PERT solar cells; this is because of the heat absorption of all (near-infrared) light that is transmitted through the solar cells in the Al-BSF layer. In contrast, in n-PERT solar cells, most of this light ends up as transmission losses.

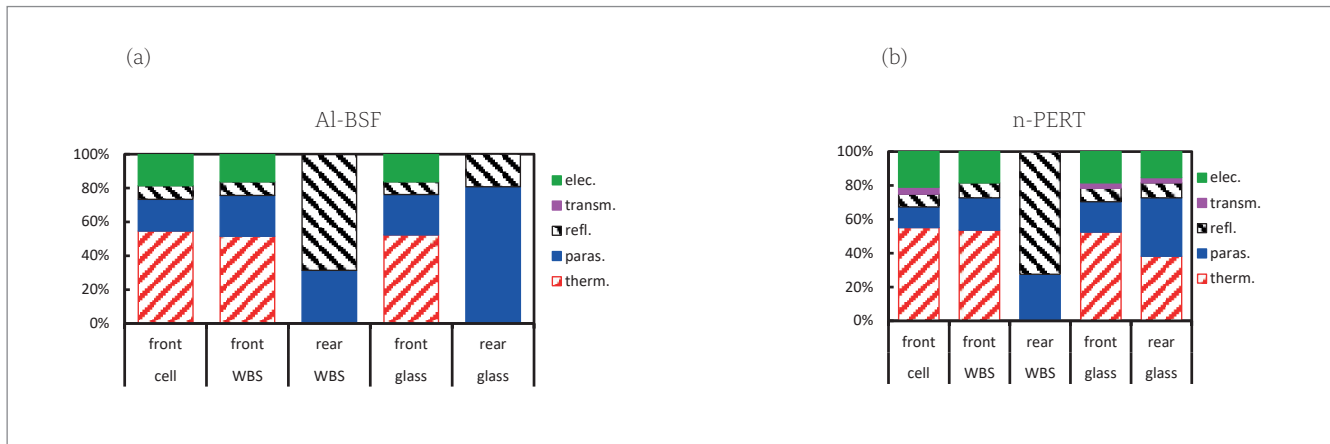


Figure 3. Relative contributions to incident energy by various processes for (a) Al-BSF and (b) n-PERT solar cells and modules. The specific processes are electric power, transmission, reflection, parasitic heating and conversion losses ('therm.'), including thermalization, recombination and entropy generation. The five columns represent, from left to right, the front side of the solar cell, the front and rear sides of a WBS module, and the front and rear sides of a glass-glass module.

To determine the effective heating term Q_{eff} for these solar modules, it is necessary to add the parasitic loss and the thermalization, recombination and entropy generation loss spectra and correct the result for the irradiance level. For two-sided irradiance, these spectra have also to be produced for the rear irradiance. Fig. 4 shows the effective heat generation as a function of the additional rear irradiance. Note that even monofacial cells in a glass-glass configuration, and also all modules with WBS, generate more heat when the rear irradiance increases; this heat is generated by parasitic absorption in the Al-BSF layer or in the backsheet. Fig. 4 also shows that the amount of rear irradiance determines whether the only truly bifacial module in this set (i.e. the n-PERT solar cell in a glass-glass configuration) generates more or less heat than the monofacial modules with a WBS.

The above analysis helps in determining the effective heat input for various device configuration and light conditions. This information has to be used as input data for the thermal modelling part of the energy yield modelling [12] in order to arrive at the actual operating temperature. However, the operating temperature also depends on the heat transfer coefficient, as well as on the heat capacity, when steady state has not been achieved. These parameters are discussed in the next section.

Module heating/cooling curves

Bifacial and monofacial modules were exposed to a constant irradiance of $1,000\text{W/m}^2$, with a black background environment to minimize the rear irradiance, using a steady-state solar simulator [13]. The measured module temperature as a function of the heating time for these two modules is plotted in Fig. 5, showing that the glass-glass module heats to about 46°C , whereas the WBS module is 2°C warmer in steady state; the graph also shows that the monofacial module reaches steady state significantly faster. The half times are determined from the fitted values (see Table 1): the half time for the WBS

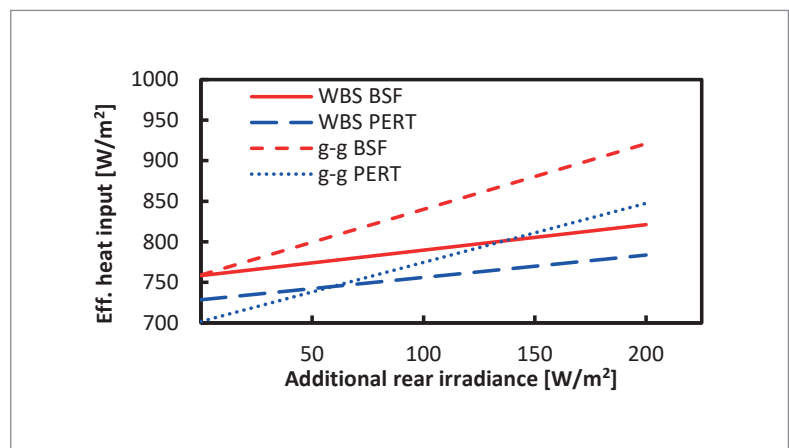


Figure 4. Effective heating terms for the two solar cell types and the two laminate type combinations. For this calculation, a constant front irradiance of $1,000\text{W/m}^2$ and a variable rear irradiance were assumed.

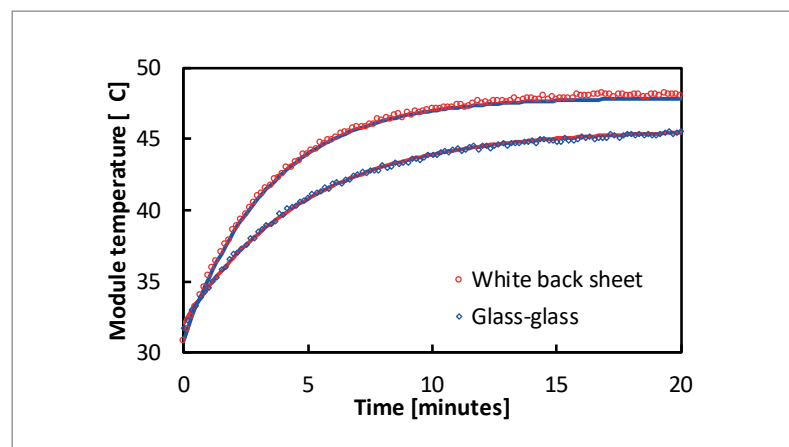


Figure 5. Heating curve for WBS (red circles) and glass-glass (blue diamonds) modules under constant irradiance conditions. The solid lines represent exponential curves fitted to the data.

module is only 140s, but the half time for the glass-glass module is almost 50% longer, at 200s.

The data were fitted to the exponential formula (see Equation 1). As explained in the previous section, under constant irradiance and ambient conditions, a is given by Q_{eff} / U . Likewise, the fitted parameter b determines the heating rate and is given by U / C_p .

Taking the values for a (determined from the fit)

	T_{ss} [°C]	Q_{eff} [W/m ²]	U [W/m ² /K]	$t_{1/2}$ [s]	C_p [kJ/m ² /K]	C_p from Hoang et al. [14] [kJ/m ² /K]
WBS	47.9	729	29.5	140	6.5	6.6
Glass-glass	45.7	702	31.3	200	9.9	10.1

Table 1. Fitted and calculated values for the heating curves in Fig. 5.

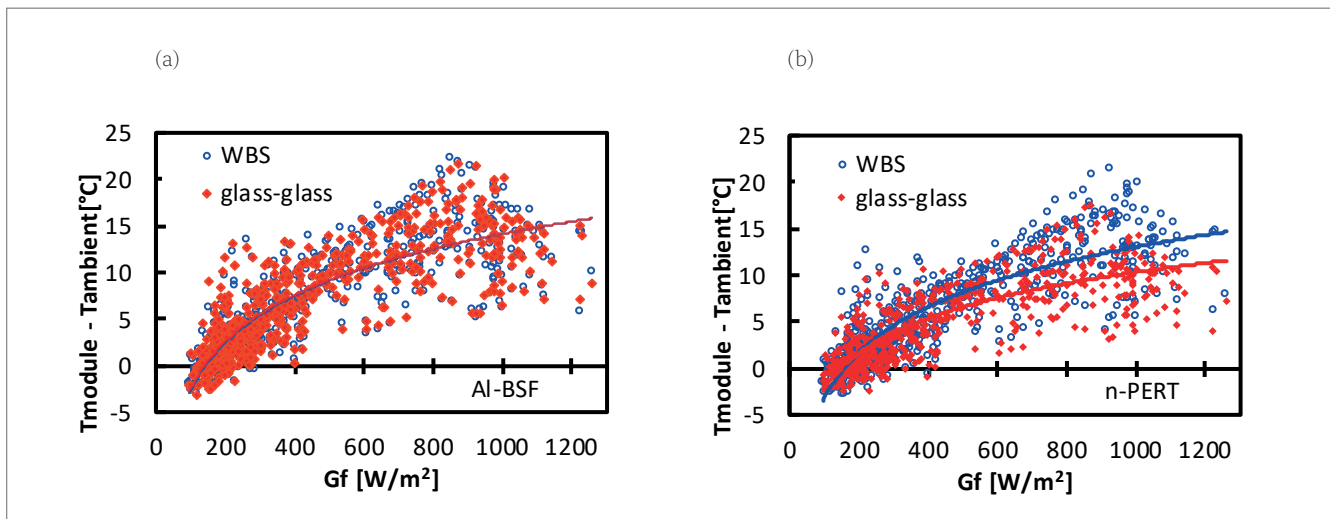


Figure 6. Increase in module temperature relative to the ambient temperature for (a) Al-BSF and (b) n-PERT solar cells in WBS (in blue) and glass-glass (in red) module configurations. The solid lines are logarithmic fits as a visual reference.

“In outdoor conditions wind and relative humidity will influence the heat transfer coefficient U .

and the calculated values for Q_{eff} (as explained by Fig. 3), the heat transfer coefficient U is calculated. From Equation 4 and the fitted value for b , the heat capacity C_p is calculated. A comparison with the heat capacity as determined from literature values for the specific heat capacities of the bill of materials is presented in Table 1. ECN.TNO's thermal model for the heating curve is validated by the good agreement between the derived experimental values for C_p and the values taken from the literature. Note that the time to reach steady state in these indoor conditions is only around 15 min.

Although in these indoor conditions the glass-glass laminate showed a 2K lower heating at 1,000W/m² irradiance, care should be taken when translating these results to outdoor conditions. Among other factors, in outdoor conditions wind and relative humidity will influence the heat transfer coefficient U , while the effective heat source term Q_{eff} will be affected by the total irradiance as well as by the ratio between front and rear irradiance, which is most relevant to outdoor conditions.

Outdoor measurements

In the first part of the outdoor results, single-cell laminates with the same two cell types and two rear materials as those used in the power spectrum analysis are monitored on ECN.TNO's rooftop installation [15]. In the second part, data

are presented for 60-cell modules with the same bifacial n-PERT solar cells, but with either a WBS or a glass panel as the rear material.

Effect of rear material choice for two different cell types

Single-cell laminates with different cell types and rear panels were installed on a rooftop at a 30-degree tilt. Data were recorded in 10-min intervals and recorded consecutively for all four samples. The irradiance was monitored to ensure constant conditions over a period of a few seconds. For each dataset, the difference between the measured module temperature with respect to the ambient temperature was determined.

Fig. 6(a) and (b) show the data for the single-cell laminates with monofacial Al-BSF solar cells and bifacial n-PERT solar cells respectively, as a function of the front irradiance for WBS or glass rear panel configurations. For clarity, a logarithmic function has been fitted to the data. The large deviations between the determined differences and the fitted curves are due to the variations in rear irradiance for a given front irradiance and the variable wind conditions. The trend in the data is clear: at a low irradiance, the modules are cooler than the ambient temperature, and with increasing irradiance, the difference increases monotonically. The Al-BSF samples show, on average, a ~14K increase, relative to the ambient temperature at 1,000W/m² front irradiance for both rear panels. The n-PERT samples with a WBS undergo a very similar increase, ~13K, but the n-PERT samples with glass as the rear panel show only a ~10K increase at 1,000W/m² front irradiance.

Although the glass–glass samples have a higher Q_{eff} (because of the rear irradiance contribution) than the WBS ones, the device temperature is not higher for the Al-BSF samples, and is in fact even lower for the n-PERT samples. Apparently, these glass–glass mini-modules have a higher heat transfer coefficient U , as was also deduced from Fig. 5. Note that the heat input term can be determined fairly accurately, but the heat transfer is much less precise, as it cannot be measured directly and depends on the module materials, geometry, humidity, wind conditions and the temperature of the air, sky and background.

Effect of albedo

For this investigation, a group of 60-cell bifacial and monofacial modules were measured on the outdoor rooftop set-up at ECNTNO [15]. Data were gathered with grey concrete (red data) and with white-painted concrete (blue data) as the albedo for a period of nine months for each. Full I – V curves and irradiance data are recorded every 10 min, leading to over 10,000 measurement points for each parameter, above concrete and above white paint. It is desired to determine the difference in temperature and performance of the modules for the two albedo conditions. For each measurement point, the differences in V_{oc} , I_{sc} and module temperature are calculated. These data were summarized by averaging the rear irradiance, rear irradiance fraction and the ΔV_{oc} , ΔI_{sc} and ΔT for 20W front-irradiance bins.

Fig. 7 shows the average of rear irradiance and rear irradiance fraction, as a function of the front irradiance. Clearly, the rear irradiance increases with front irradiance for both albedo conditions. The rear irradiance fraction is 6% for grey concrete and 20% for white-painted concrete at 1,000W/m² front irradiance. In both cases, the rear irradiance fraction is higher for lower front-irradiance conditions.

The data with low front irradiance, for the location in question, combine two typical situations.

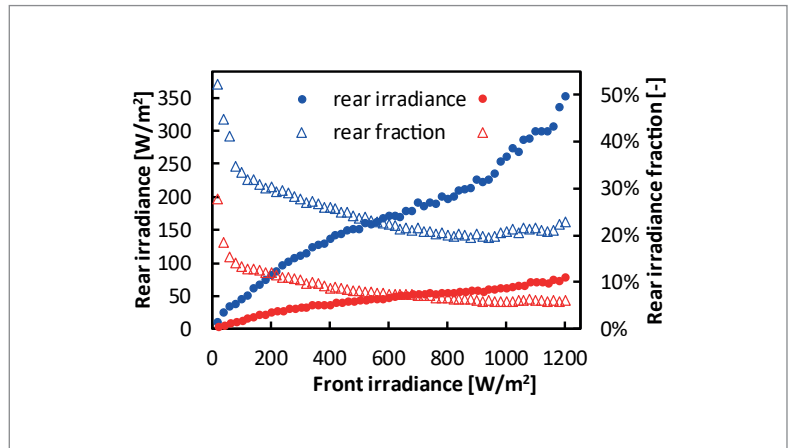


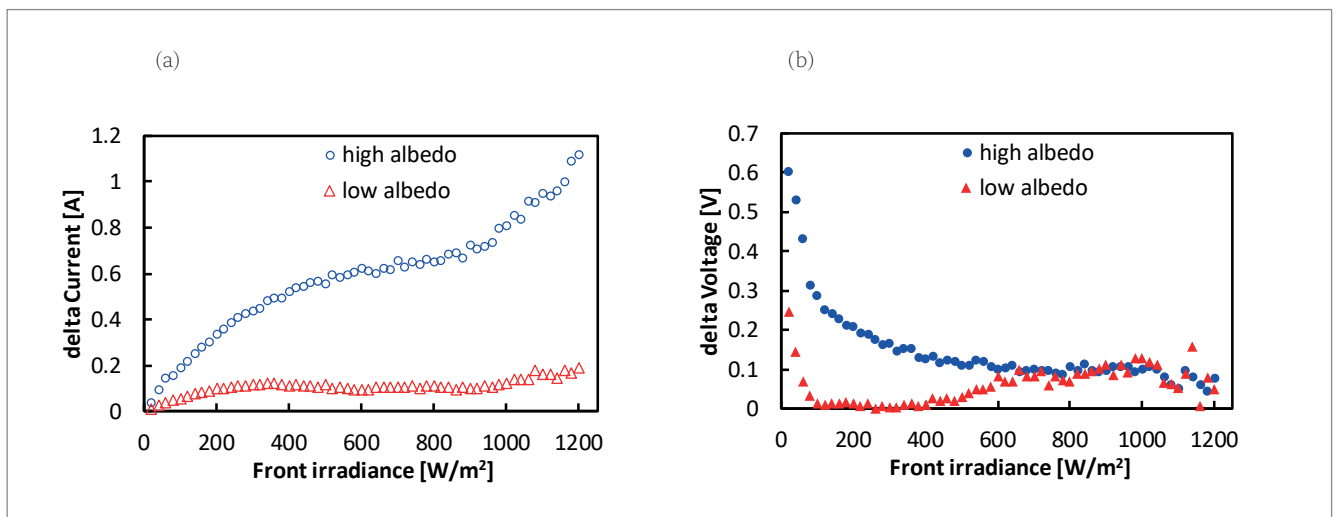
Figure 7. Average rear irradiance and rear irradiance fraction as a function of the front irradiance.

First, when the irradiance is dominated by diffuse irradiance, the front irradiance is low, but the diffuse irradiance is still incident on the rear side too, leading to a higher rear irradiance fraction than for clear-sky conditions. Second, because of the set-up and location, i.e. 30-degree tilt and latitude 51° N, in the summer months the rear sides of the panels are exposed to direct irradiance in the early and late hours of the day, leading to rear irradiance fractions in the range 50–90%.

Fig. 8(a) shows the difference in I_{sc} for the bifacial and monofacial modules; for all front-irradiance conditions, I_{sc} is larger for the bifacial module than for the monofacial one. The shape of the ΔI_{sc} curves is very similar to that of the rear irradiance curves in Fig. 7 for the same albedo. Fig. 8(b) shows the difference in V_{oc} ; at a high front irradiance, $G_f > 600\text{W/m}^2$, the difference in V_{oc} for high and low albedos is very similar, around 0.1V, despite the much higher I_{sc} for the bifacial module under these conditions.

In low front-irradiance conditions, the difference between the values for low and high albedos is much larger. Whereas at low albedo the ΔV_{oc} is around 0V between 100 and 400W/m², at high albedo the ΔV_{oc}

Figure 8. Average differences in (a) I_{sc} and (b) V_{oc} for the bifacial and monofacial modules, as a function of the front irradiance.



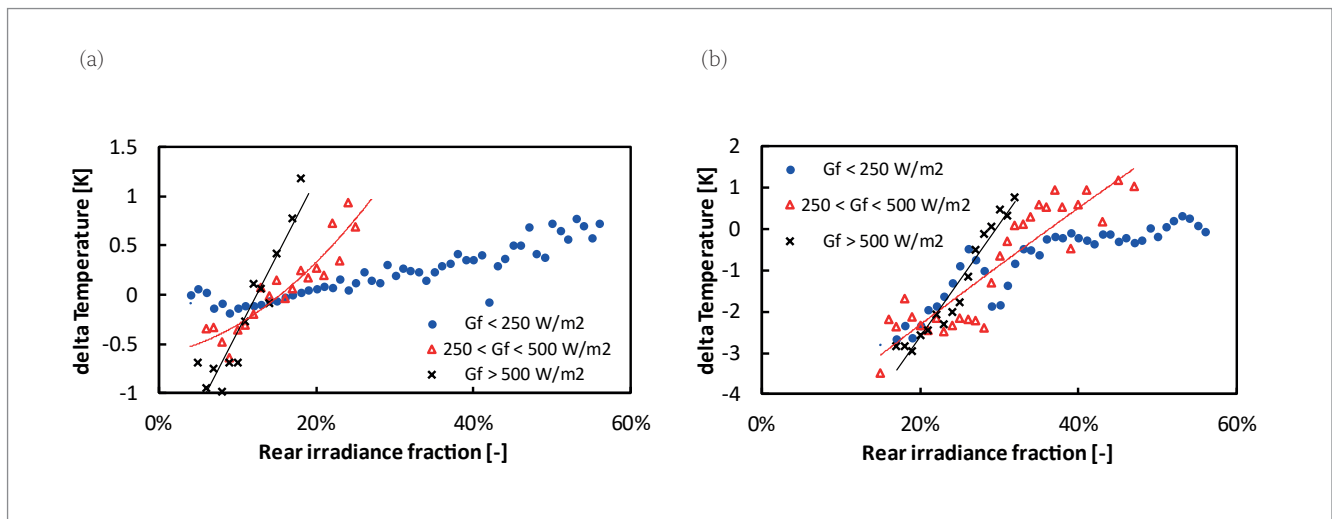


Figure 9. Average differences in module temperature as a function of the rear irradiance fraction for bifacial and monofacial modules: (a) low albedo; (b) high albedo. The data have been split into three groups: low irradiance $<250\text{W/m}^2$, intermediate irradiance, and high irradiance $>500\text{W/m}^2$. Lines have been drawn as visual references. (Note: a negative ΔT means that the bifacial module is cooler than the monofacial module.)

starts to increase. Below 100W/m^2 front irradiance, the average V_{oc} of the bifacial modules becomes much larger than that of the monofacial modules. This reflects the direct irradiance on the rear of the modules at the end of the day during the summer months, and that at low irradiance, the V_{oc} is more sensitive to additional irradiance. The bifacial V_{oc} is higher, despite the possibly higher module temperature under those low front-irradiance conditions.

Fig. 9 shows the average of the difference in module temperature between bifacial and monofacial modules for low and high albedo conditions as a function of the rear irradiance fraction. For both albedo conditions, the data have been divided into three front irradiance groups. At high albedo the minimum rear irradiance fraction is 16%, whereas at low albedo the minimum rear irradiance fraction is 4%. In addition, the range of the rear irradiance fraction is smaller for the high front irradiance group ($>500\text{W/m}^2$) than for the low front irradiance group ($<250\text{W/m}^2$).

The two graphs in Fig. 9 show the same behaviour: 1) with increasing rear irradiance fraction, the ΔT increases; 2) the slope of this trend increases with increasing front irradiance group; 3) at low rear irradiance fraction, the bifacial module is cooler, by 1 to 3K, than the monofacial module; and 4) at high rear irradiance fraction, the bifacial module is warmer, by up to 1K, than the monofacial module. It is important to realize that in the conditions that lead to warmer bifacial modules, i.e. rear irradiance fraction $>30\%$, the increase in voltage and current will yield a much larger increase in output power

than the $\sim 0.5\%$ decrease in power due to the increased module temperature.

These findings corroborate what had been deduced from the lab experiments. Fig. 4 showed that with increasing rear irradiance, the effective heat input for the bifacial module type increases faster than for the WBS module architecture. Thus, with increasing rear fraction, the bifacial heat input increases faster, leading to a larger increase in bifacial module temperature. Consequently, with increasing rear irradiance fraction, there is a shift from cooler bifacial modules at low rear irradiance (fraction) to warmer bifacial modules at high rear irradiance (fraction).

To summarize, at high rear irradiance fractions, bifacial modules can be warmer; how much depends on the irradiance level as well. The total decrease in energy yield, however, will be small, and if this occurs at a high albedo, the resulting additional yield gain will still be significant.

Conclusions

Background theory and indoor and outdoor measurements have been presented in order to provide a better understanding of the differences in thermal behaviour between monofacial and bifacial modules.

The effective heat input Q_{eff} for monofacial and bifacial solar cells and modules is derived from energy spectra on the basis of indoor measurements. This information is used as input for the module characteristics in ECN.TNO's bifacial energy yield model BIGEYE [12]. Although Q_{eff} increases faster with rear irradiance for glass–glass samples than for monofacial modules, under outdoor conditions the increase in device temperature is identical for Al-BSF cells, irrespective of rear panel material. For n-PERT solar cells in glass–glass mini-modules, a lower temperature than that for monofacial n-PERT devices is even found. This can be explained by the glass–glass modules having a higher heat transfer

“Even in cases where high rear irradiance leads to warmer bifacial modules, the energy gain due to the bifaciality is much higher than the eventual losses due to slight heating.”

coefficient U , just as was found from indoor heating curves under constant irradiance. Clearly, the higher U compensates for the higher Q_{eff} .

On ECNTNO's rooftop installation, it was shown that at high rear irradiance fractions, bifacial 60-cell modules can be warmer; how much warmer depends on the irradiance level as well. The total contribution to the yield, however, will be small, as these conditions typically occur at low total irradiance, although at high albedo the additional power is still significant. Under high front-irradiance conditions, when the rear irradiance fraction is low the bifacial module is cooler, despite the rear irradiance photocurrent generation.

To conclude, even in cases where high rear irradiance leads to warmer bifacial modules, the energy gain due to the bifaciality is much higher than the eventual losses due to slight heating. Changes in the bill of materials, e.g. to account for thinner glass, could shift the cross-over point by increasing the effective heat transfer U , and thus decrease the steady-state temperature of the bifacial PV panels relative to monofacial ones, even under high albedo conditions.

References

- [1] Olukan, T.A. & Emziane, M. 2014, "A comparative analysis of PV module temperature models", *Energy Procedia*, Vol. 62, pp. 694–703.
- [2] Dekker, N.J.J. et al. 2015, "Accurate yearly yield calculation using PV module fingerprint method – Applied for MWT, H-pattern and thin film module", *Proc. 31st EU PVSEC*, Hamburg, Germany, pp. 2047–2050.
- [3] Hansen, C. et al. 2017, "A detailed performance model for bifacial PV modules", *Proc. 33rd EU PVSEC*, Amsterdam, The Netherlands, pp. 2395–2400.
- [4] SolarWorld 2015, "Calculating the additional energy yield of bifacial solar modules", White Paper [<https://www.solarworld-usa.com/~media/www/files/white-papers/calculating-additional-energy-yield-through-bifacial-solar-technology-sw9002us.pdf?la=en>].
- [5] Soria, B. et al. 2016, "A study of the annual performance of bifacial photovoltaic modules in the case of vertical facade integration", *Energy Sci. Eng.*, Vol. 4, No. 1, pp. 52–68.
- [6] Lopez-Garcia, J., Pavanello, D. & Sample, T. 2018, "Analysis of temperature coefficients of bifacial crystalline silicon PV modules", *IEEE J. Photovolt.*, Vol. 8, No. 4, pp. 960–968.
- [7] Tiedje, T., Yablonovitch, E.D.C.G. & Brooks, B.G. 1984, "Limiting efficiency of silicon solar cells", *IEEE Trans. Electron Dev.*, Vol. 31, pp. 711–716.
- [8] Baker-Finch, S.C. et al. 2014, "Near-infrared free carrier absorption in heavily doped silicon", *J. Appl. Phys.*, Vol. 116, No. 6, 063106.
- [9] Clugston, D.A. & Basore, P.A. 1997, "Modelling free-carrier absorption in solar cells", *Prog. Photovolt: Res. Appl.*, Vol. 5, pp. 229–239.

[10] Vogt, M.R. et al. 2015, "Numerical modeling of c-Si PV modules by coupling the semiconductor with the thermal conduction, convection and radiation equations", *Energy Procedia*, Vol. 77, pp. 215–224.

[11] Romijn, I.G. et al. 2012, "Industrial implementation of efficiency improvements in n-type solar cells and modules", *Proc. 27th EU PVSEC*, Frankfurt, Germany, pp. 533–537.

[12] Janssen, G.J.M. et al. 2018, "How to maximize the kWh/kWp ratio: Simulations of single-axis tracking in bifacial systems", *Proc. 35th EU PVSEC*, Brussels, Belgium, pp. 1573–1577.

[13] Roest, S. et al. 2017, "Single side versus double side illumination method IV measurements for several types of bifacial PV modules", *Proc. 33rd EU PVSEC*, Amsterdam, The Netherlands, pp. 1427–1431.

[14] Hoang, P. et al. 2014, "Coupling optical and thermal models to accurately predict PV panel electricity production", *Sol. Energy Mater. Sol. Cells*, Vol. 125, pp. 325–338.

[15] Van Aken, B.B. & Carr, A.J. 2014, "Relating indoor and outdoor performance of bifacial modules", *Proc. 40th IEEE PVSC*, Denver, Colorado, USA, pp. 1381–1383.

About the Authors

Dr. Bas Van Aken is a specialist scientist on the systems, modules and applications team in the solar energy research group at ECNTNO, focusing on fabrication, reliability and (outdoor) performance of bifacial and back-contact modules. He previously worked on thin-film Si solar cells processed by PECVD. After gaining a Ph.D. in solid state chemistry at the University of Groningen in the Netherlands, he worked as a postdoc at Cambridge University and at the Max Born Institute for Nonlinear and Ultrafast Optics in Berlin.

Dr. Gaby Janssen received a Ph.D. in quantum chemistry from the University of Groningen. After joining ECN, she worked as a research scientist on the simulation, characterization and optimization of materials for energy conversion technologies, in particular fuel cells. In 2011 she joined the solar energy department, now a research group, at ECNTNO, where she focuses on simulation and modelling of PV cells and modules. Over the last few years she has developed an energy yield prediction model for bifacial systems.

Enquiries

ECNTNO – Solar Energy
PO Box 15
1755 ZG Petten
The Netherlands

Email: basvanaken@tno.nl

Half-cell solar modules: The new standard in PV production?

Jens Schneider, Hamed Hanifi, David Dassler, Matthias Pander, Felix Kaule & Marko Turek, Fraunhofer Center for Silicon Photovoltaics CSP, Halle (Saale), Germany

Abstract

Solar modules with half-size solar cells have the potential for becoming the new standard. The cutting of cells leads to electrical recombination losses at the cell level, which are more than compensated by reduced resistive losses as well as by current gains at the module level. At the same time, the cutting process must be optimized to avoid mechanical damage that could lead to cell breakage in the module. Module design opportunities for hot-spot protection, shading resistance and energy yield optimization are presented in this paper. Module power can be increased by 5–8%, which justifies the investment in additional equipment for cell cutting, stringing, lay-up and bussing. Half-cell technology is highly attractive for new solar module production capacity.

Motivation

An increasing number of solar module producers offer half-cell solar modules. According to ITRPV 2018 [1], the market share of half-cell solar modules is expected to be close to 40% in ten years' time. But why are half-cell modules becoming more relevant now? How large is the performance benefit and what investment is required? What is important to keep in mind and what side effects can be expected? This paper presents an overview of half-cell solar modules.

In general, half-cell modules generate higher power and energy yield through the reduction in electrical losses. Electrical losses in solar cell interconnections increase with the square of the electrical current, as defined by Ohm's law. Cutting the cells in half cuts the current in half, and the electrical losses are reduced to one quarter of the full-cell losses [2,3]. It is important to note that only series resistance losses in the cell tabs are affected. Series resistance losses at the cell level are not reduced, since the series resistance of an individual half cell is twice the resistance of a full cell, while, at the same time, the number of cells in the module is doubled, offsetting all benefits.

Why are half-cell modules only now attracting increasing interest? One reason is that the increase in solar wafer and cell size from 156mm (M1) to 161.7mm (M4) in wafer length increases the cell area and current by about 7%, and thus the electrical losses by 15%; this has stimulated the interest in current-related loss reduction. The reduced shading from cell metallization and the increase in the number of busbars also further increase cell currents. Moreover, improvements in wafer and cell process uniformity allow the sorting of full cells, rather than remeasuring half cells after cutting, which decreases the amount of

work associated with half-cell modules. Half-cell modules will be discussed next in more detail.

Cell cutting technologies

All commercially available silicon solar cells of half-cell dimension are produced in a two-step production process. First, the standard full-size solar cells are manufactured; there is no change in the processing required, except for a possible adaptation of the metallization layout. In a second step, the half-cell cutting process takes place, for which there are two major technological approaches available: laser scribing and (subsequent) cleavage (LSC) and thermomechanical-induced cell separation (TMC).

The first approach – LSC – relies on a laser ablation process, creating a full-length scribe along the half-cell edge. In some cases, this scribe does not yet fully separate the cell, but results in a groove with a depth of about one half of the cell's thickness. Subsequently, a mechanical breakage of the cell occurs, which is guided by the laser scribe. Since the laser process causes some structural damage to the material [4], the scribing is typically performed from the back side in order to avoid a shunting of the p-n junction; in this case, the laser process can be employed in a more efficient manner if there is a small gap in the rear-side metallization. For passivated emitter and rear contact (PERC) solar cells with a full-area rear-side passivation, such a gap in the rear-side metallization does not lead to any power loss. At Fraunhofer CSP, a more advanced version of this LSC process has been developed and filed for patent. The Fraunhofer CSP version relies on the application of the laser process to a slightly bent solar cell; this mechanical preload results in a one-step process in which the laser scribing and breakage occur simultaneously within the same processing unit [5].

The second approach – TMC – is based on a non-ablative process, where a small crack is induced, which then propagates by imposing a highly localized thermal gradient on the material along the half-cell edge; this thermal gradient leads to some local mechanical stress within the cell, resulting in propagation of the crack. For this process, there are already some half-cell tools commercially available (or under development), for example from German laser tool suppliers 3D-Micromac AG or Innolas Solutions GmbH. As these TMC processes are ablation free and

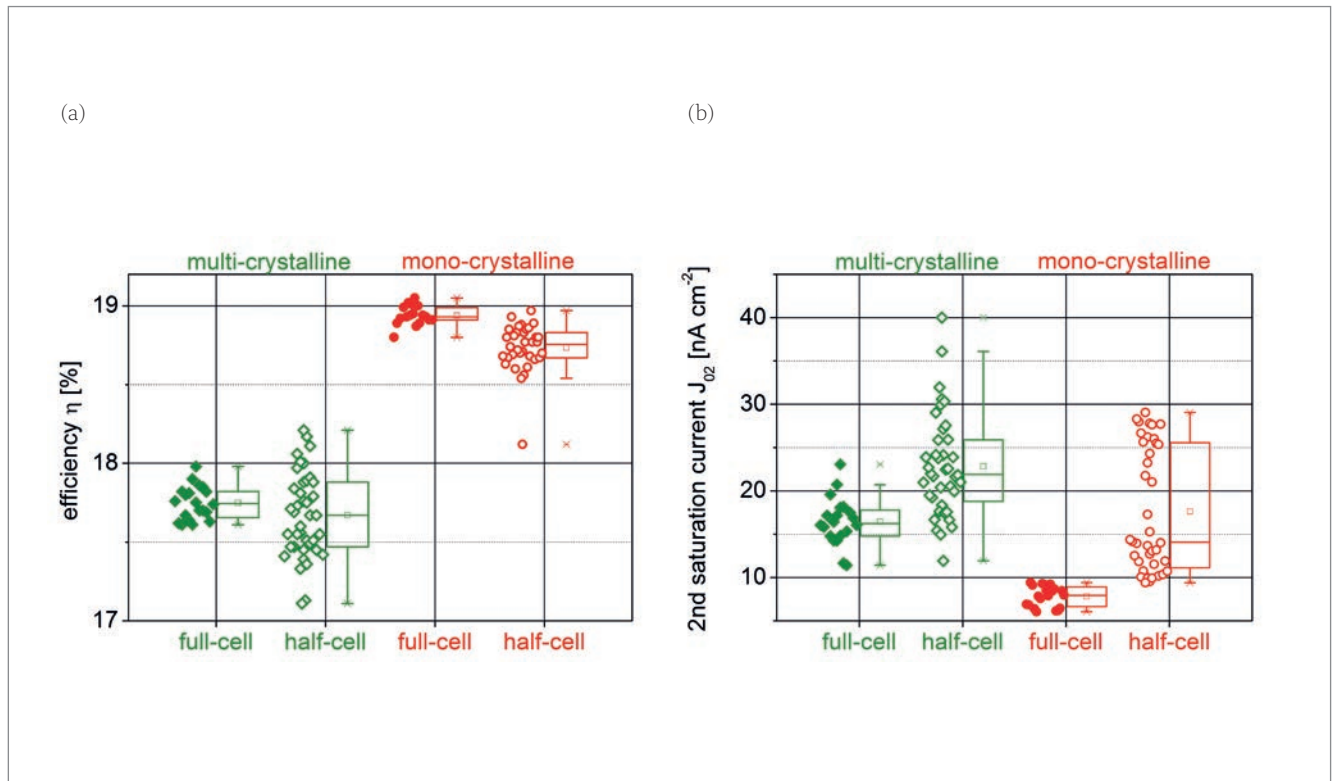


Figure 1. (a) Reduced cell efficiency resulting from the cutting process, caused by (b) the increase in the second saturation current density J_{02} [2].

have reduced total thermal impact, the structural damage can be decreased once an optimized set of process parameters has been determined.

Electrical properties

Two major quality issues must be considered with regard to the half-cell processing. First, the electrical losses due to the additional cell edge have to be minimized. Second, the mechanical strength, and thus the reliability, have to be maintained. As regards the electrical properties, it has been found that even an optimized half-cell process leads to some minor electrical losses of about 0.5%_{rel.} in the cell, caused by some additional recombination processes at the half-cell edge [6–8]. This is reflected in an increase in the J_{02} current contribution to the current losses (see Fig. 1).

While the efficiency of a half cell is slightly reduced, this is more than compensated by the gains at the module level; these gains can be distinguished into three physical mechanisms. First, the reduced cell current leads to a reduction in series resistance losses in the cell tabs, to one quarter of the full-cell module losses. Depending on cell type, these losses can add up to about 3% of the module power and are reduced to 0.75%, i.e. by about 2.25%. The resulting power gain is related to a reduction in series resistance and an improvement in fill factor of the module.

Second, the increased number of cells also leads to an increased number of cell spaces. Via reflection from the backsheet, the cell spaces contribute to a gain in short-circuit current [9]. Although an increase in total cell spacing also

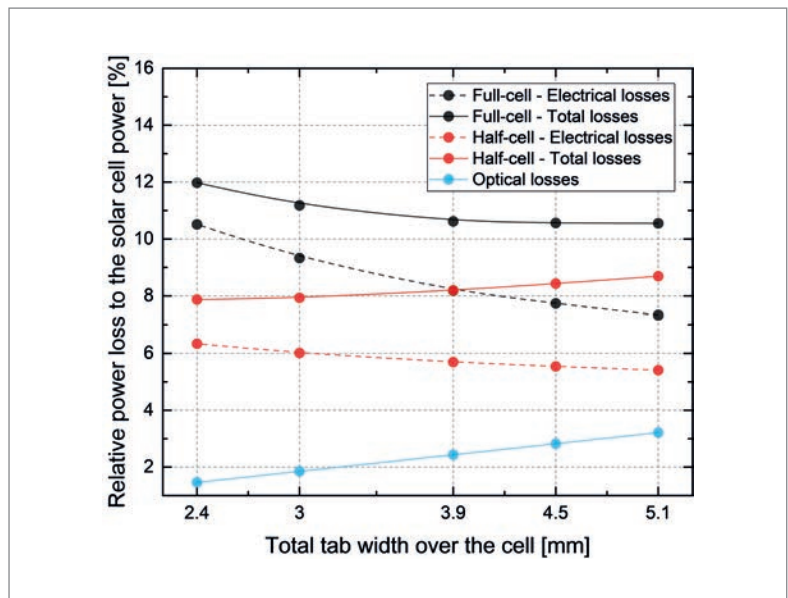


Figure 2. Electrical, optical and overall power loss of full-cell and half-cell mini-modules as a function of total tab width of all cell tabs, under standard test conditions (STC).

leads to a larger module in general and a higher cost of materials, these parameters should be reoptimized when moving to half cells. When the cell spacing between half-cell and full-cell modules is kept constant, an increase in short-circuit current of up to 3% is found [3]. Optimization of

“While the efficiency of a half cell is slightly reduced, this is more than compensated by the gains at the module level.”

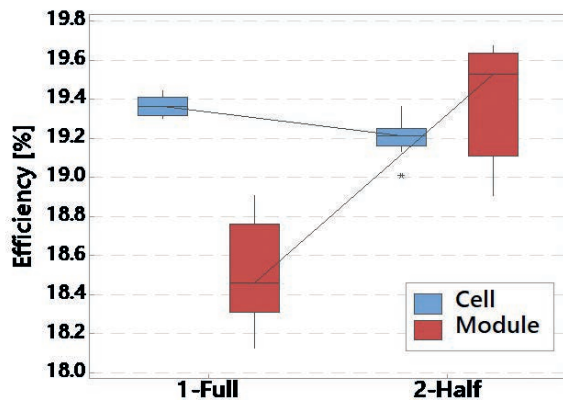


Figure 3. Solar cell and module efficiency for full cells and half cells. While half cells have slightly lower efficiency than full cells, the effect is far more than offset at the module level under STC [11].

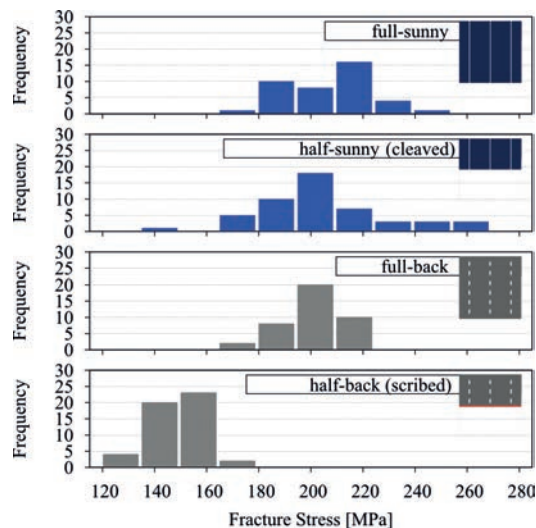


Figure 4. Results for cell breakage frequency of full- and half-size solar cells, with fracture stress applied to the cleaved sunny side and laser-scribed back side of the cells. Significantly lower fracture stresses are observed when the cells are stressed on the laser-scribed edges.

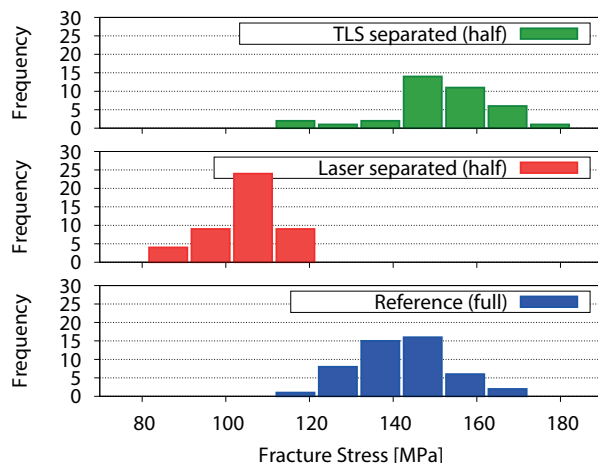


Figure 5. Results for cell breakage frequency of full-size reference and half-size solar cells cut by thermal laser separation (TLS) and by laser scribing and cleavage (LSC). The TLS process often results in no detectable damage to the half-size cells.

the module power and geometry can be nicely carried out using Fraunhofer ISE's Smart.Calc tool [10] (see also www.cell-to-module.com).

A third opportunity for improvement lies in reoptimizing the cell tab width. The cell tab cross section should be large in order to minimize electrical losses. While cell tab thickness is limited to about 200µm by mechanical properties (especially the impact on cell breakage), the width is optimized between reducing electrical losses with wider tabs and reducing optical shading losses with narrower tabs. When electrical losses are reduced, the optimum width obviously changes as well. Fig. 2 shows both optical and electrical losses of a single-cell full-cell mini-module and a comparable double-cell half-cell mini-module under standard test conditions (STC). The *optical losses* for both mini-modules are the same. The *electrical losses* in the half-cell mini-module, however, are less than those in the full-cell mini-module because of reduced current passing through the tabs. The optimized tab width for half cells based on total losses is around 0.8mm, which is about 50% of the optimized value of 1.7mm for a full-cell layout. As a result, the combined optical and electrical power loss is reduced from 10.5% to 8%, equating to 2.5%_{rel.}

Thus, whereas the *solar cell* power is reduced by more than 0.5%_{rel.}, the *solar module* power is increased, more than offsetting all losses; this is demonstrated in Fig. 3, where cell and module efficiencies for full and half cells are shown (note: module efficiency is calculated using total cell area). From the graph, it is also clear that half-cell modules are able to increase the cell-to-module (CTM) power ratio to above 100% [10]: while the CTM ratio for a full cell is only 93%, the half-cell module has a CTM ratio of even 101%, compared with the full-cell efficiency reference. In other words, the half-cell module efficiency with optimized cell spacing and tab width is 8%_{rel.} higher than the full-cell module efficiency.

Mechanical properties

The mechanical strength of the half cells is the key parameter affecting production yield and module reliability. Any reduction in mechanical cell strength leads to an increased breakage likelihood during the module operation in the field. The half cells have a lower characteristic strength than full cells. By testing cell strength from the sunny side and the back side (see Fig. 4), it was shown that the cells are mechanically damaged from the rear; thus, it is the laser scribing and not the cleaving that leads to mechanical damage.

The mechanical properties of the half cells depend, in a very subtle way, on the details of the half-cell processing and the mechanical full-cell properties. However, it has been found that TMC processes fairly generally lead to less mechanical damage than LSC approaches [6,8]. In Fig. 5, the

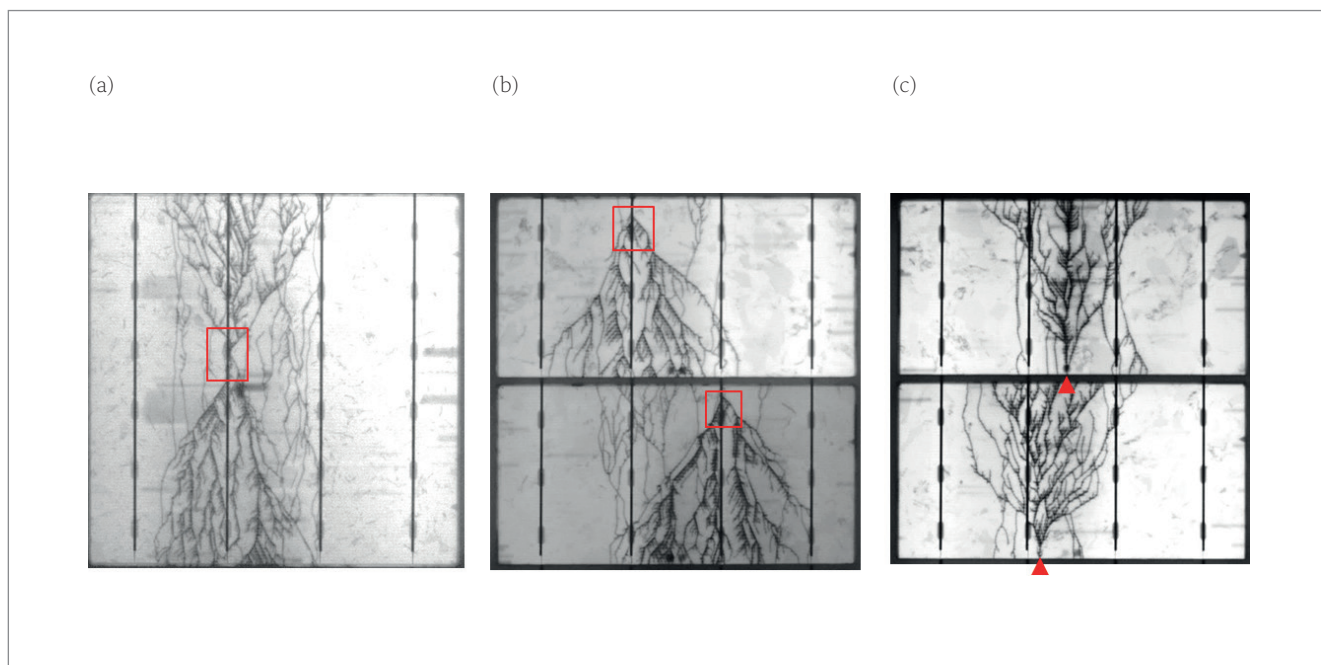


Figure 6. EL images (contrast and brightness adjusted) of broken cells from the module laminate fracture tests, with fracture origin (red square) at the busbars for (a) full cells and (b) TLS, and at the cutting edge for (c) LSC [8].

fracture stresses for cells with thermal laser separation (TLS), a type of TMC, and with LSC, and for reference cells are shown. The TLS process did not demonstrate any reduction in fracture stress; this means that it is possible to cut solar cells without incurring mechanical damage.

An increased failure rate of the solar cells is directly related to an increased failure of the cells within the modules [8]. In a four-point bending (4-PB) setup of solar modules with an in situ electroluminescence (EL) control [12], it was possible to show that half-size solar cells cut with the LSC process, and incorporated in a module laminate, are inclined to break at the laser-scribed and cleaved edge, while reference full cells, as well as half cells cut by an optimized TLS process, tend to break at the busbars; this can be seen in the EL images in Fig. 6, taken during the 4-PB experiment. Breakage of the LSC cells occurs at the laser edge at lower stresses, relevant to wind and snow loads. It is therefore particularly important to optimize and control the mechanical properties of the half cells after cutting, in order to avoid potential failure resulting from excessive cell breakage in the field.

Module redesign

Half-size cells mean that there are also twice the number of cells. To allow for bypass diodes to protect 20 to 24 cells from hotspots, module redesign is necessary, with two parallel strings on one bypass diode. At the same time, this has the advantage of similar current and voltage values compared with full-cell modules. There are two design options for half-cell modules: portrait and landscape, each with centralized or decentralized junction boxes.

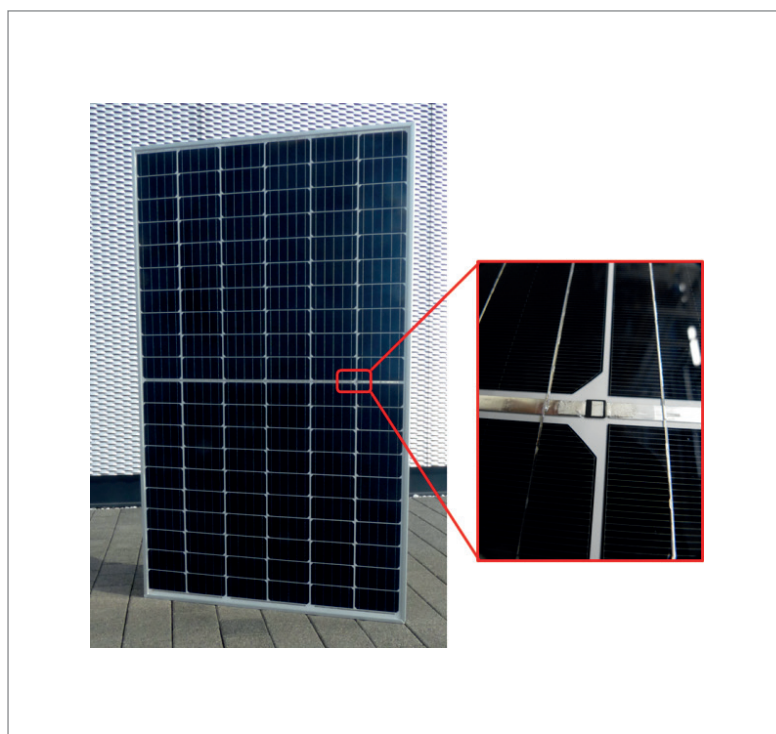


Figure 7. A half-cell module in the portrait layout, showing the integrated bypass diode, fabricated at Fraunhofer CSP.

Portrait design

In the portrait design, the module is divided into an upper and a lower block; each block has six substrings of 10 or 12 half cells connected in series. The upper and lower blocks are connected

“It is particularly important to optimize and control the mechanical properties of the half cells after cutting.”

in parallel, with bypass diodes protecting each of the parallel substrings.

Most commonly, half-cell modules are produced in the portrait design. BP Solar (BP3270T) started with 144 half cells, while Bosch Solar Energy (c-Si M60+ S) offered modules with 120 half cells with a centralized junction box. REC Solar offers their 'TwinPeak technology' half-cell module in the portrait design and decentralized junction boxes, which require fewer interconnecting ribbons inside the module and also require shorter cable sizes to connect the modules to the neighbouring modules. Fraunhofer CSP presented a portrait half-cell module with integrated bypass diodes inside the laminate (see Fig. 7). The integration of bypass diodes inside the laminate leads to a reduction in the number of distributed junction boxes from three to two, and to a decrease in material consumption.

Landscape design

Mitsubishi (PV-MLE Series) introduced a 120-half-cell module in the landscape design, while SERIS and Fraunhofer CSP presented a module with 144 half cells in a landscape design in 2013. The latter module has twelve substrings with twelve half cells, which are arranged in parallel two by two and then connected in series. The layout makes it possible to use the standard glass size for a 72-cell full-cell module. The module is aligned in a landscape orientation, and the junction box can be either centralized or decentralized and located on the top side of the module. The two-by-two interconnection of half-cell modules with a landscape layout makes them more resistant than the equivalent full-cell modules under partial shading conditions [3,13,14].

Energy yield

All previous considerations have been in relation to solar module *power* under STC, so a closer look will now need to be taken at *energy yield*. Three things to bear in mind regarding the energy yield of half-cell modules are:

1. Half-cell modules are more shading tolerant.
2. Benefits of half-cell modules very much depend on high insulation.
3. Lower losses in half-cell modules might allow them to operate at a slightly lower temperature.

In a full-cell layout, when a solar cell is being shaded and exceeding a specific shading percentage, the related string will be bypassed by the bypass diode. This process is dependent on the area of the solar cell being shaded, and the shading shape or direction is not relevant. On the other hand, half-cell modules with a landscape design exhibit a higher capacity to withstand partial shading conditions. The parallel interconnection of substrings in half-cell modules with a landscape design makes it possible to generate current in one substring while the other substring is partially shaded. This shading tolerance is highly

microCELL™

Highly Productive Laser Systems for Half-Cell Cutting



- » Excellent edge quality by TLS-Dicing™
- » Upmost throughput in the market:
 - > 5.500 wph on single lane
- » On-the-fly laser processing
- » Contactless single-pass and ablation-free cutting
- » Unbeatable cost-benefit ratio



3D-Micromac AG
Micromachining Excellence
www.3d-micromac.com

dependent on the shading direction (or module orientation). In the case of the shade moving along the y axis and shading one half cell completely (equivalent to 50% shading of one full cell), one substring cannot generate current, whereas the other one still produces current. In the case where the shade moves along the x axis, after 50% shading of two half cells the affected substring still produces electrical current [13,14]. Fig. 8 shows the power–voltage curves for half- and full-cell modules under different partial shading conditions. The high tolerance of half-cell modules makes these particular modules resistant in the case of, for example, dust accumulating in the corners of the modules.

Two solar modules with 72 full and 144 half cells on Fraunhofer CSP's outdoor roof test lab were measured over the period 08/2013 to 04/2014 (see Fig. 9). While the module power difference under STC conditions was 4.6%_{rel.}, the average energy yield difference was only 3%_{rel.}.

To carry out a comparison of the energy yields with respect to the irradiation and module temperature, the measured energy yields were evenly distributed and averaged in intervals of 50W/m² irradiation and 2°C module temperatures of the half-cell module. Fig. 10 shows that with increasing irradiation and module temperature, the difference between the energy yields increases. A relative yield difference of up to 6% between the half-cell and full-cell module was measured at high irradiation conditions. Under low-irradiation conditions, the energy yield difference can drop to less than 2% [15]. Higher irradiance leads to larger module currents and greater electrical losses; thus, the benefits for half-cell modules are greater

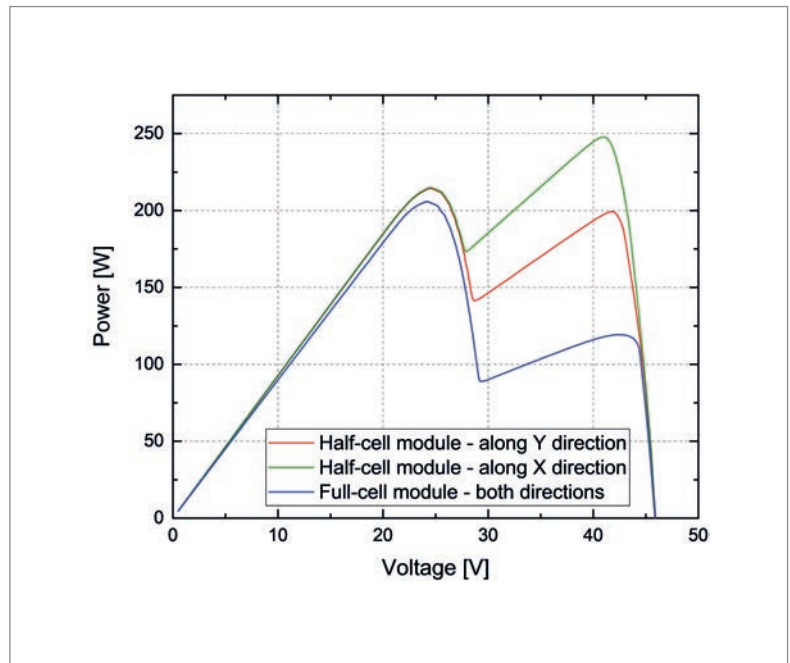


Figure 8. Power–voltage curves for comparable half-cell and full-cell modules, when one solar cell or two half cells are affected by 70% shading in two different directions. The half-cell module shaded along the x direction still has all its strings in operation [14].

at higher irradiance. Half-cell solar modules are consequently particularly well suited to applications in high-irradiation regions in sunbelt areas; for example, in Morocco an additional gain of up to 2.2% is expected, as compared to 1.5% in Germany [11].

“Half-cell solar modules offer many benefits and have the potential for setting a new standard technology.”

Figure 9. A half-cell module (left) and a full-cell module (right), installed at Fraunhofer CSP's ‘Outdoor PV Lab Halle’ outdoor setup.



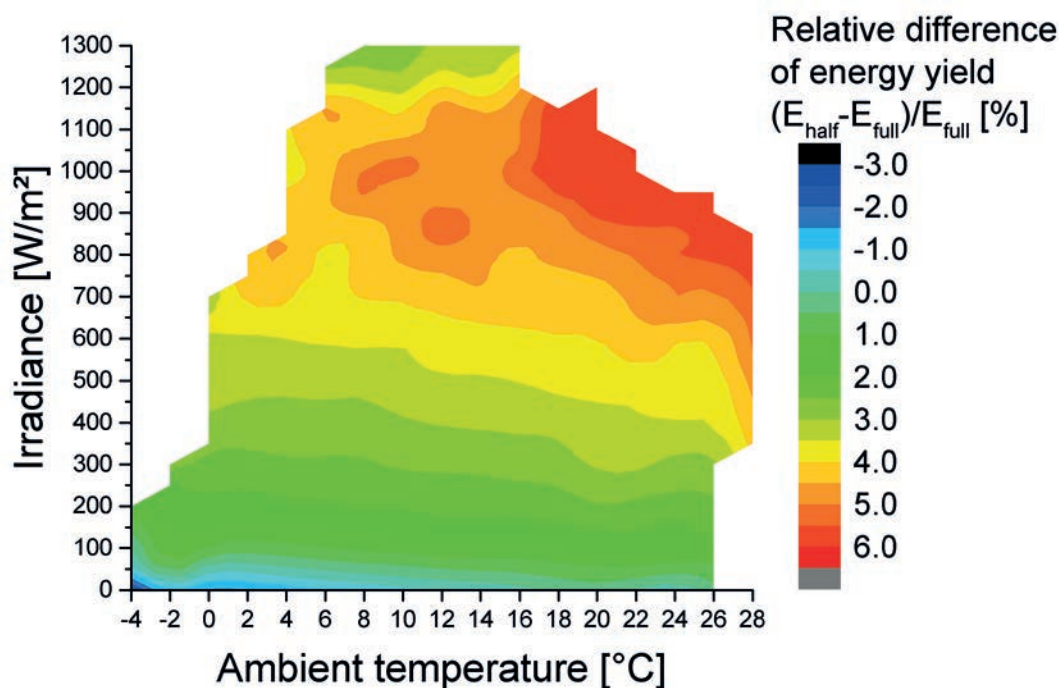


Figure 10. Relative yield gain of the half-cell module compared with the full-cell module $(E_{\text{half}} - E_{\text{full}}) / E_{\text{full}}$. The measured yield values for each module were summarized according to irradiation and temperature, and then averaged (intervals: 50W/m² irradiance, 2°C module temperature).

Investment analysis

On the assumption that a solar module factory produces one module per minute for 24 hours and 365 days per year at 300W per module, the total output is 158MW per year. If the module power is increased by 5% for half-cell modules, an extra 7.9MW is generated each year. At \$0.2 per Wp module sales price, an extra earning of more than \$1.5m per year is feasible; this extra margin would have to pay for an additional cell cutting tool, double tabber–stringer capacity, modification of lay-up and bussing. A decentralized junction box must be sourced at a similar cost to a central one. Since particularly the cell cutting tool and the additional tabber–stringer capacity require additional floor space, it is much easier to plan new solar module production capacity in a half-cell design than to retrofit existing lines. For new solar module lines, the payback period should be less than one year, making half-cell solar module lines extremely attractive.

Summary

Half cells offer a simple route to achieving substantial power gains in solar modules. A power gain of up to 5% is possible with an optimized module layout without a change in size, and up to 8% with larger modules. Payback periods of below one year are expected for new solar module lines. Half-cell solar modules are particularly well suited to sunbelt regions, since the power gain is only translated to an energy yield gain and a leveled

cost of electricity (LCOE) reduction when the irradiance is high. The solar cell cutting process must be sufficiently well controlled with regard to mechanical properties, in order to avoid cell cracking and performance losses in the field.

Once low-damage processes are under control, further developments in solar modules can include even smaller cells with multiple cuts in one direction, such as shingle cells and modules, or in two directions for more flexible module designs.

Half-cell solar modules offer many benefits and have the potential for setting a new standard technology for quite some time, at least until new module technologies are developed.

References

- [1] ITRPV 2018, "International technology roadmap for photovoltaic (ITRPV): 2017 results", 9th edn (Mar.) [<http://www.itrpv.net/Reports/Downloads/>].
- [2] Schneider, J. et al. 2014, "Solar module with half size solar cells", *Proc. 29th EU PVSEC*, Amsterdam, The Netherlands, p. 185.
- [3] Guo, S. et al. 2015, "Investigation of the short-circuit current increase for PV modules using halved silicon wafer solar cells", *Sol. Energy Mater. Sol. Cells*, Vol. 133, pp. 240–247.
- [4] Schönfelder, S. et al. 2006, "Strength characterization of laser diced silicon for application in solar industry", *Proc. 21st EU PVSEC*, Dresden, Germany, pp. 588–592.

- [5] Schneider, J., Schönfelder, S. & Kaufmann, K. 2016, "Method for splitting of plate-shaped objects made of brittle materials", European Patent Appl. No. EP2990172A1.
- [6] Eiternick, S. et al. 2014, "Loss analysis for laser separated solar cells", *Energy Procedia*, Vol. 55, pp. 326–330.
- [7] Eiternick, S. et al. 2015, "High quality half-cell processing using thermal laser separation", *Energy Procedia*, Vol. 77, pp. 340–345.
- [8] Kaule, F. et al. 2018, "Mechanical damage of half-cell cutting technologies in solar cells and module laminates", *AIP Conf. Proc.*, Vol. 1999, No. 1, 020013.
- [9] McIntosh, K.R., Swanson, R.M. & Cotter, J.E. 2006, "A simple ray tracer to compute the optical concentration of photovoltaic modules", *Prog. Photovolt: Res. Appl.*, Vol. 14, pp. 167–177.
- [10] Haedrich, I. et al. 2014, "Unified methodology for determining CTM ratios: Systematic prediction of module power", *Sol. Energy Mater. Sol. Cells*, Vol. 131, pp. 14–23.
- [11] Hanifi, H. et al. 2016, "Optimized tab width in half-cell modules", *Energy Procedia*, Vol. 92, pp. 52–59.
- [12] Sander, M. et al. 2013, "Systematic investigation of cracks in encapsulated solar cells after mechanical loading", *Sol. Energy Mater. Sol. Cells*, Vol. 111, pp. 82–89.
- [13] Lu, F. et al. 2013, "Improved PV module performance under partial shading conditions", *Energy Procedia*, Vol. 33, pp. 248–255.
- [14] Hanifi, H., Schneider, J. & Bagdahn, J. 2015, "Reduced shading effect on half-cell modules – measurement and simulation", *Proc. 31st EU PVSEC*, Hamburg, Germany, pp. 2529–2533.
- [15] Malik, S. et al. 2014, "Outdoor data evaluation of half-/full-cell modules with regard to measurement uncertainties and the application of statistical methods", *Proc. 29th EU PVSEC*, Amsterdam, The Netherlands, p. 3269–3273.

About the Authors



Jens Schneider received his Ph.D. from Technische Universität Berlin and Hahn-Meitner-Institut Berlin. He worked for CSG Solar AG from 2005 to 2011 in process development, after which he joined Fraunhofer CSP as the module technology group manager. In 2014 he became a professor at Leipzig University of Applied Science, teaching photovoltaics and sector coupling. He transferred to the Fraunhofer Center for the Economics of Materials CEM in 2019, where he is involved in directing efforts in energy system analysis.



Hamed Hanifi received his master's in electrical power engineering from Brandenburg University of Technology (BTU) in Cottbus, Germany, in 2015. Since then he has been pursuing his Ph.D. at Martin

Luther University Halle-Wittenberg, with a focus on PV module optimization for desert applications. Since 2015 he has also been working at Fraunhofer CSP, as well as at Anhalt University of Applied Sciences in Koethen, Germany, as a scientific researcher, where he specializes in optimization of cell-to-module power ratios of standard modules, and in optimization of PV modules for desert applications.



David Dassler received his M.Sc. in applied mathematics from Leipzig University of Applied Sciences. Since 2012 he has been working at Fraunhofer CSP in the reliability of solar modules and systems group, specialising in yield analysis. In 2015 he began his Ph.D., with a thesis topic of yield modelling in desert climates.



Matthias Pander studied mechanical engineering at the Leipzig University of Applied Sciences. He graduated in 2010 with a master's, for which his thesis dealt with the simulation of thermomechanical stresses in embedded solar cells. He works on PV module simulation and reliability testing in the reliability of solar modules and systems group at Fraunhofer CSP.



Felix Kaule studied mechanical engineering at HTWK Leipzig. Since 2012 he has been working as a research scientist in the mechanics of wafers and cells team at Fraunhofer CSP. His research focuses on strength analysis of silicon wafers and cells by means of the finite-element method and statistical evaluations.



Dr. Marko Turek studied physics at Dresden University, and received his Ph.D. in the field of condensed matter theory from the University of Regensburg. At Fraunhofer CSP he leads the team involved with electrical characterization of solar cells and modules. His research focuses on loss analysis of solar cells, advanced characterization methods and development of new test methods and devices.

Enquiries

Jens Schneider
Fraunhofer Center for Silicon Photovoltaics CSP
Otto-Eissfeldt Str. 12
06120 Halle (Saale), Germany

Advertisers and web index

ADVERTISER	WEB ADDRESS	PAGE NO.
3D Micromac AG	www.3d-micromac.com	133
Aiko Cells	en.aikosolar.com	5
bifiPV workshop	bifipv-workshop.com	121
Borealis AG	www.borealisempoweringsolar.com	14
DK Electronic Materials, Inc	www.dkem.cn	55
Ecoprogetti srl	www.ecoprogetti.com	108
Energy Taiwan 2019	www.energytaiwan.com.tw	37
EU PVSEC 2019	www.photovoltaic-conference.com	61
Exateq GmbH	www.exateq.de	75
Henkel AG & Company, KGaA	henkel-adhesives.com/electronics	39
Heraeus Photovoltaics	www.heraeus-photovoltaics.com	Outside Back Cover
IEEE 46th PVSC	www.ieee-pvsc.org/PVSC46	73
Innolas Solutions GmbH	www.innolas-solutions.com	33
Intersolar 2019	www.intersolar.de	10
JA Solar	www.jasolar.com	Inside Front Cover
MBJ Solutions GmbH	www.mbj-solutions.com	109
Meco Equipment Engineers B.V	www.besi.com	87
Meyer Burger	www.meyerburger.com	7
Mondragon Assembly	www.mondragon-assembly.com	41
PV IndiaTech 2019	indiatech.solarenergyevents.com	17
PV ModuleTech 2019	moduletech.solarenergyevents.com	12, 139
RENA	www.rena.com	91
Schmid Group	www.schmid-group.com	31
Sentech Instruments GmbH	www.sentech.com	99
Singulus Technologies AG	www.singulus.de	89
SNEC PV Power Expo 2019	www.snec.org.cn	28
VITRONIC Dr.-Ing. Stein	www.vitronic.com	19
Von Ardenne GmbH	www.vonardenne.biz	93
Wavelabs	www.wavelabs.de	107

To advertise within Photovoltaics International, please contact the sales department: Tel +44 (0) 20 7871 0122

THE INDISPENSABLE GUIDE FOR MANUFACTURERS IN SOLAR

NEXT ISSUE:

- Implementing Industry 4.0
- R&D spending trends
- Next-gen PERC

Photovoltaics International contains the latest cutting edge research and technical papers from the world's leading institutes and manufacturers.

Divided into six sections – Fab & Facilities, Materials, Cell Processing, Thin Film, PV Modules and Market Watch – it is an essential resource for engineers, senior management and investors to understand new processes, technologies and supply chain solutions to drive the industry forward.

An annual subscription to **Photovoltaics International**, which includes four editions, is available at a cost of just \$199 in print and \$159 for digital access.

Make sure you don't miss out on the ultimate source of PV knowledge which will help your business to grow!



SUBSCRIBE TODAY: www.photovoltaiicsinternational.com/subscriptions



Mono PERC cell production to lead solar industry in 2019

Back in 2014, p-type mono PERC cell production was less than 1GW. During 2019, production is forecast to exceed 60GW as the dominant technology type deployed by the solar industry for module assembly.

The dramatic growth in production has also been matched by continuous cell efficiency and module power improvements, including a new record (24.06%) in the past few days announced by LONGi Solar.

This article discusses the factors that have led to the dramatic growth in p-type mono PERC production in the past few years, cell efficiency increases, and how p-type mono PERC performance will continue to set the benchmarks for new n-type entrants in China over the next 12-18 months.

The topics covered in this article will also be featured in the forthcoming PV CellTech 2019 conference in Penang, Malaysia on 12-13 March 2019, in which many of the CTO's and head-of-R&D will be presenting on company technology roadmaps for the coming years.

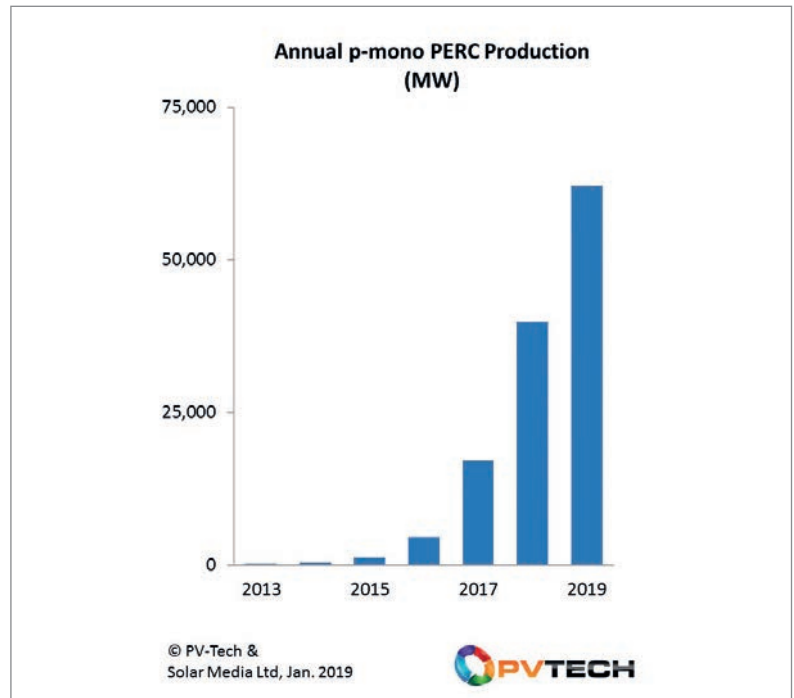
Growth of p-mono PERC

The use of rear passivation layers had originally been confined to highly advanced cell concepts such as heterojunction and interdigitated back-contact cells, with mainstream p-type cells using the established screen-printed Al-BSF method.

Depositing passivation layers on p-type cells was well established in the research community however, but was not justified before based on equipment cost and the additional complexity in cell lines. Moving away from screen-printing was recognized as key in opening up the rear surface for additional benefits such as bifaciality, not to mention any industry move to wafer thicknesses being reduced to below about 120 microns.

During 2012 to 2014, front pastes improved significantly, with increased bus-bar formation also driving efficiencies higher with minimal capex. Once front surface cell processing had gone through these improvement phases, it was time for the industry to focus on the rear surface, with the first evidence that rear passivation layers would quickly move to mainstream status.

The graphic above illustrates how much PERC has been adopted by p-mono cell producers. Indeed, during 2019, more than 50% of cell production in the industry will be from p-mono PERC; a dramatic growth trajectory rarely seen so quickly in the PV industry before.



Efficiency improvements

The growth in cell production has also been matched by a collective drive from the industry to push R&D and mass-production cell efficiencies well above the 20% level, and into territories previously considered by market observers to be the sole domain of n-type variants.

Average cell efficiencies in mass production for p-mono PERC cells have moved from initial levels of about 19% to over 21% at the end of 2018, with record levels from commercial pilot-line or R&D lines on full-size cells at levels well above this.

Indeed, most recently, LONGi Solar has recently reported another world record for full-cell size p-mono PERC cells at above 24%.

Setting the benchmark for n-type cell additions

The continued capacity expansions and efficiency increases seen from p-mono PERC based cell producers is coming also at a time when investments in n-type alternative (in particular n-PERT and HJT) are being seen in the industry.

While in the past, any new n-type entrant would benchmark performance against the two existing cell makers of n-type advanced cells (SunPower and Panasonic), today it is p-type mono PERC (and bifacial variants) that is setting the levels that these new n-type entrants need to match at a bare minimum, to justify their existence.

During 2019, p-mono PERC cell production will exceed 60%, making the technology the dominant source of module shipments during the year.

"Well defined scope and speakers covering the whole topic of PV modules"

Ronald Sastrawan, Munich Re

"A must-attend for procurement professionals looking to make smart technology choices"

Brian O'Rorke, BNRG Renewables

**20% OFF FOR
OUR READERS.
USE CODE **PVTP****



PVMODULETECH CONFERENCE

22-23 OCTOBER 2019
Penang, Malaysia

Understand the technical and logistical supply chains that determine the production and performance of solar modules.



moduletech.solarenergyevents.com

ORGANISED BY:



SOLAR MEDIA
EVENTS | PUBLISHING | RESEARCH

Heraeus Photovoltaics – Leading the Future of PV



- ☀ High quality metallization products
- ☀ One-stop total solution of PV value chain
- ☀ Efficiency gains 0.2% every year
- ☀ Sophisticated customer modification solution
- ☀ Fast responding technical services

VISIT US AT SNEC 2019

Shanghai, China | June 4 – 6, 2019
Booth W3-510

www.heraeus-photovoltaics.com

Heraeus Photovoltaics
LinkedIn



Heraeus Photovoltaics
Website

